



**HAL**  
open science

# Applications of time-resolved spectroscopy for microenvironment sensing and biomolecular interactions studies

Anastasia Ioanna Skilitsi

► **To cite this version:**

Anastasia Ioanna Skilitsi. Applications of time-resolved spectroscopy for microenvironment sensing and biomolecular interactions studies. Physics [physics]. Université de Strasbourg, 2017. English. NNT : 2017STRAE029 . tel-01777947v2

**HAL Id: tel-01777947**

**<https://theses.hal.science/tel-01777947v2>**

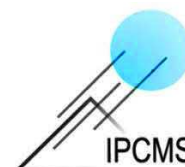
Submitted on 25 Apr 2018

**HAL** is a multi-disciplinary open access archive for the deposit and dissemination of scientific research documents, whether they are published or not. The documents may come from teaching and research institutions in France or abroad, or from public or private research centers.

L'archive ouverte pluridisciplinaire **HAL**, est destinée au dépôt et à la diffusion de documents scientifiques de niveau recherche, publiés ou non, émanant des établissements d'enseignement et de recherche français ou étrangers, des laboratoires publics ou privés.



UNIVERSITÉ DE STRASBOURG



*ÉCOLE DOCTORALE PHYSIQUE ET CHIMIE-PHYSIQUE*

Institut de Physique et Chimie des Matériaux de Strasbourg

**THÈSE** présentée par :

**Anastasia Ioanna Skilitsi**

soutenue le: **30 Novembre 2017**

pour obtenir le grade de : **Docteur de l'Université de Strasbourg**

Discipline/ Spécialité: **Physique**

---

# **Applications of time-resolved spectroscopy for microenvironment sensing and biomolecular interactions studies**

---

**DIRECTEUR DE THÈSE:**

**Dr. Léonard Jérémie**

Chargé de recherche CNRS, IPCMS

**RAPPORTEURS :**

**Dr. Ameer-Beg Simon**

Professeur, King's College London

**Dr. Mérola Fabienne**

Directeur de Recherche, Université Paris Sud

**EXAMINATEURS :**

**Dr. Didier Pascal**

Professeur, Université de Strasbourg

**Dr. Hassiepen Ulrich**

Research Investigator, Novartis Basel



# Contents

I.	Introduction .....	9
II.	Concepts and methods .....	13
II.1.	Elements of molecular photophysics.....	13
II.1.1	Photophysics of isolated molecules.....	13
II.1.2	Molecular photophysics influenced by their microenvironment.....	18
II.1.3	Excited State Lifetime.....	27
II.2.	Time Resolved Spectroscopy.....	29
II.2.1	Time Resolved Fluorescence Spectroscopy .....	29
II.2.2	Transient Absorption Spectroscopy .....	38
II.3.	Data Fitting .....	44
II.3.1	Multiexponential kinetics .....	44
II.3.2	Fitting Function .....	46
II.4.	Out-of-equilibrium experiments.....	48
II.4.1	Introduction .....	48
Stopped flow .....		49
Continuous flow .....		51
Droplet Microfluidics.....		52
II.4.2	Micro-droplets formation and mixing.....	53
II.4.3	Droplet Microfluidics combined with Time Resolved Fluorescence Spectroscopy	61
III.	4'-methoxy-3-hydroxyflavone: One of a kind fluorescent dye for protein structure sensing	65
III.1.	Introduction .....	65
III.1.1	3-Hydroxyflavone family.....	66
III.2.	Methods.....	71
III.3.	Results .....	79

IV. Cyan Fluorescent Protein and its H148G variant-Correlation of protein structures with their fluorescence properties.....	105
IV.1. Introduction .....	105
IV.1.1 Fluorescent proteins.....	106
IV.1.2 Enhanced Cyan Fluorescent Protein (ECFP) .....	108
IV.1.3 Mutants of Cyan Fluorescent Protein.....	110
IV.2. Methods.....	116
IV.2.1 Absorption and emission spectra .....	116
IV.2.2 pH Jump conditions .....	117
IV.3. Results .....	121
IV.3.1 Detection of spectral dependence .....	121
IV.3.1 pH Jump experiment.....	127
IV.4. Discussion and Conclusions.....	131
V. Towards sensitive, high-throughput, biomolecular assays based on fluorescence lifetime .	133
V.1. Introduction.....	133
V.1.1 High-throughput biosensing- application areas .....	134
V.1.2 Droplet Microfluidics for High-throughput bioassays .....	135
V.1.3 Fluorescence-based detection techniques used in High throughput biosensing .....	136
V.1.4 Fluorescence lifetime techniques for High throughput screening- Challenges to overcome.....	140
V.2. Time Correlated Single Photon Counting .....	142
V.2.1 Principle .....	142
V.2.1 Poisson Noise/ Shot Noise .....	142
V.2.2 Pile up effect .....	143
V.2.3 Which is the adequate amount of photons? .....	146
V.2.4 Experimental section .....	148
V.2.1 Field Programmable Gate Array (FPGA) .....	153
V.3. Application on a high throughput Enzymatic activity assay .....	157
V.4. Discussion and Conclusions.....	170

VI.	Publications.....	171
VII.	Final Conclusions and Perspectives.....	175
VIII.	Bibliography.....	178

**Φτάσε όπου δεν μπορείς!**

**Reach where you cannot!**

Αυτό θες, κατά κει με σπρώχνεις, κατά κει μ'έσπρωχνες πάντα, άκουγα μέρα νύχτα την προσταγή σου, μάχουμουν, όσο μπορούσα, να φτάσω όπου δεν μπορούσα, αυτό είχα βάλει χρέος μου, αν έφτασα ή δεν έφτασα, εσύ θα μου πεις. Όρθιος στέκουμαι μπροστά σου και περιμένω.

Στρατηγέ μου, τελεύει η μάχη, κάνω την αναφορά μου, να που πολέμησα, να πως πολέμησα, λαβώθηκα, δείλιασα, μα δε λιποτάχτησα, τα δόντια μου καταχτυπούσαν από το φόβο, μα τύλιγα σφιχτά το κούτελό μου μ'ένα κόκκινο μαντίλι, να μην ξεκρίνονται τα αίματα, κι έκανα γιουρούσι.

Ένα ένα μπροστά σου τα φτερά της καλιακούδας μου ψυχής θα τα μαδήσω, ωσότου ν'απομείνει ένα σβωλαράκι χώμα κι αυτή. Θα σου πω τον αγώνα μου, ν'αλαφρώσω, θα πετάξω από πάνω μου την αρετή, την ντροπή, την αλήθεια, ν'αλαφρώσω.

**Νίκος Καζαντζάκης (1883-1957) “Αναφορά στον Γκρέκο”**

**Nikos Kazantzakis (1883-1957) “Report to Greco”**

# Acknowledgements

First of all, I would like to express my sincere gratitude to my PhD supervisor Dr Jeremie Leonard for his guidance and assistance during the last three years. I learnt a lot on his side, concerning not only experimental physics but also research curiosity, willingness to go in depth in every observation and exploring new ideas and approaches to reach a better understanding. Thanks for everything Jeremie.

I would like to express my thanks to the collaborators in all of the projects that I have been involved. These are: Yves Mely, Andrey Klymchenko, Helene Pasquier, Wilfried Uhring, Timothe Turko, Ulrich Hassiepen and Sophie Barre. It has been a pleasure and an honor to work with all of you. Special thanks to Olivier Cregut, our laser-technician-magician for all the enormous help and guidance in the lab. IPCMS is just a building but with Olivier it becomes a research facility.

I owe many thanks to the extended biodyn-group lab members, both past and present members. These are: Damianos, Johanna, Vincent, Yussef, Li, Arthur, Edoardo, Fatema, Mussa, Thomas, Alex and Stefan. Thank you guys for all the long days spent together, for your help, your guidance, your ideas, your laughter, your jokes, your encouragement, your presence, your patience, the coffee breaks, the lunches, the merendinas etc. You have been a real second family for me; I would have not made it without you. Furthermore the CNRS-rugby-team was a wonderful break from my routine, we spent lots of fun and active moments together, thanks you guys!

Lots of thanks go to my friends and acquaintances. Huge thanks go to my close-friends that most live far but very-very close to my heart. These are: Giorgos (Germany), Georgia (Cyprus), Lamis (Netherlands) and Panos (UK). Thank you guys for sharing my good and bad moments, for being there, for understanding and loving me. You are my shelter and I am really lucky to have you in my life and be part of yours.

Last and most importantly, I am grateful to my family: My parents, Maria and Sotiris, and my brothers, Haris and Giorgos. They have always supported unconditionally my crazy dreams and ideas. They helped me develop my personality and be the person that I am today. My dearest mom has always stood by me like a pillar in all times believing and seeing great things in me that I could not see. My beloved dad recently passed away but I am sure he will watch me becoming a doctor and be proud of me from up there. The minimum thing I can do is to dedicate this degree to my family. No words can be enough to thank you.

Thank you all so much!



# I. Introduction

In the past decades, interactions and networks of interactions have revolutionized the understanding of relationships between biomolecular interactions, cellular function and disease. The in-depth understanding of biomolecular dynamic interactions is central to diagnosis and disease treatment<sup>1</sup> as well as for highly-functional products design, such as nanoparticles applied in food industry<sup>2</sup>, cosmetics etc.

The fundamental characteristic of biomolecular interactions for functional adaptability and versatility is their structural heterogeneity, i.e. coexistence of multiple molecular conformations. Structures, relative abundances and dynamics of the different conformers need to be identified as they hold crucial information on the biological mechanism at the very molecular level. Several high or very high spatial resolution techniques such as Nuclear Magnetic Resonance Spectroscopy (NMR), mass spectrometry, Atomic Force Microscopy (AFM) etc. have been applied in this direction<sup>3-9</sup>. However in most cases they reveal average structures and thus are not considered the best candidates to resolve structural heterogeneity. On the other hand fluorescence spectroscopy methods have been proven to be powerful tools for the quantitative and qualitative investigation of homologous and heterologous biomolecular interactions. Despite providing relatively low spatial resolution, time-resolved or single-molecule fluorescence spectroscopies remain unique in disentangling structural heterogeneity, structural intermediates, highly fluctuating or intrinsically disordered conformations<sup>10-13</sup>.

Time-Resolved Fluorescence (TRF) spectroscopy has long been an important arrow in the quiver of fluorescence spectroscopy, applied to investigate biomolecular interactions and structure. To this end, environment-sensitive fluorophores may be used to synthetically label biological macromolecules and report on their local structural changes. Such structural probes are chosen or specifically functionalized to take advantage of changes in their fluorescence properties in response to a physicochemical modification of their microenvironment, such as difference in polarity, hydrogen bonding, pH, presence of quenchers etc.

TRF monitors events taking place during the lifetime of the chromophore excited singlet state. This time scale ranges from subpicoseconds to tens of nanoseconds. Photophysical events occurring in this time domain include interaction with solvent molecules or local structural

conformational changes gating the interaction with neighboring amino acid residues or nucleotides. Generally, the fluorescence decay kinetics is resolved in terms of multi exponential components, where the values of time constants and their corresponding amplitudes are associated with particular conformations and their relative populations. Though the quantitative structural interpretation is challenging and requires a deep understanding of the fundamental photophysical mechanism controlling the emissive properties of the fluorophores. Besides, large-scale conformational changes in biomolecules, such as protein folding or ligand binding, which connect to the effective biological functions, occur on time scales significantly slower<sup>14,15</sup> (ms to sec) than those accessible with TRF. Other experimental approaches may be used, such as stopped-flow experiments, to trigger on a short-enough time scale the out-of-equilibrium conditions which result in slower structural dynamics or population exchange between the subpopulations revealed e.g. by TRF spectroscopy. In this context, the present thesis has applied time-resolved spectroscopy to investigate the photophysics of different environment-sensitive molecular systems, but also as a bio-sensing approach to reveal molecular interactions or structural dynamics on a much slower time scale, using droplet microfluidics to trigger structural relaxation through out-of-equilibrium initial conditions. Three projects were developed in the present PhD and were collaborations with interdisciplinary areas of science.

First, transient absorption (i.e. pump-probe) and time resolved fluorescence spectroscopies were used to perform a fundamental investigation of the photoreactivity of a derivative of 3-Hydroxychromone<sup>16,17</sup>, named 4-Methoxy-3-Hydroxyflavone (4M3HF), in different solvents varying polarity and H-bonding capabilities. This fluorophore undergoes an ultrafast excited-state intramolecular proton transfer<sup>18</sup> and exhibits solvent-sensitive dual emission which turns out to be controlled by the H-bonding capabilities of its microenvironment. It was recently functionalized as a synthetic, fluorescent amino acid or nucleotide and shown to be a very promising structural probe for the investigation of protein-DNA interactions in particular<sup>19</sup>. The target was to rationalize the effect of the micro-environment (solvent in this context) on the photophysics of this probe in order to rationalize the structural information revealed by the probe when it is covalently incorporated in a biomolecule.

As a second environment-sensitive molecular probe, focus was brought on the fluorescence properties of two derivatives of the green fluorescent protein, namely Enhanced-Cyan Fluorescent Protein (ECFP) and one of its mutants. These proteins undergo pH-sensitive

structural conformations resulting in the alteration of the fluorescence decay kinetics. In the present work, it was performed an in depth investigation of the proteins' structural relaxation kinetics upon pH jump. To this end, droplet microfluidics have been used to initiate out-of-equilibrium conditions by rapid mixing ( $\leq 1$  ms) within the very small (few 100 pl) volume of water-in-oil droplets. This allows the characterization of pH-induced structural relaxation dynamics (during the time scale of droplets propagation in the microfluidic channel) while revealing the transient structural heterogeneity (encoded in the fluorescence multiexponential decay kinetics).

Finally, with a more applied research target, we have been exploring the implementation of TRF by Time-Correlated Single Photon Counting (TCSPC) in very high throughput conditions as a mean to perform efficient biomolecular interactions/activity assays, appealing both for academic and industrial arenas. In this topic, the originality was the effort to replace fluorescence intensity detection by fluorescence lifetime detection, which is technologically more challenging. The advantage for bio-sensing, however, is that the fluorescence lifetime of a fluorophore is an intrinsic measure of the fluorophore interacting with its environment, remaining unaffected by set-up or sample preparation conditions. The combination of the above mentioned tools with an innovative engineering approach (microelectronics) led to the demonstration that TCSPC can be implemented in very high-throughput conditions in droplet microfluidics. Advantages of the present setup are the high precision, the remarkable low material consumption and most remarkably the high speed of the measurements, reaching kHz sample (droplet) rate.

In conclusion, this PhD work explored the use of UV-Vis time-resolved spectroscopy for the investigation of biomolecular interactions in a comprehensive manner, spanning from 1) the in-depth investigation of the emissive properties of biosensors in order to allow their quantitative use in biomolecular interaction studies, to 2) the development of an original experimental approach to enable resolving the structural relaxation kinetics of an out-of-equilibrium distribution of biomolecular structures, and finally 3) the technological application of TRF for precise, rapid, cost effective, biomolecular interaction assays.



## II. Concepts and methods

In the present chapter, the photophysical concepts underlying the use of fluorescent chromophores are introduced for microenvironment sensing in general and biomolecular interaction sensing in particular. We also describe the experimental approaches used throughout this PhD work to investigate the influence of the environment on the photophysical properties of various chromophores. These are time-resolved fluorescence (TRF) and UV-Vis transient absorption (TA, i.e. pump-probe) spectroscopies. We also demonstrate the droplet microfluidics approach that has been utilized, in combination with TRF, for two distinct purposes. On the one hand we have explored the use of microfluidics for creating out-of-equilibrium conditions and investigating the kinetics of the resulting biomolecular structural changes, (by implementing TRF alongside droplet circulation in the microfluidic chip). On the second hand we used droplet microfluidics as an efficient tool for fast handling/manipulation of very small-volume aqueous samples, to explore the applications of TRF for high-throughput biomolecular interaction assays.

### II.1. Elements of molecular photophysics

#### II.1.1 Photophysics of isolated molecules

The Perrin Jablonski diagram visualizes the possible photophysical processes occurring after molecule excitation, without taking into consideration the possible interactions with other molecules or its micro-environment. The possible processes could include: photon absorption (the fastest process), internal conversion (IC), fluorescence emission, intersystem crossing (ISC) and phosphorescence<sup>20</sup>. Herein we will shortly introduce the respective processes which are depicted in the Figure 1.

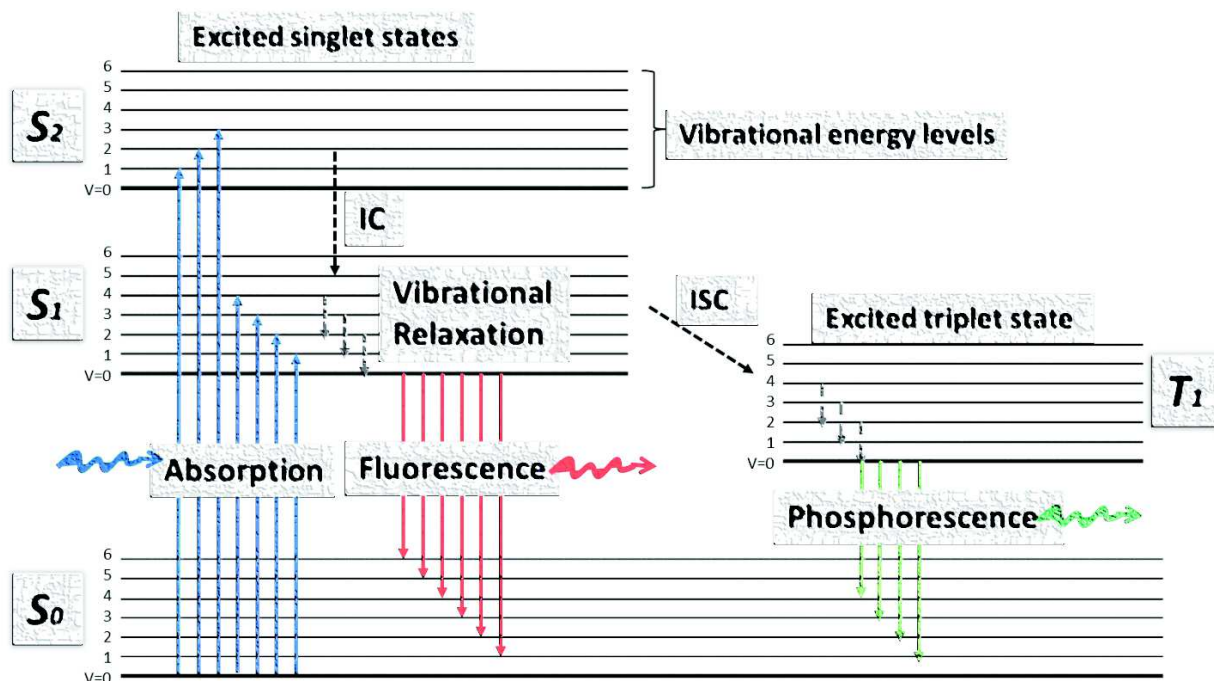


Figure 1-Jablonski energy diagram depicting the transition between electronic states of a molecule. Dashed lines indicate non-radiative transitions, IC stands for internal conversion, ISC stands for intersystem crossing. All of these transitions will be explained in the following parts.

## Photon absorption

Generally the absorbance  $A(\lambda)$  of a sample follows the Beer-Lambert law defined as:

$$A(\lambda) = \log \frac{I_{\lambda}^0}{I_{\lambda}} = \varepsilon(\lambda)lc$$

Where  $I_{\lambda}^0$  and  $I_{\lambda}$  represent the light intensities of the beams entering and exiting the absorptive medium respectively,  $\varepsilon(\lambda)$  is the molar absorption coefficient (expressed in  $L \cdot mol^{-1} \cdot cm^{-1}$ ),  $c$  is the concentration of absorbing species ( $mol \cdot L^{-1}$ ) and  $l$  is the absorption path length (cm).

According to the Born-Oppenheimer approximation, the electron motions are faster than those of the nuclei (molecular vibrations). The promotion of an electron to another molecular orbital upon excitation takes nearly  $10^{-15}$  s (i.e. the optical period), which is rapid in comparison with

molecular vibrations ( $10^{-10}$ - $10^{-13}$  s). This observation leads to the Franck-Condon principle which states that an electronic transition occurs without changes in the positions of the nuclei in the molecular entity and its environment. The resulting state is therefore named Franck-Condon (FC) state.

The FC geometry and ground state solvation shell are, in general, not the equilibrium geometry and solvation shell of the electronically excited state, thus triggering rapid (i.e. sub picosecond) vibrational and solvent dynamics and relaxation in the excited state. This is called intramolecular vibrational relaxation (IVR) and solvent relaxation, or solvation respectively.

## **Fluorescence emission**

The emission of photons from  $S_1$  to the  $S_0$  state (or from any higher state to a lower energetically state) is called fluorescence emission. According to the empirical Stokes Rule, which is dating before the Perrin-Jablonski diagram, the wavelength of a fluorescence emission needs to be higher than that of absorption due to vibrational/solvent relaxation that will be introduced below, and may occur already in the excited state before radiative decay. The energy gap between the maxima of the absorption and fluorescence bands is named Stokes shift.

To this point, it has to be underlined that although emission of a single photon is equally fast process as the absorption ( $\approx 10^{-15}$  s), the fluorescence emission of an ensemble of molecules lasts for much longer time due to the fact that the excited molecules stay for a certain time ranging from tens of ps to hundreds of ns in  $S_1$ , before they may emit a photon. More precisely, as it will be clarified later, fluorescence emission decreases exponentially with a characteristic time which is the average lifetime of the  $S_1$  state.

## **Vibrational relaxation**

The molecules of interest have a specific number of electronic states accompanied with a number of vibrational sublevels<sup>20,21</sup>. After excitation of the molecule, to higher vibrational sublevels of an electronic state, relaxation will take place to lower vibrational sublevels, typically on the sub-ps to few ps time scale.

## **Internal Conversion**

The non-radiative transition between two electronic states of the same spin multiplicity is called internal conversion<sup>20,22</sup>. This process is accompanied by vibrational relaxation to the lowest vibrational level of the final electronic state. Internal conversion is more efficient from  $S_2$  to  $S_1$  because of the smaller energy gap in comparison to the transition from  $S_1$  to  $S_0$ . Thus internal conversion from  $S_1$  to  $S_0$  is a process possibly competing with fluorescence emission and also with intersystem crossing to a triplet state.

## **Intersystem crossing**

Intersystem crossing is a non-radiative process occurring between two iso-energetic vibrational levels belonging to electronic states of different multiplicities<sup>20,23</sup>. Crossing between states of different multiplicity is principally forbidden. However, spin-orbit coupling (coupling of orbital magnetic moment and spin magnetic moment) can be big enough to realize this. Thus the probabilities of having intersystem crossing are solely dependent on the singlet and triplet states of the system.

## Phosphorescence

Whenever an intersystem crossing occurs, phosphorescence may occur<sup>20,24</sup>. It is a radiative process from a triplet or higher spin multiplicity state to the singlet ground state  $S_0$ . Such transitions are also "forbidden", and may occur due to spin-orbit coupling. Therefore the phosphorescence transition probabilities may be very weak, thus possibly resulting in very long triplet state lifetimes (unless other non-radiative, e.g. intersystem crossing to the ground state) contribute shortening the triplet state lifetime.

## II.1.2 Molecular photophysics influenced by their microenvironment

All the processes introduced above occur already in a so-called non-reactive molecule in condensed phase (solvent, or protein environment). In addition, the molecular excited state may become reactive, in a way that depends on its interaction with the environment. If the system is not considered isolated (gas-phase) numerous other processes triggered by the microenvironment interactions can influence the excited state dynamics. A few examples in this category are excitation energy transfer to one or multiple neighboring molecules, solvation (reorganization of the solvent molecules to accommodate the excited-state electronic configuration of the molecule), photo-induced intermolecular reaction (e.g. proton/electron transfer from the excited molecule to a solvent or another molecule in close proximity) etc. Some of these processes will be shortly described followed by examples on environmental sensitive fluorophores in the consecutive pages. The list of these fluorophores is fortunately long and rich. Their response to environment is compelled by excited state reactions, such as conformational changes, proton-electron transfer etc. and non-covalent interactions, such as van der Waals interactions, dipole-dipole etc. and H-bonding interactions. Some of the most commonly studied and applied categories of fluorophores are the molecular rotors, the solvatochromic dyes, the pH sensitive dyes, dyes able to undergo energy or electron/proton transfer and other.

## **Processes that environmentally sensitive fluorophores can reveal**

### **a. Micro-environment relaxation/ solvation and solvatochromism**

Solvatochromism is named the phenomenon where spectral bands exhibit shifts as a result of direct intermolecular interactions in the solute-solvent system. The inaugural observation point of this phenomenon lies in 1970, where Galley and Purkey<sup>25</sup> as well as Rubinov and Tomin<sup>26</sup> reported independently that some organic molecules in frozen organic polar glasses demonstrate fluorescence spectral shifts after excitation on their red edge of absorption spectrum. Both of the teams reasoned these results based not only in molecular vibrations but also in fluctuations of the structure of the solvation shell surrounding the molecules.

Each molecule in the ground state has a specific charge distribution matching the special configuration of its nuclei and electrons. The micro-environment adjusts to this molecular configuration achieving minimum energy of system. However, after excitation of the molecule charge redistribution takes place instantaneously. The micro-environment will sense the difference and re-adjust dielectrically; besides dielectric relaxation shifting of the nuclei and solvent reorientation may occur. The micro-environment rearrangement is described under the term solvation; its rate depends on the mobility of solvent molecules and their dipole moments<sup>27</sup>, as presented in Figure 2. Therefore due to the detected spectral shifts estimation of the micro-environment polarity can be achieved. There are plentiful fields of applications where solvatochromism is utilized; these include characterization of mixed solvents<sup>28,29</sup>, characterization of polymers<sup>30,31</sup> etc. The motivation to study mixed solvents raises because the majority of chemical reactions carried out in the laboratory or in industry take place in a solution, including pure solvents and more usually mixtures<sup>32,33</sup>. Despite their apparent utility, the use of solutions in chemical processes must be analyzed from environmental and safety points of view because solution use is inherently wasteful since is usually added to reactants to promote reaction, and is later removed from the chemical product prior to disposal or reuse. Therefore the development and characterization of environmental friendly solvents is of great interest in the direction of Green Chemistry<sup>34</sup>.

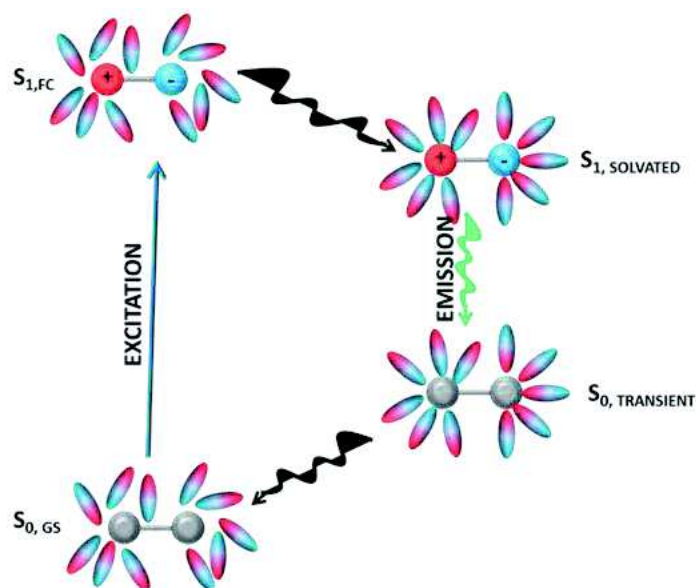


Figure 2-Schematic illustration of solvatochromic phenomenon.

## b. Energy transfer

Fluorescence quenching can occur in molecular interactions through radiative and non-radiative excitation energy transfer<sup>35,36</sup>. Energy transfer can occur either from an excited donor molecule to a chemically different acceptor molecule, referred to as heterotransfer, or from chemically same donor and acceptor, referred to as homotransfer. Numerous are the interaction mechanisms that can initiate energy transfer. These include Coulombic interactions that are composed of long-range dipole-dipole interactions and short-range interactions. The interactions taking place as a result of intermolecular orbital overlap are only short range. On the other hand the long range dipole-dipole interactions are described by the Förster mechanism.

## Förster resonance energy transfer (FRET)

Förster demonstrated that the efficiency of this energy transfer process  $E$  depends on the inverse sixth-power distance between donor and acceptor<sup>37</sup>:

$$E = \frac{1}{\left(1 + \frac{R}{R_0}\right)^6}$$

where  $R_0$  is the distance at which half of the energy is transferred, depending on the spectral characteristics of the dyes and their relative orientation.

Parameter  $R_0$  can be determined from the spectroscopic data, i.e. from the spectra of fluorescence and absorption, and it mainly lies in the order of 15–60 Å<sup>20,38</sup>. Förster resonance energy transfer (FRET)<sup>39</sup> is commonly used as a tool for biomolecular interactions studies in order to report aggregation<sup>40,41</sup>, conformational changes<sup>42,43</sup>, molecular association<sup>44,45</sup>, measure distances<sup>36</sup> etc. Donor and acceptor are covalently linked usually to bigger molecules that are free to move towards or apart from each other. The detected variations in their transfer efficiency will provide essential information regarding their spatial relation. At this point it has to be emphasized that the donor-acceptor pair needs to fulfill certain conditions. They must demonstrate maximal brightness, photostability and well preserved physicochemical properties that are not affected by other microenvironment conditions<sup>46</sup>. A fluorophore playing an essential role in abundant FRET applications will be thoroughly discussed in chapter IV.

### c. Charge transfer

Photoinduced charge transfer is an important category of photoinduced reactions. Proton transfer usually occurs in molecules with easy protonating groups, such as -OH. Two categories of proton transfer exist: intramolecular when the proton leaves one group of the molecule and attaches to another and proton dissociation when the proton leaves the molecule and attaches to a group of its micro-environment. Electron transfer takes place between electron donor and electron receptor, leading to the formation of two radicals (molecules with unpaired electrons). When the charge carrier is captured by an acceptor or by a solvent molecule the donor eventually goes to a distinct (charged) electronic ground state and the charge-separated state may recombine on various time scales. The photoinduced charge transfer is always accompanied by structural changes which may be evidenced by time-resolved spectroscopy and UV-Vis pump probe in particular.

#### **Excited-State Intramolecular Proton Transfer (ESIPT)**

One very interesting example of photoinduced ICT is Excited-State Intramolecular Proton Transfer (ESIPT). 3-hydroxyflavones (3HF)<sup>16,47-49</sup> undergo an ultrafast ESIPT reaction which is the origin of their two, well separated fluorescence emission bands<sup>50-54</sup>. Their relative intensity is highly solvent dependent, and can be used to detect changes in the nature of the molecule microenvironment in a so-called ratiometric detection method<sup>55</sup>. The 3HF molecule after absorption of a quantum of light populate the normal N\* state followed by solvent relaxation. The N\* state can afterwards pursue two different paths, either relax to the ground N state via photon emission or undergo ESIPT forming the tautomeric T\* excited state. The later subsequently decays to the T ground state by photon emission. T state will eventually relax via a proton back transfer occurring in the ground state, thus reforming the initial N ground state. It has to be underlined that all the four states N, N\*, T and T\* have different distribution of charges and this leads to different interaction with their micro-environment. For the intensively studied 4'-dialkylamino-3-hydroxyflavone (see Figure 3), the strongest dipole moment is usually considered

to be in the N\* state <sup>56</sup>, probably due to electronic charge transfer from the 4'-dialkylamino group to the chromone moiety, resulting in a substantial solvatochromism <sup>47,49,57</sup>. On the other side, due to proton transfer, the separation of changes in T\* will be dramatically smaller, verified by the reported much weaker solvatochromism <sup>58</sup>. Thus only the N\* state presents a significant emission red shift as a response to higher solvent polarity. In addition, the significant spectral difference between N\* and T\* enables their band positions as independent variables. An example of 4'-dialkylamino-3-hydroxyflavone (DMA-3HF) is shown in the Figure 3 below<sup>58</sup>.

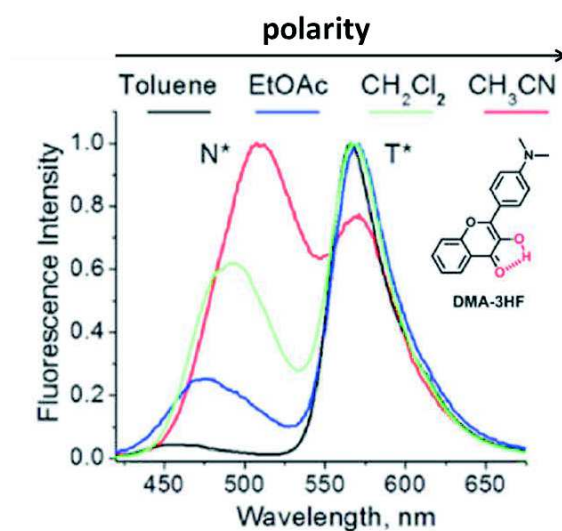


Figure 3-Adopted from<sup>57,58</sup>. 4'-dialkylamino-3-hydroxyflavone dye undergoes ESIPT and exhibits solvent-dependent dual emission.

The ratio between both fluorescence bands intensities is profoundly sensitive to the solvent polarity and hydrogen bonding capability. Hence the ratiometric detection of the fluorescence intensities of both bands may be used for intrinsic probing of the fluorophore microenvironment. Thorough examination of a 3HF derivative will be presented in chapter III.

## Photoinduced Electron Transfer (PET)

PET takes place when the relative electron affinity of two nearby molecular moieties (named donor and acceptor) is strongly modified upon photoexcitation of one of the two. In a fluorophore, the excited state lifetime and therefore fluorescence emission may be significantly quenched by PET when a ‘quencher’ (here electron donor or acceptor) is in close proximity even if they have no ground state interaction<sup>59–61</sup>. This intermolecular reaction is the origin of photosynthesis in plants and artificial systems for solar energy conversion based on photoinduced charge separation<sup>62</sup> as well as for fluorescence probes studying biomolecular reactions<sup>63</sup>. Figure 4 schematically illustrates PET.

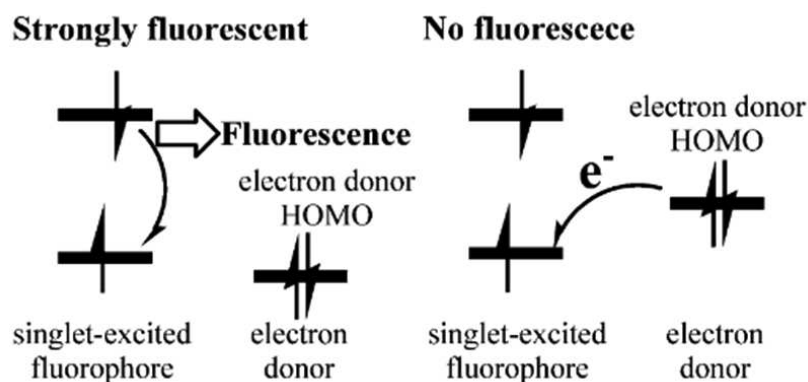


Figure 4-adopted from<sup>64</sup>. On the left, the HOMO (highest occupied molecular orbital) energy level of the electron donor moiety is too low to allow electron transfer. Consequently, emission from the singlet-excited fluorophore is not affected. On the right, the HOMO energy level is high enough to allow electron transfer, thus the fluorescence decreases.

An example of electron transfer in nature is taking place in DNA (Deoxyribonucleic acid)<sup>65–67</sup> molecules. Electrons travel through a multistep hopping process over long distances along the DNA. The electron transfer efficiency is determined by two factors the electron transfer rates and other competing reactions (e.g. with water<sup>68</sup>). A microenvironment sensitive probe which is proposed to undergo efficient PET is 2-Aminopurine (2AP). 2AP is a fluorescent analogue of adenine that has been employed for decades to probe DNA structure at the single nucleic acid

level<sup>69,70</sup>. Its attractive property is that when isolated in solution has a mono-exponential excited-state decay with a lifetime of 10 ns<sup>71,72</sup>, though upon incorporation as a synthetic nucleotide in ssDNA (single-stranded DNA) or dsDNA (double-stranded DNA) sequences, 2AP exhibits a dramatic fluorescence quenching characterized by a distribution of excited-state lifetimes spanning from the subpico- to nano-second time scales<sup>73-76</sup>. The quenching of 2AP fluorescence has long been proposed to derive from pi-stacking interactions with neighboring nucleobases and the broad range of detected times scales implies a diversity of local geometrical arrangements of 2AP with respect to nearby nucleotides<sup>77-79</sup>. 2AP was recently used also by the biodyn team as a mean to characterize the conformational heterogeneity of a DNA hairpin (DNA hairpin is formed when two regions of a single-stranded DNA assemble a helix that ends in a loop with unpaired or non-Watson–Crick-paired nucleotides)<sup>80</sup>.

On another direction, suppression of PET and/or internal charge transfer (ICT) process can lead to OFF/ON fluorescence emission at acidic pH for chemically synthesized dyes (i.e. aza-BODIPY<sup>81</sup>). Overall there are two types of pH sensitive fluorescent probes reported<sup>81</sup>. The first type responds to pH changes around their pKas with distinct change in fluorescence intensity, i.e. the “on/off” or “off/on” probes. The others are called ratiometric probes, which are differentially sensitive to pH at two excitation or emission wavelengths<sup>82-85</sup>. ICT and FRET are the most commonly exploited sensing mechanisms for the design of these ratiometric fluorescent probes<sup>46,86</sup>. pH plays a vital role in numerous intracellular biological processes, including cell growth and differentiation<sup>87</sup>. Abnormal intracellular pH values are associated with many diseases including cancer<sup>88</sup> and Alzheimer's<sup>89</sup>. Therefore the tightly regulated intracellular pH indicates that the explicit measurement and characterization of intracellular pH can provide essential information on cellular functions and pathological processes. This need to develop fluorescent pH sensitive probes lead to the development of a long list of advantageous probes<sup>81,90-92</sup>.

## Twisted Intramolecular Charge Transfer (TICT)

Grabowski et al<sup>93-95</sup> in order to explain the observed dual fluorescence emission of (Dimethylamino)benzonitrile (DMABN)<sup>96</sup>, with a ‘normal’ band (named B band) and an ‘anomalous’ red shifted one (named A band) depending on the conformational freedom of the dimethylamino group; they introduced the Twisted Intramolecular Charge Transfer (TICT) model. Their conclusion was that there is an excited state reaction path from the near planar conformation (emitter of B band) to a photochemical product with an energetic minimum at the perpendicular conformation (emitter of A band). The back reaction, B to A, is also possible leading to an excited state equilibrium<sup>97,98</sup>. The activation energies are involved in both forward and backward reactions and are highly affected by the viscous properties of the solvent<sup>98</sup>. Viscosity is a term describing the measure of the fluid resistance against gradients in flow (shear rate). Shear rate is the rate of velocity change, where one fluid layer passes on top of a second adjacent fluid layer, measured in s<sup>-1</sup>. There are various methods to measure viscosity; one of them is with molecular rotors, which are fluorescent molecules able to form TICT states upon photoexcitation. This leads to two competing de-excitation pathways; photon emission or non-radiative de-excitation from the TICT state<sup>99-102</sup>. Considering that TICT formation is among others (molecular size, geometry, flexibility and temperature) also highly viscosity dependent<sup>103-105</sup>, the fluorescence emission of molecular rotors will also be solvent-dependent. Thus molecular rotors are emerging as novel biosensors able to report on the viscosity of their liquid micro-environment<sup>106-108</sup> but also in living cells, where viscosity has been linked to malfunction and disease<sup>109,110</sup>. Their characteristic is an emission intensity change in response to solvent viscosity change. The high rotational flexibility of their conjugated system results in a poor emission when they are present in non-viscous environments. However when they are present in viscous environment their quantum yield dramatically increases as a response to flexibility restriction<sup>111,112</sup>.

Starting point of synthetically designed molecular rotors was set by Kelly et al who designed and studied a molecular brake based on a molecule able to complex reversibly with Hg<sup>+2</sup> ions and restrict the rotation around its single bond<sup>113</sup>. Many reports followed in the same direction<sup>114-116</sup>.

All the above was a description of some processes that environmentally sensitive fluorophores can reveal upon excitation with immediate consequence on their deactivation processes.

### II.1.3 Excited State Lifetime

The average excited state lifetime is also called fluorescence lifetime. It is dependent on all deactivation processes; radiative and non-radiative, as shown in Figure 5.

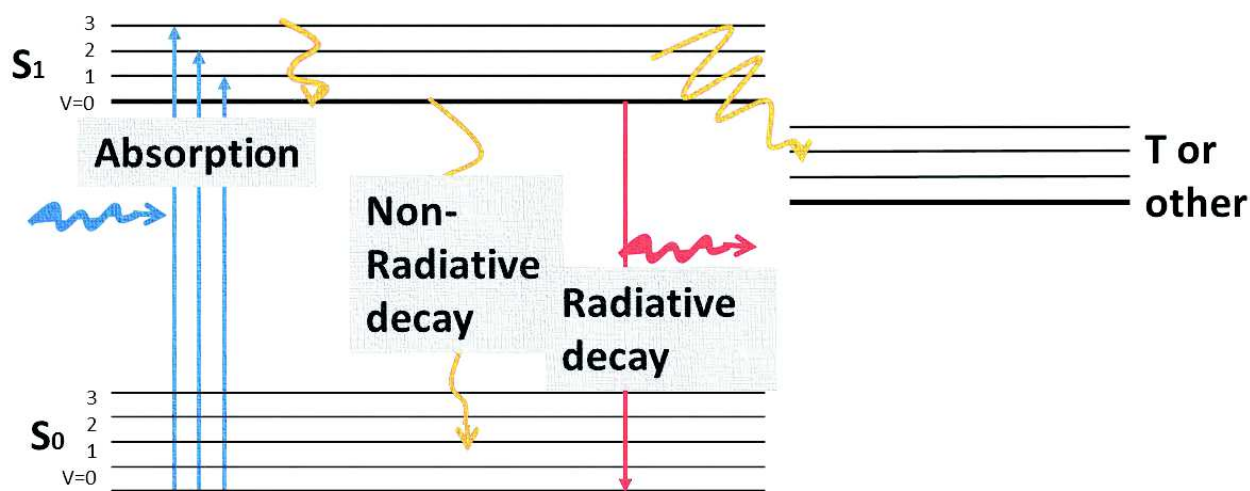


Figure 5-Schematic illustration of radiative and non-radiative de-excitation processes.

Assuming that we describe the kinetics of a population in the excited state with a rate equation then we can write:

$$\frac{dn^*(t)}{dt} = -kn^*(t) + f(t)$$

Here  $n^*$  is the number of the excited molecules,  $f(t)$  is an arbitrary function of time describing the time course of the excitation and  $k$  is the sum of all deactivation rates.

$$k = k_r + k_{non,r}$$

with  $k_r$  the radiative rate and  $k_{non,r}$  the sum of all non-radiative rates.

If the excitation stops at time  $t=0$ , then the decrease of the excited population can be described as following:

$$\frac{dn^*(t)}{dt} = -kn^*(t) \Rightarrow$$
$$n^*(t) = n^*(0)e^{-kt} = n^*(0)e^{-\frac{t}{\tau}}$$

Where the lifetime  $\tau$  is given by:

$$\tau = \frac{1}{k} = \frac{1}{k_r + k_{non,r}}$$

The excited state lifetime can be profoundly influenced by the micro-environment in which the molecule of interest is placed, via a variety of environment-dependent photophysical processes, some of them have been introduced above. The parameters affecting such photophysical processes include temperature, pH, polarity, hydrogen bonding, viscosity, presence of quenchers etc. For example concerning the temperature parameter; a temperature increase usually leads to a decrease in fluorescence lifetime corresponding to a faster overcoming of an excited state potential energy barrier. Attention should be paid to avoid possible erroneous interpretation arising from the simultaneous effects of several factors.

## II.2. Time Resolved Spectroscopy

### II.2.1 Time Resolved Fluorescence Spectroscopy

#### II.2.1.1. Theory

Since the first published observation of the fluorescence phenomenon by G.G. Stokes 165 years ago<sup>117</sup> the relative simplicity and unparalleled sensitivity of fluorescence measurements have led to a colossal advance in both measurement techniques and applications. These techniques utilize one or more characteristics associated with fluorescence emission. Fluorescence measurements can be split generally in two categories, steady state and time resolved fluorescence (TRF) measurements<sup>20</sup>. Both have developed to be powerful tools in the study of physical, chemical and biological systems.

Steady state measurements are performed with constant illumination of the sample and detection of the intensity or emission spectrum<sup>118,119</sup>. Although it requires a rather simple and cost efficient set-up, it can only provide an average value of the time resolved phenomena at the origin of the intensity decay of the sample. This can be easily understood by the single decay relationship given for a fluorophore.

As long as some population  $n^*(t)$  exists in a singlet excited state, photons may be emitted via the radiative decay channel which is always present with a fixed rate, intrinsically given by the electronic structure of the molecule. Hence, according to equation above, the number of photons emitted per time unit is:

$$F(t) = kr \times n^*(t) = kr \times n^*(0)e^{-\frac{t}{\tau}} = F_0e^{-t/\tau} \quad (t>0)$$

where  $F_0$  the fluorescence emission rate at  $t=0$ .

Therefore, we see here that the fluorescence emission decay time is a measurement of the molecular excited state lifetime  $\tau$ .

Measuring fluorescence intensity  $F_{ss}$  in a steady-state experiment, corresponds to a time-integrated measurement of the fluorescence signal:

$$F_{s,s} = \int_0^{\infty} F_0 e^{-t/\tau} dt = F_0 \tau = k_r n_0^* \tau$$

Here it is clear that although the intensity measured by the steady state experiment is proportional to the time constant  $\tau$  it is also proportional to the number of molecules promoted to the excited state and thus to the fluorophore excitation probability, controlled by the excitation light intensity and its perturbations. This can lead to erroneous interpretation and over-simplification of important dynamics. For example although the kinetics of a molecule would need two or more decay times, steady state measurements would reveal only a weighted average of these decay times.

## Fluorescence Quantum Yields

The fluorescence quantum yield  $\Phi_F$  describes the fraction of excited molecules that return to the ground state  $S_0$  with emission of fluorescence photons. More precisely it is the ratio of the emitted photon number to the absorbed photon number. With the notations introduced above, this writes as following:

$$\Phi_F = \frac{F_{SS}}{n_0^*} = k_r \tau = \frac{k_r}{k_r + k_{non,r}}$$

The fluorescence quantum yield is therefore controlled by  $k_{non,r}$ , and therefore may be significantly altered by a modification in the interactions with the environment. The most used method to measure a molecule's fluorescence quantum yield relies on comparing fluorescence intensities of the molecule of interest with molecular standards used as reference. These standards are used to calibrate the instrument response and do not need to match spectrally with the studied

sample; comparable spectral region is adequate. Their main characteristic needs to be their reliably reported quantum yield with quoted uncertainties.

## Fluorescence Quenching

The general term describing all the processes leading to a decreased fluorescence intensity, lifetime and quantum yield is quenching. Dynamic quenching describes the deactivation of the excited state fluorophore by contact with some other molecules contained in the solution, the so called quenchers. Here the fluorophore returns to the ground state through diffusive encounter with one or more quenchers. Stern -Volmer equation describes the intensity decrease occurring due to dynamic quenching as following:

$$\frac{F_Q}{F} = 1 + K[Q] = 1 + k_Q\tau_0[Q]$$

Where F is the intensity of the fluorophore,  $F_Q$  is the intensity of the fluorophore with the presence of a quencher, [Q] is the concentration of the quencher, K is the Stern-Volmer quenching constant,  $k_Q$  is the bimolecular quenching constant and  $\tau_0$  is the lifetime without quenching effect. Here the value of K will indicate the tendency of the fluorophore to be quenched or not by the specific quencher.

In addition to dynamic quenching, there is a second quenching mechanism called static quenching. Static quenching is usually described either by the existence of an effective quenching sphere or by a ground-state non-fluorescent complex formation. The aforementioned takes place in the ground state and does not depend on diffusion or molecular collisions.

## Structural heterogeneity revealed by distribution of fluorescence lifetimes

Environmental-sensitive fluorophores may induce the formation of different populations already present in the ground state. Therefore the photo-excitation leads to excitation of different populations resulting in the population of different excited states. Distributions of excited

conformers will lead to distribution of detected lifetimes. In addition, even if in the ground state there is solely one population still the excited chromophore can interact with solvent molecules or neighboring amino acid residuals leading to the formation of multiple populations.

Fluorescence lifetime measurements are very useful thus in reporting the existence of different conformations created in the ground or excited state of the same molecule. Conventionally the decay is resolved in terms of exponential components. The values of the decay rates and pre-exponential factors of each component can be associated with the relative population of each distinct conformation. However when the number of conformers is big the identification with different conformations can be challenging, especially if interconversion between substates is also taking place. As illustrated in Figure 6, the microenvironment can contribute to a distinct distribution of different conformers which lead to distribution of lifetimes.

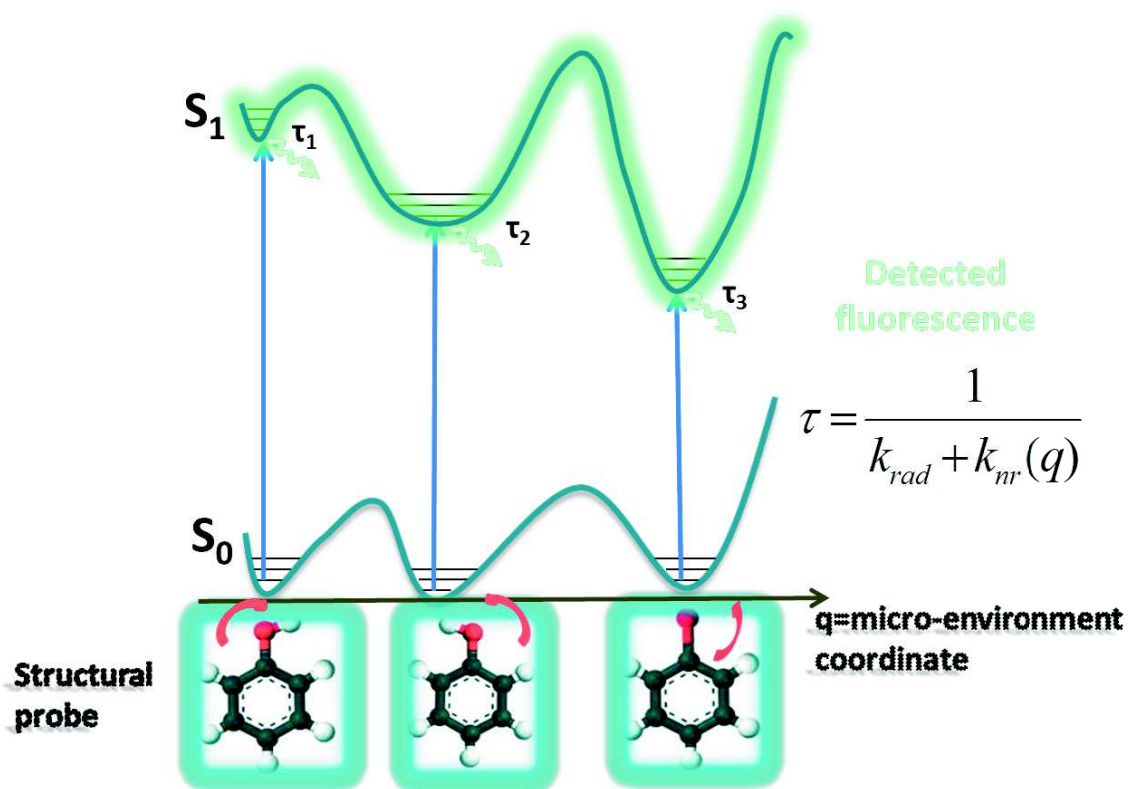


Figure 6-Paradigmatic illustration explaining that the micro-environment coordinates can lead to the formation of different conformers in the ground state (for example due to a flexible bond) which can be excited, populate different excited states and thus emit fluorescence with multiple fluorescent lifetimes.

On the other hand fluorescence intensity is by far the most commonly used method through the years. It is a method directly related to changes in fluorophore concentrations. Although it is a method easily applied (simple instrumentation needed) and rather sensitive, it is defenseless against the perturbations of the signal caused by differences in concentration, fluctuation of the laser source, auto-fluorescence etc. Moreover the intensity measurements interpretation can be difficult or misleading. Probes may become saturated or bleached, or unevenly spread across the structure of interest resulting in an inaccurate representation of the level or distribution of the target molecule. Therefore TRF provides an intrinsic measurement describing the time of a fluorophore spent on the excited state after excitation from a pulsed excitation light. Due to its intrinsic character it is robust against experimental artifacts; enabling this technique to reveal the coexistence of multiple molecular structures through the multiexponential decay detection.

### II.2.1.2. Experimental Approaches

There are many ways to conduct TRF measurements, two of them are Time Correlated Single Photon Counting (TCSPC) and streak camera; both were used to conduct experiments in the present thesis.

#### Streak camera

The key principles of optical streak camera operation were demonstrated during late 1940's to early 1960's. Courtney-Pratt in 1949 introduced a deflectable image converter able to measure temporal/spatial characteristics of light emitted during explosive burning in lead azide with a sub-nanosecond resolution<sup>120,121</sup>. Zavoiskii and Fanchenko in 1950's precisely calculated the conditions under which picosecond resolution could be achieved with these devices and registered the fundamental limitations<sup>122,123</sup>. They underlined that picosecond resolution required high electric fields (possibly tens of kV/cm) in order to extract photoelectrons with uniform velocity from the cathode. Progress was retarded until 1966, when the invention of the mode-locked Nd: glass laser provided the short pulses needed for the streak camera. At the beginning they were only used to examine the pulses generated from this new laser source, providing a direct measurement of its intensity profile<sup>124-127</sup>. Shortly after that streak cameras were used to monitor fast electron-induced fluorescence<sup>128-132</sup>.

Streak camera is a device able to measure ultra-fast light phenomena and deliver intensity vs. time or wavelength or position information. It got its name from the high speed rotating drum cameras. These cameras would "streak" reflected light onto film. No other instruments which directly detect ultra-fast light phenomena have better temporal resolution than the streak camera.

Its principle is illustrated in Figure 7 and consists of several steps. Initially pulsed excitation is used to impulsively trigger fluorescence emission from a sample including fluorescent molecules. Then the fluorescence photons enter the camera through the slit and arrive at the photocathode. Subsequently the incident light on the photocathode is converted into a number of photoelectrons proportional to the intensity of the light. Next step is the passage through a pair of accelerating

electrodes, where a high voltage ramp is applied at a timing precisely synchronized to the excitation light pulse. Thus a high speed sweep is initiated during which the photoelectrons emitted at different times are deflected in different angles in the vertical direction. Deflected electrons enter the micro-channel plate (MCP), where they are multiplied by several thousands. Then they impact against the phosphor screen and are converted again to photons. The phosphor image is recorded by a CCD camera, where the photons corresponding to the earliest fluorescence photons that arrived on the slit will be placed in the highest position and the rest will be sequentially positioned in order from top to bottom, meaning that the vertical axis of the phosphor screen serves as time axis. Moreover, the brightness of the various phosphor images is proportional to the intensity of the respective incident optical pulses. A schematic illustration can be found in Figure 7.

This way the optical intensity from the phosphor image, and the time and incident light position from the location of the phosphor image can be determined. An additional desired feature is the simultaneous measurement of light intensity on both the temporal and spatial axis (wavelength axis). This can be achieved by positioning a spectrometer in front of the slit of the streak camera, the spatial axis along the photocathode is used as a wavelength axis. This enables resolving spectrally the fluorescence decay kinetics.

One major advantage of the streak camera compared to some other techniques such as TCSPC, is its multichannel character, enabling spectral (or spatial) resolution along the photocathode wire. Moreover the time resolution nowadays can reach a few hundreds of fs<sup>133</sup>.

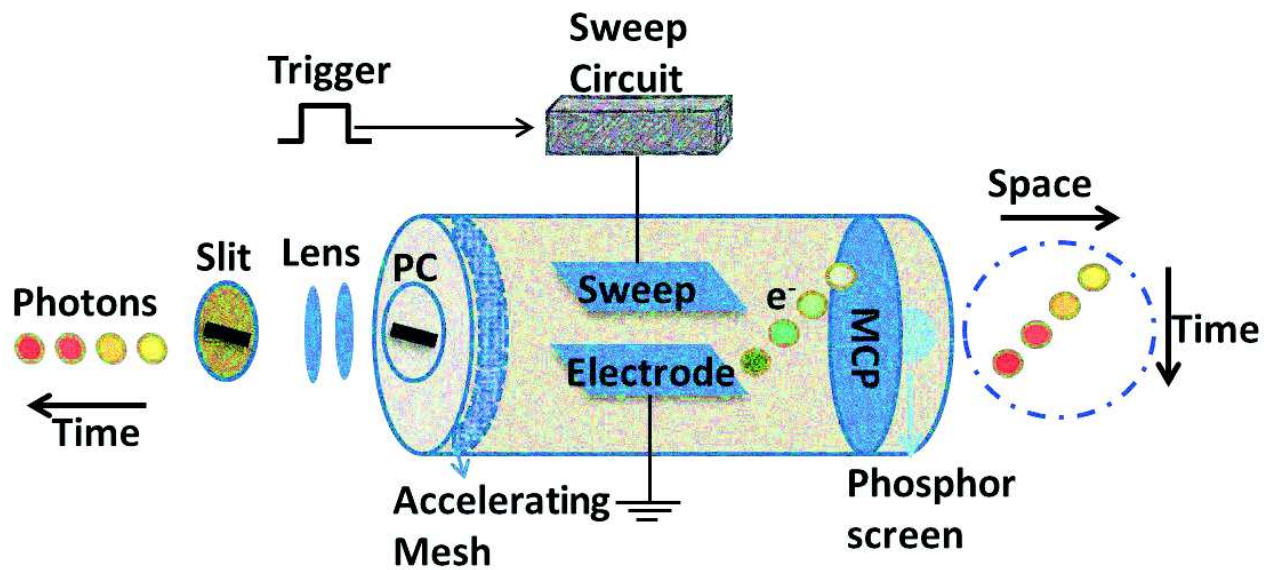


Figure 7-Schematic illustration of operating principle of streak tube.

## Time Correlated Single Photon Counting (TCSPC)

Historically the first publication on TCSPC is attributed to Bollinger and Thomas in 1961<sup>134</sup>. Although they mainly used alpha, gamma, and neutron excitation; their technique resembles the modern concept of TCSPC acquisition.

The concept of this technique is illustrated in Figure 8. TCSPC is the most accurate and sensitive Time resolved fluorescence detection tool, achieving typically 50 ps time resolution. Mainly a pulsed excitation light beam is required; usually this corresponds to a pulsed laser, which excites the sample. The principle of this method lies on the repetitive precisely timed registration of single photons, corresponding to the fluorescence signal, with respect to the exciting pulse. The reference for the timing is the corresponding used excitation pulse<sup>135</sup>. The maximum repetition rate for the excitation source is determined by the decay times of the sample. The time interval between the start and the stop signal are measured, where the start signal corresponds to excitation laser pulse and the stop the single photon detection. Subsequently the events are

collected in a memory by adding a '1' in a memory location with an address proportional to the detection time.

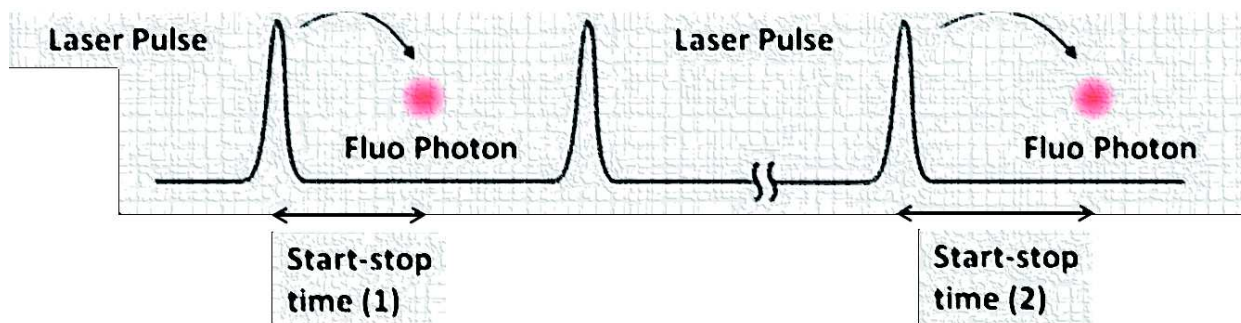


Figure 8-Schematic illustration of the TCSPC technique, where the start signal corresponds to the excitation laser pulse and the stop to the single photon detection.

After numerous photon detections, the histogram of the detection times, i.e. the waveform of the fluorescence decay kinetics is reconstructed in the memory. The conditions are adjusted so that less than one photon is detected in average per laser pulse. This precondition is due to the dead time following each photon detection, during which the detection remains blind to other coming photons<sup>136</sup> and it usually longer than the Fluorescence Lifetime (FLT). Thus the probability of a second photon arriving during the dead time must remain non-significant in order to avoid distortions of the measured fluorescence decay kinetics due to the so called pile-up effect<sup>137 138</sup>, as will be further discussed in Chapter V.

TCSPC has several advantages, such as high sensitivity and very large dynamic range. Moreover it is a cost efficient technique with low intensity excitation pulse is needed. Main disadvantage of the TCSPC is its limited time resolution. The measurement uncertainty comes from the so called jitter, corresponding to differences of the successive signals shape. Another disadvantage is that is a single wavelength detection method.

Other experimental techniques of measuring TRF spectra are Fluorescence upconversion<sup>139</sup>, optical Kerr gating<sup>140</sup> (different version of fluorescence upconversion) and phase fluorimetry<sup>20</sup> (time resolution obtained in frequency domain).

## II.2.2 Transient Absorption Spectroscopy

### II.2.2.1. Principle

A widely used technique of time-resolved spectroscopy based on the absorption measurement and not in fluorescence this time, is transient absorption, also called pump-probe spectroscopy. Its principle is based on a two-step sequence: i) a short laser (pump) pulse overlapping the molecule absorption spectrum excites the molecular system, and ii) a second (probe) pulse, delayed with respect to the pump, is used to monitor the sample transmission (absorbance). By computing the difference between the probe transmission in the presence and absence of the pump, we thus monitor the pump-induced absorption change  $\Delta A$ . By varying stepwise the time delay between both pulses, one measures the entire time-dependence of the absorption change. With a probe pulse characterized by a very broad spectrum from the UV to the IR, one may therefore observe the entire UV-Vis spectrum of the transient species generated upon impulsive pump pulse absorption.

The major advantage of pump probe in comparison with TRF spectroscopy is that it can not only measure the changes in the excited state but also of the photoproducts resulting from the photoexcitation. TRF can solely detect the excited state via its transition dipole moment to the ground state. On the other hand, the spectra resolved in pump-probe experiments are more complex leading to a difficult interpretation in comparison with TRF experiments. Therefore the most solid solution is the combination of the two techniques, in order to isolate the excited state information and enrich the results with complete ultrafast description of the investigated system.

### II.2.2.2. Set-up description

The pump probe setup for transient absorption (TA) detection has been described thoroughly elsewhere <sup>141</sup> and is displayed in Figure 9. Briefly as shown in Figure 9, in our set up ultrafast pulses centered at 800 nm are produced by a Ti: Sapphire oscillator with a full width half maximum of 40 nm and duration of 20 fs at 60 MHz repetition rate. The aforementioned pulses are amplified with a Chirped Pulse Amplifier (CPA) achieving 40 fs pulses with energy of 0.5 mJ at 5 kHz. The beam is split aiming to use one for pump and one for probe.

The pump has to be adjusted to the absorption characteristics of the studied molecule. Our experimental set-up allows two options: it can pass through a  $\beta$ -barium borate (BBO) crystal to produce 400 nm beam by second harmonic generation or it can pass through a Non-collinear Optical Parametric Amplifier (NOPA, TOPAS, from Lightconversion) if different wavelengths are needed. These pulses are periodically blocked and unblocked by an optical chopper (a rotating disc including slots) in order to measure the probe transmission with and without excitation:  $I_{exc}$  and  $I_{no,exc}$ .

The probe passes through a delay line allowing scanning the pump-probe time delay between 0-5 ns, with 13 fs defined steps. A CaF<sub>2</sub> crystal is used to convert the original 800 nm to a white-light continuum, ranging between 300-1000 nm, with white light generation. The probe pulses intensity is measured using an appropriate detectors (a CCD camera), whereby the entire spectrum can be recorded at once). It is essential for the detector to be synchronized with the chopper in order to separate the measurements of pumped and non-pumped sample.

According to the absorption law, the probe pulse intensity equals with

$$I_{exc} = I_0 * 10^{-A_{exc}}$$

Here  $I_0$  is the incident's pulse intensity and  $A_{exc}$  the absorption of the excited sample of interest.

With the same way of thinking, when the sample is not excited

$$I_{no,exc} = I_0 * 10^{-A_{no,exc}}$$

By calculating the logarithm of the ratio of these two quantities we obtain:

$$\Delta A(\lambda, t) = A_{exc} - A_{no,exc} = \log \frac{I_{no,exc}}{I_{exc}}$$

This underlines that in order to record the absorption changes in the sample induced by the excitation pump pulse, there is no need of measuring the intensity of the incident pulse  $I_0$ . Absorption change expressed by the last equation is the typical signal measured in pump-probe spectroscopy. Briefly the spectral dimension is derived with a spectrometer whereas the time dimension with the mechanical delay line applied on the probe.

The final information collected can also be described as following:

$$\Delta A(\lambda, t) = \sum_i \varepsilon_{S_i}(\lambda) \Delta C_{S_i}(t) L$$

Here  $\varepsilon_{S_i}$  is the extinction coefficient in state  $S_i$ ,  $\Delta C_{S_i}$  is the concentration change in state  $S_i$  after excitation and  $L$  is the sample's path length.

To improve the sensitivity of the measurement, the spectral distribution of the probe is recorded simultaneously in the presence and in the absence of the perturbation of the sample at each laser shot. This is achieved, by splitting the probe beam into two equal beams: the first partial beam crosses the perturbed part of the sample while the second one crosses an unperturbed part of the sample (reference beam). These two beams are then directed onto the slit of a spectrograph at two different heights, and are read by two different 1D diode arrays.

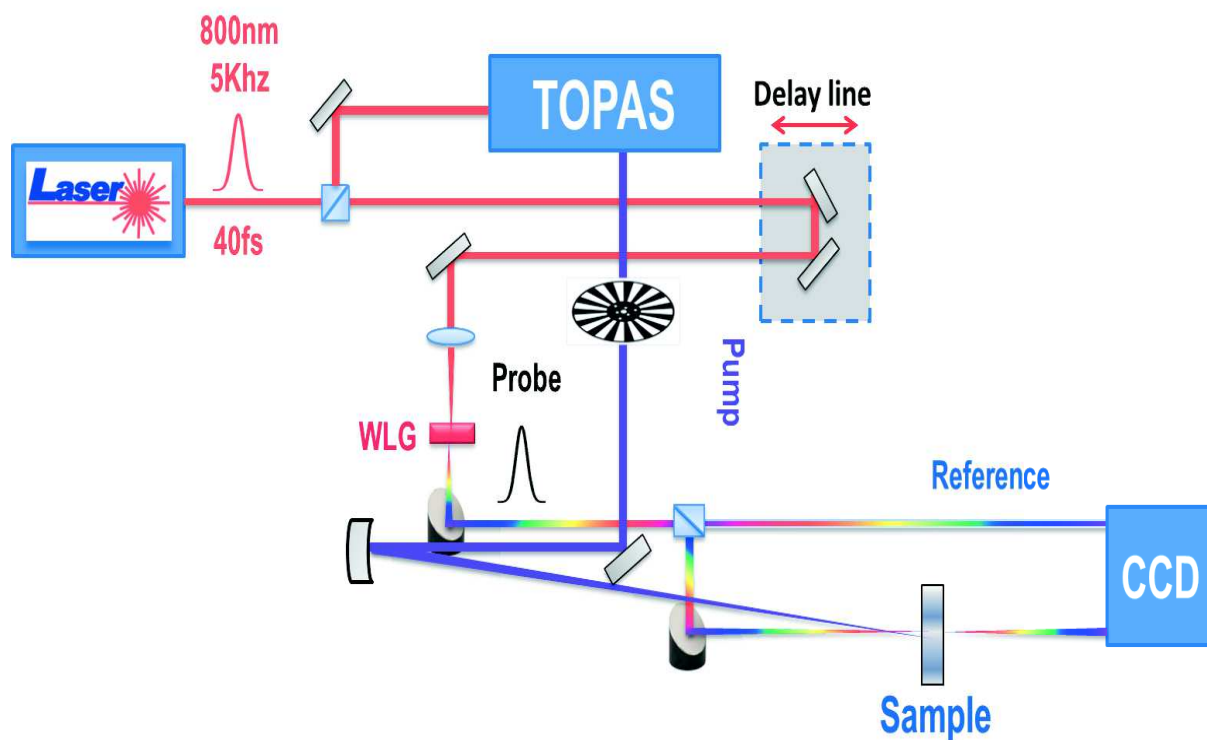


Figure 9-Schematic illustration of the pump-probe set-up. Pulses are generated in the oscillator, amplified and split in two. One is send to the delay line and then through a CaF<sub>2</sub> crystal we achieve white light generation, which will be used as a probe. The second beam is the pump and passes through the TOPAS to reach the desired wavelength. Both of the beams are send to the sample and the transient absorption spectrum is recorded by a CCD camera (two 1D photodiode arrays). The reference beam is used for later corrections of the fluctuations during the white light generation.

### II.2.2.3. Transient absorption spectra

As previously emphasized the pump probe detected spectra are more difficult to interpret in comparison with the TRF ones, mainly because they include multiple contributions. Therefore a deeper look on these contributions is needed.

Initially when the pump pulse excites the sample (a few % of it), molecules are transferred to the first excited state. This transfer leads to a decrease of the ground state population and part of the absorption signal appears. Accordingly, at the wavelengths of ground state absorption the absorption difference becomes negative. This negative contribution is expected to be spectrally identical to the ground state absorption measured separately by a spectrophotometer and is named Ground State Bleaching (GSB) It remains unless all the excited molecules eventually return to their original ground state.

Next contribution is named Stimulated Emission (SE) and it is observed when the probe stimulates the emission of the excited molecules and thus their return to the ground state. The SE signal will also be negative, since it results in an effective amplification (negative absorption) of the probe pulse. SE has a spectral signature closely related to the molecule fluorescence spectrum, and therefore exhibits a red Stokes shift, compared to the absorption spectrum, due to excited state relaxation.

The last contribution is due to induced absorption and is named excited state absorption (ESA). This contribution results from the re-absorption of a probe photon by the molecules populating the first excited state and results to a positive contribution to the  $\Delta A$  signal. Here it needs to be noted that ESA can be initiated not only from the singlet excited state but also from a triplet excited state populated by intersystem crossing. A scheme of all the above contributions is given in Figure 10.

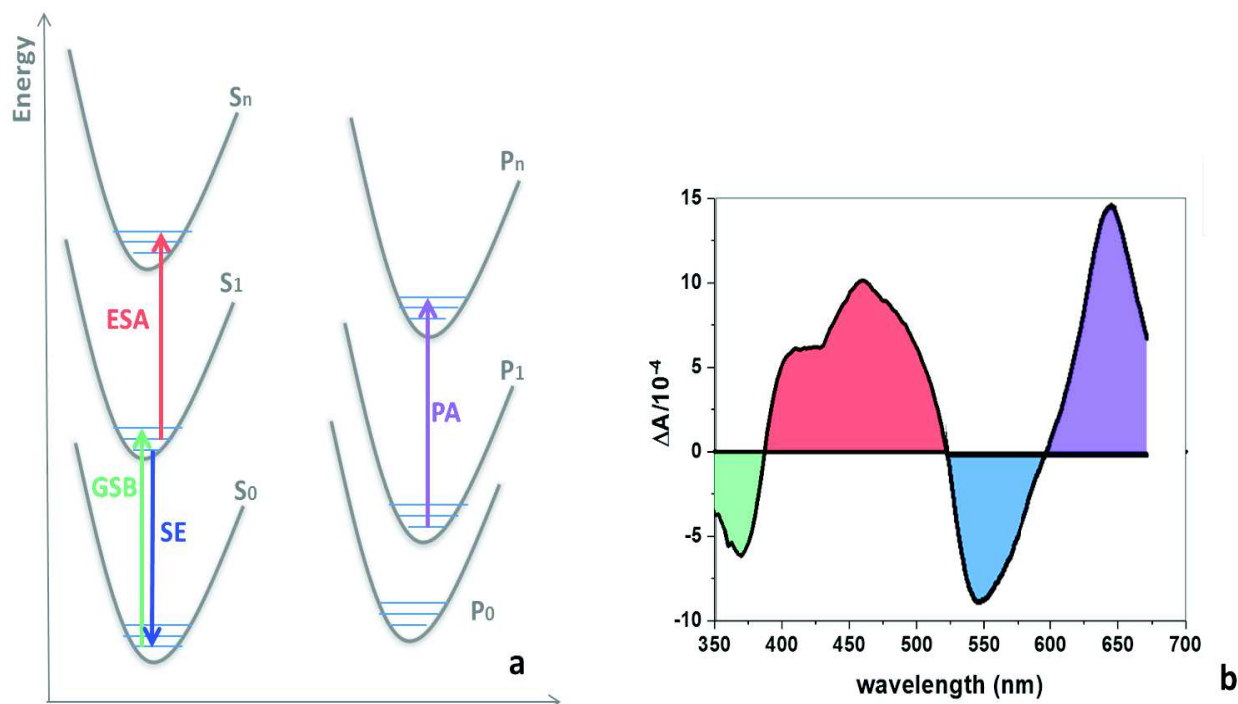


Figure 10-Schematic illustration of a. the possible detected phenomena and b. observed signals in TA spectroscopy (green corresponds to GSB, red to ESA, blue to SE and magenta to ESA or Photoproduct Absorption). The present example is a transient spectrum of 4M3HF in MeOH, which will be presented in chapter III.

Besides identifying the electronic origin of the various contributions to the transient absorption signal, the interpretation of the data includes identifying the various time scales over which electronic state population and spectral signatures (e.g. vibrational relaxation) evolve from the initial excited state produced by the pump pulse until the formation of the photoproduct or recovery of the initial ground state.

## II.3. Data Fitting

### II.3.1 Multiexponential kinetics

As we already introduced above, while in TRF spectroscopy one may only observe the decay of the excited state, the fluorescence decay signal may be multiexponential due to a distribution of ground state chromophores which then have a distribution of excited state lifetimes.

In transient absorption spectroscopy, we observe the decay kinetics of different electronic states, which may have spectrally overlapping signatures, and therefore also result in multiexponential decay kinetics. In the following we derive, in a simple photoreaction scheme, the expressions of this multiexponential behavior as a function of the various decay rates from the one electronic state to the next.

If we assume a total population of molecules  $P_{\text{total}}$  from which only a fraction of  $P_0$  is excited from the ground  $S_0$  state to the first  $S_1$ ; then these molecules will decay to the  $S_2$  state with a decay rate of  $k_{12}$  before returning to the original  $S_0$  state with a decay rate of  $k_{20}$  (shown in Figure 11).

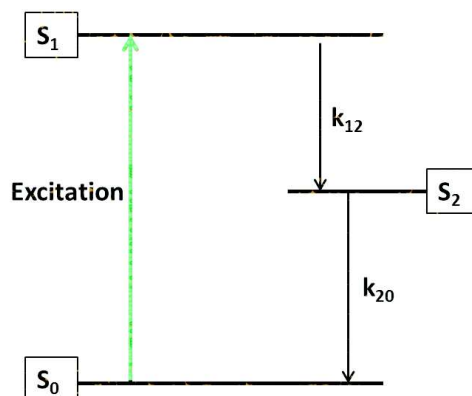


Figure 11-Schematic illustration for the rate equation system.

The respective populations  $c_i$  can then be described with the following set of rate equations:

$$\begin{aligned}\frac{dc_1(t)}{dt} &= -k_{12} * c_1(t) \\ \frac{dc_2(t)}{dt} &= -k_{20} * c_2(t) + k_{12} * c_1(t) \\ \sum_{i=0}^2 c_i(t) &= P_{total}\end{aligned}$$

Solving the above rate equations will lead to:

$$\begin{aligned}c_1(t) &= P_0 * e^{-k_{12}*t} \\ c_2(t) &= \frac{P_0 * k_{12}}{k_{12} - k_{20}} * (e^{-k_{20}*t} - e^{-k_{12}*t}) \\ c_0(t) &= \frac{P_0}{k_{12} - k_{20}} * (k_{20} * e^{-k_{12}*t} - k_{12} * e^{-k_{20}*t}) + P_{total}\end{aligned}$$

If the sample has 1 cm thickness then the absorption before excitation can be written:

$$A_0(\lambda) = P_{total} * \varepsilon_0(\lambda)$$

Here  $\varepsilon$  is the molar absorptivity. At a time  $t$ :

$$A(\lambda, t) = c_1(t) * \varepsilon_1(\lambda) + c_2(t) * \varepsilon_2(\lambda) + c_0(t) * \varepsilon_0(\lambda)$$

The differential absorption can thus be written:

$$\begin{aligned}\Delta A(\lambda, t) &= A(\lambda, t) - A_0(\lambda) \\ &= c_1(t) * \varepsilon_1(\lambda) + c_2(t) * \varepsilon_2(\lambda) + (c_0(t) - P_{total}) * \varepsilon_0(\lambda) \\ &= c_1(t) * (\varepsilon_1(\lambda) - \varepsilon_0(\lambda)) + c_2(t) * (\varepsilon_2(\lambda) - \varepsilon_0(\lambda)) \\ &= P_0 * e^{-k_{12}*t} * \varepsilon_1(\lambda) + \frac{P_0 * k_{12}}{k_{12} - k_{20}} * (e^{-k_{20}*t} - e^{-k_{12}*t}) * \varepsilon_2(\lambda) \\ &\quad + \frac{P_0}{k_{12} - k_{20}} * (k_{20} * e^{-k_{12}*t} - k_{12} * e^{-k_{20}*t}) * \varepsilon_0(\lambda)\end{aligned}$$

This can be written more comprehensively if we select the exponential common factors as following:

$$\Delta A(\lambda, t) = \left( P_0 * \varepsilon_1(\lambda) - \frac{P_0 * k_{12}}{k_{12} - k_{20}} * \varepsilon_2 + \frac{P_0 * k_{20}}{k_{12} - k_{20}} * \varepsilon_0(\lambda) \right) * e^{-k_{12} * t} \\ + \left( \frac{P_0 * k_{12}}{k_{12} - k_{20}} * \varepsilon_2 + \frac{P_0 * k_{12}}{k_{12} - k_{20}} * \varepsilon_0 \right) * e^{-k_{20} * t}$$

This can be easily written as a sum of exponentials:

$$\Delta A(\lambda, t) = \sum_i^n A_i * e^{-k_i * t}$$

Here  $A_i$  represents the constants. The present model can be expanded for more exciting states according to the data described.

### II.3.2 Fitting Function

Hence, in both TRF as well as TA spectroscopies, we expect to observe multiexponential decay kinetics. These decay kinetics are also *a priori* convolved by the instrument response function (IRF). We systematically assume that the IRF can be modeled by a Gaussian function with a width  $\sigma$ . Hence for all the time-resolved spectroscopy experiments we perform, we define the following fitting function:

$$A(\lambda, t) = \sum_i A_i * e^{-\frac{(t-t_0)}{\tau_i}} \otimes \frac{1}{\sigma\sqrt{2\pi}} e^{-\frac{t^2}{2\sigma^2}}$$

Since we assume a Gaussian function for the IRF, the convolution with the exponentially decaying functions can be written analytically, which then yield in the following fitting function:

$$A(t) = C + \frac{A}{2} \exp\left(\frac{\sigma^2}{2\tau^2}\right) \exp\left(-\frac{t-t_0}{\tau}\right) \otimes \left[ 1 + \operatorname{erf}\left(\frac{t-t_0-\sigma^2/\tau}{\sigma\sqrt{2}}\right) \right]$$

Where erf is the error function resulting from the convolution of the Heaviside step function  $H$ , whose value is zero for negative argument and one for positive argument, by a Gaussian function.  $C$  stands for a possible constant offset.

Based on these equations we run the fitting function with an increasing number of exponentials until the fit is converged and the needed parameters (time constants, amplitudes, time zero and standard deviation) are found. The programs used for that were in our case origin-lab and python. Target is to reduce the difference between experimental data points  $y_i$  recorded at time  $t_i$  and the fitting curve  $f(t_i)$ , also known as reduced  $\chi^2$ :

$$\chi^2 = \sum_i (y_i - f(t_i))^2$$

Ideally the difference between data and fit (residuals) should correspond to points randomly distributed around zero with small amplitude.

Whenever the noise distribution on the experimental data points is known, this knowledge may be exploited to further constrain the determination of the parameters of the fitting function. This is the case in particular for fluorescence decay kinetics recorded in photon counting mode, where the characteristic Poisson statistics applies. In such a case a so-called “weighted”  $\chi^2$  function may be defined (to be minimized by the fitting procedure), which takes into account the rms noise  $\sqrt{y_i}$  which affects the measurement of a  $y_i$  photon number:

$$\chi^2 = \sum_i \left( \frac{y_i - f(t_i)}{\sqrt{y_i}} \right)^2$$

## II.4. Out-of-equilibrium experiments

### II.4.1 Introduction

When studying biomolecular interactions, the time scale over which this reaction takes place can vary widely. Figure 12 depicts a range of characteristic time scales of molecular-scale biological processes. The axis shows the fast time scales ranging from bond vibrations to protein folding durations and spanning from fs to s.

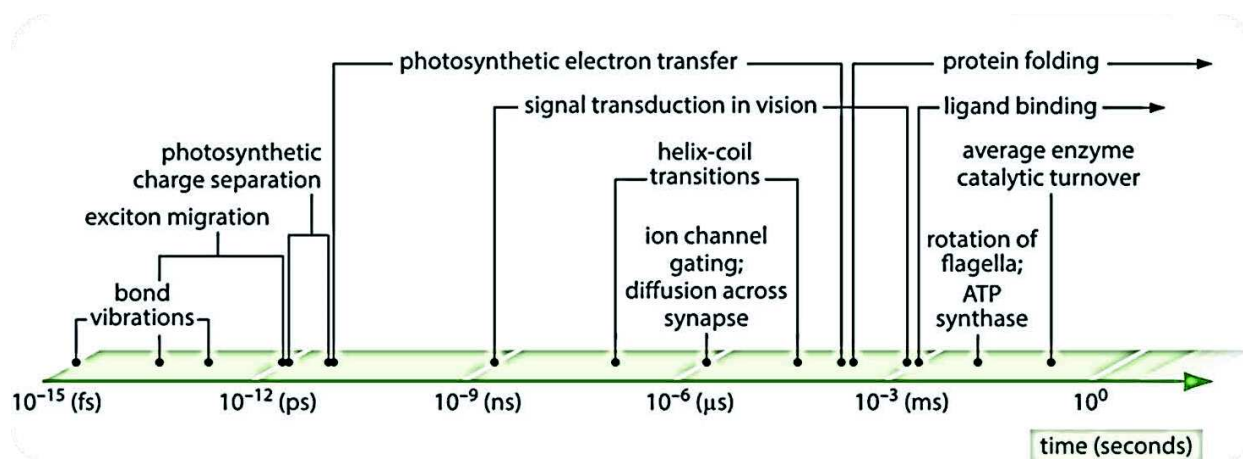


Figure 12-Characteristic time scales of molecular-scale biological processes.

The experimental approaches aforementioned in the previous sections provide in depth information for biomolecular interactions. However, each one monitors events within a specific time range. Specifically, pump probe monitors events occurring within fs to ns range, TRF within ps to hundreds of ns. However, larger-scale conformational changes with biological interest, occur on significantly slower time scales (up to seconds, minutes). For this reason we may combine TRF with other tools creating out-of-equilibrium initial conditions and unravel such conformational dynamics.

During the last two decades microfluidic analytical devices have become an increasingly popular research topic<sup>142–147</sup>. Their advantages are numerous not only because they offer the possibility of creating initial out-of-equilibrium conditions<sup>148</sup> but also because they include inherent low sample hold up volume, rapid response times and flexible operation<sup>149–152</sup>. These benefits as well as their predisposition to automation make them ideal for use both in fundamental research and in applications including high throughput analytical systems<sup>153–156</sup>.

Three techniques are used for out-of-equilibrium initial conditions generations, continuous flow, stopped flow and droplet microfluidics.

## **Stopped flow**

The technique was developed in 1940 by B. Chance<sup>157</sup> and is now an established technology for monitoring biochemical reactions in out-of-equilibrium conditions. This technique involves two or more reactants held in separate reservoirs (usually syringes) that are prevented from freely flowing by syringe pumps. The reaction is initiated by depressing the reactant syringes, and subsequent reactants release into the connected mixing chamber. There the solutions are mixed and the reaction is initiated. Traditionally stopped-flow is used in combination with UV/Vis detection methods – both absorption and fluorescence spectroscopy- to monitor the change in absorbance or emission of the reactants/products in solution as a function of time. The reaction progresses by filling the expanding stopping syringe until continuous flow rate has been reached. At this point the flow and the reaction is stopped allowing the researcher to calculate the initial rate of reaction. The Figure 13 shows schematically the principle of this method.

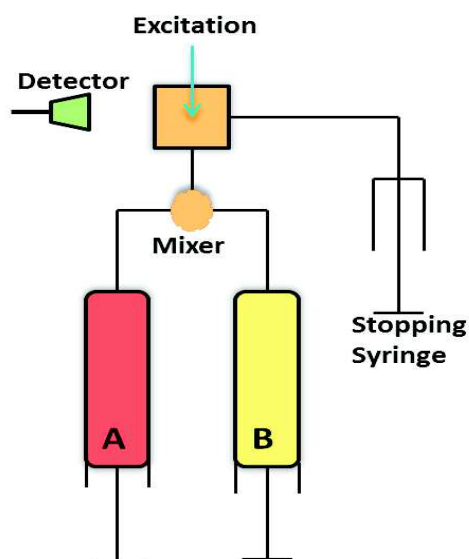


Figure 13-Schematic illustration of a typical stopped flow apparatus, where two reactants A and B under pneumatic drive activation are driven from syringes through a mixer. The resultant mixture passes through a measurement flow cell and last reaches the stopping syringe.

Unfortunately conventional stopped-flow devices often display a complex design, occupy much space and demand high cost both in purchasing and maintenance. The need of high volume samples raises even more the expenses. For these reasons a powerful droplet microfluidic technique was introduced, which combines the advantages of a simple, low-cost set-up with low sample consumption and using disposable polymer chips. The realization of droplet microfluidic experiments not only minimizes sample volumes but also offers easy handling and elimination of interferences by cross-contamination.

## Continuous flow

Various examples of continuous flow applications have been reported. One very interesting example is hydrodynamic focusing, where microfluidic continuous flow mixers are able to reach mixing times of less than  $10 \mu\text{s}$ <sup>158</sup>. The basic principle of hydrodynamic focusing includes: a central sample solution with a low flow rate flowing through the intersection of side emerging fluid traveling at a much higher flow rate, thus enabling the compression of the inner sample flow<sup>159–162</sup>. This is performed without inducing turbulence but by using an open architecture allowing mixing process observation. Three intersecting rectangular inlet channels can be used; the two side-inlets hydrodynamically focus the flow-inlet into a thin stream exiting the intersection and at the same time molecules from the side flow rapidly diffuse across the inlet stream, resulting in fast mixing.

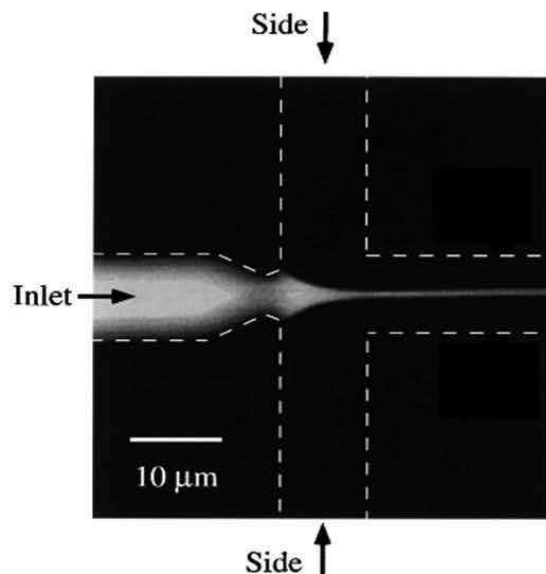


Figure 14-Adapted from<sup>158</sup>. Hydrodynamic focusing region, where two side channels press the stream of the inlet channel and due to simultaneous diffusion across the same stream fast mixing is achieved.

Generally though, the main idea in continuous flow experiments is shown in the Figure 14. In this technique, two reagents, A and B, are allowed to mix at some time point, while the mixture flows

into a long capillary. Continuous flow experiments are adequate for certain applications where well-defined molecular transport between two or multiple reagents streams is targeted. However they may suffer of the no-slip boundary condition. Basically meaning that a parabolic profile flow appears where the reagents velocity is zero at the bottom and top boundaries. This effect can be a big disadvantage because precipitation of solid reactants on the bottom and top can obstruct the flow with time. Another drawback is the difficulty to relate the propagation length to the reaction time for two reasons: First because of the parabolic profile and second due to the slow mixing induced solely by diffusion<sup>163–165</sup>; thus the starting point of the reaction cannot be well defined.

## **Droplet Microfluidics**

As a method of rapidly mixing reagents we used in this PhD work Droplet microfluidics (D $\mu$ F), which is a promising tool for biotechnologies since it lowers the sample volume from 100  $\mu$ L range in stopped-flow experiments down to 100 pL range or less at the single micro-droplet level<sup>166</sup>.

D $\mu$ F enables the manipulation of discrete fluid packets in the form of micro-droplets that provide numerous benefits for conducting biochemical assays. D $\mu$ F technology utilizes two immiscible fluids in microfluidic channels to create monodisperse water in oil (w/o) micro-droplets. Flow instabilities within these droplets are taken advantage of for fast mixing inside the droplets<sup>164,167</sup>. These droplets, acting as an individual reaction vessel, have the volumes of a few hundred pL to nL and can be generated at rates of up to several kHz (or even more) while maintaining exquisite control over their flow rate, speed and size. In addition numerous functional components for controlling droplets have been developed, such as droplets generation and mixture<sup>168</sup>, sorting<sup>169,170</sup>, splitting<sup>171</sup> and merging with other droplets<sup>172</sup>. The manipulation methods are often divided into two categories; passive and active. The passive ones employ numerous channel geometries to perform such manipulations. The active ones utilize electro-hydrodynamics<sup>173</sup>, or magnetic forces<sup>174</sup> to manipulate droplets.

## II.4.2 Micro-droplets formation and mixing

The history of micro-fluidics counts less than 20 years. In 2001 Sugiura et al. reported on the formation of both oil-in-water<sup>175</sup> and water-in-oil<sup>176</sup> droplets in a microfluidic structure. Droplets formation was achieved by forcing the dispersion phase through a narrow channel (15  $\mu\text{m}$ ) into the continuous phase, as depicted in Figure 15 . A flat, disc shaped formation on a 30  $\mu\text{m}$  long terrace extends to a drop-off. As the disk extends out to the edge of the terrace, an imbalance in the interfacial tensions between the flat disk and a sphere results to spontaneous formation of a spherical droplet falling off the terrace into a well. This process leads to a highly monodisperse collection of droplets at the 10  $\mu\text{m}$  length scale.

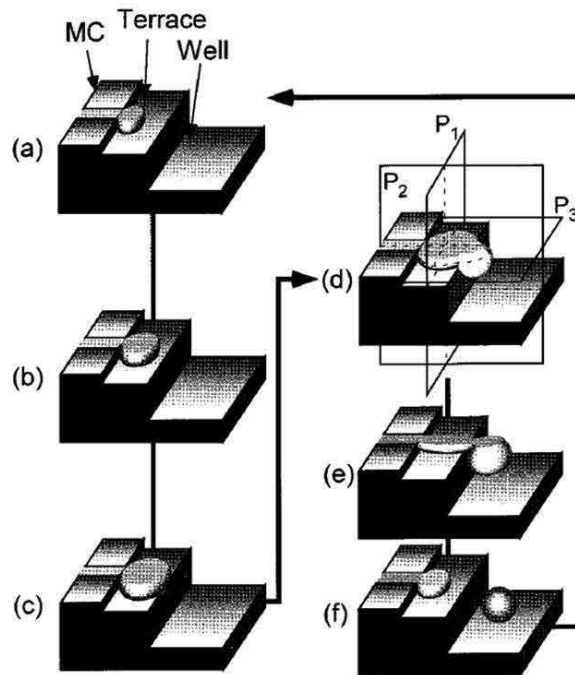


Figure 15- Adapted from <sup>175</sup>. Schematic illustration of the droplet-formation mechanism caused by interfacial tension. Dispersed phase passed through the micro-fabricated channel inflated on the terrace in a disk-like shape (a-c). The dispersed phase flowed into the well and transformed into a spherical droplet (d-f).

During the same year Thorsen *et al* performed droplet microfluidic experiments using a microfluidic T-junction<sup>177</sup>. In this work, they stated that droplet formation is determined by the combination of surface tension and shear forces. They approximated the size of a droplet under external shear force by equating the Laplace pressure with the shear force as following:

$$r \sim \frac{\sigma}{\eta \dot{\epsilon}}$$

Where  $r$  corresponds to the final droplet radius,  $\sigma$  is the interfacial tension between the water-oil surfactant;  $\eta$  is the viscosity of the continuous phase and  $\dot{\epsilon}$  is the shear rate.  $\dot{\epsilon}$  was estimated as  $\dot{\epsilon} \sim 2u/y_0$ , with  $u$  is the velocity of the fluid and  $y_0$  is the estimated channel radius. Figure 17 b shows how they created micrometer-sized droplets by flowing water into a channel through which oil is flowing.

Micro-chips with planar geometries are easily designed and produced with soft lithography. Abundant geometries were presented with planar configuration. Some of these configurations are Y-junction<sup>178</sup>(Figure 16a) , flow-focusing<sup>179</sup> and T-junction<sup>180</sup> (Figure 16b). As expected the channel geometry is the leading factor for the different droplet generation mechanisms. In the present project only T-junction micro-chips were used.

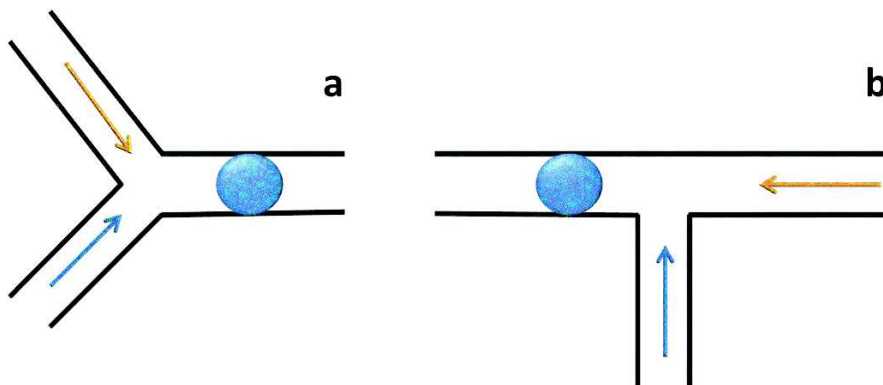


Figure 16-Schematic illustration of a.Y-junction and b. T-junction geometries for droplet formation in different droplet microfluidics chip geometry. In yellow arrow is the oil and in blue the liquid compound.

Nisisako et al<sup>181</sup> generated pico/nanoliter-sized water droplets in a continuous phase flow at a T-junction geometry (Figure 17a) . The channel for the dispersed phase was 100x100 μm, whereas the channel for the continuous phase is 500x100 μm. For given experimental parameters, regular-sized droplets were reproducibly formed at a uniform speed. The diameter of these droplets is controllable in the range from 100–380 μm as the flow velocity of the continuous phase was varied from 0.01-0.15 m/s.

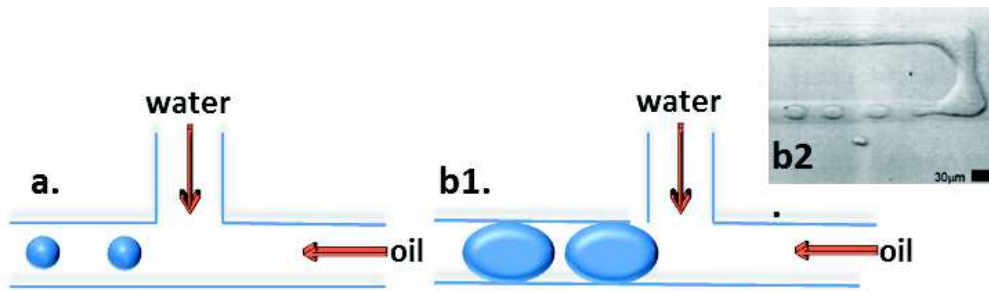


Figure 17-Sketch of a microfluidic T-junction used to create a. water droplets and b1 plugs in oil (b2 photograph of the discontinuous water phase introduced into the continuous oil phase<sup>177</sup>). Water stream comes from the vertical direction meeting the perpendicular flow from the oil channel. The channel dimensions are typically on the order of 50-100 μm.

In 2006 Garstecki et al<sup>182</sup> displayed the breakup process in T-junction geometry in the limit of low capillary numbers,  $C < 10^{-2}$ . The capillary number represents the relative effect of viscous forces versus surface tension acting across an interface between two immiscible liquids as following:

$$C = \frac{\eta v}{\gamma},$$

with  $\eta$  is the dynamic viscosity,  $v$  is the mean velocity of the droplet and  $\gamma$  is the interfacial tension. An example of their study is given at Figure 17 b. Their new input in the field was a scaling law for the length of the water droplets  $L$  with the channel width  $w$ , as following:

$$\frac{L}{w} = 1 + \alpha \frac{Q_{water}}{Q_{oil}}$$

Here  $\alpha$  is a dimensionless parameter on the order of one, and  $Q$  the flow rate of the water and oil respectively. This way they proved experimentally the correlation of the droplets size with the channel geometry.

Later, Abate et al<sup>183</sup> studied the impact of inlet channel geometry on microfluidic droplet formation, showing that for T-junction geometry forms monodisperse emulsions at low and moderate capillary numbers  $0.04 < C < 0.1$ . Fortunately Song et al<sup>164</sup> proved that droplet microfluidics were not doomed by long mixing times. They presented a microfluidic system that could be used to control networks of many chemical reactions on the millisecond scale, which will be presented in detail in the next section.

In a T-junction chip, flow instabilities between two immiscible liquids cause droplet formation<sup>184</sup>. In such geometry, the aqueous and oil phase are usually injected at right angles to each other and shear forces result to droplets formation. When the droplet diameter is bigger than the width of the channel and the droplet forms a plug, mixing within the droplet is enhanced by the contact of the droplet with the channel wall, as shown in the Figure 18. This contact induces the formation of a double recirculating flow pattern within the droplet, which increases the rate of mixing due to advection forces. This double recirculation flow has been observed optically<sup>164</sup> and measured, using particle image velocimetry (PIV)<sup>185</sup>. PIV performs velocity measurements by seeding the fluid of interest with tracer particles which, for adequately small particles, are assumed to follow the flow dynamics. The seeded fluid is then illuminated so that particles visualization is possible. The motion of the seeding particles is used to calculate velocity and direction of the studied fluid.

In an attempt to achieve fast mixing, further reduction of the droplet's volume can be achieved by altering the channel width, relative viscosity of fluids and respective flow rates of the water and oil phases. However, the double recirculating flow pattern does not induce rapid movement of droplet contents across the centerline of the droplet limiting thus the mixing ability of the droplets. In order to overcome this limitation, winding channels have been introduced. Indeed when a droplet enters a winding channel, the shear forces experienced on either side of a droplet become uneven, and the droplet contents are forced to undergo a phenomenon known as "stretching and folding" (Figure 18), due to which the recirculation patterns begin to cross the center of the droplet. The same technique was used for the manufacturing of our own chips, as it

will be seen if Figure 21. This induces chaotic advection which folds and stretches the droplet contents resulting in shortening the distance over which diffusion takes place, therefore mixing acceleration is achieved. Additionally increasing droplet velocity leads to magnification of the shear force differences on either side of the droplet, and increases further the mixing rate<sup>164</sup>. A mixing time of a few ms is usually achieved under these conditions<sup>148</sup>, although rapid mixing on the  $\mu\text{s}$  timescale has also been reported<sup>169</sup>. Furthermore studies have been conducted over the effect of the angle of the winding channels on droplet mixing, and concluded that a  $45^\circ$  winding channel provided faster mixing than either  $90^\circ$  or  $135^\circ$  bends<sup>186</sup>.

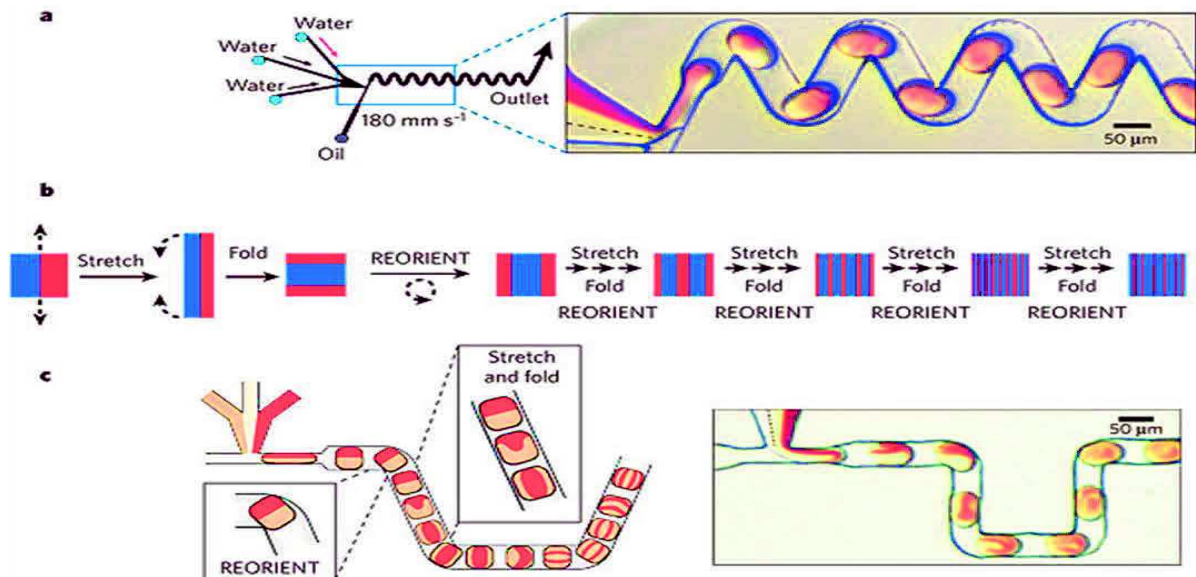


Figure 18-a. Droplet mixing. Arrow color corresponds to dye in stream solution. Dashed line in image indicates merging of the streams. b. Schema of a fluid element undergoing stretching, folding and reorientation. c. Microphotographs of a microfluidic network in which flow patterns inside plugs in the microchannel demonstrate flow folding and stretching pattern. Figure from<sup>166</sup>.

Numerous pursuits for improved mixing have been documented<sup>187</sup>. As an attempt to enhance the asymmetry of shear forces on either side of the droplet as it traverses the winding channels; a few research groups have implemented saw-tooth edged winding channel design<sup>188 189</sup> (Figure 19a). Furthermore many interesting additional ideas for droplet mixing have also been introduced without gaining widespread approval from the  $\text{D}\mu\text{F}$  community. One of them is active droplet

mixing induced by laser pulses<sup>190</sup>. With the help of two pulsed lasers operating in a time-varying pattern, asymmetric mixing could be induced in droplets (Figure 19b). The laser pulse locally heats the droplet and induces flow toward this heated spot. However, since droplets must be stopped in order for the mixing to occur the big advantage of fast handling is lost. Thus the applicability of this technique in microfluidic systems requiring high throughput is problematic since the maximum processing rate of droplets for mixing has been 1 per second.

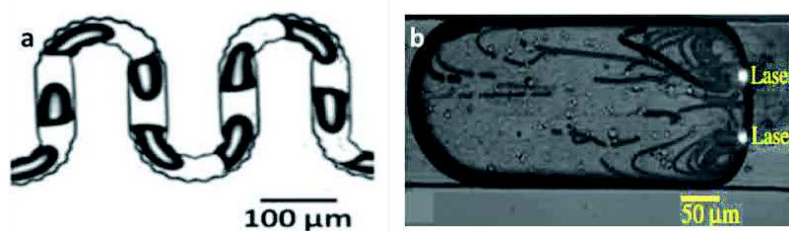


Figure 19- a. From<sup>188</sup>, rapid mixed of reagents in a saw-tooth edged channels. b. From<sup>190</sup>, visualization of the flow fields with tracers using two stationary off-center laser spots.

For all different chip geometries the droplet flow rate has to be controlled. Mainly there are two methods used: syringe pumps and pressure-driven controls. Although syringe pumps is the traditional method there are many arguments against it. First, it has a long response time of the flow rate, ranging from seconds to minute, making it a bad candidate for HTS applications. Moreover there is always the danger that the piston of the syringe pump will generate oscillations at low flow rate, making this way the experiment untrustworthy. Last but not least, it is difficult to set up and control.

### II.4.2.1. Micro-droplet devices (chips) design and fabrication

The design of the microchips is described in detail elsewhere <sup>164</sup>, here the main idea is roughly presented. PDMS chips were produced by soft lithography technique at the clean-room facilities of IPCMS. The microfluidic devices were designed in AutoCAD 2012 software with three aqueous square channel sections and one for oil with dimensions of  $50 \times 50 \mu\text{m}^2$  leading to a T junction. The designs were printed in high resolution to produce the photomasks. Molds were prepared in a silicon wafer spin-coated with an SU8-2050 (MicroChem) photoresist. The design (as seen in Figure 20) was transferred from the photomasks to the mold by photolithography in glass petri disc. The mold was then developed, and the casting with PDMS (Sylgard) was carried out. The PDMS chips were cleaned using neutral detergent, rinsed with demineralized water, washed with isopropyl alcohol and dried with nitrogen. They were irreversibly sealed with glass slide using oxygen plasma (plasma active Diemer). Last a 1% solution of 1H,1H,2H,2H-perfluorodecyltrichlorosilane (Alfa Aesar) in perfluorodecalin (PFD, Alfa Aesar) was directly inserted with a syringe in the channels to render the chips hydrophobic and then rinsed with  $\text{N}_2$ .

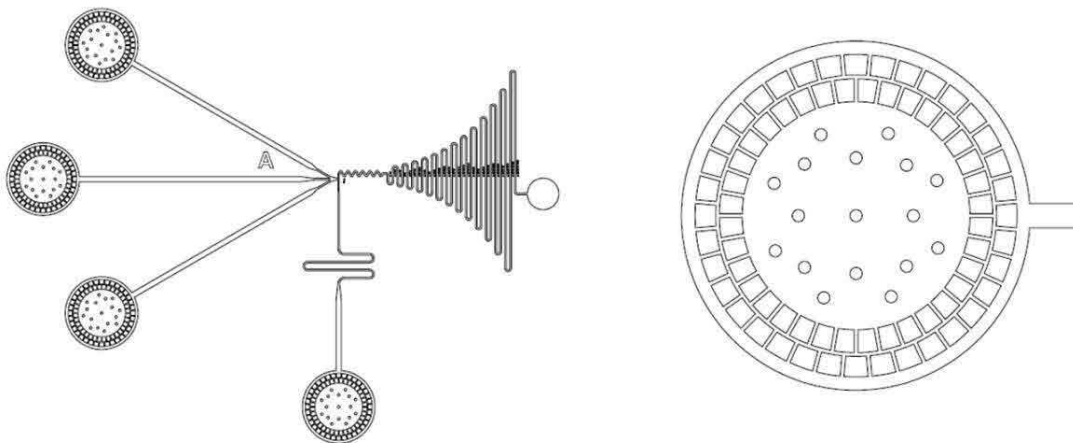


Figure 20-a. Overview of a device drawing (AutoCAD). The three input channels for aqueous solutions are presented on the left and the one for oil is located at the bottom. b. Zoom on an input, where a filter is used composed of blocks spaced less than the width of the channels in order to avoid blocking.

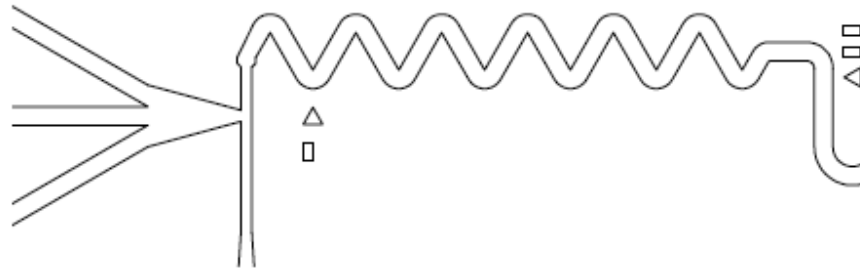


Figure 21-Photograph of the mixing region in one of our microfluidic chips.

The original microfluidic devices were produced using microelectronics technologies, such as photolithography and etching in silicon <sup>191</sup>. The big drawback of those techniques was their high cost and the demand of a clean environment. Hence, soft lithography technique was proposed <sup>192</sup> in order to fabricate microfluidic chips in poly(dimethylsiloxane) (PDMS) rapidly and cost-efficiently. Some additional advantages of PDMS are the nontoxicity, optical transparency, flexibility and the ability to be sealed reversibly or irreversibly <sup>193</sup>.

### **Measurement of the droplet's flow speed**

A white LED panel (Phlox SA) driven by a function generator (DS340, Stanford Research Systems) is utilized to shine light on the microfluidic chip. Two 10  $\mu$ s light pulses separated by a well-defined time interval reach the microfluidic chip whose transmission is recorded by a CCD camera (C8484, Hamamatsu) in a single image acquisition with the help of a flip-mirror. The above results in the superposition of two images separated in time by a known delay. This known delay is also the time during which the droplets propagate. The propagation length is measured and the droplet's speed is calculated. This later will enable establishing the relationship between propagation distance and relaxation time along the channels of the microfluidic chip, as depicted in Figure 22.

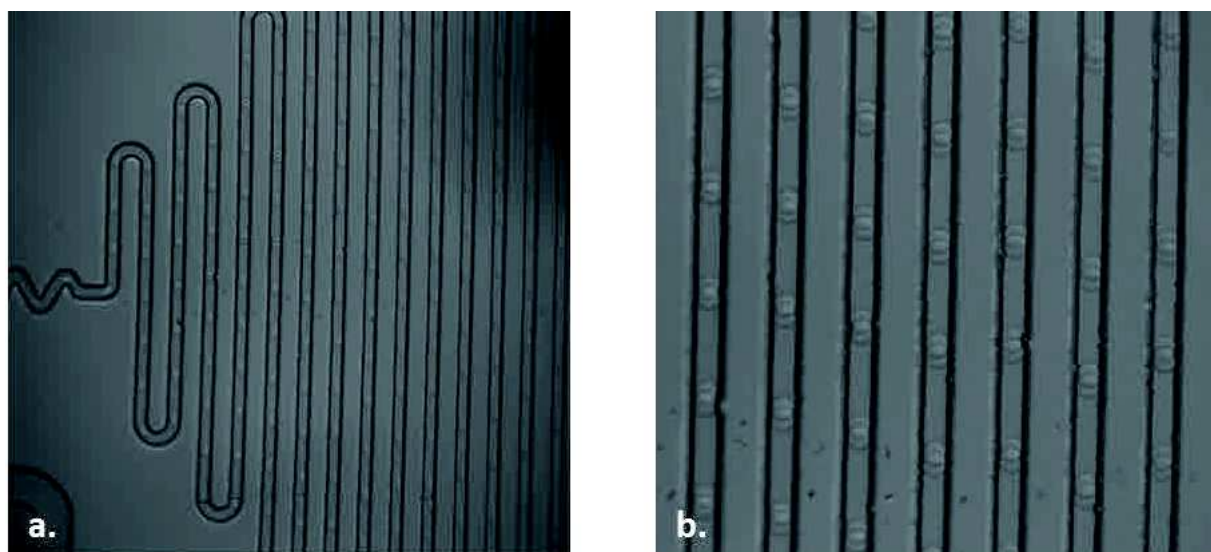


Figure 22-Droplets flowing in a  $50 \times 50 \mu\text{m}$  channel with speed 50 mm/s between light pulses separated by 0.5 ms a. full picture b. zoom.

### II.4.3 Droplet Microfluidics combined with Time Resolved Fluorescence Spectroscopy

As presented in the previous sections of this chapter pump probe monitors events occurring within fs to ns range, TRF within ps to hundreds of ns. However, larger-scale conformational changes with biological interest occur on significantly slower time scales (up to several seconds or minutes). For this reason TRF has been successfully combined with droplet microfluidics in this PhD work.

A novel experimental approach based on the combination of Droplet Microfluidics with TRF offers the possibility of investigating relaxation dynamics of structurally heterogeneous biomolecular systems. Droplet Microfluidics was employed to produce with minimal material consumption an out-of-equilibrium molecular system by rapid mixing, and TRF detection was utilized as a reporter of the structural heterogeneity along the relaxation of the system during its propagation through the microfluidic channel.

Structural relaxation studies in out-of-equilibrium biomolecules using TRF detection were previously implemented with stopped flow<sup>194–196</sup> and continuous flow<sup>197–200</sup> apparatuses. Those approaches achieved reporting structural heterogeneity and structural intermediates along the duration of the reaction. In the present study TRF is combined with Droplet Microfluidics, leading to a more advantageous approach. Droplet Microfluidics offers fast mixing (ms), long propagation times with no reagent dispersion and precise relation between the propagation length and time. Therefore tracking of structural relaxation of out-of-equilibrium molecular complexes from ms up to seconds is facilitated. The concentration and number of reagents is adjustable in contrast with continuous flow techniques that for fast mixing require fast diffusion of one reagent in large excess across a very large concentration jump<sup>167,201,202</sup>.

In the present project wide field imaging of the microfluidic chip is realized along the photocathode wire of a streak camera as shown in Figure 23. In detail: The microfluidic chip is illuminated with a sheet of light produced by a cylindrical lens and wide field imaging of the excitation line is implemented on the photocathode of a streak camera (SC). The photocathode is a 4.5 mm long wire offering a 2 mm-wide field of view with the present optical set-up. Under these conditions several kinetic traces can be recorded simultaneously at different locations corresponding to different propagation times in the microfluidic channel. The data acquired with the SC along the main microfluidic channel was organized in a matrix incorporating fluorescence decay curves as a function of propagation time. Numerous fluorescence kinetic traces are recorded successively at consecutive locations along the main microfluidic channel. Every fluorescence kinetic trace derives from averaging over a large number of successive identical droplets acquired at different reaction time. The fluorescence decay kinetics can be recorded on distinct temporal window spanning from ns to ms, with the shortest time window offering the best time resolution of ~8 ps.

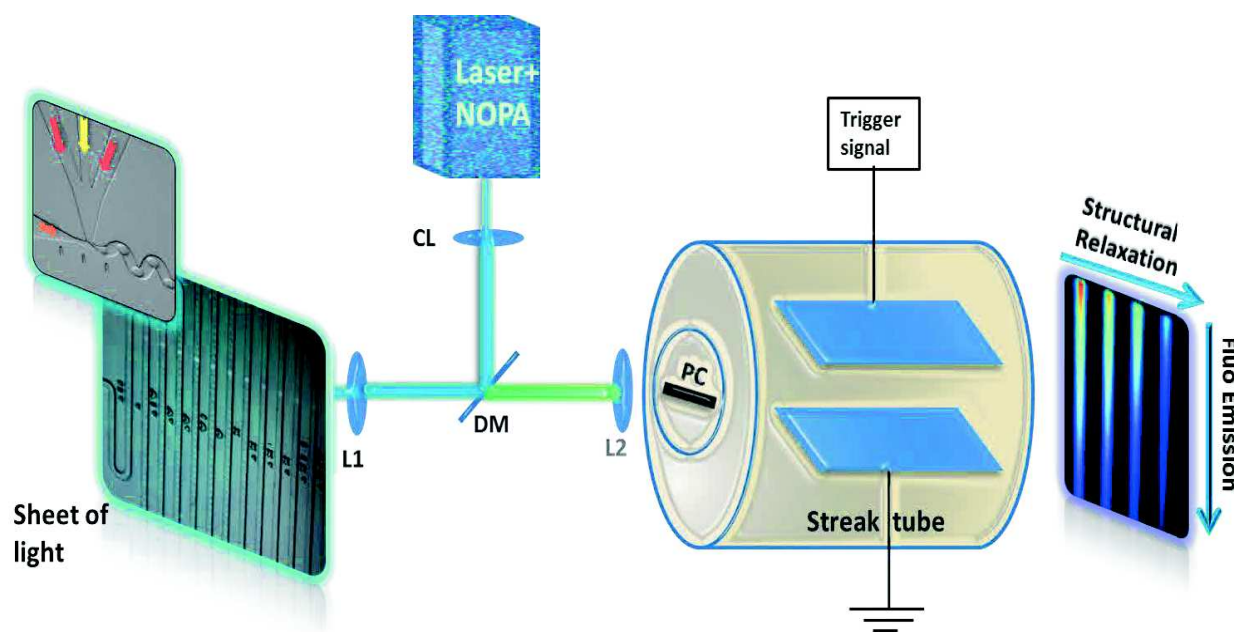


Figure 23- Schematic illustration of the set up combining Droplet Microfluidics with TRF. Fluorescence emitted by individual droplets circulating in the main microfluidic channel is imaged along the photocathode (PC) wire of a streak camera. 2D datasets are acquired with the dimension along the PC wire being the structural relaxation time axis (propagation in the microfluidic chip over seconds) and the second dimension being the fluorescence decay kinetics, which reveals the distribution of lifetimes.

Maillot et al <sup>148</sup> published a proof-of-principle experiment of this approach. In that study the fluorescence decay kinetics of a test biomolecular complex, bovine serum albumin (BSA), with Patent Blue V (PBV), a dye used for the visual inspection of sentinel lymph nodes prior to biopsy in early breast cancer patients were used<sup>203</sup>. The evolution of the fluorescence decay kinetics of PBV bound to BSA along its propagation in the microfluidic chip after the fast mixing (<10 ms) of both molecules in droplets was detected. Fluorescence decay kinetics over the entire structural relaxation of the out-of-equilibrium complex were acquired; evidencing heterogeneous structural relaxation over a 120 ms time scale.

In the present project, with a newly built set-up, the applications of this approach were expanded with a pH-jump experiment that allowed tracking of the structural relaxation in fluorescent proteins. This part will be thoroughly explained in chapter IV.



# III. 4'-methoxy-3-hydroxyflavone: One of a kind fluorescent dye for protein structure sensing

## III.1. Introduction

The transfer of a proton or a hydrogen atom from one group to another is classified among the fastest chemical reactions in nature, occurring in a scale of  $10^{-13}$ - $10^{-14}$  s<sup>204</sup>. This transfer is important for many biological processes, such as enzymatic reactions<sup>205</sup>. According to each system the reaction can be intramolecular or intermolecular and arise by thermal or photoinduced activation and overcoming a negligible or big energy barrier.

Here we will be mostly interested in excited state intramolecular proton transfer (ESIPT), where an intramolecular proton donation from a donor and an acceptor takes place. This proton donation leads to a formation of tautomeric species with Stokes shifted emission spectra<sup>206</sup>. An exceptionally interesting dye family exhibiting ESIPT is the 3-hydroxyflavone (3HF) family. In the present chapter a derivative of this family- very promising for protein structure sensing- is being presented.

In the following the 3HF family is briefly described together with some cornerstone publications and investigations on numerous derivatives. My main results on the 4'-methoxy-3-hydroxyflavone derivative will be displayed in the form of a manuscript under preparation for submission.

### III.1.1 3-Hydroxyflavone family

Due to their environmental sensitivity, numerous studies have been conducted on the photophysical properties of 3HF. 3HF undergoes ESIPT evidenced by spectrally separated dual emission of excited normal (N\*) and tautomeric (T\*) form. Generally increase of the polarity and H-bond donor ability of solvents inhibit the ESIPT reaction and thus decrease the relative intensity of the ESIPT product (T\*)<sup>207</sup>. In addition the position of the T\* peak is insensitive to solvent polarity, exhibiting though high sensitivity to H-bond donor ability<sup>208</sup>. This results to a class of fluorophores able to provide two independent pieces of information regarding their surrounding environment. The use of this ratiometric probe enables deriving information on the solvent polarity and electronic polarizability<sup>207</sup>, hydrogen bond donor<sup>204</sup> ability and electrostatic field effects<sup>209</sup> of its micro-environment. Thus legitimately it became a preferred probe for applications ranging from protein probing or protein-protein interaction monitoring<sup>210,211</sup> to micelles<sup>212–214</sup>, bio-membranes and phospholipid models<sup>55,215–217</sup>.

Since its introduction, by Sengupta and Kasha<sup>16</sup>, 3HF has been extensively studied. The above-mentioned authors suggested a tunneling process rather than an energetic barrier when ESIPT occurs. Fast after that, McMorro and Kasha<sup>218</sup> in an extension of their original aforementioned study<sup>16</sup> stated that previously the presence of H-bonding impurities in their supposedly dry carbon solvents controlled and competed with the ESIPT detected processes.

Two main possible models describing the deactivation pathways are feasible and have appeared in literature through the years. The most plain model is the kinetic, where from the first excited Frank Condon state ESIPT takes place, probably by overcoming an energy barrier, populating the tautomeric T\* state and then relaxes to the ground state by photon emission, then through dark back proton transfer the photocycle is fulfilled<sup>219</sup>. Another possibility, consistently presented, is the equilibrium model<sup>220,221</sup>, which is easily rendered by analysis resulting in both forward and reverse ESIPT rates and thus solvent-dependent equilibrium between N\* and T\*. Upon excitation the initially populated N\* undergoes dual decay pathway with time constants  $t_1$  (back to the ground state) and  $t_2$  (T\* formation). Accordingly T\* kinetics are described by a single rise and decay with time constants  $t_2$  and  $t_1$  respectively. An additional complication for both models is the

one driven by heterogeneity in the ground state and thus at least two normal excited species will be formed originating multiple detected ESIPT traces.

Interestingly, double rise times for the tautomeric formation have been regularly reported and multiple were the given interpretations for different members of the same family. Initially it was attributed by Muehlpford et al to intramolecular redistribution and relaxation<sup>222</sup>(3HF). In the same line Chou et al<sup>223</sup> (4'-diethylamino-3-hydroxyflavone) provided a detailed model for the ESIPT relaxation mechanism, where the sequence of the proposed events was the following: after N absorbs a quantum of light, it undergoes FC excitation accompanied by an instant dipolar change due to charge transfer reaction. Solvent relaxation takes place in order to lead the system to an energetically favorable configuration. Nevertheless, since N and T\* have the same dipolar vectors ESIPT reaction can take place decoupled from the solvent relaxation process directly after FC excitation. However they pointed out that in their study the quantitative correlation between ultrafast decay in short wavelengths and rise at long wavelengths (sub ps) was difficult mainly due to their wavelength dependence. Ameer-Beg et al interpreted their data by assuming that the slower rise time (picosecond regime) is the time required for the intermolecular hydrogen bonding to be broken before the ultrafast ESIPT<sup>224</sup> (3HF&derivatives). Schwartz et al suggested that a double ESIPT can be a result of a monosolvate undergoing dual proton transfer, which causes a rapid ESIPT in polar protic solvents<sup>225</sup> (3HF). Ormson et al<sup>226</sup>(4'-N,N-dimethylamino-3-hydroxyflavone) suggested that twisted excited state takes place and that particularly in hydrogen bonding solvents; molecular twisting can compete with proton transfer. Parsapour et al<sup>227</sup> (4'-(N,N-dimethylamino)- $\alpha$ -naphthyl-3-hydroxychromone) argued that normal and tautomeric molecules are likely to have different equilibrium phenyl torsion angles thus the ground state molecule probably has phenyl further out of plane than either of the excited states. So they expected that instantaneous proton transfer rate will vary as the torsion proceeds. Following the same way of thinking Strandjord et al<sup>228</sup>(3HF) studied the structural effects on the proton transfer kinetics of 3HF and concluded that the proton transfer activation energy is a function of the torsional angle of the phenyl ring. In the same route Klymchenko et al<sup>229</sup> (2-aryl-3-hydroxychromones) studied the perturbation of planarity causing solvent dependent variations in quantum yield measurements in an analog of 3HC named 3-Hydroxyquinolones.

It is thus difficult but necessary to distinguish the differences and the common ground between the extended 3HF family members. Numerous research groups have used ultrafast techniques to

understand the population dynamics of different species on femtosecond time scales in a variety (in polarity or in hydrogen bonding abilities) solvent environments. The most extensively studied representative of this family is the “mother molecule” 2-phenyl-3-hydroxy-flavone (3HF)<sup>212,213,218,224,225,228,230–247</sup>. The common ground here is that in 3HF, protic solvents may disrupt the intramolecular H bond and trigger the N\* fluorescence, but the ESIPT reaction remains very fast, with a dominating sub100 fs component, resulting in a very weak N\* emission.

Considering the 4'-substituted derivatives of the mother 3HF molecule, the most commonly studied ones were 4'-N,N-diethylamino-3-hydroxyflavone<sup>48,223,248–252</sup> and 4'-N,N-dimethylamino-3-hydroxyflavone<sup>226,253–259</sup> (and some with additional substitutions to these aforementioned<sup>220,227,260,261</sup>). Under these 4'-substitutions, the charge transfer character of N\* may strongly favor the intramolecular H-bond disruption by protic solvents, such that the N\* emission band largely dominates in most protic solvents.

Herein, aiming for the gold intermediate of moderate N\* emission intensity and optimized sensitivity of the ratiometric detection principle lead us to study 4'-methoxy-3-hydroxyflavone (4M3HF), that carries a methoxy-group in the para position on the phenyl moiety (depicted in Figure 25). The electron donor strength of the 4-methoxyphenyl is weaker than the 4-diethyl/dimethyl-amino group substitutions<sup>56,262,263</sup> and is expected to facilitate the ratiometric detection<sup>264–266</sup>. Figure 24 illustrates the four level model of the ESIPT transformation for 4M3HF molecule.

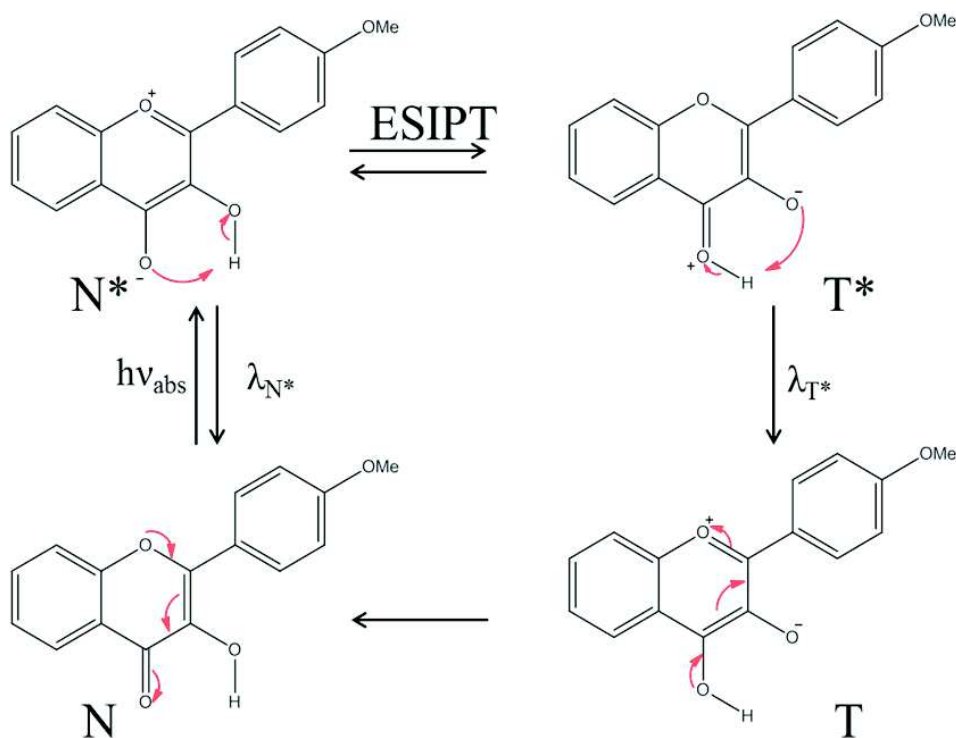


Figure 24-Schematic illustration of ESIPT reaction in 4M3HF.

The progression of events that results in two emission bands is the following (Figure 24). Absorption of a quantum of light populates the normal  $N^*$  state followed by solvent shell relaxation. Subsequently  $N^*$  state can emit a quantum of light or undergo ESIPT to the tautomeric  $T^*$  state. The emission of a quantum of light from  $T^*$  results in populating the ground  $T$  state with subsequent relaxation and proton back transfer occurring in the dark to the ground  $N$  state, closing the photocycle. This results to a two well-separated emission bands resulting from the formation of two excited-state tautomers (normal  $N^*$  and tautomeric  $T^*$ ), the relative intensity of which is controlled by the speed or equilibrium displacement of the ESIPT reaction, hence by the physico-chemical nature of the local environment. The ratio of the fluorescence intensities of both bands thus appears as an intrinsic probing of the fluorophore microenvironment<sup>207</sup>. For this reason, 3HF derivatives became an essential tool for monitoring site specifically the biomolecular interaction and their corresponding conformational changes<sup>267,268</sup>.

Keeping in view the applications, the recent work of Sholokh<sup>19</sup> successfully demonstrated the advantages of 4M3HF in biomolecular interactions and it is our task to rationalize the photophysical origin of its fluorescence emission properties.

With our investigation it has been shown that 4M3HF is a 3HF derivative presenting indeed high sensitivity in the H-bonding with its surrounding molecules and negligible polarity sensitivity. Thus its conformational isomerization and disruption of intramolecular hydrogen bonds is controlled by the intermolecular H-bonding formation. This one of a kind character enables it an advantageous label for protein probing and protein-protein interaction monitoring<sup>269</sup>.

Femtosecond TA spectroscopy with broadband UV-Vis probing, TRF spectroscopy, steady state absorption and quantum yield measurements were used to investigate the ESIPT reaction kinetics of 4M3HF in solvents of varying polarities and hydrogen bonding abilities. The examination was grounded on the comparison of the excited state spectroscopic signatures of 4M3HF to those of methylated-4M3HF, where the hydroxyl group is replaced by a methoxyl group, precluding the ESIPT reaction. Dr Andrey Klymchenko (Laboratory of Biophotonics and Pharmacology, Strasbourg) and Dr Yves Mély (Laboratory of Biophotonics and Pharmacology, Strasbourg), provided the studied molecules and contributed at the interpretation of the results. The structure of the molecule is shown in the Figure 25.

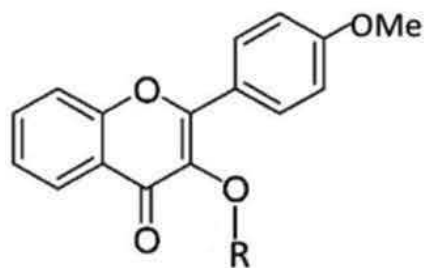


Figure 25-Structure of compounds 4M3HF for R=H and its methylated compound for R= CH<sub>3</sub>.

In the following section, the used experimental data analysis techniques are presented accompanied with the results of this project in a form of a paper under preparation.

## III.2. Methods

### A. Concerning the analysis of TRF spectroscopy data:

A streak camera was used to record the spectrally-resolved fluorescence decay kinetics. Figure 26 displays an example of the data obtained for 4M3HF in DMF, on a 1 ns time window with a 7 ps time resolution. Spectral integration for  $\lambda < 475$  nm and  $\lambda > 525$  nm yields the decay kinetics of two different excited state bands, corresponding to the normal N\* and tautomeric T\* states. We performed independent but also global fittings. Global fitting refers to simultaneous fitting of two or more datasets by permitting parameter sharing between the fitted curves. In the present case the time constants were shared to identify if the decay of species corresponds to rise of another species, which was actually the case, shown in Figure 26c. Their global fit reveals the dominating time scales for the decay of N\* (found by spectral integrating 400-475 nm) and simultaneous rise of T\* (found by spectral integrating 525-625 nm), i.e. for the ESIPT reaction, and also the corresponding one for the decay of T\*. A more detailed and accurate investigation of the early time kinetics was carried out by TA spectroscopy with a 60 to 80 fs time resolution.

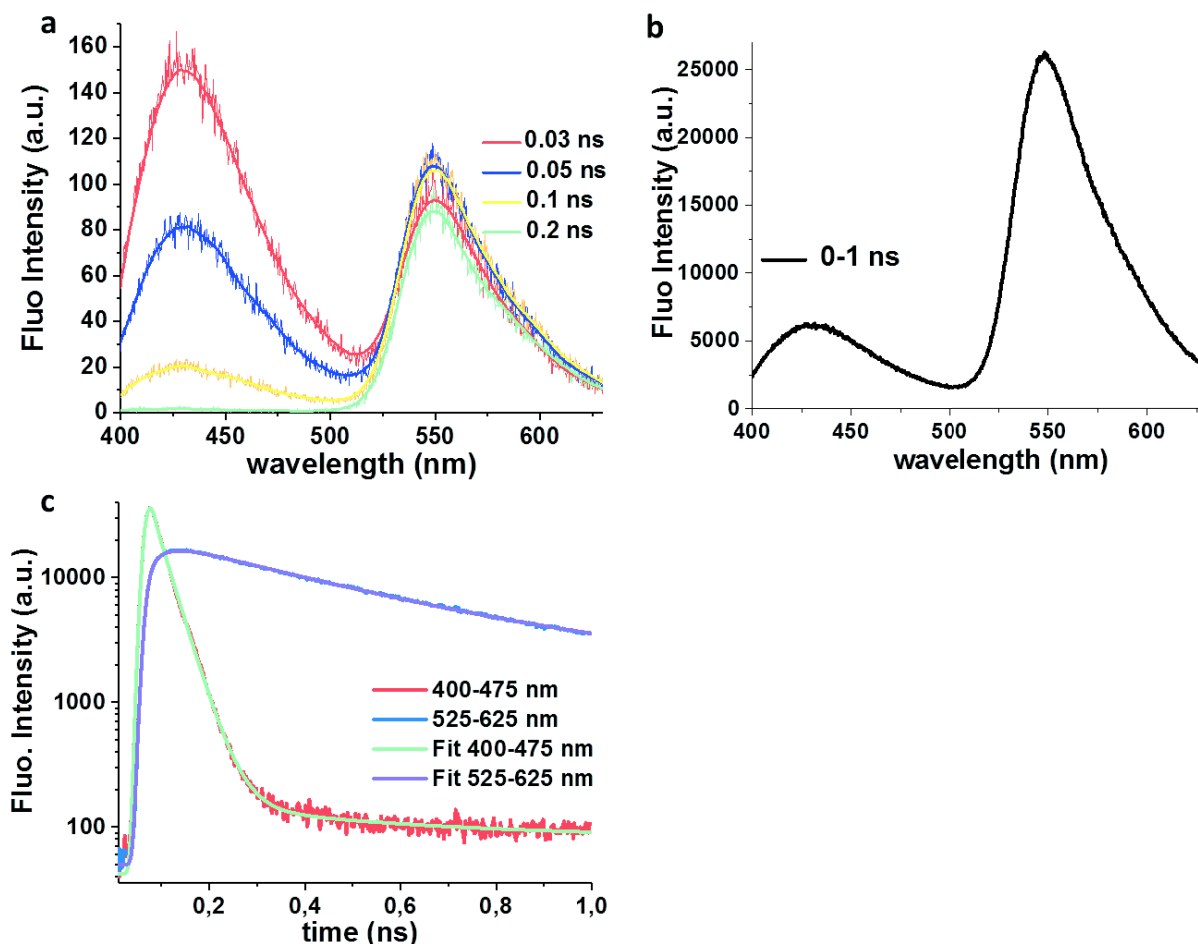


Figure 26-TRF Spectroscopy of 4M3HF in DMF. a. Fluorescence spectra of selected time delays after laser pulse excitation at 343 nm. b. Same as above integrated of the full recorded spectrum. c. Decay kinetics of the N\* (in red) and T\* (in black) bands integrated over the  $\lambda < 475$  nm and  $\lambda > 525$  nm spectral windows, respectively. Both curves are fitted globally.

TRF spectroscopy measurements were performed with a streak camera (Hamamatsu, C10627). The set-up is based on a femtosecond fiber laser (Amplitude systems, Tangerine) pumping a home-made OPA that generates pulses at 343 nm with energies of 33 nJ/pulse. The polarization of the beam was set in magic angle (54.7) with respect to the detection polarization axis, in order to eliminate any fluorescence anisotropy kinetics.

The steady-state absorption spectra were recorded on a Perkin Elmer Lambda 950 UV/VIS spectrometer. Fluorescence emission quantum yields were determined by comparison with the Quinine sulfate in 0.1M H<sub>2</sub>SO<sub>4</sub><sup>270</sup> with a Horiba Fluoromax4 spectrometer.

## **B. Concerning the analysis of the TA data:**

It was performed following several steps. Initially the raw acquired data is corrected from erroneous signal through:

### **a. Solvent correction**

Solvent correction is needed due to the non-zero absorption of the solvent containing the molecule of interest. This contribution is removed by separate recording of the pump-probe signal on solely solvent under the same experimental conditions as the ones when the molecule was included. This correction is done with subtraction of the two signals.

$$\Delta A(\lambda, \Delta t)_{corrected} = \Delta A(\lambda, \Delta t) - \text{factor} * \Delta A(\lambda, \Delta t)_{solvent}$$

The factor here has to be introduced due to the strong absorption of the beam by the molecule leading to a decrease in the solvent's signal.

### **b. Group Velocity Dispersion/ Chirp Correction**

Since a crystal (CaF<sub>2</sub>) is utilized in order to generate the probe which has to be propagated via reflections a non-uniformity of the refractive index versus wavelength is unavoidable. Thus as a consequence of this Group Velocity Dispersion (GVD) the components of the probe allocated in the blue range of the spectrum will arrive later on the sample in comparison with the red than will

arrive sooner. This effect can influence the final data at shorter times since in shorter wavelengths the signal will seem to rise faster than in longer wavelengths. This is corrected by chirp fitting allowing determining for each wavelength the amount of time  $\delta t(\lambda)$  induced by GVD. The data is finally corrected by interpolating the signal at each wavelength at a time  $t_{corrected} = t + \delta(t)$ . Thus:

$$\Delta A_{corrected}(\lambda, \Delta t_{corrected}) = \Delta A(\lambda, \Delta t + \delta t(\lambda))$$

Following step is to fit the corrected data.

The pump probe setup for TA detection uses the 40 fs pulses of a Ti: sapphire regenerative amplifier (5 kHz) to pump a commercial optical parametric amplifier followed by second harmonic generation (TOPAS; Light Conversion) generating 33nJ pulses at 343 nm. The probe white-light continuum is generated in a 2 mm CaF<sub>2</sub> plate. The polarization of the pump beam is set at the magic angle (54.7°) with respect to that of the probe. The samples were circulated through a 0.2 mm path length quartz fused silica flow cell using a peristaltic pump.

## Singular Value Decomposition (SVD)

Singular Value Decomposition is a mathematical tool used for noise filtering and data reduction<sup>271</sup>. Since not all the wavelengths carry contributions from all the molecular states and a single fit is not adequate to reveal the entire dynamics a mathematical tool like SVD is needed. This can be advantageous by highlighting a certain number of kinetic traces that has to be fitted, filtering out the noise. The number of the kinetic traces that will be taken into account depends solely on the dataset and it is derived by determining the non-significant traces, as shown further.

To take it from the beginning, SVD of a matrix  $A$  is the factorization of  $A$  into a product of three matrices as  $A = USV^T$  where the columns of  $U$  and  $V$  are orthogonal and the matrix  $S$  is diagonal with only positive real entries. To gain insight into the SVD, the rows of the ( $n * d$ ) matrix  $A$  are

treated as  $n$  points in a  $d$ -dimensional space and the problem is now targeted on finding the best  $k$ -dimensional subspace with respect to the set of points. The matrix can be written as:

$$A_{n,d} = U_{n,n} S_{n,d} V_{d,d}^T$$

If we want to analytically calculate the SVD of the matrix  $A$ , then we need to find the eigenvalues and eigenvectors of  $AA^T$  and  $A^T A$ . Then the eigenvalues of  $A^T A$  will constitute the columns of  $V$ , the eigenvectors of  $AA^T$  constitute the columns of  $U$ . Last the singular values of  $S$  will be the square roots of eigenvalues from  $AA^T$  or  $A^T A$ . The singular values are then the diagonal entries of the  $S$  matrix arranged in descending order. In our case the matrix  $A_{n,d}$  consists our data: each column is a kinetic trace and each line a spectrum. The matrix  $U$  then includes transients as columns and the matrix  $V$  spectra. The selected singular values would then be in descending order starting from the first transient of  $U$  and the first spectrum of  $V$  as the most important. As depicted in the Figure 27 final goal is to reach as fewer singular transients as possible without discarding any important data information. In the case shown in the figure only 4 singular kinetic traces are taken into consideration, the fifth has only a non-resolved peak that will not add any information to our fit and it is therefore disregarded. Usually the number of singular transients is 1-2 for TRF and 4-5 for pump-probe experiments.

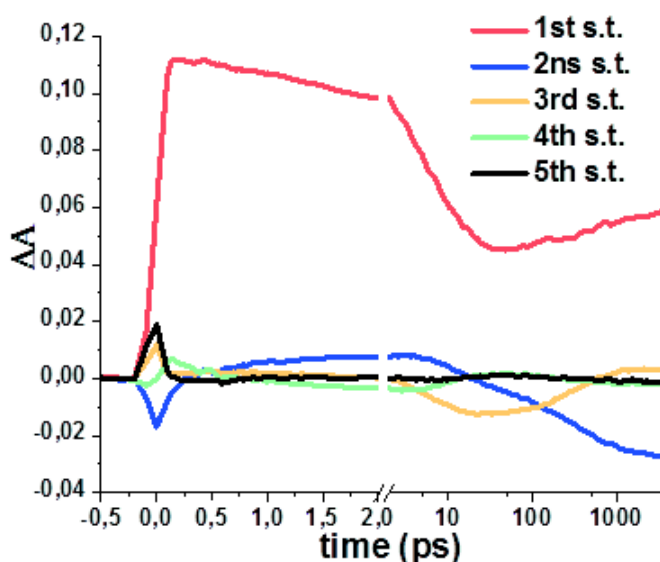


Figure 27-The 5 first singular kinetic traces derived from SVD analysis for 4-Methoxy-3-Hydroxyfavone in DMF solvent.

## Global fitting

The method used to fit all the singular kinetic traces derived from SVD analysis was global fitting, which is generally a process for fitting one or more fit models to one or multiple input datasets simultaneously<sup>272–275</sup>. When a parameter is shared, a single parameter value is calculated for all datasets; when a parameter is not shared, a separate parameter value is calculated for each dataset. In the present case all the data sets were fitted by sharing the time constants deriving from a sum of exponential decay. The time needed for the convergence of global fitting can be reduced by providing educated guesses for the parameters. This guess can be more or less elaborate and consist of only a few averaged parameters and a minimum amount of lifetimes. One example of the four first singular kinetic traces fitted globally is shown in Figure 28.

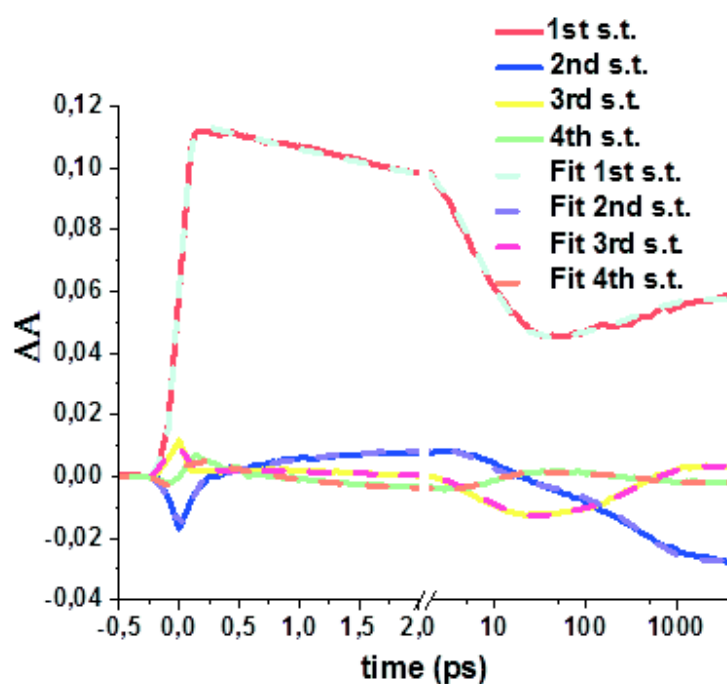


Figure 28-The 4 first singular kinetic traces were fitted globally. Data acquired for 4-Methoxy-3-Hydroxyfavone in DMF solvent.

In order to cross-check if the fifth kinetic trace that was discarded previously was indeed the correct decision; the residuals of the four kinetic traces that were fitted are plotted together with

the fifth kinetic trace. Figure 29b reveals that indeed the fifth kinetic trace is in the noise level with exception the artifact close to time zero induced by pump scattering.

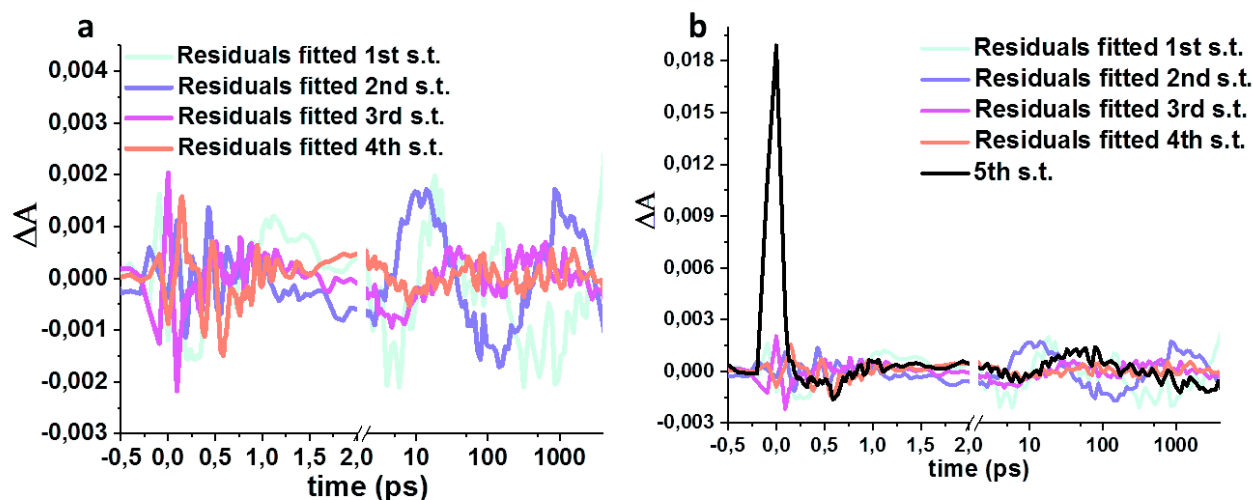


Figure 29-a. Plotted residuals corresponding to the four first fitted kinetic traces. b. The residuals plotted together with the fifth kinetic trace.

## Decay Associated Spectra (DAS)-

**Each DAS spectrum represents the absorption of a state on a specific time constant**

An additional tool for data analysis is Decay Associated spectra (DAS). Each DAS is associated with solely one time constant and corresponds to the spectral evolution occurring within this time constant. The time scales, with which each DAS is associated, are derived by the global fitting applied on the most important  $n$  singular kinetic traces determined by the SVD analysis. Thus the DAS are the product of the fitted amplitudes, the  $n$  singular values and the  $n$  first  $V$  matrix spectra. One example of DAS can be found in Figure 30.

The importance of DAS is defined by the step identification of the molecular dynamics. This means that, since each DAS is associated with one time constant, we are able to identify the species involved in the reaction within this time constant and follow their changes spectrally.

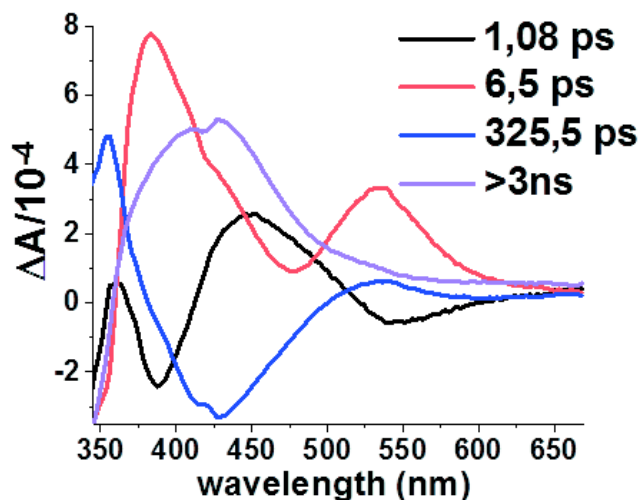


Figure 30-Decay Associated Spectra corresponding to 4-Methoxy-3-Hydroxyfavone in DMF solvent.

In conclusion, in the present study femtosecond TA spectroscopy with broadband, UV-Vis probing, TRF spectroscopy, steady state absorption and quantum yield measurements were used to investigate the ESIPT reaction kinetics of 4M3HF in solvents of varying polarities and hydrogen bonding abilities. Specifically we used successively methanol (MeOH, polar, protic), dimethylformamide (DMF, polar, aprotic but H-bond donor), acetonitrile (ACN, polar, aprotic but H-bond acceptor) and toluene (non-polar, aprotic). The examination was grounded also with the comparison of the excited state spectroscopic signatures of 4M3HF to those of methylated-4M3HF, where the hydroxyl group was replaced by a methoxyl group, precluding the ESIPT reaction. All the details can be found in the following attached under-preparation paper.

### III.3. Results

## Ultrafast photophysics of the environment-sensitive 4'-methoxy-3-hydroxyflavone fluorescent dye

Anastasia Ioanna Skiliti<sup>1</sup>, Damianos Agathangelou<sup>1</sup>, Ievgen Shulov,<sup>2</sup> Jamie Conyard<sup>1</sup>, Stefan Haacke<sup>1</sup>, Yves Mély<sup>2</sup>, Andrey Klymchenko,<sup>2</sup> Jérémie Léonard<sup>1</sup>

1. Institut de Physique et Chimie des Matériaux de Strasbourg, & Labex NIE CNRS Université de Strasbourg, Strasbourg, France

2. Laboratoire de Biophotonique et Pharmacologie, CNRS - Université de Strasbourg, Illkirch, France

[Jeremie.Leonard@ipcms.unistra.fr](mailto:Jeremie.Leonard@ipcms.unistra.fr)

---

**ABSTRACT:** The excited state intramolecular proton transfer (ESIPT) of 3-hydroxyflavone derivatives results in a fluorescence spectrum composed of two emission bands, the relative intensity of which is strongly influenced by the interaction with the microenvironment. We use time-resolved fluorescence and ultrafast transient absorption spectroscopies to investigate the photophysics of 4'-methoxy-3-hydroxyflavone in different solvents characterized by various polarities and hydrogen (H) bonding capabilities. We evidence that in this compound, the ESIPT reaction rate varies by more than 3 orders of magnitude, depending on the H-bonding capability of its microenvironment. This remarkable property is attributed to the moderate electron-donating strength of the 4'-methoxy substituent, and turns this fluorescent dye into a very promising fluorescent probe of biomolecular structures and interactions, where local structural heterogeneity may possibly be revealed by resolving a distribution of ESIPT reaction rates.

---

### Introduction

The influence of the microenvironment on fluorescence emission has long been exploited for fluorescence sensing.<sup>1, 2</sup> In this context, chromophores undergoing excited state intramolecular proton transfer (ESIPT) and 3-hydroxyflavone (3HF, or phenyl-3-hydroxychromone) derivatives in particular are of great interest due to the dramatic influence of the interaction with the environment on the ESIPT mechanism and consequently on the related chromophore fluorescence properties.<sup>3</sup>

The intramolecular H-bond from the 3-hydroxyl group to the neighboring 4-carbonyl group (see Figure 1) in the ground state N (normal) form, results in an ultrafast (<50 fs), barrierless proton

transfer in the first  $S_1$  excited state  $N^*$  producing the tautomeric form in its  $S_1$  state, named  $T^*$ .<sup>4-6</sup> The consequence is that upon excitation of the  $N$  form (around 350 nm) the green emission of the  $T^*$  form is observed rather than that of  $N^*$ , resulting in a prominent apparent Stokes shift of over  $5000\text{ cm}^{-1}$ .<sup>7</sup> Of central interest for fluorescence sensing, the disruption of the intramolecular hydrogen (H) bond impairs this ultrafast ESIPT and therefore turns on the (blue) emission of the  $N^*$  form. This may be caused by the interaction with H-bond donor molecules such as water or protic solvents in general<sup>8-12</sup> or with H-bond acceptor molecules.<sup>13</sup>

Besides the “extreme sensitivity to hydrogen bonding perturbations”<sup>8</sup> of the fluorescence emission properties of 3HF, the strength of the intramolecular H bond may be fine-tuned by acting on the pi-electron system conjugation across the two rings of the compound. This may be achieved by modifying the planarity of the molecule by steric effects (modification of the size of the phenyl group)<sup>14, 15</sup>, by functionalizing the compound with electron donating groups such as the dialkylamino group and/or extending electronic conjugation.<sup>16-19</sup> The electron donor groups confer to the  $N^*$  state a much larger charge transfer character,<sup>16, 20, 21</sup> which thus becomes strongly sensitive to the environment polarity. As a consequence, even in aprotic solvents, the  $N^*$  emission is observed in polar solvents and is strongly solvatochromic.<sup>18, 22, 23</sup> This is interpreted as the effect of solvation on the ESIPT reaction which now occurs between two, solvated  $N^*$  and  $T^*$  states carrying very different dipoles.<sup>17, 24-26</sup> In these conditions, the reverse ESIPT from  $T^*$  to  $N^*$  may become fast leading to equilibration of both solvated states before (slower) radiative decay occurs from either state.<sup>27</sup>

The outstanding sensitivity of the fluorescence emission of 3HF derivatives to environment polarity, electric fields, and H-bonding capability triggered a strong interest in these compounds for fluorescence sensing of local biophysical properties in micelles, membranes, or fluorescence sensing of biomolecular interactions.<sup>3, 28-36</sup> One major motivation for the synthesis of specific 3HF derivatives targeting such applications resides in the so-called ratiometric fluorescence sensing.<sup>23, 33</sup> Indeed the fluorescence emission of 3HFs is in general characterized by two well-separated emission bands (from  $N^*$  or  $T^*$ ), the relative intensity of which is controlled by the speed or equilibrium displacement of the ESIPT reaction, hence by the physico-chemical nature of the local environment. The ratio of the fluorescence intensities of both bands thus appears as an intrinsic probing of the fluorophore microenvironment.<sup>23</sup>

In this paper, we investigate the solvent-dependent photophysical properties of 4'-methoxy-3HF (compound **1**), which carries a methoxy group in the *para*-position on the 2-phenyl moiety (see Figure 1). The compound was recently functionalized as a synthetic amino acid offering very promising fluorescence properties for protein interactions studies.<sup>32</sup> The motivation for synthesizing this compound was to optimize the ratiometric sensing of hydration in biomolecules, based on the following reasoning.<sup>30, 37, 38</sup> In 3HF, protic solvents may disrupt the intramolecular H-bond and turn on the  $N^*$  fluorescence, but the ESIPT reaction remains very fast, with a dominating sub-100 fs component, resulting in a very weak  $N^*$  emission.<sup>4, 5</sup> In the 4'-*(dialkylamino)*-3-hydroxyflavone (FE, see Figure 1) instead, the charge transfer character of the  $N^*$  state slows down the ESIPT reaction in polar solvents and blocks it in protic solvents, such that the  $N^*$  emission band largely dominates in most protic solvents.<sup>12, 27</sup> Considering now the series of 3-hydroxychromones carrying 2-phenyl (3HF), 2-(4'-methoxyphenyl) (i.e. compound **1**) or 2-(4'-*N,N*-dialkylaminophenyl) (FE) groups (see Figure 1), the electron donor strength of the 4'-methoxyphenyl moiety is intermediate and may hence result in an intermediate ESIPT rate,<sup>39</sup>

meaning an intermediate N\* emission intensity, which is likely to optimize the sensitivity of the ratiometric detection principle.

While the recent work of Sholokh et al.<sup>32</sup> demonstrates the success of the above reasoning at developing efficient fluorescent probes for sensing biomolecular interactions, the present work aims at rationalizing the photophysical origin of the fluorescence emission properties of **1**. In order to distinguish the specific signatures of solvation or intramolecular dynamics from those of the ESIPT reaction we investigate also compound **2** (see Figure 1), where the 3-hydroxyl group is replaced by a 3-methoxyl group, thus precluding the ESIPT reaction. We observe that the ESIPT reaction time scale of **1** in various solvents spans from sub 100 fs to as much as 100 ps, and that this time scale is primarily affected by the H-bonding capability of the solvent. This unprecedented variability of ESIPT rates enhances the sensitivity of **1** at probing local H-bonding in proteins by the ratiometric method. What is more, it paves the way to unraveling distributions of various H-bonding environments in ensemble measurements, provided time-resolved spectroscopy is used to reveal this broad distribution of time constants.

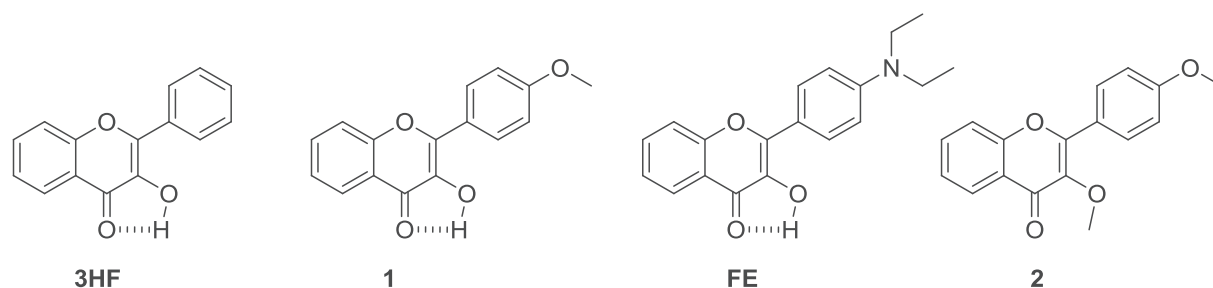


**Figure 1.** Structure of 3HF and its derivatives substituted at the 2-phenyl group.

## Methods

All solvents and chemicals were purchased from Sigma-Aldrich or Alfa Aesar. 4'-methoxy-3-methoxyflavone was purchased from Alfa Aesar. For absorption and fluorescence studies, the solvents were of spectroscopic grade (Sigma-Aldrich). Proton NMR spectra were recorded on a 400 MHz Bruker spectrometer. Mass spectra were recorded on Bruker HCT Ultra and Agilent Technologies Accurate-Mass Q-TOF LC/MS 6520 mass spectrometers.

For the synthesis of 4'-methoxy-3-methoxyflavone (**2**), 4'-methoxy-3-hydroxyflavone (1 eq., 100 mg, 0.373 mmol) and potassium carbonate (3 eq., 154 mg, 1.12 mmol) were placed in a dried, argon-flushed flask. Dry DMF (8 mL) was added with a syringe. The obtained mixture was preheated to 40°C for 30 min, then iodomethane (10 eq., 0.232 mL, 3.73 mmol) was quickly added dropwise using a syringe. Reaction mixture was stirred at 40°C overnight until full consumption of starting material (monitored by TLC). After completion, the solvent was removed under reduced pressure. The obtained residue was then redissolved in a mixture of dichloromethane and water. The organic layer was washed with brine, dried over Na<sub>2</sub>SO<sub>4</sub>, filtered and concentrated. The crude material was purified by preparative TLC chromatography (SiO<sub>2</sub>, DCM/MeOH, 98:2) to yield 79 mg (75%) of 4'-methoxy-3-methoxyflavone (**2**). <sup>1</sup>H NMR (400

MHz, Chloroform-*d*)  $\delta$  8.24 (ddd,  $J = 8.0, 1.7, 0.5$  Hz, 1H), 8.10 (d,  $J = 9.1$  Hz, 2H), 7.64 (ddd,  $J = 8.6, 7.1, 1.7$  Hz, 1H), 7.50 (dd,  $J = 8.5, 1.1$  Hz, 1H), 7.36 (ddd,  $J = 8.0, 7.1, 1.1$  Hz, 1H), 7.01 (d,  $J = 9.1$  Hz, 2H), 3.88 (s, 3H), 3.87 (s, 3H). HRMS ( $m/z$ ):  $[M+H]^+$  calcd. for C<sub>17</sub>H<sub>15</sub>O<sub>4</sub>, 283.0965; found, 283.0959. (Figures S1 and S2 in SI).

The steady-state absorption spectra were recorded on a Perkin Elmer Lambda 950 UV/VIS spectrometer. Fluorescence emission quantum yields were determined with an Horiba Fluoromax4 spectrometer, by comparison with Quinine sulfate in 0.1 M H<sub>2</sub>SO<sub>4</sub>, as a reference.<sup>40</sup>

Time-resolved fluorescence (TRF) spectroscopy measurements were performed with a streak camera (Hamamatsu, C10627) mounted on the output port of a spectrograph. The camera was operated in photon counting mode, with streaking time windows of 1 ns - achieving the best time resolution of 7 ps – to 5 ns, depending on the fluorescence decay kinetics. The set-up is based on a femtosecond amplified fiber laser (Amplitude systems, Tangerine), operated at 50 kHz. Its third harmonic at 343 nm was used to excite the compounds. The polarization of the beam was set at magic angle (54.7°) with respect to the detection polarization axis, in order to eliminate any fluorescence anisotropy kinetics.

The pump probe setup for transient absorption (TA) spectroscopy has been described elsewhere.<sup>41, 42</sup> In brief, it uses the 40 fs pulses of a Ti: sapphire regenerative amplifier (5 kHz) to pump a commercial optical parametric amplifier (TOPAS; Light Conversion) followed by second harmonic generation producing 33 nJ pulses at 343 nm. The probe white-light continuum is generated in a 2 mm thick CaF<sub>2</sub> crystal. The polarization of the pump beam is set at the magic angle (54.7°) with respect to that of the probe. The samples were circulated through a 0.2 mm path length quartz fused silica flow cell using a peristaltic pump. Two-dimensional (2D) data sets were acquired displaying the spectrally-resolved (300 to 700 nm) pump-induced absorbance change  $\Delta A$  as a function of pump probe delay. All TA data presented here are post-processed in order to (i) subtract the “solvent” signal around time-zero resulting from the coherent interaction of pump and probe laser fields, and (ii) compensate for the group velocity dispersion in the probe beam – independently determined from the pure solvent signal - so as to define time zero accurately (within ~20 fs) at all wavelengths. Singular Value Decomposition (SVD) was used for data reduction and noise filtering. Global fitting of the dominant 4 singular traces was performed. The fitting function was a sum of exponential decays convolved with a normalized Gaussian curve of standard deviation  $\sigma$  standing for the temporal Instrument Response Function (IRF). The residuals of the fits of the four singular transients were structureless, and of amplitude similar to or larger than that of the 5<sup>th</sup> and 6<sup>th</sup> singular transients, justifying that only the first four singular transients were considered as significant in this global analysis. The result of the global fitting was analyzed by computing and displaying the Decay Associated Spectra (DAS). Each decay time constant is associated to a DAS representing the spectral dependence of the prefactor of this decay component in the original 2D data set. The DAS reveal the spectral evolution occurring within their associated time constant, along the course of the molecule photoreaction.

## Experimental results

The photophysics of **1** has been systematically investigated in four different solvents characterized by different polarities and H-bonding capabilities, which are methanol (MeOH, polar, protic), dimethylformamide (DMF, polar, aprotic but H-bond acceptor), acetonitrile (ACN, polar, aprotic) and toluene (non-polar, aprotic). More specifically the four solvents listed in Table 1 are characterized by their solvent polarity scale  $E^T$ ,<sup>43</sup> H-bond donor ability (acidity)  $\alpha$ ,<sup>44</sup> and H-bond acceptor ability (basicity)  $\beta$ .<sup>45</sup>

**Table 1.** Maximum emission wavelength of compounds **1** and **2** in different solvents characterized by their Abraham's H-bond acidity and basicity,  $\alpha$  and  $\beta$ , respectively, and by their polarity scale  $E^T$  as given by Reichardt.<sup>43</sup>

Solvent	$\alpha$	$\beta$	$E^T_N$	<b>1</b> , $\lambda_{\max}$ (nm)		<b>2</b> , $\lambda_{\max}$ (nm)
				N*	T*	N*
MeOH	0.43	0.47	0.762	428	530	441
DMF	0	0.74	0.386	417	541	431
ACN	0.07	0.32	0.460	416	532	431
Toluene	0	0.14	0.099	-	534	428

Figure 2 displays the steady-state absorption and emission spectra of **1** and **2** in the four solvents. For both compounds the absorption spectra are weakly affected by the solvent, with a maximum absorption wavelength  $\lambda_{\max}$  at 350-355 nm for **1** and at 325-330 nm for **2**. In the latter compound, where ESIPT is prohibited because the 3-OH group is replaced by a 3-MeO group, only a single N\* emission band at a  $\lambda_{\max}$  of 430-440 nm (see Table 1) is observed, being very weakly affected by the solvent. In the case of **1**, however, the emission of the ESIPT product (T\* form) is observed at longer wavelengths (530 to 540 nm) in addition to the N\* emission (420-430 nm) in MeOH and DMF. In the case of ACN, the N\* band becomes much weaker than the T\* band and in toluene, only the T\* emission is observed. The fact that the N\* band dominates the emission in polar, protic solvents such as MeOH, but disappears in non-polar, non-protic solvents such as toluene, is similar to previous observations made with the related 4'-diethylamino-3-hydroxyflavone.<sup>23</sup> However, the very weak intensity of the N\* band in the polar ACN, as well as the negligible dependence with solvent polarity of the N\* emission  $\lambda_{\max}$  (best evidenced in Figure 2b for compound **2**) are in marked contrast with the case of 4'-diethylamino-3-hydroxyflavone.

23, 24

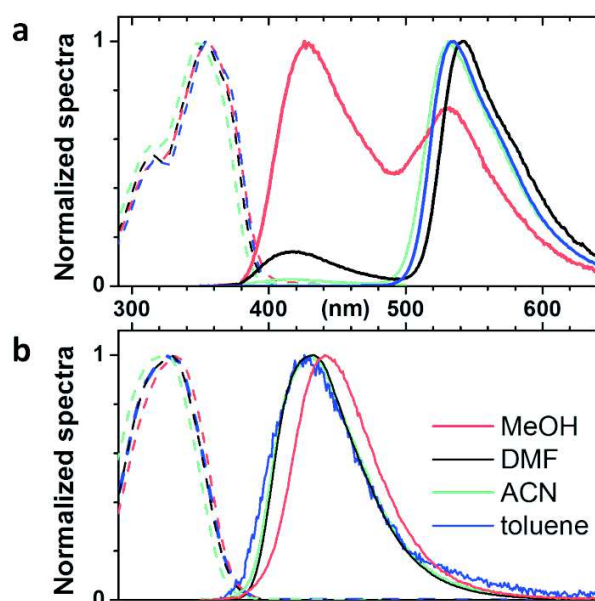


**Figure 2.** Steady-state absorption (dashed lines) and emission (full lines) spectra of **a.** compound **1** and **b.** compound **2** for which no ESIPT reaction is possible, in MeOH (red), DMF (black), ACN (green) and toluene (blue).

A streak camera was used to record the spectrally-resolved fluorescence decay kinetics. Figure 3a displays the data obtained for compound **1** in MeOH, on a 1 ns time window with a 7 ps time resolution. Spectral integration for  $\lambda < 475$  nm and  $\lambda > 510$  nm yields the decay kinetics of the  $N^*$  and  $T^*$  bands respectively, as shown in Figure 3b. Their global fit (see Material and Methods) reveals two dominating time scales of 120 ps which accounts for the decay of  $N^*$  and simultaneous rise of  $T^*$ , i.e. for the ESIPT reaction, and 220 ps corresponding to the decay of  $T^*$ . It also reveals that the asymptotic part of the  $N^*$  decay kinetics is well fitted by the 220 ps time scale characterizing the  $T^*$  decay, but with an amplitude at least 40 times weaker than that of the dominating 120 ps  $N^*$  decay component. Finally, in order to achieve a nearly perfect fit ( $\chi^2 = 1.02$ ; see the weighted residuals in Figure 3b) a shorter time constant of  $\sim 40$  ps is needed to correctly account for the early decay of  $N^*$  and rise of  $T^*$ , pointing to biexponential kinetics of the ESIPT reaction. The relative amplitude of the 40 ps and 120 ps time constants in the decay kinetics of  $N^*$  are 1 to 4 in this fit. A more detailed and accurate investigation of the early time kinetics is the goal of the transient absorption spectroscopy experiments performed with a 60 to 80 fs time resolution and described in detail below.

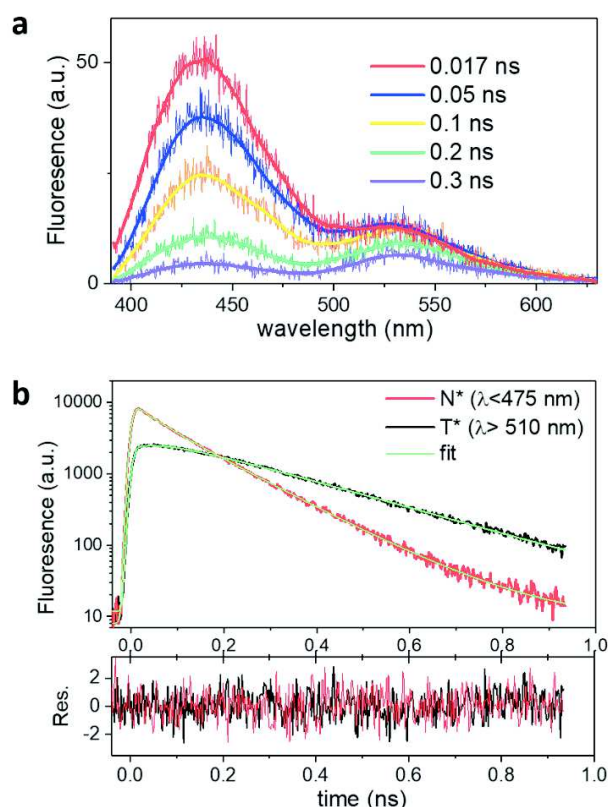


**Figure 3: TRF spectroscopy of compound 1 in MeOH.** **a.** Fluorescence spectra at a selection of time delays after pulsed laser excitation at 343 nm. Solid thick lines result from numerically smoothing the raw data (thin lines) **b.** Decay kinetics of the N\* (in red) and T\* (in black) bands integrated over the  $\lambda < 475$  nm and  $\lambda > 510$  nm spectral windows, respectively. Both curves are fitted globally (green lines) and the weighted residuals are displayed below.

TRF data were acquired similarly for compound **1** in the other three solvents. The decay kinetics of the spectrally integrated N\* and T\* bands and their simultaneous fits are displayed in Figure 4 in the case of DMF and ACN. The simultaneous decay of N\* and rise of T\*, corresponding to the ESIPT reaction speed is well fitted by a 34 ps time constant in the case of DMF, but not resolved (i.e. faster than 7 ps) in the case of ACN. In both solvents the T\* decay appears to be monoexponential with time constants of 0.51 ns in the case of DMF (best determined on the 5 ns time window, see Figure 4a inset), and of 0.43 ns in ACN. In both solvents, the T\* decay time constant is also found to characterize the asymptote of the N\* decay, but with an amplitude much weaker (~500 times weaker in the case of DMF) than the dominating N\* decay time. Finally, in toluene (data not shown here), only the T\* band is observed which is instantaneously formed and decays monoexponentially with a 3.0 ns time constant.

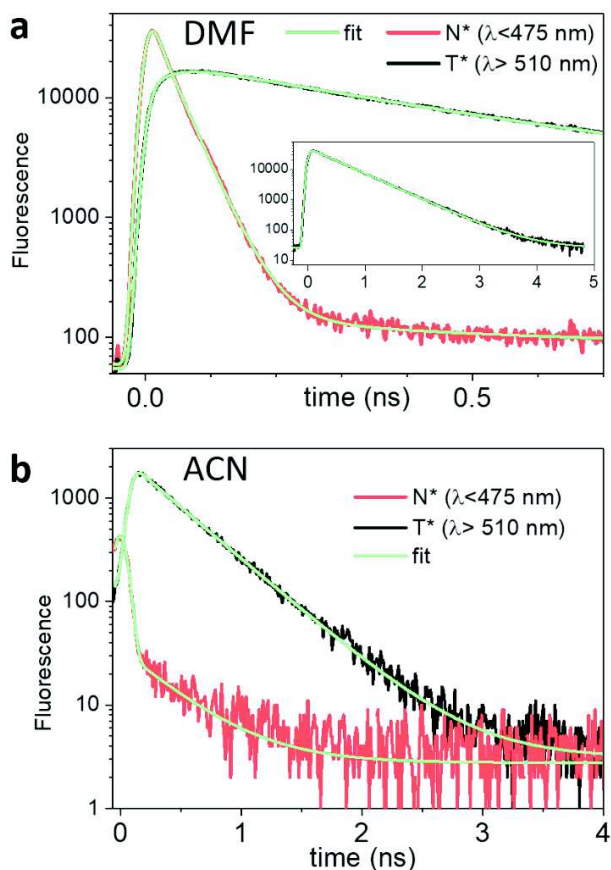


**Figure 4:** TRF spectroscopy of compound **1** in **a. DMF** and **b. ACN**. Decay kinetics of the N\* (in red) and T\* (in black) bands are integrated over the  $\lambda < 475$  nm and  $\lambda > 510$  nm spectral windows, respectively. For each panel, both curves are fitted simultaneously (green lines).

The fastest components of the ESIPT reaction - which are not time-resolved with the streak camera - can be accurately investigated by femtosecond transient absorption (TA) spectroscopy. Figure 5 displays the TA data obtained for **1** in MeOH, upon excitation at 343 nm. We now provide a detailed description and assignment of the observed transient spectra, showing that the ESIPT reaction indeed starts on the sub 10-ps time scale already. In panel 5b, the negative signal (blue) in the range  $\lambda < 380$  nm corresponds to the Ground State Bleach (GSB), i.e. the pump-induced depletion of ground state population. At early times a positive band (red) is observed at 500-550 nm corresponding to an Excited State Absorption (ESA) of the pump-induced population in N\*. In the spectral region between 420-475 nm, corresponding to the N\* emission (Figure 5a), Stimulated Emission (SE) is expected as a negative signature of the N\* state, but is not observed due to the spectral overlap with the more intense ESA band, actually stretching from 380 to 550 nm (Figure 5c). Thus, the apparent rise of the blue side of this broad ESA band (around 400 nm) on the 1 ps time scale is compatible with a red-shift of the overlapping SE, expected to be associated with solvent or intramolecular relaxation on this time scale. The ESIPT

reaction is observed to occur on the few ps to 100 ps time scale, in line with the above conclusions of TRF spectroscopy. Indeed, while the GSB remains intense (i.e. no ground state recovery), we observe simultaneously the decay of the N\* signatures (especially the 500-550 nm ESA feature) and the rise of a new ESA band centered at 640 nm, and of a negative contribution around 550 nm attributed to SE from the T\* state by comparison with the steady-state emission (Figure 5a). The positive feature seen around 460 nm at 100 ps is also attributed to the blue edge of the very broad ESA of T\* which also overlaps with the SE signature. For T\* the SE is more intense than the ESA, resulting in a net negative contribution at ~550 nm.

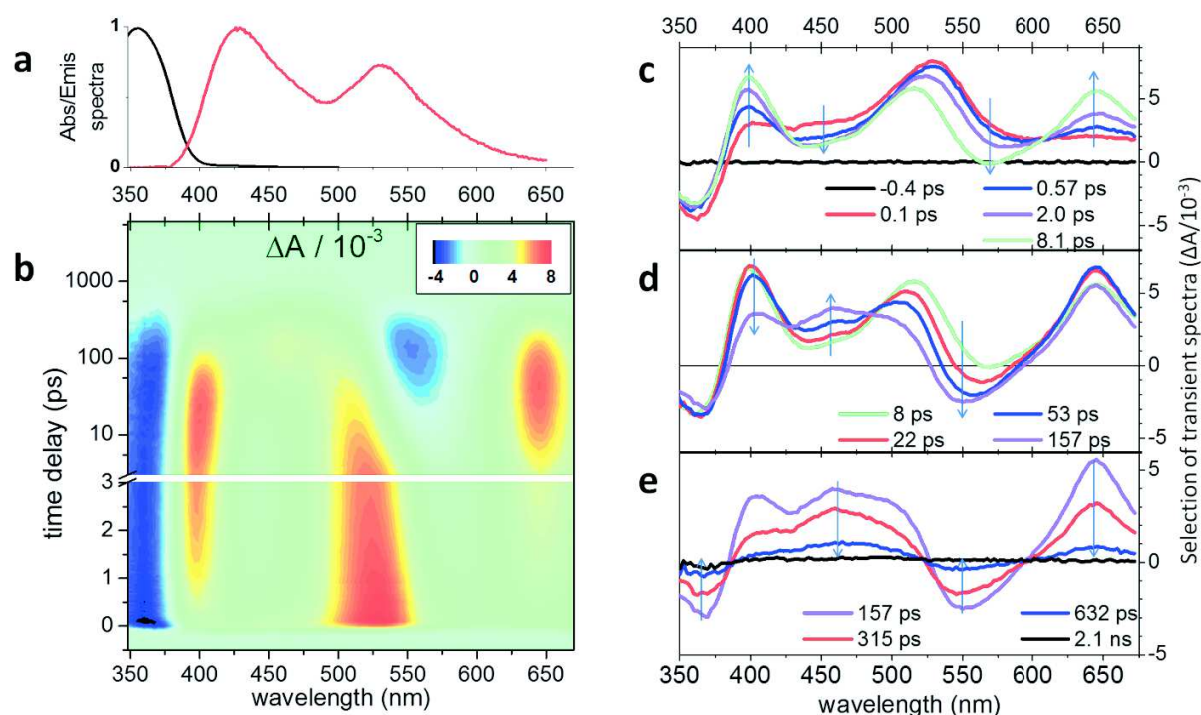


**Figure 5.** TA spectroscopy of compound 1 in MeOH, upon 343 nm excitation. **a.** Steady-state absorption (black) and fluorescence (red) emission spectra. **b.** 2D-map representation of the pump-induced absorbance change  $\Delta A$  (coded in false colors) as a function of probe wavelength (in nm) and pump-probe time delay (in ps). Negative contributions (blue-coded) are Ground-State Bleach (GSB) and Stimulated Emission (SE), identified by the comparison with the steady-state absorption and fluorescence spectra, respectively (panel **a**). Positive contributions (red-coded) are pump-induced absorption bands of the excited or photoproduct states **c**, **d**, **e**. Selection of transient spectra from panel **b** illustrating the spectral evolution (blue arrows) over short, intermediate and longtime scales, respectively.

Accurate insight in the shape of the successive spectral signatures is obtained in Figures 5c, 5d and 5e which display the same TA data set in three typical time windows. On the 0.1 to few ps time scale (Figure 5c), the spectral relaxation of N\* is observed with the rise of its ESA at 400 nm and the deepening of its SE at 450 nm. Noticeably, on the same time scale already, the T\* signatures (ESA at 630 nm and SE at 550-575 nm) start rising. Then, on the 8 to 160 ps time

window (Figure 5d) we observe the decay of the ESA and SE signatures of N\*, and further growth of the SE and ESA signatures of T\*, while the GSB ( $\lambda < 375$  nm) remains at a constant level. These are the most obvious signatures of the ESIPT reaction. Finally on longer time scales (Figure 5e), the entire transient spectrum decays to zero while preserving its overall shape, indicating the decay of T\* to reform the original ground state N. More precisely, as already reported,<sup>39</sup> the decay of T\* to T is followed by a much faster back proton transfer from T to N in the ground state, such that an effective direct decay from T\* to N is detected in the present TA data.

Before the quantitative analysis of the ESIPT reaction time scales (see below), we now confirm the above assignments of the various TA signatures of compound **1**, by comparing with the TA data obtained in the same conditions on compound **2** in MeOH, where only N\* is observed, as displayed in Figure 6. In line with the  $\sim 35$  nm blue shift of the absorption spectrum of compound **2** with respect to **1** (see Figure 2), the GSB of the N state is observed at shorter wavelengths ( $\lambda < 360$  nm). The characteristic signature of N\* is composed of a SE band clearly observed here as a negative contribution around 460 nm (best seen after several ps), sandwiched by two ESA bands at 370-430 nm and 490-520 nm. The N\* spectral signature relaxes on the few ps time scale (see Figure 6c), with the gradual increase of both ESA bands and the deepening of the SE band which eventually overcomes the underlying ESA contribution to produce a net negative contribution around 460 nm. Here we note, that this spectral relaxation is also observed in **1** (relaxation of the 400 nm ESA band in Figure 5c), but the simultaneous rise of the T\* with its positive ESA signature around 460 nm masks the negative SE of N\* at the same wavelength (Figure 5c and 5d). Eventually, the N\* signature of **2** (Figure 6d) decays on the sub 100 ps time scale without displaying the characteristic T\* signatures evidenced in **1**, as expected since the ESIPT reaction is precluded here. Instead, a weak, broad photoproduct spectrum spanning from 370 to over 500 nm is observed which is very long-lived (no decay on the 6 ns time scale). This final signature, indicative of possible photodegradation of **2**, is not observed in **1**, where the formation of T\* (and subsequent decay to the ground state with rapid reformation of N) is the major non-radiative decay channel from N\*.

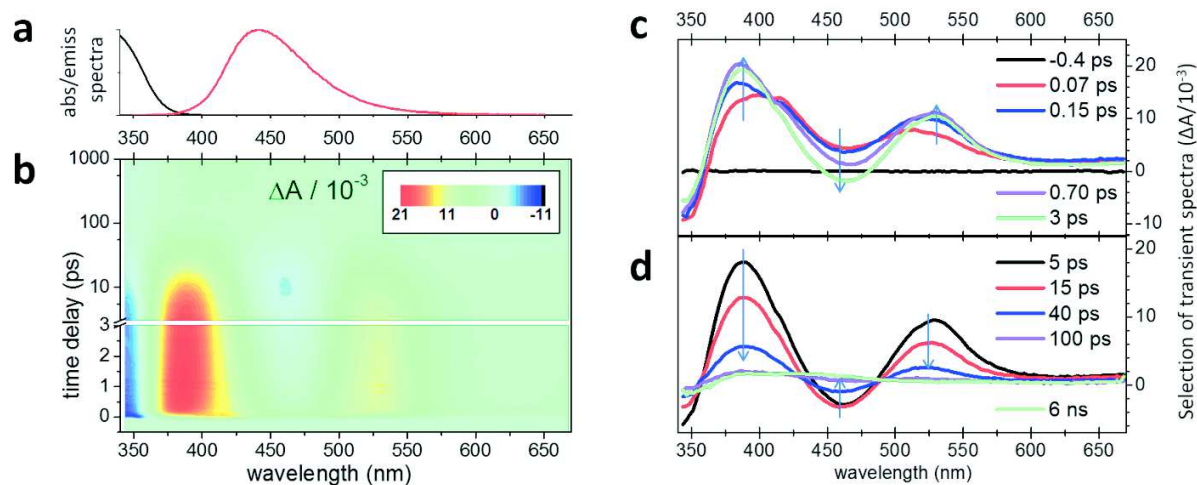


**Figure 6.** TA spectroscopy of compound **2** in MeOH, upon 343 nm excitation. **a, b.** Same as in Figure 5. **c, d.** Selection of transient spectra illustrating the spectral evolution (blue arrows) over short, and longtime scales, respectively.

The quantitative analysis of the TA kinetics of both compounds in MeOH is performed by global analysis as described in the Materials and Methods section and illustrated by the Decay-Associated Spectra (DAS) displayed in Figure 7. In the case of **1** (Figure 7a), four time constants of 0.7, 7.7, 105 and 230 ps are needed to fit globally the kinetics of all spectral signatures. The 230 ps DAS includes the spectral contributions of the GSB and of the T\* ESA and SE (see the similarity of the overall DAS shape with the 315 ps transient spectrum in Figure 5e). Hence it must be attributed to the T\* decay and simultaneous GSB recovery. We note the perfect agreement between the T\* decay time constant obtained here from TA and from TRF above (220 ps). At  $\lambda > 520$  nm, the 105 ps and 7.7 ps DAS have the same shape and opposite sign as compared to the 230 ps DAS, indicating that they represent T\* formation on these two distinct time scales. At  $\lambda < 520$  nm, the shape of the 105 ps DAS in **1** is similar to that of the 26 ps DAS of **2** (Figure 7b), with the decay of the (negative) SE around 460 nm and of the (positive) ESA around 380 nm. These DAS must therefore be attributed to the same process, namely to the decay of N\* in both compounds. Therefore in the case of **1**, the 105 ps DAS represents the simultaneous decay of N\* and rise of T\*, i.e. the ESIPT reaction, on this time scale, also in very good agreement with the time scale determined with the streak camera for the dominating N\* decay time constant.

Both compounds display TA kinetic components in the sub-ps and few ps time scales. For **2** in methanol the 0.4 ps and 5 ps DAS (Figure 7b) correspond to spectral relaxation consisting of the rise of both ESA bands and deepening of SE on the 0.4 ps time scale, and further deepening of the SE on the 5 ps time scale. Such time scales and spectral evolutions are typically due to vibrational and/or solvent relaxation away from the Franck Condon (FC) state.<sup>46, 47</sup> For **1**, a similar spectral relaxation of N\* occurs, also characterized by two time scales of 0.7 ps and 7.7 ps. Indeed, at  $\lambda < 520$  nm, the 0.7 ps DAS of **1** resembles the 0.4 ps DAS of **2** (i.e. increase of the

380 nm ESA band and deepening of SE). The 7.7 ps remains flat at 450 nm because, as already mentioned above, the further deepening of the N\* SE, clearly observed in **2** (5 ps DAS Figure 7b), is compensated by the simultaneous rise of the T\* ESA at this wavelength in **1**. At  $\lambda > 520$  nm, the difference between the DAS of **1** and **2** are attributed to the signatures of T\*, which is prominent in the 7.7 ps DAS of **1** and already weakly apparent in the 0.7 ps DAS as well. We conclude that in **1**, the ESIPT reaction occurs with non-exponential kinetics reproduced here by three time constants of 0.7, 7.7 and 105 ps with a major contribution of the longest two. The shortest two time constants also correctly reproduce the spectral relaxation of N\*, which, as demonstrated by the investigation of **2**, shows multi- or non-exponential kinetics on time scales similar to the fastest ESIPT kinetic components in **1**. The fact that the 0.7 and 7.7 ps time constants must be attributed simultaneously to solvent relaxation and ESIPT reaction in **1** does however not imply that both processes are operating in concert in this compound, but most likely on time scales too similar to be disentangled in the present global data analysis scheme.

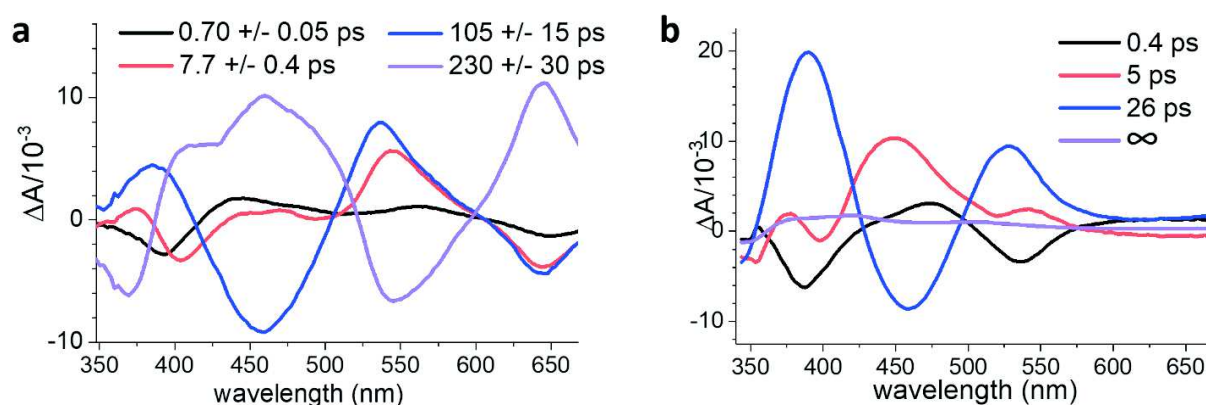


**Figure 7. Global analysis of the TA data of a. compounds a. 1 and b. 2 in MeOH.** The transient absorption Decay-Associated Spectra (DAS) obtained after the global analysis (see text) represent the time constants over which decay (positive DAS) and rise (negative DAS) all spectral features of the TA datasets displayed in Figures 5 and 6, respectively. The error bars on the time constants in panel **a** are estimated from the dispersion of the results of the same analysis performed on TA datasets recorded in two distinct experimental runs. This ~ 7 to 15% uncertainty typically applies to all time constants extracted in this paper.

In the same line, TA spectroscopy data were acquired and analyzed for **1** in the other three solvents as displayed in Figure 8. In DMF, the data are qualitatively very similar to those already discussed in detail above in MeOH. Also two fast time constants of 0.5 and 4 ps are needed to fit the N\* spectral relaxation, with the T\* formation already starting on the 4 ps time constant. A second time constant of 26 ps appears as the dominant time scale for the N\* decay and T\* formation (blue DAS in Figure 8a bottom), while a 530 ps time constant (pink DAS) accounts for the ground state N recovery and the T\* decay, also in perfect agreement with the 510 ps time constant inferred from TRF spectroscopy. As compared to the case of MeOH, the faster N\* decay and longer T\* lifetime explains the weaker intensity of the N\* emission relative to T\* in the

steady-state fluorescence spectrum of **1** in DMF (Figure 2). In the case of ACN, only one time constant of 0.34 ps accounts for the N\* spectral relaxation, since the ESIPT reaction is even faster and occurs on a 5.5 ps time constant (blue DAS in Figure 8b bottom), while T\* decays to reform N on the 400 ps time scale, also in very good agreement with the results of TRF spectroscopy. This even faster T\* formation explains the even lower-intensity N\* emission band (Figure 2). Finally, in the case of toluene, only the T\* signature is observed, indicating that T\* is formed within the experimental time resolution, i.e. on a time scale faster than 60 fs. This is also faster than vibrational relaxation and implies the formation of a vibrationally “hot” T\* state. Hence the spectral relaxation observed in N\* in the other solvents is here observed in T\* with a similar bi-exponential relaxation of the T\* spectral shape mostly resulting in the gradual deepening of the T\* SE signature (see the 0.77 ps and 6.5 ps DAS in Figure 8c bottom). We note that the assignment to intramolecular relaxation of the 6.5 ps DAS obtained here in toluene is also supported by the very similar shape of the 8 ps DAS observed by Chevalier et al.<sup>48</sup> in the T\* state formed by the <3 ps fast ESIPT of 3HF in ACN, and attributed to intramolecular relaxation as well. In toluene, the T\* state of **1** decays on the 3.0 ns time scale (as already concluded from TRF spectroscopy) also to reform N.

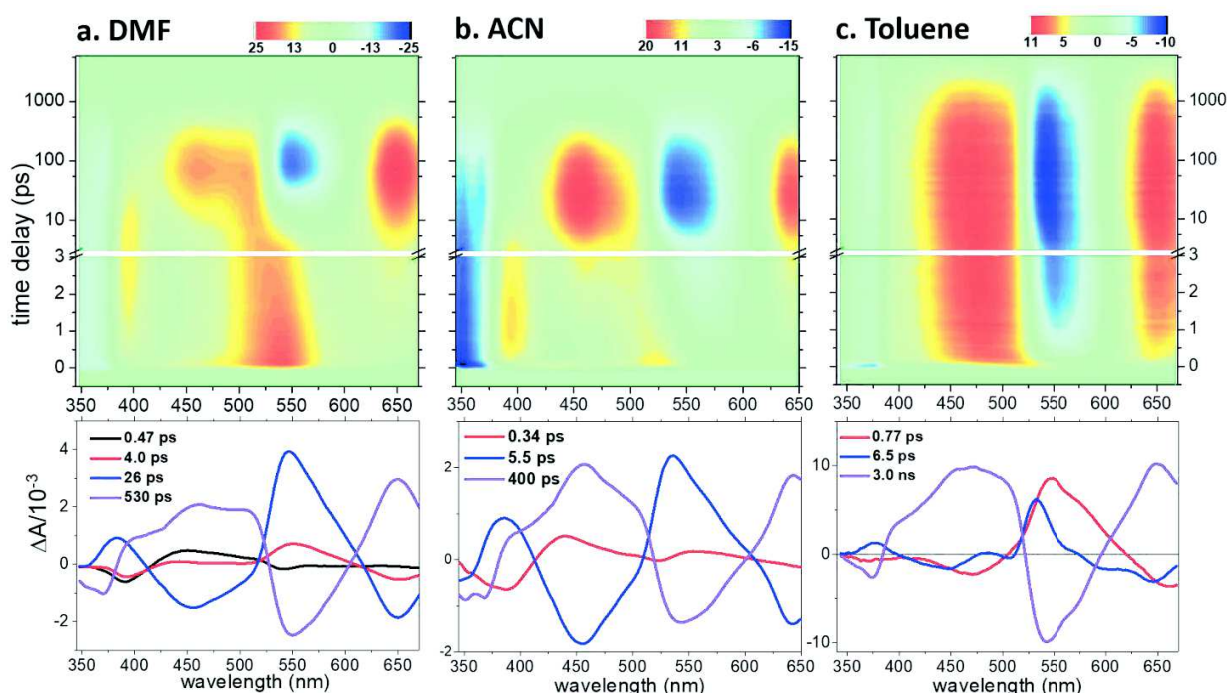


**Figure 8.** TA spectroscopy of compound **1** in a. DMF, b. ACN, c. toluene, upon 343 nm excitation. Each column corresponds to a different solvent, with the 2D map representation of the TA data in the top panel and the DAS resulting from the corresponding global analysis in the bottom panel.

Table 2 summarizes the time scales extracted from the global analysis of the TA data of **1** in the four solvents. The T\* lifetime is quoted as t<sub>4</sub> and appears nearly proportional to the measured total fluorescence quantum yield, except in the case of ACN, where the t<sub>4</sub> value is close to that observed in DMF, while the QY is nearly 3 times lower. For all solvents except toluene, time constants t<sub>2</sub> and t<sub>3</sub> correspond to ESIPT reaction kinetics, while t<sub>1</sub> is primarily attributed to solvent or intramolecular relaxation in N\*. In toluene instead, the ESIPT reaction kinetics is faster than the experimental time resolution, and the t<sub>1</sub> and t<sub>2</sub> values represent the time scales for intramolecular relaxation in T\*.

**Table 2.** Time constants extracted from global analysis of the TA of compound **1** in the four solvents. For all solvents except toluene, t<sub>1</sub> is primarily due to solvent or intramolecular relaxation in N\*, t<sub>2</sub> and t<sub>3</sub> correspond to ESIPT reaction kinetics. t<sub>4</sub> is the lifetime of T\*. The relative uncertainty on all time constants is in the range 7 to 15%. The last column gives the fluorescence quantum yield (QY) of compound **1** in each solvent.

<b>Solvent</b>	<b>t<sub>1</sub>/ps</b>	<b>t<sub>2</sub>/ps</b>	<b>t<sub>3</sub>/ps</b>	<b>t<sub>4</sub>/ps</b>	<b>QY (%)</b>
<b>MeOH</b>	<b>0.7</b>	<b>7.7</b>	<b>105</b>	<b>230</b>	<b>3.9</b>
<b>DMF</b>	<b>0.47</b>	<b>4</b>	<b>26</b>	<b>530</b>	<b>5.6 +/- 0.1</b>
<b>ACN</b>	<b>0.34</b>		<b>5.5</b>	<b>400</b>	<b>2.0 +/- 0.4</b>
<b>Toluene</b>	<b>0.8</b>	<b>7</b>		<b>2970</b>	<b>35 +/- 1</b>

## Discussion

In line with all 3HF derivatives, we observed that the ESIPT reaction is extremely fast (<60 fs) in the apolar, aprotic toluene solvent, where the T\* signature appears within the instrument response time. This is usually explained by the fact that in such a solvent, the intramolecular H bond is presumably not disrupted and the ESIPT proceeds with its expected intrinsic ultrafast speed through a very low potential energy barrier, if any<sup>9, 39</sup>. In the other three solvents, the T\* formation kinetics is observed to be multi-exponential. Non-exponential (e.g. bi-exponential) T\* formation kinetics have already been reported in a number of previous, ultrafast spectroscopy investigations of hydroxychromone derivatives.<sup>4, 5, 24, 26, 48, 49</sup> Two possible scenarios have been discussed to explain this finding. The first one is invoked in the case of 3HF, where protic solvent molecules or protic impurities in aprotic solvents may form complexes with the solute, resulting in the disruption or weakening of the intramolecular H bond to various degrees.<sup>8, 11, 50</sup> In such a case, the non-exponential kinetics would result from the distribution of distinct ESIPT rates characterizing the distribution of ground state N species involved in various types of complexes. Alternatively, a non-exponential T\* formation is also observed in polar solvents for the case of 3HF derivatives exhibiting a strong charge transfer (CT) character in the N\* state. In such a case it has been argued that the N\* state dipole moment is significantly different from that of the

ground state N, whereas the dipole moment of T\* would be similar to that of N. Therefore, while the ESIPT reaction would be favored by the out-of-equilibrium solvent shell in the Franck Condon N\* state, the rapid solvent relaxation stabilizing the N\* state would slow down the ESIPT channel by introducing a solvent-induced energy barrier between the relaxed (solvated) N\* state and the less polar T\* state.<sup>24, 25</sup> In such a scenario, the non-exponential T\* formation results from an effective time-dependent ESIPT rate, which slows down while solvation proceeds in N\*. Ultimately, in the case of the dialkylamino compounds, an equilibrium is reached due to balance between forward and backward ESIPT reaction between solvated N\* and T\* states. The two scenarios introduced here may be recast in a simple rate equation model displayed in Figure 9, where the forward and backward ESIPT reactions are introduced with rates  $k_+$  and  $k_-$ , while  $k_N$  and  $k_T$  represent the radiative decay rates of N\* and T\* states respectively.<sup>24, 27</sup> The case where an equilibrium is reached between solvated excited states, characterized by the equilibrium constant  $K = k_+/k_-$ , is referred to as the thermodynamic model. The case corresponding to  $k_- \ll k_+$  is referred to as the kinetic model.<sup>3</sup> It describes an irreversible ESIPT which may occur for a displaced excited state equilibrium between solvated states, or between non-equilibrated excited states in the case of ultrafast ESIPT (i.e. the case of toluene here).

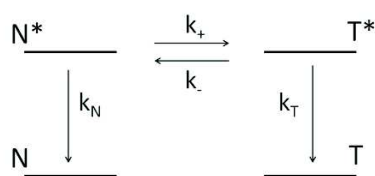


**Figure 9: Definition of the rate equation model commonly introduced to describe the ESIPT reaction in hydroxychromone derivatives.**

In the present case of **1**, the steady-state emission spectra, in particular Figure 2b, show that there is hardly any solvatochromic effect on the N\* band (which is identical in ACN and toluene) in contrast with previous reports on the dialkylamino compounds.<sup>23, 24</sup> Also the TRF data show that in polar solvents (DMF and ACN, see Figure 4), the T\* and N\* decay times do not become identical, as would be expected when equilibrium occurs in the excited state between N\* and T\*, as previously reported in the dialkylamino derivative.<sup>27</sup> More precisely, under the assumption that the ESIPT rates ( $k_+$ ,  $k_-$ ) are much faster than the N\* and T\* lifetimes, the relative amplitude of the T\* decay time constant in the N\* decay kinetics is a measure of the putative equilibrium constant  $K = k_+/k_-$ . As illustrated by the fits in Figure 4, this ratio is found to be larger than 500 (limited by the noise floor in the asymptote of the N\* decay kinetics) in DMF and larger than 10 in ACN (limited by the non-resolved N\* decay component). We conclude that for **1**, the ESIPT occurs according to the kinetic rather than thermodynamic model. For this reason and for the lack of solvatochromism, we conclude that the non-exponential T\* formation kinetics should be attributed to the existence of structural heterogeneity (e.g. forms of **1** with formed and disrupted intramolecular H bond), similar to the case of 3HF, rather than to a solvation-controlled ESIPT process. A rate equation model describing such structural heterogeneity as a result of a

thermodynamic equilibrium between distinct N ground states engaged in various types of complexes with the solvent molecules was previously introduced in the case of 3HF in protic solvents.<sup>11</sup>

Despite this qualitative similarity between compound **1** and 3HF regarding the effect of solvent polarity on the ESIPT reaction kinetics, the slowing down of the ESIPT reaction in protic solvents is much more pronounced in **1** than in 3HF. Indeed the formation of T\* was reported to be dominated by a sub-100 fs and a minor ~10 ps time scales for 3HF in ethanol<sup>5</sup> or methanol<sup>4</sup>. For compound **1** instead, the T\* formation in MeOH appears multiexponential with a 7.7 ps and a 105 ps time scales of similar relative amplitudes, as well as a minor contribution of a 0.7 ps time scale (see the signature of the T\* ESA band around 640 nm in Figure 5a). In the polar, aprotic ACN, the 5.5 ps dominating ESIPT rate is close to the 2 to 3 ps time constant reported for the resolved ESIPT component of 3HF in the same solvent.<sup>13, 48</sup> Nonetheless, in DMF, which has a polarity similar to ACN, the ESIPT is decelerated by a factor of 5 for **1** but only by a factor of 2 for 3HF.<sup>13</sup> Altogether, the moderate electron-donor strength of the methoxy group - which is expected to weaken the intramolecular H bond - results in a much larger range of ESIPT rates observed in **1** (from sub 60 fs to over 100 ps) as compared of 3HF. This is attributed to the enhanced effect of H-bond donor (MeOH) and acceptor (DMF) solvent molecules at disrupting the intramolecular H bond.

We finally discuss the implications of such a broad distribution of ESIPT reaction rates on the determination of the physicochemical properties of the microenvironment of compound **1**, by the ratiometric detection method. Following the model introduced in Figure 9, the ratio  $R = I_N/I_T$  of the total emission intensities in the N\* and T\* bands writes (See Supplementary Note 1):

$$R = \frac{I_N}{I_T} = \frac{k_N}{k_T} \frac{1}{\tau_T k_+}$$

where  $\tau_T$  is the T\* excited state lifetime ( $\tau_T^{-1} = k_T + k_- + k_T^{nr}$ , where  $k_T^{nr}$ , not represented in Figure 9, accounts for all other possible non radiative decay channels from T\*). This simple formula illustrates the strength of the ratiometric detection scheme since, apart from the radiative decay rates  $k_N$  and  $k_T$  which are intrinsic properties of the fluorophore, R depends only on the forward ESIPT reaction rate  $k_+$  and on  $\tau_T$ , which are controlled by the interaction of the fluorophore with its microenvironment via H-bonding, polarity or viscosity effects.

If we now consider two distinct subpopulations  $N_a$  and  $N_b$  which coexist in the ground state with relative proportions  $\alpha$  and  $1 - \alpha$ , and are characterized by distinct ESIPT forward rates given by  $k_+^a$  and  $k_+^b$ , we may also write the ratio R between the total emission intensities in both N\* and T\* bands. Assuming that the spectral shape of either band is the same for both subpopulations (this is likely to be the case in **1** since there is hardly any solvent effect on either band central wavelength), then we compute:

$$R = \frac{I_N^{tot}}{I_T^{tot}} = \frac{I_{Na} + I_{Nb}}{I_{Ta} + I_{Tb}}$$

We immediately see that the ratiometric detection provides an average result for the ensemble of subpopulations. This can be further illustrated in a simplified case study where we assume that only the ESIPT reaction rates differ between the subpopulations and that it occurs irreversibly ( $k_- \sim 0$ ) and rapidly, i.e.  $k_+ \tau_N \sim 1$ , in both cases. In this simplistic example the ratio R defined for the ensemble of two subpopulations simplifies to the average of the R values corresponding to each subpopulation (see Supplementary Note 2):

$$R \approx \alpha R_a + (1 - \alpha) R_b, \text{ with } R_{a,b} = \frac{k_N}{k_T} \frac{1}{\tau_T k_+^{a,b}}$$

Hence, for applications using **1** as a fluorescent probe in biomolecules, whenever a distribution of ESIPT rates is expected, corresponding to a distribution of distinct microenvironments, the ratiometric detection will capture an average information masking the actual local heterogeneity. This conclusion generally applies to steady-state fluorescence detection as opposed to time-resolved detection which instead allows resolving the distribution of lifetimes corresponding to distinct microenvironments. In the present case of significant contributions of ESIPT rates in the sub 10 ps range as in MeOH or ACN, a sub-picosecond time resolution (as in TA spectroscopy) is necessary to reveal the existence of subpopulations undergoing such fast ESIPT reactions.

## Conclusion

The detailed investigation of the ESIPT reaction kinetics of **1** in various solvents by ultrafast spectroscopy reveals the remarkably large range of ESIPT rates that are observed as a function of H-bonding capabilities of the microenvironment. This is attributed to the well-suited, intermediate electron donor strength of the 4' -MeO group, which seems to weaken the intramolecular H bond of **1** (as compared to 3HF), and to reduce the charge transfer character of the N\* state as compared to 4' -dialkylamino-3HF. This enhanced range of observed ESIPT time scales (covering over 3 orders of magnitude from sub 100 fs to 100 ps) improves the sensitivity of the compound used as a reporter for H-bonding interactions with its microenvironment, and therefore as a fluorescent probe for protein structure or interactions.<sup>30, 32</sup> Furthermore, we propose that it also offers the unprecedented opportunity to monitor distributions of ESIPT rates corresponding to distributions of chromophores subpopulations undergoing various degrees of H-bonding interactions with their microenvironment. 4'-methoxy-3-hydroxyflavone therefore appears to be a promising fluorescent probe of local structural heterogeneity in biomolecules, i.e. coexistence of multiple biomolecular conformers, provided the distribution of corresponding ESIPT rates is experimentally time-resolved. The present set of

observations will be of great interest for the assessment of future simulation work on quantitative structural interpretation of the observed ESIPT rates in such applications.

## Acknowledgments

This work is supported by the Région Alsace via the contrat doctoral No. 493-14-C22, the Institut Carnot MICA via the ‘TR-Fluofluidics’ project, and the French Agence Nationale de la Recherche via the ANR-15-CE11-0006 ‘PICO2’ project.

## References

1. A. P. Demchenko, *Introduction to fluorescence sensing*, Springer, 2009.
2. A. S. Klymchenko, *Accounts of Chemical Research*, 2017, 50, 366-375.
3. A. P. Demchenko, K.-C. Tang and P.-T. Chou, *Chem. Soc. Rev.*, 2013, 42, 1379-1408.
4. B. J. Schwartz, L. A. Peteanu and C. B. Harris, *J. Phys. Chem.*, 1992, 96, 3591-3598.
5. S. Ameer-Beg, S. M. Ormson, R. G. Brown, P. Matousek, M. Towrie, E. T. J. Nibbering, P. Fogg and F. V. R. Neuwahl, *J. Phys. Chem. A*, 2001, 105, 3709-3718.
6. A. N. Bader, F. Ariese and C. Gooijer, *J. Phys. Chem. A*, 2002, 106, 2844-2849.
7. P. K. Sengupta and M. Kasha, *Chem. Phys. Lett.*, 1979, 68, 382-385.
8. D. McMorro and M. Kasha, *J. Am. Chem. Soc.*, 1983, 105, 5133-5134.
9. D. McMorro and M. Kasha, *J. Phys. Chem.*, 1984, 88, 2235-2243.
10. G. J. Woolfe and P. J. Thistlethwaite, *J. Am. Chem. Soc.*, 1981, 103, 6916-6923.
11. A. J. G. Strandjord and P. F. Barbara, *J. Phys. Chem.*, 1985, 89, 2355-2361.
12. V. V. Shynkar, A. S. Klymchenko, E. Piémont, A. P. Demchenko and Y. Mély, *J. Phys. Chem. A*, 2004, 108, 8151-8159.
13. A. Douhal, M. Sanz, L. Tormo and J. A. Organero, *ChemPhysChem*, 2005, 6, 419-423.
14. A. J. G. Strandjord, D. E. Smith and P. F. Barbara, *J. Phys. Chem.*, 1985, 89, 2362-2366.
15. A. S. Klymchenko, V. G. Pivovarenko and A. P. Demchenko, *Spectrochimica Acta Part A: Molecular and Biomolecular Spectroscopy*, 2003, 59, 787-792.
16. P. T. Chou, M. L. Martinez and J. H. Clements, *J. Phys. Chem.*, 1993, 97, 2618-2622.
17. A. Sytnik, D. Gormin and M. Kasha, *Proc. Natl. Acad. Sci. USA*, 1994, 91, 11968-11972.

18. A. S. Klymchenko, V. G. Pivovarenko, T. Ozturk and A. P. Demchenko, *New Journal of Chemistry*, 2003, 27, 1336-1343.
19. P.-T. Chou, Huang, S.-C. Pu, Y.-M. Cheng, Y.-H. Liu, Y. Wang and C.-T. Chen, *J. Phys. Chem. A*, 2004, 108, 6452-6454.
20. S. M. Ormson, R. G. Brown, F. Vollmer and W. Rettig, *Journal of Photochemistry and Photobiology A: Chemistry*, 1994, 81, 65-72.
21. N. A. Nemkovich, W. Baumann and V. G. Pivovarenko, *Journal of Photochemistry and Photobiology A: Chemistry*, 2002, 153, 19-24.
22. T. C. Swinney and D. F. Kelley, *J. Chem. Phys.*, 1993, 99, 211-221.
23. A. S. Klymchenko and A. P. Demchenko, *Phys. Chem. Chem. Phys.*, 2003, 5, 461-468.
24. P.-T. Chou, S.-C. Pu, Y.-M. Cheng, W.-S. Yu, Y.-C. Yu, F.-T. Hung and W.-P. Hu, *J. Phys. Chem. A*, 2005, 109, 3777-3787.
25. C. A. Kenfack, A. S. Klymchenko, G. Duportail, A. Burger and Y. Mély, *Phys. Chem. Chem. Phys.*, 2012, 14, 8910-8918.
26. S. Ameer-Beg, S. M. Ormson, X. Poteau, R. G. Brown, P. Foggi, L. Bussotti and F. V. R. Neuwahl, *J. Phys. Chem. A*, 2004, 108, 6938-6943.
27. V. V. Shynkar, Y. Mély, G. Duportail, E. Piémont, A. S. Klymchenko and A. P. Demchenko, *J. Phys. Chem. A*, 2003, 107, 9522-9529.
28. A. S. Klymchenko and A. P. Demchenko, *J. Am. Chem. Soc.*, 2002, 124, 12372-12379.
29. A. P. Demchenko, Y. Mély, G. Duportail and A. S. Klymchenko, *Biophysical journal*, 2009, 96, 3461-3470.
30. O. M. Zamotaiev, V. Y. Postupalenko, V. V. Shvadchak, V. G. Pivovarenko, A. S. Klymchenko and Y. Mély, *Bioconjugate Chemistry*, 2011, 22, 101-107.
31. D. Dziuba, I. A. Karpenko, N. P. F. Barthes, B. Y. Michel, A. S. Klymchenko, R. Benhida, A. P. Demchenko, Y. Mély and A. Burger, *Chem. A Eur. J.*, 2014, 20, 1998-2009.
32. M. Sholokh, O. M. Zamotaiev, R. Das, V. Y. Postupalenko, L. Richert, D. Dujardin, O. A. Zaporozhets, V. G. Pivovarenko, A. S. Klymchenko and Y. Mély, *J. Phys. Chem. B*, 2015, 119, 2585-2595.
33. V. V. Shynkar, A. S. Klymchenko, C. Kunzelmann, G. Duportail, C. D. Muller, A. P. Demchenko, J.-M. Freyssinet and Y. Mely, *J. Am. Chem. Soc.*, 2007, 129, 2187-2193.
34. D. A. Yushchenko, J. A. Fauerbach, S. Thirunavukkuarasu, E. A. Jares-Erijman and T. M. Jovin, *J. Am. Chem. Soc.*, 2010, 132, 7860-7861.
35. V. V. Shvadchak, L. J. Falomir-Lockhart, D. A. Yushchenko and T. M. Jovin, *Journal of Biological Chemistry*, 2011, 286, 13023-13032.

36. V. Y. Postupalenko, O. M. Zamotaiev, V. V. Shvadchak, A. V. Strizhak, V. G. Pivovarenko, A. S. Klymchenko and Y. Mely, *Bioconjugate Chemistry*, 2013, 24, 1998-2007.
37. R. Das, A. S. Klymchenko, G. Duportail and Y. Mely, *Photochemical & Photobiological Sciences*, 2009, 8, 1583-1589.
38. K. Enander, L. Choulier, A. L. Olsson, D. A. Yushchenko, D. Kanmert, A. S. Klymchenko, A. P. Demchenko, Y. Mély and D. Altschuh, *Bioconjugate Chemistry*, 2008, 19, 1864-1870.
39. A. N. Bader, V. G. Pivovarenko, A. P. Demchenko, F. Ariese and C. Gooijer, *J. Phys. Chem. B*, 2004, 108, 10589-10595.
40. W. H. Melhuish, *J. Phys. Chem*, 1961, 65, 229-235.
41. J. Briand, O. Braem, J. Rehault, J. Léonard, A. Cannizzo, M. Chergui, V. Zanirato, M. Olivucci, J. Helbing and S. Haacke, *Physical Chemistry Chemical Physics*, 2010, 12, 3178-3187.
42. M. Paolino, M. Gueye, E. Pieri, M. Manathunga, S. Fusi, A. Cappelli, L. Latterini, D. Pannacci, M. Filatov, J. Léonard and M. Olivucci, *Journal of the American Chemical Society*, 2016, 138, 9807-9825.
43. C. Reichardt, *Chemical Reviews*, 1994, 94, 2319-2358.
44. M. H. Abraham, H. S. Chadha, G. S. Whiting and R. C. Mitchell, *Journal of Pharmaceutical Sciences*, 1994, 83, 1085-1100.
45. M. H. Abraham, *Journal of Physical Organic Chemistry*, 1993, 6, 660-684.
46. M. L. Horng, J. A. Gardecki, A. Papazyan and M. Maroncelli, *J. Phys. Chem*, 1995, 99, 17311-17337.
47. M. Glasbeek and H. Zhang, *Chemical Reviews*, 2004, 104, 1929-1954.
48. K. Chevalier, M. M. N. Wolf, A. Funk, M. Andres, M. Gerhards and R. Diller, *Phys. Chem. Chem. Phys.*, 2012, 14, 15007-15020.
49. K. Chevalier, A. Grün, A. Stamm, Y. Schmitt, M. Gerhards and R. Diller, *J. Phys. Chem. A*, 2013, 117, 11233-11245.
50. M. C. Etter, Z. Urbańczyk-Lipkowska, S. Baer and P. F. Barbara, *Journal of Molecular Structure*, 1986, 144, 155-167.



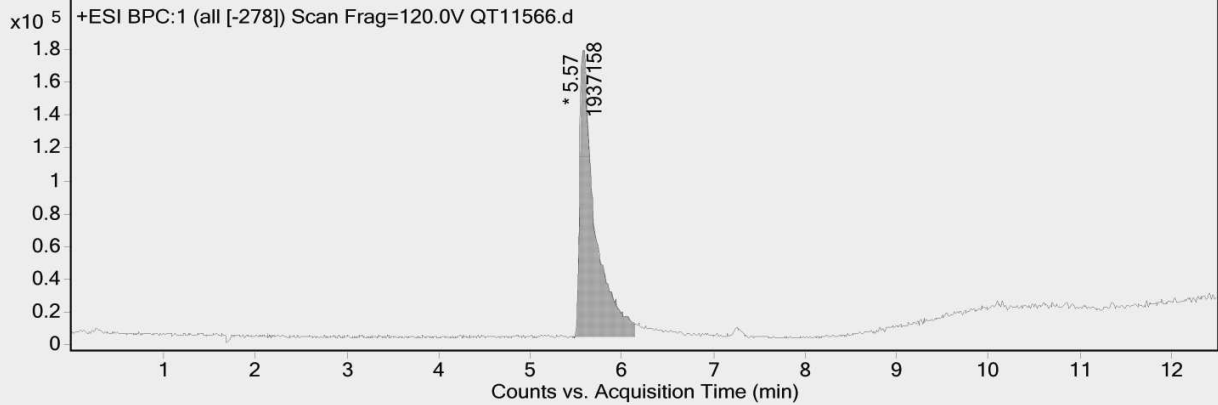
## Qualitative Analysis Report

<b>Data Filename</b>	QT11566.d	<b>Sample Name</b>	FlOMe
<b>Inj. Vol.</b>	0.1	<b>Position</b>	P1-D1
<b>Instrument Name</b>	SCA Illkirch QToF	<b>User Name</b>	PW
<b>Acq Method</b>	C18-2,1x5x1,8,m	<b>Acquired Time</b>	12/18/2015 10:04:46 AM
<b>IRM Calibration Status</b>	Success	<b>DA Method</b>	C18-2,1x5x1,8,m
<b>Comment</b>			

Sample Group      Info.

### User Chromatograms

Fragmentor Voltage 120    Collision Energy 0    Ionization Mode ESI

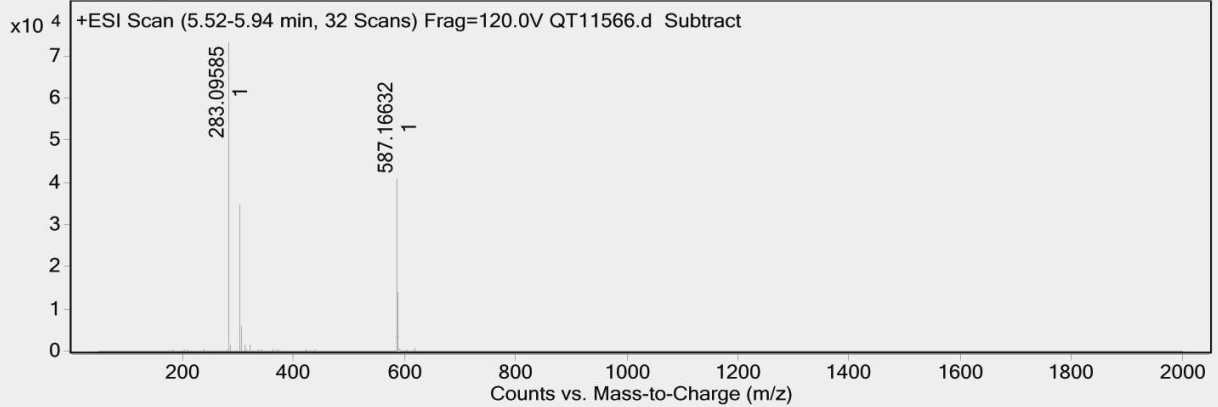


#### Integration Peak List

Start	RT	End	Height	Area	Area %	AreaSum%
5.46	5.57	6.14	174884	1937158	100	100

## Qualitative Analysis Report

Spectrum Source      Fragmentor Voltage 120      Collision Energy 0      Ionization Mode ESI  
 Peak (1) in "+ BPC:1 (all [-278]) Scan"



#### Peak List

m/z	z	Abund	Formula	Ion
283.09585	1	76010.9	C17 H15 O4	(M+H)+
284.0991	1	12248.2	C17 H15 O4	(M+H)+
305.0776	1	34644.8		
306.0808	1	5931.1		
587.16632	1	41628.9	C34 H28 Na O8	(M+Na)+
588.16941	1	14080	C34 H28 Na O8	(M+Na)+

#### Formula Calculator Results

Formula	Best	Mass	Tgt Mass	Diff (ppm)	Mz	Ion Species	Score
C17 H14 O4	TRUE	282.08857	282.08921	2.25	283.09585	C17 H15 O4	98.41
C34 H28 O8	TRUE	564.17709	564.17842	2.36	587.16632	C34 H28 Na O8	97.13

Figure S2. LCMS data of 4'-methoxy-3-methoxyflavone.



**Supplementary Note 1: Relation between the ratio of the total N\* and T\* fluorescence intensities and the parameters of the rate equation model.**

Within the model introduced in Figure 9, the time evolution of the excited state populations N\*(t) and T\*(t) writes:

$$\begin{aligned}\frac{dN^*}{dt}(t) &= -\frac{N^*(t)}{\tau_N} + k_- T^*(t) \\ \frac{dT^*}{dt}(t) &= k_+ N^*(t) - \frac{T^*(t)}{\tau_T}\end{aligned}$$

where  $\tau_N$  and  $\tau_T$  are the N\* and T\* lifetimes, i.e. the inverse of the sum of all radiative and non-radiative decay channels:  $\tau_N^{-1} = k_N + k_+ + k_N^{nr}$  and  $\tau_T^{-1} = k_T + k_- + k_T^{nr}$ .

The ratiometric approach measures the ratio  $R=I_N/I_T$  between the measured fluorescence intensities of the N\* and T\* bands. By definition, the intensity of the N\* band (and similarly for the T\* band) writes:

$$I_N = k_N \int_0^\infty N^*(t) dt$$

with  $k_N$  the radiative decay rate. Hence, instead of resolving the set of differential equations (as done e.g. in Shynhar et al. , J. Phys. Chem. A, 2003, 107, 9522-9529), we may integrate both equations, which yields:

$$\begin{aligned}N_0 &= \frac{I_N}{\tau_N k_N} - k_- \frac{I_T}{k_T} \\ 0 &= k_+ \frac{I_N}{k_N} - \frac{I_T}{\tau_T k_T}\end{aligned}$$

with  $N_0$ , the population initially promoted to N\* upon light absorption from N. The second line directly gives the ratio R between the total emission intensities in both bands:

$$R = \frac{I_N}{I_T} = \frac{k_N}{k_T} \frac{1}{\tau_T k_+}$$

Using in addition the first line allows us to conclude:

$$I_N = \frac{N_0 k_N \tau_N}{1 - k_+ k_- \tau_N \tau_T} \quad (\text{Eq. 1})$$

$$I_T = \frac{N_0 k_+ k_T \tau_N \tau_T}{1 - k_+ k_- \tau_N \tau_T} \quad (\text{Eq. 2})$$

**Supplementary Note 2: Case study about the ratiometric detection of two sub-populations *a* and *b* characterized by distinct ESIPT rates**

As described in the main text we may introduce:

$$R = \frac{I_{Na} + I_{Nb}}{I_{Ta} + I_{Tb}}$$

In the simplistic case of two subpopulation differing only by their ESIPT rates  $k_+$  (i. e.  $k_+^a \neq k_+^b$ ), with both ESIPT reactions occurring irreversibly ( $k_- \sim 0$ ) and rapidly ( $k_+ \tau_N \sim 1$  for each subpopulation), then Eq. 1 and 2 above write:

$$I_{Na} \sim \alpha N_0 k_N \tau_{Na} \sim \alpha N_0 k_N / k_+^a, \quad I_{Nb} \sim (1 - \alpha) N_0 k_N \tau_{Nb} \sim (1 - \alpha) N_0 k_N / k_+^b$$

$$I_{Ta} \sim \alpha N_0 k_T \tau_T, \quad I_{Tb} \sim (1 - \alpha) N_0 k_T \tau_T$$

with  $\alpha$  and  $(1 - \alpha)$  the relative proportions of species *a* and *b*, respectively.

And finally:

$$R \sim \alpha \frac{k_N}{k_T} \frac{1}{\tau_T k_+^a} + (1 - \alpha) \frac{k_N}{k_T} \frac{1}{\tau_T k_+^b}$$



# **IV. Cyan Fluorescent Protein and its H148G variant-Correlation of protein structures with their fluorescence properties**

## **IV.1. Introduction**

Green fluorescent protein (GFP) and its numerous homologs are widely used in modern applications as universal genetically encoded fluorescent labels. Many studies have targeted the development of fluorescent proteins (FPs) with novel characteristics and enhanced properties<sup>276</sup>. However the successful mutants were usually the result of random mutagenesis, with a trial-and-error process that can be time consuming and costly. Thus a better understanding of the reasoning behind the observed fluorescent properties can be certainly useful to aid directed mutagenesis. More precisely, the correlation of protein structures with their fluorescence properties, with particular focus on conformational heterogeneity or population exchange should allow a fine optimization of FP's performances. Therefore in the present project pH-jump experiments were used as a tool to decipher the time scales of population exchange upon medium acidification of Enhanced Cyan Fluorescent Protein (ECFP), which is a very important probe for certain category of biological applications.

The present project was initiated thanks to collaboration with Dr. Helene Pasquier (Laboratoire de Chimie Physique, University Paris Sud), who also kindly provided the studied molecules. Our prime goal here was to demonstrate and exploit the strength of our innovative experimental approach, combining TRF and D $\mu$ F, while simultaneously gaining information on a system with biomolecular interest (interactions, rearrangement etc.). Thus the research interest of Dr. Helene Pasquier in understanding the relationship between structure and photophysical properties in fluorescent proteins could be coupled with our innovative approach. At the present stage, we have been able to demonstrate the success of our innovative experimental approach at resolving the kinetics of structural modifications upon sudden pH change. A manuscript is currently in preparation, including possibly additional data with different approaches that will help refine the interpretation and conclusions regarding ECFP's photophysics.

### IV.1.1 Fluorescent proteins

Some marine organisms, such as plankton, fish and jellyfish are capable of emitting light produced in their organisms via chemical reactions (also commonly observed in fireflies). This process is called bioluminescence and one of the most famous organisms in which it was first observed is a jellyfish called *Aequorea Victoria*. Up to date, it is not actually known what the reason for their luminescence is; actually it is extremely rare to be observed when left alone in nature.

The fluorescent proteins (FPs) responsible for the fluorescence emission are utilized for scientific purposes<sup>277,278</sup>. The use of FPs led to a scientific revolution in the field of life sciences, starting a novel era of direct observation and quantification of cellular processes. The extensive spectrum of FPs with a wide range of enhanced characteristics allows their use in numerous different set ups and applications.

Since the cloning of the famous Green Fluorescent Protein (GFP) almost 20 years ago, gradual progress has been made in our understanding of the principles governing the diverse biochemical and photophysical properties of members of this unique family. In 2008 the Royal Swedish Academy of Science decided to award the Nobel Prize in Chemistry jointly to O. Shimomura, M. Chalfie and R.Y. Tsien for the discovery and development of GFP. But in order to give a short overview of the starting point one must get to know better GFP, which was the inaugural point.

In 1960 Osamu Shimomura started a project targeting the elucidation of the bioluminescence mechanism of the *Aequorea Victoria* jellyfish. Shimomura and Johnson discovered that two proteins were involved in *Aequorea* bioluminescence, a calcium binding protein which they named aequorin and a green fluorescent protein<sup>279</sup>. In 1962 they published a paper on extraction, purification and properties of aequorin which was much easier to isolate<sup>280</sup>. By 1971 enough GFP was collected in order for its analysis to start. Soon after the purification and crystallization of GFP was described along with its intermolecular energy transfer between GFP and aequorin in the jellyfish<sup>281–284</sup>. During the late 70's Doug Prasher started cloning GFP and was the first to get the idea that this might be used for imaging. Prasher sequenced and cloned GFP<sup>285</sup>. In 1992 Marty Chalfie received the GFP gene from Prasher and with the help of a student succeeded in creating green fluorescent *E. coli* proving that it did not need any other enzymes to become fluorescent<sup>286</sup>. In the same year Roger Tsien reports the achievement of the first wavelength

mutation of GFP<sup>287</sup>. Wild type GFP although it was the precursor of big scientific progress it had yet many disadvantages for fluorescence experiments, such as two excitation peaks, mediocre brightness etc. Fortunately Tsien engineered the Enhanced GFP<sup>288,289</sup> (EGFP) with a six-fold increased brightness and a single excitation peak, making it the basis for the majority of the commonly used FP. The follow up idea of Tsien was the use of Fluorescence resonance energy transfer (FRET) experiments between GFP and its mutants.

In FRET when a donor fluorophore is excited by light absorption, and under the condition that an acceptor fluorophore is in close proximity, the excited state energy will be transferred from the donor to the acceptor. This will result to a donor's fluorescence intensity and excited state lifetime reduction, and accordingly to an acceptor's emission intensity increase. This is also illustrated at the Figure 31 schematic below.

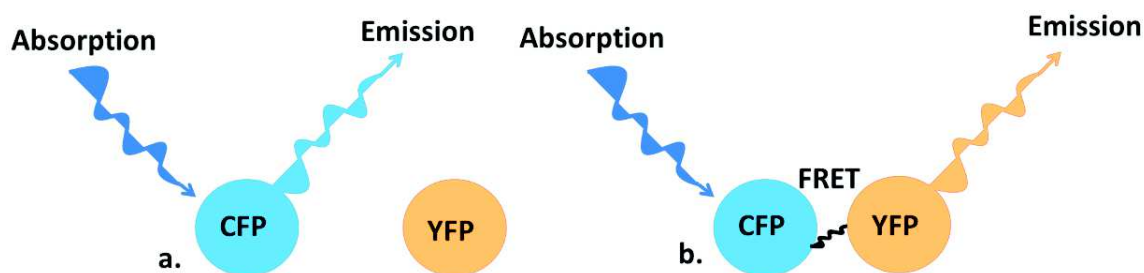


Figure 31-Schematic illustration of a. before FRET, with excitation and emission of the donor (CFP) molecule b. after FRET, with excitation of a donor accompanied with energy transfer to an acceptor (YFP) in close proximity and emission of the acceptor.

Förster demonstrated that the efficiency of this process  $E$  depends on the inverse sixth-distance between donor and acceptor<sup>37</sup>:

$$E = \frac{1}{\left(1 + \frac{R}{R_0}\right)^6}$$

where  $R_0$  is the distance at which half of the energy is transferred, depending on the spectral characteristics of the dyes and their relative orientation. For more details on FRET, the reader can seek information in chapter II.

A few years later Stryer and Haugland proved that this could be used as a spectroscopic ruler<sup>36</sup>. By measuring  $E$  and calculating  $R_0$  (typically 10–100 Å, 1-10 nm), the distance could be derived. Thus since FRET is remarkably sensitive to the distance between donor and acceptor<sup>290</sup>, FRET-based biosensors, composed of fluorophores and sensing domains, have been widely used as minimally invasive spectroscopic rulers<sup>35,291</sup>. These rulers can monitor a wide variety of biochemical activities that produce changes in molecular proximity<sup>292</sup>, such as protein–protein interactions<sup>293,294</sup>, conformational changes<sup>295,296</sup>, intracellular ion concentrations<sup>297–300</sup>, and enzyme activities<sup>301–304</sup>. Depending on whether the two fluorophores are conjoined to the same molecule or not, FRET biosensors can be separated into two big categories: 1. intramolecular type, where donor and acceptor fluorophores are conjoined to the same molecule, here molecular conformational induce FRET changes; and 2. intermolecular type, where donor and acceptor fluorophores are fused to different molecules, here FRET changes are a result of independent molecules proximity. In both types of FRET biosensors, choosing optimal FRET pairs is the key to high performance biosensors in living cells. Important requirement for the successful consequence of these studies are fluorophores with maximal brightness, photostability and well preserved physicochemical properties, in order to ensure high sensitivity, reproducibility and precise interpretation. Here, it needs to be underlined that a mono-exponential decay for the FPs used in FRET is desired because this way an observed multiexponential behavior during FRET experiments will be attributed to distribution of donor-acceptor distances. Whereas, if the FPs used in FRET have already complicated (multi-exponential) kinetics the interpretation during FRET experiments can be laborious and erroneous. Considerable progress has been made on this direction with the engineering of novel Enhanced cyan fluorescent protein<sup>305–307</sup> (ECFP). Up-to-date ECFP together with Enhanced Yellow Fluorescent Protein (EYFP) is the most widely FRET pair used<sup>308–313</sup>.

#### **IV.1.2 Enhanced Cyan Fluorescent Protein (ECFP)**

ECFP, one of the two most important proteins for FRET experiments, was a result of the original GFP with replacement of the central tyrosine residue of its chromopeptide Ser65-Tyr66-Gly67 with a tryprophan. Some further mutations targeting a sufficient level of fluorescence led to the

ECFP as we know it today<sup>314</sup>. Figure 32 demonstrates these mutations placed around the protein barrel, both in remote surface positions and much closer to the chromophore.

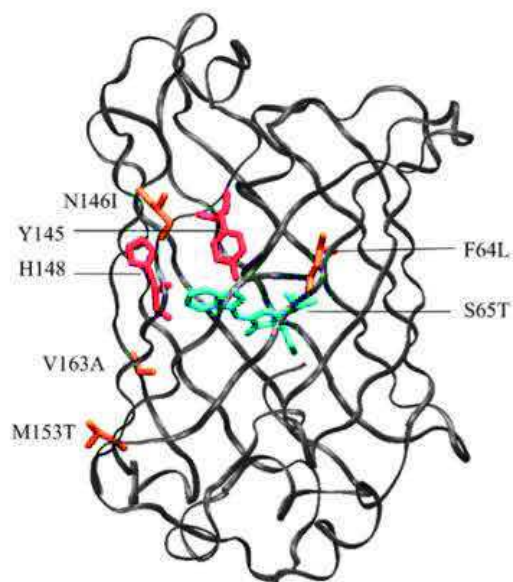


Figure 32-Adopted from <sup>315</sup>. Schematic 3D structure of ECFP indicating mutation locations compared to AvGFP. The chromophore is displayed in blue and mutations outside the chromopeptide in yellow. In red are presented the side chains of His148 and Tyr145 located on strand 7. Crystallographic structure 1OXE <sup>316</sup>.

Soon it was clear that ECFP was coming along with several drawbacks. The major spectroscopic disadvantages are its highly complicated fluorescence emission and its dim fluorescence<sup>317-319</sup> (brightness is only about 40 % of that of EGFP, QY=0.37). Moreover, its pH sensitivity is potentially another flaw when biochemical activities other than pH need to be addressed. NMR<sup>320</sup> and x-ray crystallographic studies<sup>316</sup> propose that the main reason for the complex fluorescence emission kinetics detected is the coexistence of two ECFP conformations. The major structural change differentiating the two conformations is an alternate displacement of the His148 and Tyr145 side chains. In the dominant ECFP conformation His148 is found on the exterior of the protein while in the minor conformation it is located on the surface of the protein lying in the entrance of the chromophore pocket.

Time-resolved fluorescence spectroscopy studies of ECFP<sup>321</sup> have been conducted as a function of emission wavelength, temperature and pH revealing complex (multiexponential) fluorescence decay kinetics. In neutral pH, the complex kinetics are constituted by a major-lifetime component and a distribution of shorter-lived components. It is reported that the relative amplitudes of the lifetime components are highly affected by temperature and pH changes, implying that the different configurations must undergo dynamic exchange. When the medium containing the protein is acidified a rapid decrease in relative lifetime, up to 40%, is observed<sup>322,323</sup>. The transition point for this intensity change is appointed to be at pH 5. The lifetime decrease in decreasing pH conditions (up to pH 5) is accompanied by varying weights of similar lifetime constants<sup>321</sup>. The main difference is detected in the decrease of the relative amplitude of the longest component<sup>321</sup>. It can be speculated that the main reason for these observations could be the protonation state of His148 which in both crystallographic conformers of ECFP is one of the closest titratable residues in the vicinity of the chromophore<sup>316,320,322,323</sup>. A complete correlation of the protein's fluorescent properties with its structure is yet to be given. Such a description could lead to a general understanding of fluorescence properties of FPs and to the engineering of novel optimum FPs.

The multiexponential decay of ECFP cannot be plainly ascribed, as is generally attributed to conformational changes characterized by NMR and X-ray crystallographic studies<sup>316,320</sup>. Moreover with TRF measurements from Villoing et al<sup>321</sup> it has been shown that this complex kinetics is strongly sensitive to temperature and pH, which shows that the multiple configurations that underlie this complexity must be under dynamic exchange. This motivates the pH jump experiments that have been conducted in this study and are described in the next pages, with main target the deciphering of the time scale for the aforementioned population exchange.

### **IV.1.3 Mutants of Cyan Fluorescent Protein**

Numerous novel cyan fluorescent proteins, such as mCerulean3<sup>306</sup>, mTurquoise2<sup>305</sup>, and Aquamarine<sup>307</sup>, were recently engineered<sup>305-307</sup>. mCerulean3 and mTurquoise2 were retrieved

through a combination of site-directed mutagenesis and medium to large scale random mutagenesis. They bear numerous mutations compared to ECFP, whose role in the final characteristics of these proteins remains unclear and do not offer much to the general understanding of the structure to photophysics relationships. Aquamarine on the other hand was the fruitful result of step by step evaluation of critical mutation positions within a family of spectrally identical and evolutionary close variants. All mutation points were selected through screening of amino-acids choices at targeted positions that were already appointed by structure-photophysics analyses. All three mutants exhibit not only an enhanced fluorescence quantum yield approaching unity but also near-single exponential fluorescence emission decays accompanied with a distinctive pH stability of their fluorescence. Moreover as shown in the Figure 33, their spectral resemblance to the original ECFP makes it easier to replace it in application without the need of big set-up modifications.

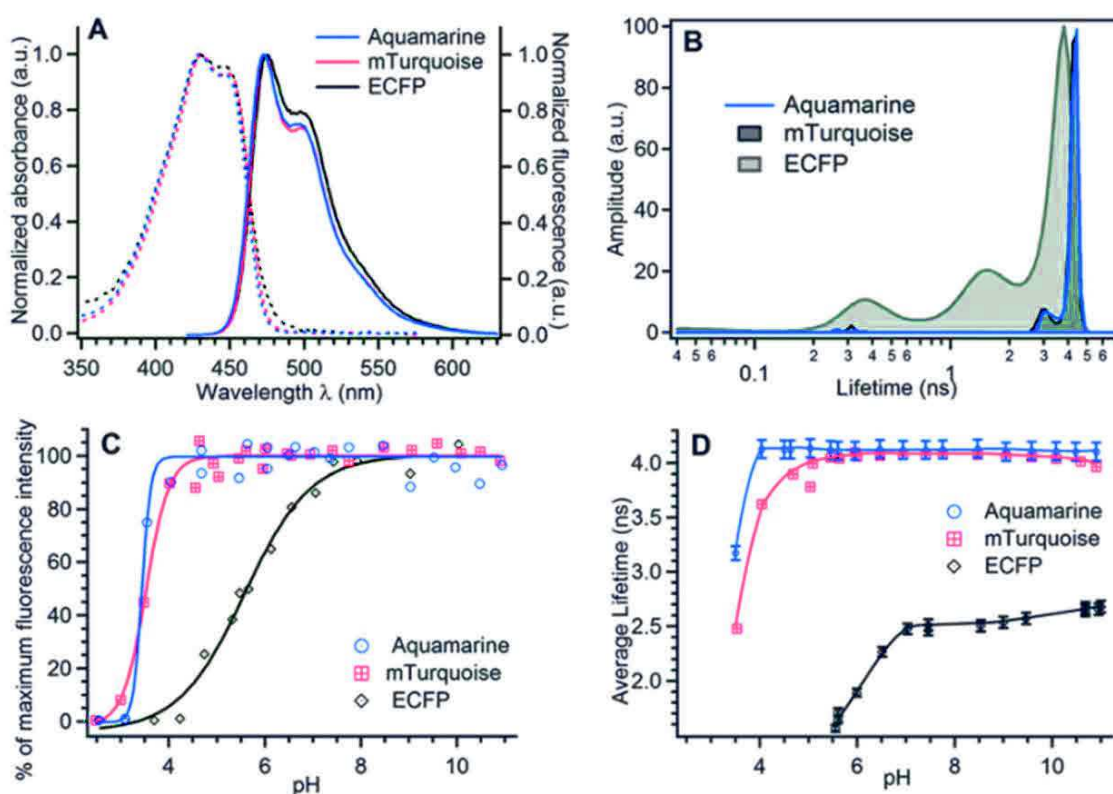


Figure 33-Adopted from <sup>307</sup>. Photophysical properties of purified Aquamarine. (A) Absorption (dashed lines) and emission (solid lines) spectra normalized to maximum of the chromophore band. Emission spectra were recorded with excitation at 420 nm. (B) Fluorescence lifetime

distributions at neutral pH obtained from MEM analysis of the fluorescence decay curves. (C) pH dependence of the fluorescence intensity excited at 420 nm and detected at 474 nm. Solid lines correspond to the best fits to a sigmoidal analytical model. Experimental data were normalized to 100% maximum of their analytical fits. (D) pH dependence of the average fluorescence lifetime determined from integration of the lifetime distributions. Solid lines are for eye guidance only.

From the three above mentioned mutants, Aquamarine displays the most notable interest since it is engineered by the mutation of only two residues buried in the chromophore pocket as shown in the Table 1. However the common mutation characteristics of these successful derivatives are the side chains of residues H148 and T65S which are located very close to the chromophore, and expected to have a prominent influence on its photophysics<sup>288,319,324–326</sup>.

Table 1-Adopted from<sup>315</sup>. Mutations of CFP leading to the novel fluorescent proteins.

<b>ECFP Variant</b>	<b>Mutations</b>	<b>QY</b>
ECFP <sup>327</sup>	-	0.37
mCerulean3 <sup>306</sup>	H148G, T65S, +8 other	0.87
mTurquoise2 <sup>305</sup>	H148D, T65S, +4 other	0.93
Aquamarin <sup>307</sup>	H148G, T65S	0.89

### **T65S Mutation**

Mutation at position 65S was one of the initial mutations included in GFP leading to the enhanced GFP (EGFP)<sup>328</sup>. Insight to this mutation was given by Goefhart et al<sup>305</sup> with x-ray crystallographic structures of SCFP3A and mTurquoise, that differ only by the T65S mutation and by 50% difference in quantum yield. They concluded that the difference in quantum yield is

probably not the result of different structures, since no resolved major differences were observed. This led Mérola et al<sup>315</sup> to propose a mechanism interpreting the consequences of this mutation. It was proposed that since ECFP has greater flexibility in comparison with GFP<sup>316,320,329</sup> two different configurations would coexist. This would lead to an average lifetime dependent on the balance between a high fluorescent rigid conformation and a quenched flexible one<sup>330</sup>. Thus the mutation T65S would favor the rigid conformation leading to highly fluorescent molecule. This is not obvious in the crystallographic study due to the nature of this technique to select the most stable conformations and thus end up only with the major form. However it is clear<sup>331</sup> that the single T65S mutation brings dramatic improvement to the performance of ECFP, reaching a 48% fluorescence QY increase accompanied with simplification of the FLT distributions as shown in the Figure 34 and an improvement of the pH stability in the acid range. All the above characteristics of the mutant are mainly attributed to an increased local rigidity<sup>331</sup>. However T65S mutation is not adequate to achieve the desired fluorescent properties and usually some further engineering is introduced<sup>331</sup>. In all favorable ECFP variants, the above mutation is complemented by another substitution in position 148.

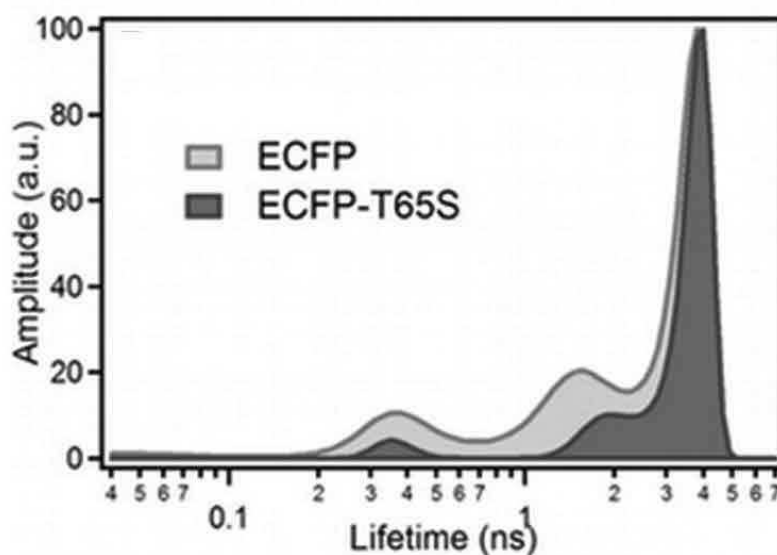


Figure 34-Adopted from<sup>331</sup>. Fluorescence lifetime distributions of ECFP and ECFP-T65S variant in neutral pH.

## H148 position

The problem is more complicated regarding the interpretation of H148 mutation position because two different substitutions, H148D and H148G, seem to function equally well in different mutants. Up-to-date, no crystallographic studies of single point mutations at position 148 have been reported. Villoing et al<sup>321</sup> reported a higher average fluorescence lifetime upon single H148D mutation of CFP, but since the mutant remained non-monoexponential, the multiexponential character of CFP could not be attributed to solely the 148 position. X-ray crystallographic studies and molecular dynamic simulation<sup>316,329,332,333</sup> showed that the residue 148 undergoes different types of conformational changes in CFP. Bae et al<sup>316</sup> evidenced two alternate positions of H148 named A' and B', with the A' being the most populated in CFP. In other proteins, such as Cerulean and mTurquoise the B' position is found to be more populated while they are also more fluorescent than CFP. These different conformations are didactically presented in the Figure 35.

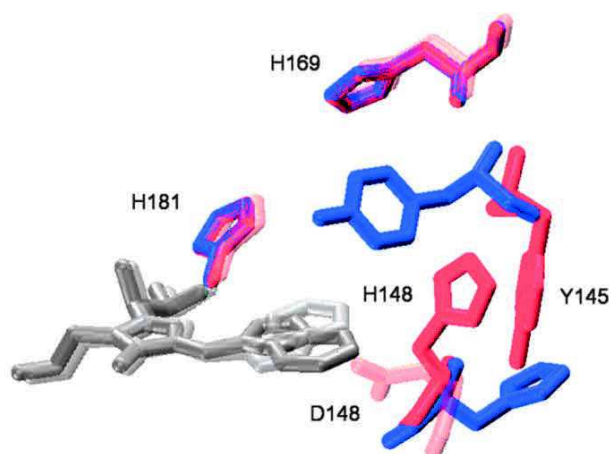


Figure 35-adopted from <sup>321</sup>. Relative positions of nearby titratable side chains in the chromophore region of the two conformations of ECFP (blue, major conformation A'; red, minor conformation B') and in Cerulean (transparent orange), according to X-ray crystallographic structures<sup>316,332</sup>.

Thus it can be implied that A' state corresponds to a less well optimized chromophore pocket. Aquamarine and mCerulean3 both carrying the H148G mutation may therefore adopt the preferred B' state, removing this way any heterogeneity caused by the H148 position. This needs further understanding and better reasoning in order to reach a correlation of the protein structures

with their fluorescent properties. A, in depth, comparison between CFP and its mutant carrying only the H148G has not been reported before and is included in the present study of this PhD project. A detailed comparison can provide valuable information about the limitation of heterogeneity caused by the H148 position and also compare it with the published results of Villoing et al <sup>321</sup> regarding the mutant carrying only the H148D mutation. Here it needs to be noted that for the engineering of Aquamarine the position H148 was tested with different substitutions<sup>307</sup>. As shown in the Table 2 the substitution H148G was preferred due to the longest lifetime detected.

Table 2-Results adopted from<sup>307</sup>. Lifetimes and pH stability, which was monitored through the pK<sub>1/2</sub> of fluorescence loss at acid pHs for mutants substituted in position H148.

<b>Mutant</b>	<b>FLT (ns)</b>	<b>pK<sub>1/2</sub></b>	<b>Mutant</b>	<b>FLT (ns)</b>	<b>pK<sub>1/2</sub></b>
ECFP (H148D)	3.3	5.5	ECFP (H148D, T65S)	4.02	4.0
ECFP (H148G)	3.37	4.9	ECFP (H148G, T65S)	4.12	3.3
			Aquamarine		

## IV.2. Methods

### IV.2.1 Absorption and emission spectra

ECFP and ECFP-H148G were prepared in buffer solutions of citric acid at pH 5 and MCBtP (equimolar mixture of the usual buffers MES, CAPS and Bis-trispropane) at pH 7.4. pH 5 was chosen as a transition point of the intensity change observed in fluorescence upon acidification<sup>321</sup>. Figure 36 displays the steady state absorption and the fluorescence emission acquired in a 1 mm thick quartz cuvette, for the two different pH solutions with protein concentration of 30  $\mu$ M and buffer concentration 33 mM, excitation was at 450 nm.

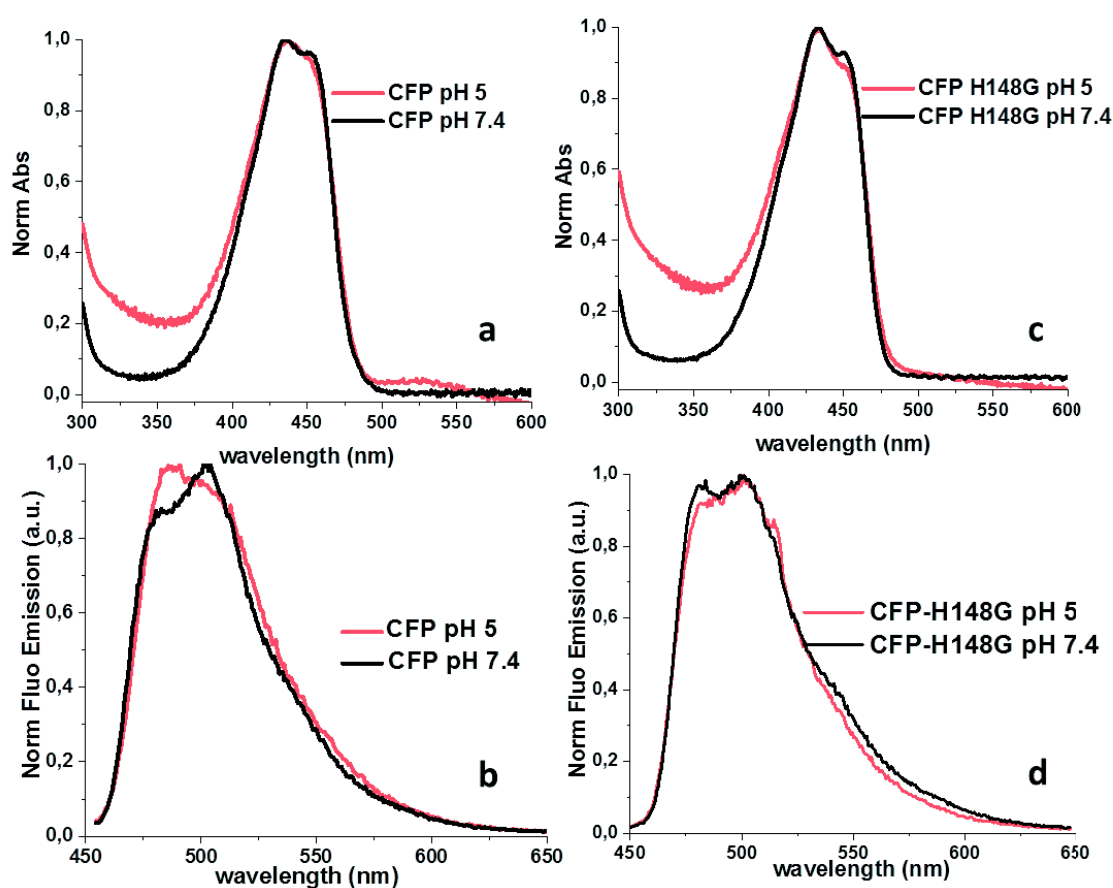


Figure 36-Normalized absorption spectra and fluorescence emission a. and b. ECFP and c and d.ECFP-H148G in pH 5 and 7.4.

## IV.2.2 pH Jump conditions

pH-jump experiments were performed in microfluidic droplets enabling rapid mixing of reagents, in order to produce out-of-equilibrium initial conditions. The droplets are approximately 250 pl and propagate with a speed of 12 mm/s in the microfluidic channel. Specifically, Figure 37 displays a sketch of the local experimental approach. Microfluidic chips made of polydimethylsiloxane (PDMS) are manufactured with rapid prototyping and used to mix of the desired reactants in micro droplets<sup>148</sup>. Three aqueous inlets and one oil inlet intersect in the mixing T-junction point, creating water-in-oil micro-droplets in a 50  $\mu\text{m}$ \*50  $\mu\text{m}$  channel. The velocity, size and concentration of the droplets are precisely controlled by a pneumatic flow control system (Elveflow-Elvesys, France). At the intersection of the aqueous solutions with immiscible oil, droplets form. The mixing inside droplets is accelerated by chaotic advection induced by the wiggling shape of the channel after T-junction<sup>164</sup>. The mixing region is followed by a long main channel folded in successive rectilinear segments of exponentially increasing length.

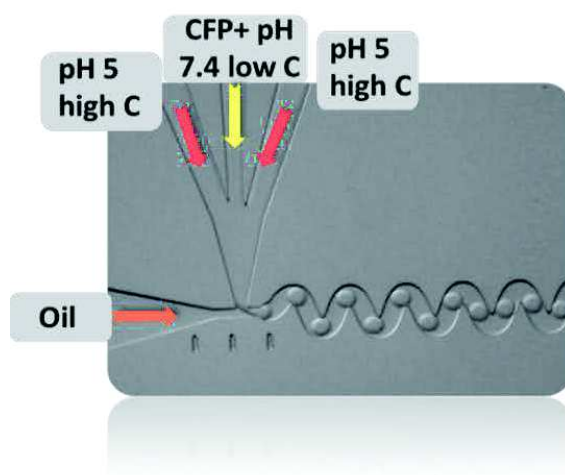


Figure 37-Microfluidic chip-Photograph of the mixing region (T-junction) of a microfluidic chip.

The microfluidic chip is illuminated with a sheet of light at 450 nm produced by a cylindrical lens and wide field imaging of the excitation line is implemented on the photocathode of a streak camera (SC). The photocathode is a 4.5 mm long wire offering a 2 mm-wide field of view with

the present optical set-up. Under these conditions several kinetic traces can be recorded simultaneously at different locations corresponding to different propagation times in the microfluidic channel. The data acquired with the SC along the main microfluidic channel was organized in a matrix incorporating fluorescence decay curves as a function of propagation time. Up to 25-30 fluorescence kinetic traces are recorded successively at consecutive locations along the main microfluidic channel. Every fluorescence kinetic trace derives from averaging over a large number of successive identical droplets acquired at different reaction time. The fluorescence decay kinetics can be recorded on distinct temporal window spanning from ns to ms, with the shortest time window offering the best time resolution of  $\sim 8$  ps.

The method used to fit all the kinetic traces derived was global fluorescence decay fitting, which is generally a process for fitting one or more fit models to one or multiple input datasets simultaneously<sup>272-275</sup>. In the present case all the data sets were fitted by sharing the time constants deriving from a sum of exponential decay functions and leaving free the amplitudes to adjust until the fit is converged. This model was adopted under the assumption that the lifetime components are invariant across the dataset, which was shown by the independent experiments in cuvettes. Additionally weighting is useful in the procedure of reducing Chi-Square (as explained in Chapter II). The weighting factor adjusts the parameters of the curve so that the error at each point of the curve is minimized, in the present study instrumental weighting was used, where the weighting factor was set equal with:  $1/\sqrt{\text{data}}$ .

For the pH-jump experiments, as shown in Figure 37, two inlets of 240 mM citric acid with pH 5, one containing 30  $\mu\text{M}$  protein in 2 mM MCBtP solution at pH 7.4 and last one containing immiscible oil, mixture of perfluorodecalin (PFD, Alfa Aesar) with the surfactant 1H,1H,2H,2H-perfluorooctanol (Alfa Aesar) in a ratio 10:1 were used. The flow speed for these experiments was 12 mm/s and the mixing time (the average time needed to achieve homogeneous mixing) 25 ms. The method for experimental identification of mixing time within microfluidic droplets was described by Maillot et al<sup>148</sup>. In this study, fluorescein was mixed with potassium iodide and the fluorescence decay kinetics were monitored in successive positions along propagation in the main microfluidic channel, as illustrated in Figure 38. Due to collisional quenching potassium iodide strongly quenches the fluorescence lifetime of fluorescein. Therefore the mixing time is defined as the time at which the average fluorescence lifetime has dropped by 90% in comparison with the initial 4.2 ns fluorescence lifetime.

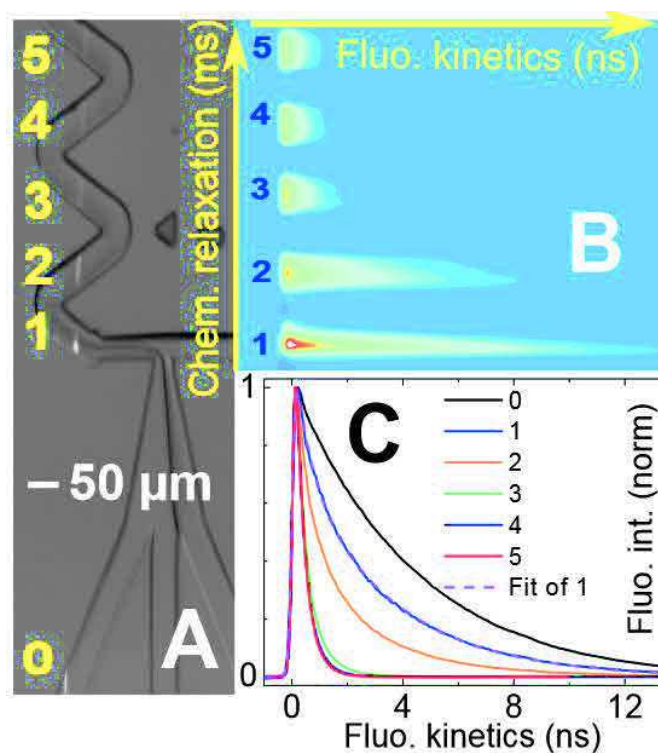


Figure 38-Adapted from<sup>148</sup>. Mixing time measurements A) Microfluidic chip illuminated by the excitation line. The intersection regions of the excitation line with the microfluidic channel are labeled 0 to 5. B) 2D streak camera data: several fluorescence kinetic traces are acquired simultaneously along the propagation in the channel. C) Fluorescence kinetic traces at each of the five positions in the microfluidic chip.

Figure 39 corresponds to a detailed illustration of the experimental steps followed for the pH – jump experiments and the corresponding data analysis.

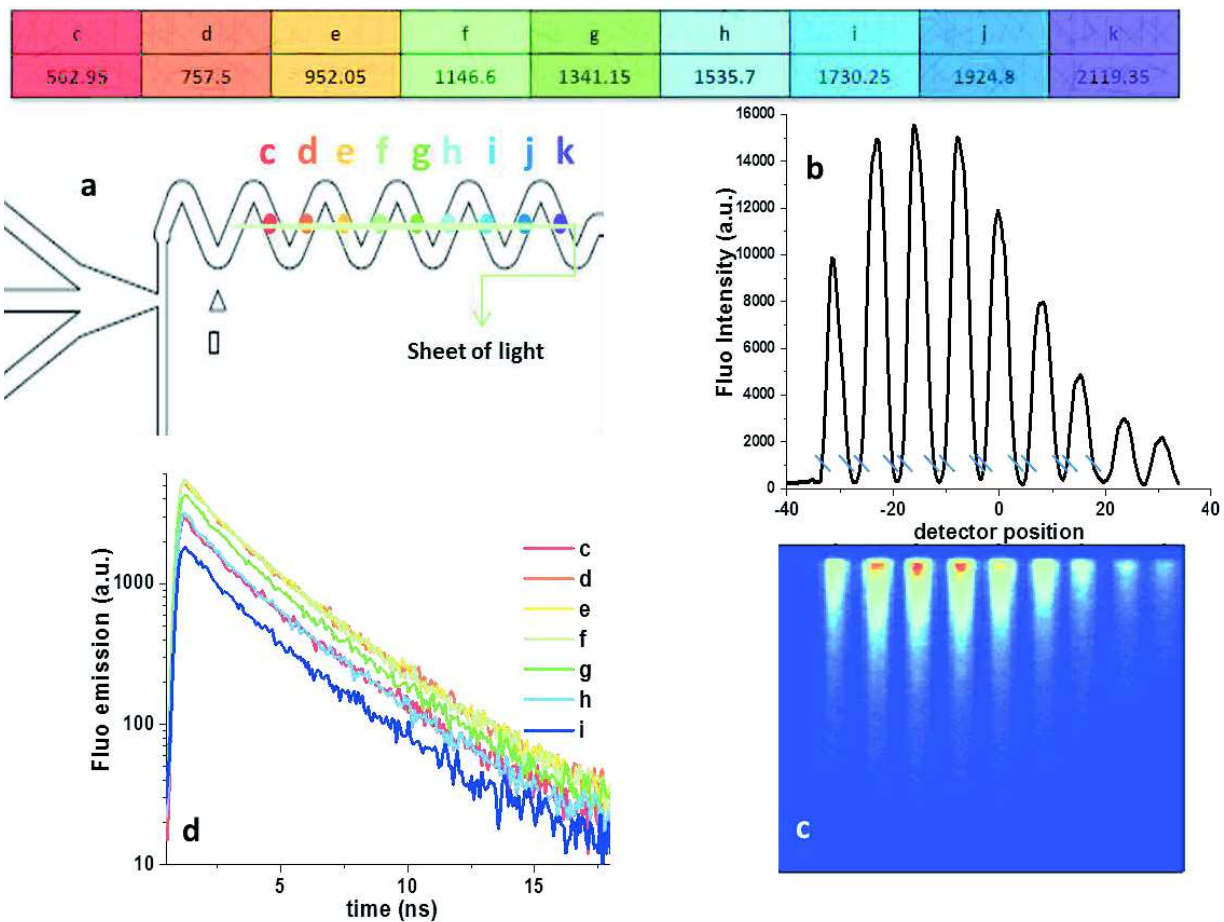


Figure 39-schematic illustration of the experimental steps. On top of the graph the table shows the known propagation distances (in  $\mu\text{m}$ ), having as time zero the T-junction point, in the microfluidic channel. a. Schematic illustration of the chip with the corresponding positions. b. Collection of fluorescence at the same known positions. The data is cut as shown with the blue lines, in order to get the fluorescence decay curve corresponding to each known position in the channel. c. 2D map of the collected data, shown in b. d. Fluorescence decay curves corresponding to each position. The 2 last positions of j and k are disregarded since not enough photons were collected and these positions were recorded again to the next acquisition. Since the photocathode has a limited length; it offers a  $\sim 2$  mm-wide linear field of view and not all the chip is acquired at once. Thus kinetic traces are recorded at successive locations across the chip.

## IV.3. Results

### IV.3.1 Detection of spectral dependence

Initial step was to check if there is some detection spectral dependence in ECFP since there is some debate in literature. Villoing et al<sup>321</sup> report that that the average lifetime is 2.52 (+/-0.04) ns at detection at 474 nm and drops to 2.24 ns at 530 nm. This red shift was not detected by Habushi et al<sup>318</sup>. The present study verifies slight emission wavelength dependence.

First step was to perform SVD analysis, a mathematic tool that has been described in detail in chapter II. As shown in the Figure 40 only one significant kinetic trace was found and all the rest were less than 5%. Here it is shown the protein in pH 7.4, but also in pH 5 again only one significant kinetic trace was seen. However since SVD is a tool for data reduction and noise filtering, its nature is to disregard the very small amplitude signals.

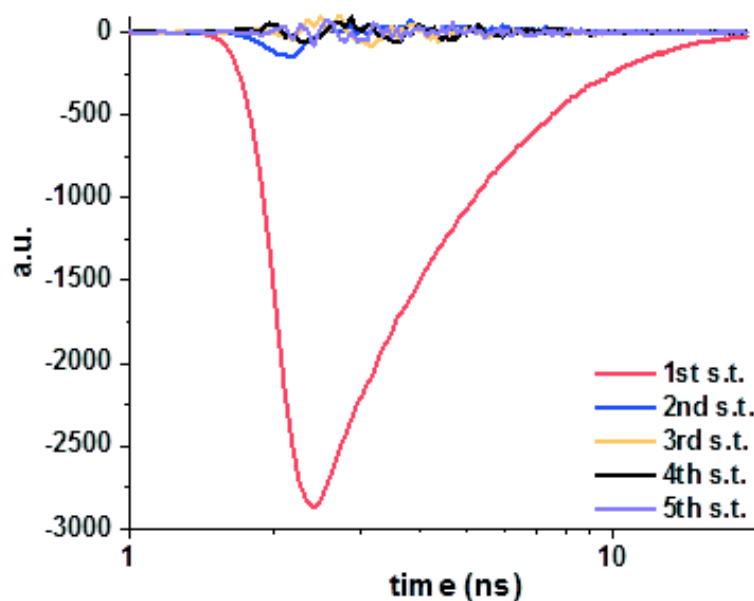


Figure 40-Singular kinetics traces obtained from SVD analysis of the SC data for ECFP at pH 7.4.

Thereafter spectra of ECFP at pH 7.4 were plotted at different times, accompanied with their normalized version. Here traces of emission wavelength dependence were observed as shown in the Figure 41.

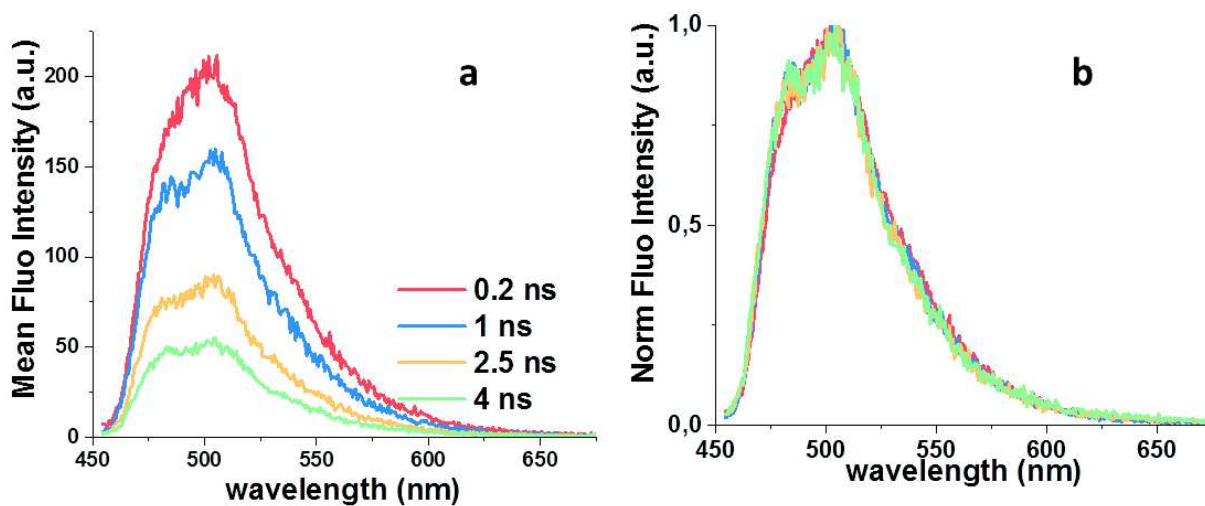


Figure 41-a. Spectra plotted in different times and b. their normalized version for ECFP at pH 7.4.

For the mutant ECFP-H148G also slight spectral shifts were observed.

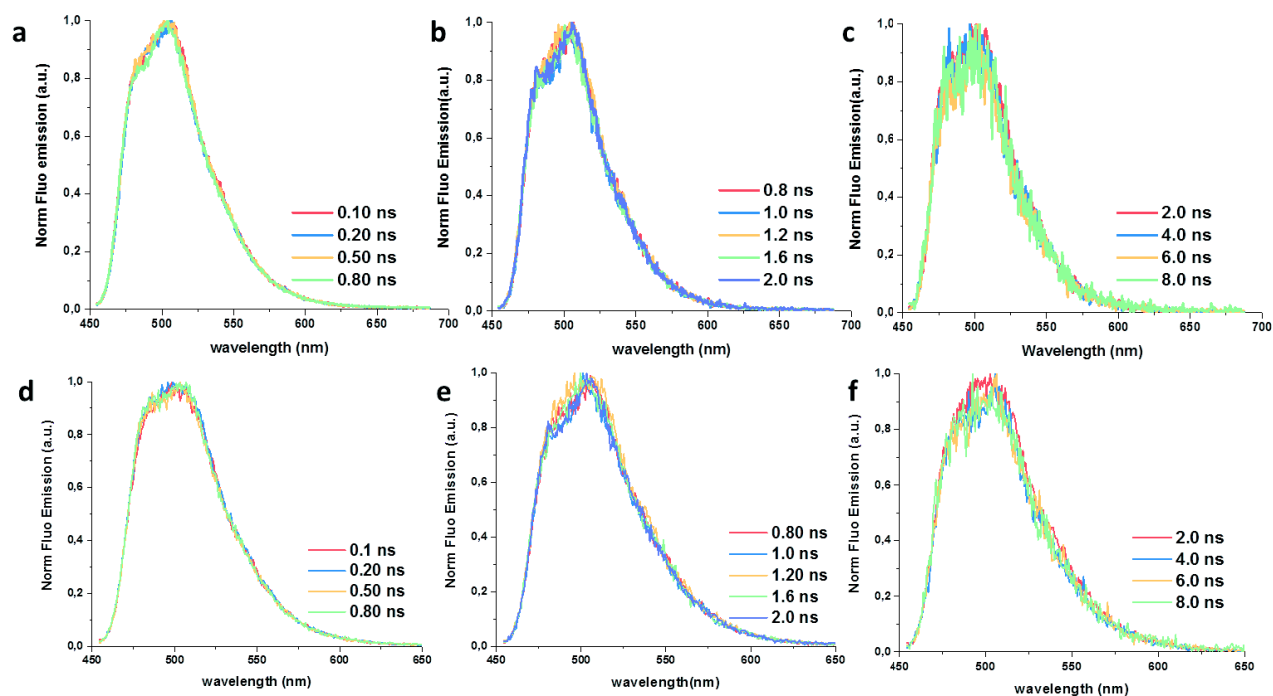


Figure 42-Normalized spectra plotted in different times for ECFP-H148G at a, b, c pH 7.4 and d, e, f pH 5.

For each protein and pH value, the time resolved fluorescence data were then spectrally integrated in one unique kinetic trace for each of the three time windows recorded with the SC, as shown in Figure 43. The 1 ns time window offers the higher time resolution and samples the shortest decay times while the longest decay times are best sampled by the 20 ns time windows. The spectrally-integrated kinetic traces recorded on the three time windows were therefore appended to enable a fit by a sum of three or four exponential functions. This allows us to compare reliably the relative amplitudes of the different time constants and determine accurately the average lifetimes.

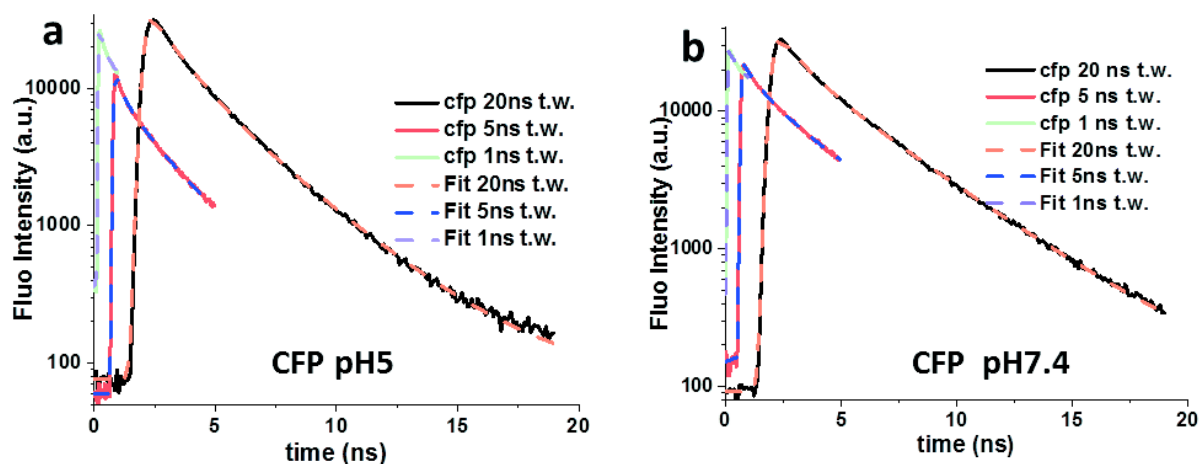


Figure 43-Global fitting of kinetic traces for ECFP from 3 different time windows 1, 5 and 20 ns in two different pH conditions pH 5 and 7.4.

Following Figure 44 depicts the appended kinetic trace for ECFP in pH 7.4 and 5 with the corresponding residuals of the fit and the Table 1 includes all the fluorescence lifetime constants derived. Three time constants were sufficient to accurately fit each of them. The fastest time constant of both differs a few hundreds of femtoseconds in different pH conditions, the second is common with again an 8% difference. The last one has the dramatic change, dropping from 3.57 to 2.68 ps upon acidification. This allows us to perform global fitting to both appended fluorescent decay curves in the different pH conditions, as depicted in Figure 44. Here all the time constants were shared and the amplitudes were free until the fit was converged.

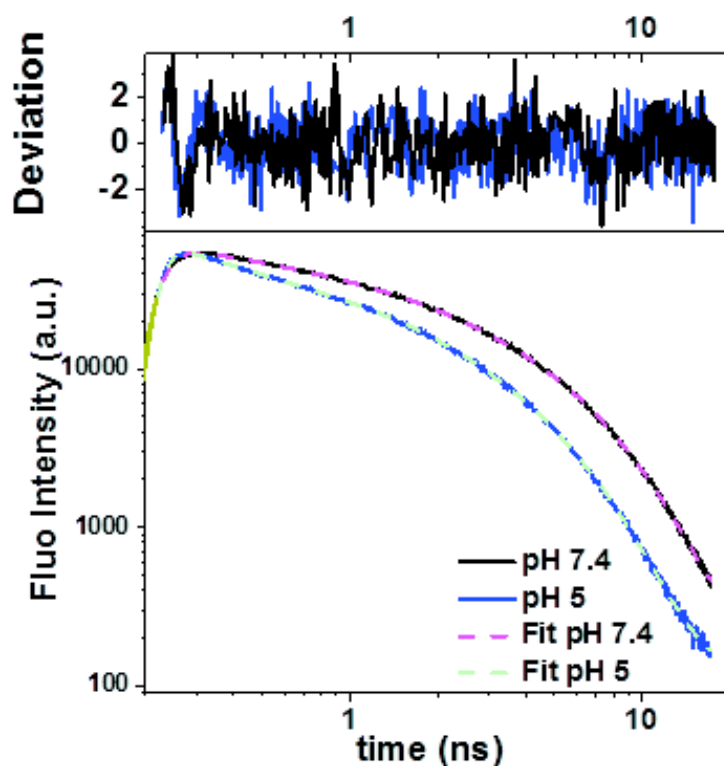


Figure 44-Independent fits for ECFP in 2 different pH conditions. Appended spectrally-averaged fluorescence kinetics traces of ECFP at pH 7.4 and 5 (bottom) with the corresponding residuals of the fit (top).

Table 3-Fluorescence lifetime components of ECFP, from independent and global fits.

ECFP	$t_1$ (ns)	$A_1$ (%)	$t_2$ (ns)	$A_2$ (%)	$t_3$ (ns)	$A_3$ (%)	$t_4$ (ns)	$A_4$ (%)	Reduced $\chi^2$	Average lifetime (ns)
pH 7.4	0.26	18	1.09	28	-	-	3.57	54	1.3	2.28
pH 5	0.18	31	1	32	2.68	37	-	-	1.4	1.37
Global pH 7.4	0.17	14	1	31	2.65	0*	3.5	55	1.26	2.26
Global pH 5		31		31		38		0*		1.37

In the Table 3 it is obvious that the global fit of the appended curves for two different pH conditions reveals that in the case of ECFP, only the longest of the four time constants is strongly affected by change in pH, decreasing from 3.5 ns at pH 7.4 to 2.65 ns at pH 5. Therefore, for the following pH-jump experiments aiming at evidencing the pH-dependence of the decay kinetics, the most appropriate SC time window will be 20 ns, where the change from 3.5 to 2.65 ns is best characterized.

For the mutant ECFP-H148G, the same experimental approach and analysis as above reveals that three time constants were sufficient to fit the appended curves derived in the two different pH conditions, as shown in Figure 45. In contrast with ECFP, the mutant has ~17% higher average lifetime in pH 7.4 and appears to be relative insensitive to acidification, with ~22% drop in average lifetime (Table 4). Here the suitability of global fit is not clear since the values for the time scales derived from independent fits are not identical for different pH conditions.

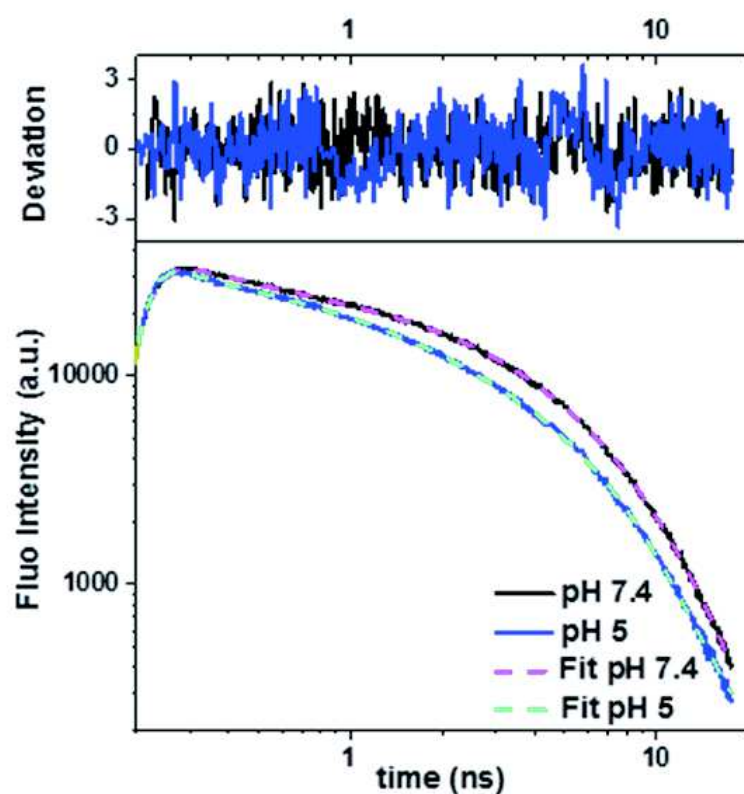


Figure 45-Independent fits for ECFP-H148G in 2 different pH conditions. Appended spectrally-averaged fluorescence kinetics traces of ECFP-H148G at pH 7.4 and 5 with the corresponding residuals of the fit (top).

When comparing the decay kinetics of both proteins (ECFP and ECFP-H148G) at a given pH value, it appears that the mutation affects mostly the one or two longest time constants. The relative amplitude of the shortest time constant (order of 200 ps) are close, and only the longest two seem to be strongly affected by the mutation. The time constant of 2.65 ns observed in ECFP corresponds to a population that may vanishes completely after mutation. Here the interpretation and the existence or absence of exchange population is difficult to be attributed due to the relative small changes between the two pH conditions.

Table 4-Fluorescence lifetime components of ECFP-H148G, independent fits.

ECFP-H148G	t <sub>1</sub> (ns)	A <sub>1</sub> (%)	t <sub>2</sub> (ns)	A <sub>2</sub> (%)	t <sub>3</sub> (ns)	A <sub>3</sub> (%)	Reduced $\chi^2$	Average lifetime (ns)
pH 7.4	0.22	25	1.76	19	4.2	56	1.14	2.74
pH 5	0.12	17	0.81	32	3.65	51	1.3	2.14

### IV.3.1 pH Jump experiment

In order to rationalize the reasons behind the aforementioned population exchange in ECFP the evolution of the fluorescence decay kinetics is followed upon pH-jump. In the following part, we will focus on the pH-dependence of the ECFP decay kinetics measured on the 20 ns time window only. As a preliminary step towards the pH-jump experiment, we first analyze globally the two decay kinetics observed in cuvettes at fixed pH 7.4 and pH 5. Figure 46 presents the result of this analysis and Table 5 contains the results of the fits. The shortest 170 ps time constant evidenced above on Figure 44 is not correctly resolved on the 20 ns time scale, and therefore disregarded in the fit of Figure 46. However the intermediate, pH-independent time constants of 1 ns is kept in the fitting function. In addition we introduce the two longer time constants of 2.65 and 3.5 ns. All time constant are maintained fixed to their values determined in Figure 44; only the amplitudes are adjusted by the fitting routine for both curves simultaneously. From pH 7.4 to 5, as expected, the average lifetime is decreased from 3.5 ns to 2.65 ns. This results in a population exchange between the longest time constants of 3.5 ns in pH 7.4 and 2.65 ns upon acidification. Indeed,

upon acidification, the time constant of 3.5 ns is replaced by 2.65 ns whereas the amplitudes of the shortest two time constants is hardly pH-dependent with an increase of no more than 5%.

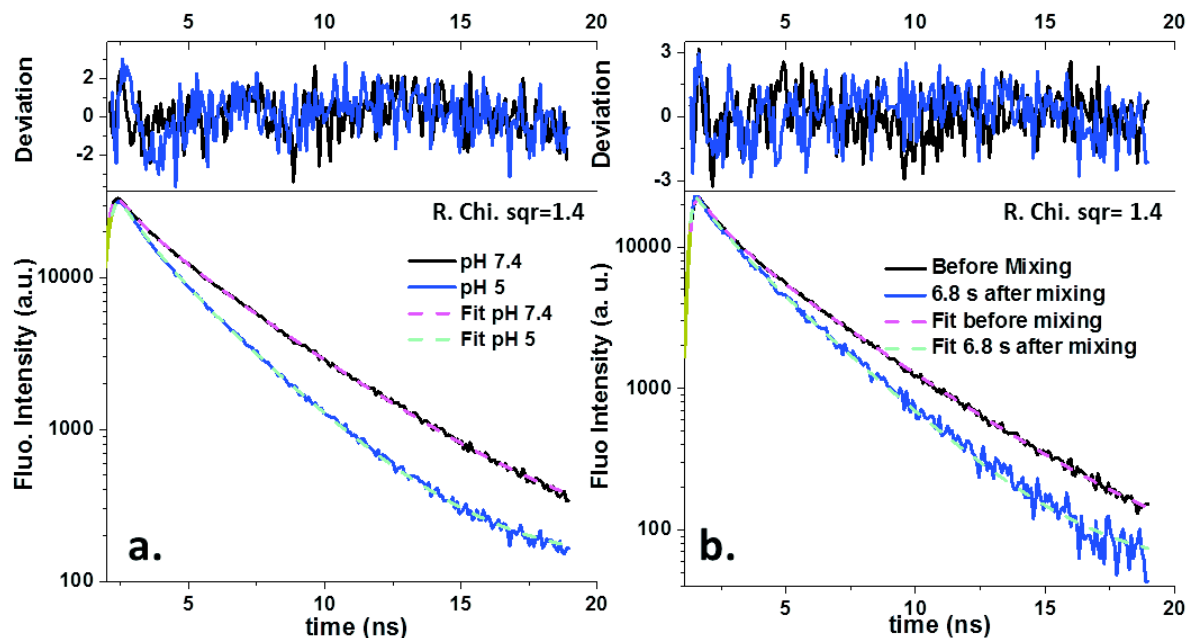


Figure 46-Comparison of fluorescence decay kinetics recorded in cuvette and droplets. a. Globally fitted fluorescence decay curves of ECFP in two different pH conditions, measured in cuvette, in 20 ns SC time b. Globally fitted fluorescence decay curves of ECFP corresponding to the initial point in the chip before mixing (pH 7.4) as well as the last point of the chip after 6.8 s propagation time (pH 5).

Table 5-Comparison of the relative amplitude percentage of the fixed time constants corresponding to each FLT in cuvette vs in microfluidic droplets.

tau (ns)	pH 7.4 cuvette	pH 5 cuvette	pH 7.4 droplets	pH 5 droplets
1	38%	43%	45%	33%
2.65	0%	57%	0%	67%
3.5	62%	0%	55%	0%

For the pH-jump experiment, we record in 20 ns SC time window at consecutive locations along the main microfluidic channel, which provides us with 25-30 fluorescence kinetic traces. The first point on the chip corresponding to the initial point before mixing and acidification as well as the last point of the chip corresponding to 6.8 s propagation time were globally fitted as shown in Figure 46, using the same analysis strategy as in Figure 44 above. Table 5 confirms that the fluorescence kinetics observed in cuvettes are reasonably well reproduced in microfluidic droplets. We indeed also observe that the amplitude of the shortest (1 ns) time constant is hardly pH-dependent, with an average value of 40% of the average sum of amplitudes. Moreover the dominating 3.5 ns time constant at pH 7.4 vanishes at pH 5 where the 2.65 ns time constant appears.

The final step was to globally fit all the kinetic traces recorded along propagation in the microfluidic chip. The same fitting procedure was applied with the additional condition that the amplitude of the 1 ns time constant was set equal to the 40% of the sum of the other two amplitudes of 2.65 and 3.5 ns (average of what found in Table 5 for the 1 ns lifetime), derived from the results shown previously for the 20 ns time window. Starting point for our fits is considered 30 ms, in order to surely avoid the mixing region. Figure 47 displays the evolution of these amplitudes as a function of the propagation time in the main channel. The presented three experiments and analysis procedure reveal the time scale for structural relaxation from the high-pH species to the low-pH species. The global mono-exponential fit of this time evolution reveals a reaction time of 0.32 s.

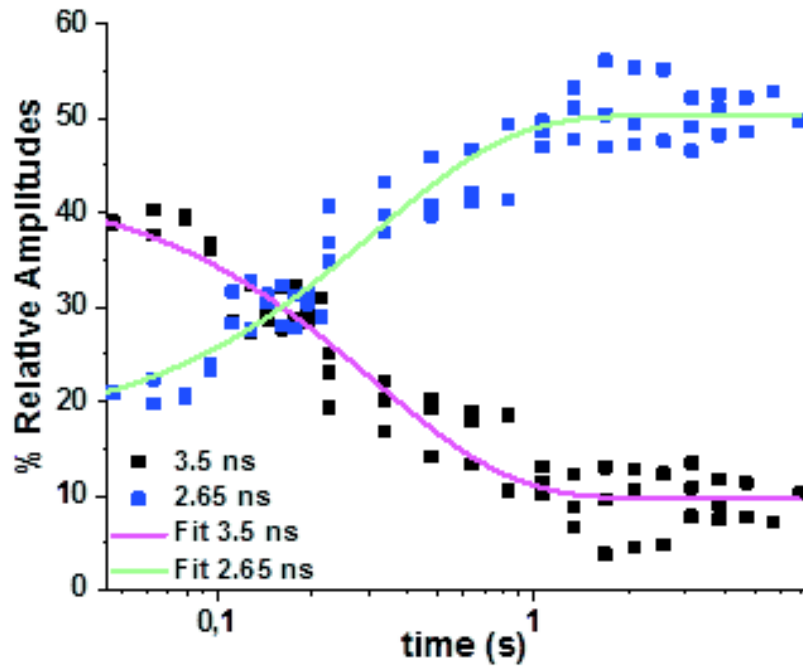


Figure 47-Relative amplitudes of the 2.65 and 3.5 ns time constants as a function of reaction time after pH-jump for ECFP acquired in microfluidic droplets. A global mono-exponential fit was performed for the relative amplitudes corresponding to the longest two time constants in three experiments. This reveals 0.32 s reaction time.

#### IV.4. **Discussion and Conclusions**

The present data support the hypothesis that fluorescence decay times correspond to distinct protein structures already preexisting in the ground state (i.e. structural heterogeneity). It appears that the photoreactivity (excited state lifetime) of the chromophore displaying the shortest time constant is hardly affected by the pH-induced structural changes. This time constant would correspond to a protein structure where the chromophore binding pocket is hardly affected by the pH. Only one sub-population of the ECFP protein, corresponding to the long-lived chromophores, is affected by the pH. For this population, the chromophore excited-state lifetime reduces from 3.5 ns at pH 7.4 to 2.65 ns at pH 5 due to a structural change occurring on the 320 ms time scale, which alters the local interaction of the chromophore with its binding pocket. The present results highlight a slow, pH -induced configuration change taking place in the ground state. This slow phenomenon suggests that the structural mechanism may involve a high potential barrier crossing, possibly caused by a large structural change or a set of necessarily concomitant smaller structural changes leading to an unlike event.

On the other hand, the detailed comparison of ECFP with its mutant ECFP-H148G provides valuable information about the relationship between the structure of the protein and its fluorescence properties. This allows the prediction of further mutations leading to optical fluorescence proteins appropriate for quantitative imaging and solid data interpretation. A manuscript is currently in preparation with Helene Pasquier, including additional data with different approaches that will help refining the interpretation and conclusions on this project.

On the other hand, the second target of this project was to reach the first successful application of the original experimental approach combining TRF and Droplet Microfluidics for biomolecular interactions studies. The presented experimental work exhibited that this novel experimental set up can efficiently reveal structural dynamics on the ms to sec (or even min with the help of a longer main channel). Thus this approach lays the foundations for further research of interactions within out-of-equilibrium biomolecular complexes. The perspectives of this set-up will also be discussed in Chapter VII.



# **V. Towards sensitive, high-throughput, biomolecular assays based on fluorescence lifetime**

## **V.1. Introduction**

High throughput sample manipulation and signal detection is essential for bioassays since it enables the rapid and cost-efficient collection of valuable information concerning the potency of biological products and drugs. Droplet microfluidics is an emerging technology that fulfills these two conditions of speed and low-cost and can thus be applied for smart sample-handling. This technology can be combined with detection techniques based on fluorescence; which are widely exploited in high-throughput bioassays nowadays including cytometry, cell sorting etc. Most of the applications based on fluorescence have, until now, utilized fluorescence intensity, mainly because of its easy instrumentation. Our concern in this Chapter V is to investigate whether fluorescence intensity can be replaced by fluorescence lifetime detection in modern high throughput bioassays. Although the conceptual advantages of TRF over fluorescence intensity detection urge us to do so, there are specific technical issues to overcome. In this Chapter V we describe our work at exploring high-throughput TRF detection by implementing time-correlated single photon counting at the individual droplet level, with a droplet circulation rate approaching 1 kHz inside the microfluidic channel.

## V.1.1 High-throughput biosensing- application areas

### High-throughput screening (HTS)

High-throughput screening (HTS) is usually the initial step towards drug discovery. Once a potentially interesting target is identified, a molecular starting point can be found by “screening” systematically the interaction with a large number of compounds (i.e. small molecules). For example the Novartis Pharma Company has around 2.5 million compounds in its library. An assay needs to be fast, reliable and cost efficient. HTS is largely performed by robotic systems, which are adapted and programmed for this task.

A few words about the history of this field would start with 1980's, until when 10-100 compounds could be tested per week. In 1986 Pfizer was involved in natural products screening<sup>334</sup>. They used 96-well plates and from a starting point of 800 compounds per week, they reached 7200 compounds per week in three years. By 1992 after technological advancement thousands of compounds could be tested per week. Nowadays hundreds of thousands compounds can be tested in a day.

HTS is a field with astonishing rate of evolution and level of investment. The advances made over the past 20 years have revolutionized drug screening and development.

### High throughput flow cytometry and cell sorting

Flow cytometers are used as research and clinical tool, where the properties of each respective sample, such as cell, are individually evaluated<sup>335-337</sup>. A flow system manages the passage of cells one by one through an interrogation point, where they are illuminated by a light source. Different techniques and probes are used to label the samples, such as fluorescently tagged antibodies to mark and identify cells<sup>338</sup> (immunofluorescence) or stains<sup>339</sup> (i.e. to quantify DNA content), or fluorescent proteins. Consequently emitted fluorescence will be detected providing a number of parameters either to yield statistics about subpopulations samples or by the use of a sorting apparatus to isolate samples of interest for further study. However since each sample is analyzed individually, the development of flow cytometers and Fluorescence-Assisted Cell

Sorting (FACS) is currently focused on enhancing performance by increasing accessibility and throughput<sup>340-343</sup>. The consequence is the report of a big applications variety based on this technology<sup>343-347</sup> and different fluorescence techniques.

### **V.1.2 Droplet Microfluidics for High-throughput bioassays**

On account of the highly complex nature of biological systems and our subsequently limited predicting ability on the biological activity of new chemical entities, High Throughput Screening (HTS) is the epicenter of modern drug discovery. The ability to design and synthesize numerous compounds has raised the demand for novel assay technologies and the use of high-density assay plates. The volume reduction of assays and the concomitant decrease in the use of biological reagents are considered key factors to constrain the costs at this early stage of drug discovery process. However, assay miniaturization depends on multiple factors, including the ultra-low volume handling ability of liquids and the demand for highly sensitive and fast readouts. Up to date the standard microplates widely applied in industries use 10-100  $\mu$ l sample volume per well and the acquisition time for the microplate readers is at least 0.1-1 s. In modern drug research, screening compounds in microplates is the main automated method to discover and develop new medicines<sup>348</sup>. With the specific targets and compound libraries increasing rapidly, the current screening throughput will not be adequate to meet requirements in the following years. For further expanding the screening capacities, most pharmaceutical companies are on the search of new screening technologies to decrease the assay volume and improve the accuracy and precision of the liquid dispensation while reducing the costs<sup>349,350</sup>.

Droplet microfluidics constitutes an advantageous technique for High throughput screening and sensitive bioassays such as cell sorting<sup>351,352</sup>. This technique facilitates high throughput conditions by sustaining low cost and minimal sample volumes. Water in oil droplets are used to accommodate the reactants into picoliter volumes rather than microliters that are being used in common methods (microplates). Droplets can encapsulate cells<sup>353</sup>, proteins<sup>354</sup>, DNA<sup>355</sup>, enzymes<sup>356</sup> and other particles or molecules that are in the inner aqueous phase. After the first step of encapsulation, there are numerous ways used to manipulate the droplets. Additional

reagents can be injected into the already formed droplets<sup>357</sup> at adjustable rates and induce mixing if needed. Different chip geometries can also facilitate droplet splitting<sup>358</sup>, droplet sorting etc. Nearly any bioassay that is performed in microplates can be performed by droplet microfluidics.

As an example droplet microfluidics were utilized as a smart-handling device for cell sorting on a proof of principle enzymatic activity assay by Baret et al, in 2009<sup>341</sup>. In this application mixtures of *E. coli* cells, expressing either a reporter enzyme or an inactive variant, were compartmentalized with a fluorogenic substrate. After 14 h of incubation the droplets containing the active enzyme were 100-fold more fluorescent than the rest of the droplets. The sorting took place at rates of 300 droplets/s by electric field application on the more fluorescent droplets leading them to a separate reservoir.

### **V.1.3 Fluorescence-based detection techniques used in High throughput biosensing**

Multiple variants of fluorescence-based detection techniques are widely used in high throughput bioassays due to their sensitivity and cost-effectiveness, including: fluorescence intensity (FLINT), fluorescence polarization/anisotropy (FP), single-molecule detection methods, such as fluorescence correlation spectroscopy (FCS) and last but not least fluorescence lifetime (FLT). In the same track suitable design and production of reagents to match the potential of each fluorescent readout is crucial in achieving a tractable HTS assay as well as new fluorescent probes to enable multiplexing of assays. Each method utilizes different features of fluorescence and presents distinct advantages and limitations, principally in terms of sensitivity, speed and susceptibility to artifacts<sup>359 360</sup>.

Some basic principles for the above mentioned methods used in HTS have to be stated here.

### **Fluorescence Intensity (FLINT)**

In this method the change in steady-state total light output of fluorescent or fluorescently labeled molecules is monitored with easily applied instrumentation. Unfortunately it is sometimes inaccurate because it can be affected by auto-fluorescence, background emission, photo-bleaching, etc<sup>361,362</sup>.

### **Fluorescence Polarization/Anisotropy (FP)**

For a small fluorescently labeled molecule, the interaction with a macromolecule is monitored through the increase in FP, which occurs with the change in fluorophore mobility upon complex formation. Free fluorophores have low polarization due to fast rotation relative to fluorescence lifetime, while fluorophores bound to a large biomolecule (for example due to complex formation) have high polarization due to slow rotation. FP can be determined both by steady-state and time-resolved measurements<sup>363 364</sup>. The French physicist F. Perrin was the first to describe the quantitative relationship of the observed polarization with molecular size and solution viscosity<sup>365</sup>.

### **Fluorescence Correlation Spectroscopy (FCS)**

FCS was originally demonstrated by the American D. Magde<sup>366</sup>, in the group of W. Webb, it is a sensitive analytical tool observing a small number of molecules (nM-pM concentrations range) in a restricted volume ( $\mu\text{m}^3$  range) defined by the excitation laser focus volume. It is used to exploit fluctuations, due to diffusion, physical or chemical reactions, aggregation, etc., in the detected fluorescence intensity after sample excitation. The collected data is then analyzed using the temporal autocorrelation, which searches for temporal patterns, meaning correlation between points separated by various time lags. Fluorescence Intensity Distribution Analysis (FIDA)<sup>367</sup> belongs to the FCS family and is a technique able to determine both the concentration and specific brightness values of fluorescently labeled molecules in solution.

## **Fluorescence Lifetime (FLT)**

FLT is an intrinsic parameter measuring the excited state lifetime of a fluorophore after excitation by a light pulse. Changes in the fluorophore's physicochemical micro-environment can lead to detected changes in the FLT, leading to abundant information for molecule-molecule or molecule-microenvironment interactions. Due to its intrinsic character it is robust against experimental artifacts.

### **On the advantages of Fluorescence Lifetime**

FLINT is by far the mostly used method through the years; here fluorescence intensity is directly related to changes in fluorophore concentrations. However, although it is a method easily applied (simple instrumentation needed) and rather sensitive, it is defenseless against the perturbations of the signal caused by differences in concentration, fluctuation of the laser source, auto fluorescence etc. Moreover the intensity measurement interpretation can be difficult or misleading. Probes may become saturated or bleached, or unevenly spread across the structure of interest resulting in an inaccurate representation of the level or distribution of the target molecule. Ratiometric measurements limit to some extent these problems, although they, by no means, provide a complete solution.

A recently added arrow in the quiver of HTS is FLT. In this technique fluorophores are excited by short (ps), high-frequency laser pulses and the characteristic lifetime is determined. The lifetime of a fluorophore is an intrinsic parameter only affected by the local micro-environment. The unique character of fluorescence lifetime allows this way easy discrimination against scattered excitation and background fluorescence. It is still technically challenging, since the instrumentation used so far is quite sophisticated; but highly promising.

Of central relevance here, we note that due to its intrinsic character it is robust against experimental artifacts. Indeed, as introduced in Chap II, a change in the interaction of fluorophores with their environment, which results in a change in their non-radiative decay rate, translates into a change of fluorescence quantum yield (QY). The later will result in a change in fluorescence intensity  $I$ , since:

$$I = nN_{exc}QY$$

where  $\eta$  is the fluorescence collection and detection efficiency and  $N_{exc}$  is the number of absorbed photons, proportional to the excitation light intensity. Therefore the change in the detected fluorescence intensity may be related to a change in QY (which is what one wants to detect in an interaction assay), but it may also be due to a change fluorescence light collection efficiency (e.g. caused by scattering, reabsorption, etc.) or by a change in the number  $N_{exc}$  of excited fluorophores (e.g. caused by a change in fluorophore concentration, excitation light scattering, photobleaching, etc.). In marked contrast, according to the notations introduced in Chapter II:

$$QY = k_{rad}\tau$$

the fluorescence lifetime  $\tau$  is an intrinsic measurement of the QY, which therefore does not suffer from the above-mentioned artifacts.

Finally we note that besides TRF detection, another way of overcoming the artifacts of conventional FLINT relies in the ratiometric detection of two emission intensities which are equally affected by a change in  $\eta$  and  $N_{exc}$ . This requires the use of specifically designed chromophores exhibiting a double-band fluorescence spectrum. Such an example is described in detail in Chapter III. However, in many bioassays relying for instance on the use of fluorescent proteins naturally expressed in cells (meaning at a concentration which is not accurately controlled), the ability to detect FLT is potentially a great advantage over FLINT<sup>343</sup>.

#### V.1.4 Fluorescence lifetime techniques for High throughput screening- Challenges to overcome

Although the discussion over the use of FLT for HTS began more than 15 years ago<sup>368 369 370</sup>, it was not commonly applied to applications. The first attempt to use FLT in high throughput condition was conducted by Lebakken et al in 2007<sup>371</sup>. The investigation was elaborating FLT detection as a potential signal for assaying kinases. Kinases are enzymes that catalyze the transfer of phosphate groups from high-energy, phosphate-donating molecules to specific substrates<sup>372</sup>. The hindrance of this application was the fluorescence dye choice, which has a lifetime below 2 ns resulting in an insignificant assay signal window of 0.6 ns with sub-ns time resolution, limiting dramatically the efficiency of the proposed assay.

A few years later, Doering et al<sup>373</sup> reported another application based on the same principle for enzymatic activity essays. Success this time was based on two aspects; the choice of a longer lived blue fluorescent dye and the efficient quenching process, by introducing a specific interaction between label and quencher. In the same principle more lifetime-based assays followed<sup>374 375 376</sup>. However a technological challenge has always been the long acquisition time needed per sample, reaching 1s. TCSPC is the most sensitive technique that can be applied (down to the single photon detection level) for FLT detection<sup>377</sup>. Nevertheless, it is usually considered inapplicable to HTS because counting photons one by one would be time consuming<sup>378 379</sup>.

7 years ago, J.M. Muretta et al introduced an alternative technique for FLT measurements<sup>378</sup>. The Direct Waveform Recording (DWR) method is based on an intense (1  $\mu$ J/pulse) high-repetition (10 kHz) laser excitation source and a digitizer recording a complete fluorescence decay curve for every laser pulse. In comparison with the classic TCSPC technique it has several drawbacks. Firstly expensive instrumentation is needed, including digitizer, microchip laser etc. Moreover it is not able to detect weak fluorescence signal and its intense pulsed excitation source may not be suitable for biological material. The Instrument Response Function (IRF) is much longer than in TCSPC. Another point is that the range of excitation range is very limited since microchip laser have to be used instead of the wide range of diode lasers.

Against to the common belief stating TCSPC a technique too slow to be used in high throughput conditions; recently we have demonstrated that it is indeed applicable under High-Throughput

conditions reaching hundreds of samples per second <sup>380</sup>. This was shown by thorough examination of the fundamental limitations in the photon acquisition rate imposed by the photon detection technique in a proof-of-principle experiment. As a fast sample handling platform we used Droplet microfluidics (D $\mu$ F), enabling sample volume from 10  $\mu$ l range per well in microplates down to 100 pl range in micro-droplets <sup>166</sup>.

In the present chapter we demonstrate a novel cost-efficient implementation of FLT detection by TCSPC in microfluidic <sup>381</sup>. We illustrate the potential of this very sensitive technology in the context of an enzymatic activity assay based on fluorescently-labeled biomolecules. It is shown to enable reliable discrimination between positive and negative control samples at a throughput as high as several hundred samples per second.

## V.2. Time Correlated Single Photon Counting

### V.2.1 Principle

TCSPC is a superior technique in sensitivity, dynamic range and data accuracy for lifetime measurements of low signals emitted by fluorescent molecules in response to synchronized light excitation pulses. Typically this technique offers picosecond accuracy and high photon efficiency that facilitate precise multiexponential decay detection. TCSPC data obeys Poisson noise statistics leading to noise that cannot be described by a constant number added to each data point of the decay curve but is equal with the square-root of the signal itself. Except of the poissonian noise the most well-documented distortion of detected signal in TCSPC is the so called pile-up effect. More precisely detectors can time-stamp at most one photon per signal cycle; since they remain disabled for a period of time after photodetection. In order to avoid the undesirable effects of pile up, the photon counting rate needs to be limited accordingly.

### V.2.1 Poisson Noise/ Shot Noise

The detection of individual photons can be considered as detection of independent events following a random temporal distribution. Thus photon counting is a classical Poisson process, where the number of measured photons is  $N$  and the average  $\langle N \rangle$  during a time interval  $t$  and can be described by a discrete probability distribution  $P$  as following:

$$P(N) = \frac{e^{-\langle N \rangle} \langle N \rangle^N}{N!}$$

The above equation corresponds to a standard Poissonian distribution corresponding to an average value of  $\langle N \rangle$  photon counts. The uncertainty defined by this distribution is known as

Poisson noise or shot noise. The concept of Poisson noise was first discussed by Walter Schottky in 1918 for fluctuations of current in vacuum tubes<sup>382</sup>.

Since the incident photon count follows a Poisson distribution, its variance will be equal with the mean value.

$$E(N) = V(N) = \langle N \rangle$$

Here E is the photon count expectation and V is the photon count variance.

The standard deviation  $\sigma_N$  and the signal-to-noise (SNR) for a single measurement would be:

$$\sigma_N = \sqrt{V(N)} = \sqrt{\langle N \rangle}$$

$$SNR = \frac{\langle N \rangle}{\sigma_N} = \frac{\langle N \rangle}{\sqrt{\langle N \rangle}} = \sqrt{\langle N \rangle}$$

Considering the above, the SNR is improved by increase of the measurement duration and thus of the measured  $\langle N \rangle$ .

## V.2.2 Pile up effect

In TCSPC experiments, each single photon detection event is followed by a dead time  $T_D$ , during which the detection system remains disabled for further detection<sup>136</sup>. The  $T_D$  is the time needed for electronic resetting and is usually much longer than the FLT that is addressed. Thus for each laser pulse only one detection event at maximum is possible.

Photon detection probability obeys the Poisson probability, which is illustrated in Figure 48. It shows (left hand side) that if 1 photon arrives on the detector in average, it means that in reality there is a 26% probability that 2 or more photons arrive simultaneously. If this is the case they would still account for 1 unique detection event (because of the long dead time), and the photon counting probability is thus distorted according to the so-called pile-up effect that we describe

below. Hence to make sure that no more than 1 photon arrives at the detector at each detection event, one should have an average photon detection probability much less than 1 per laser pulse. For instance, to reduce the probability to have 2 or more photons simultaneously to less than  $10^{-4}$ , one needs to detect no more than 0.01 photons per laser pulse in average.

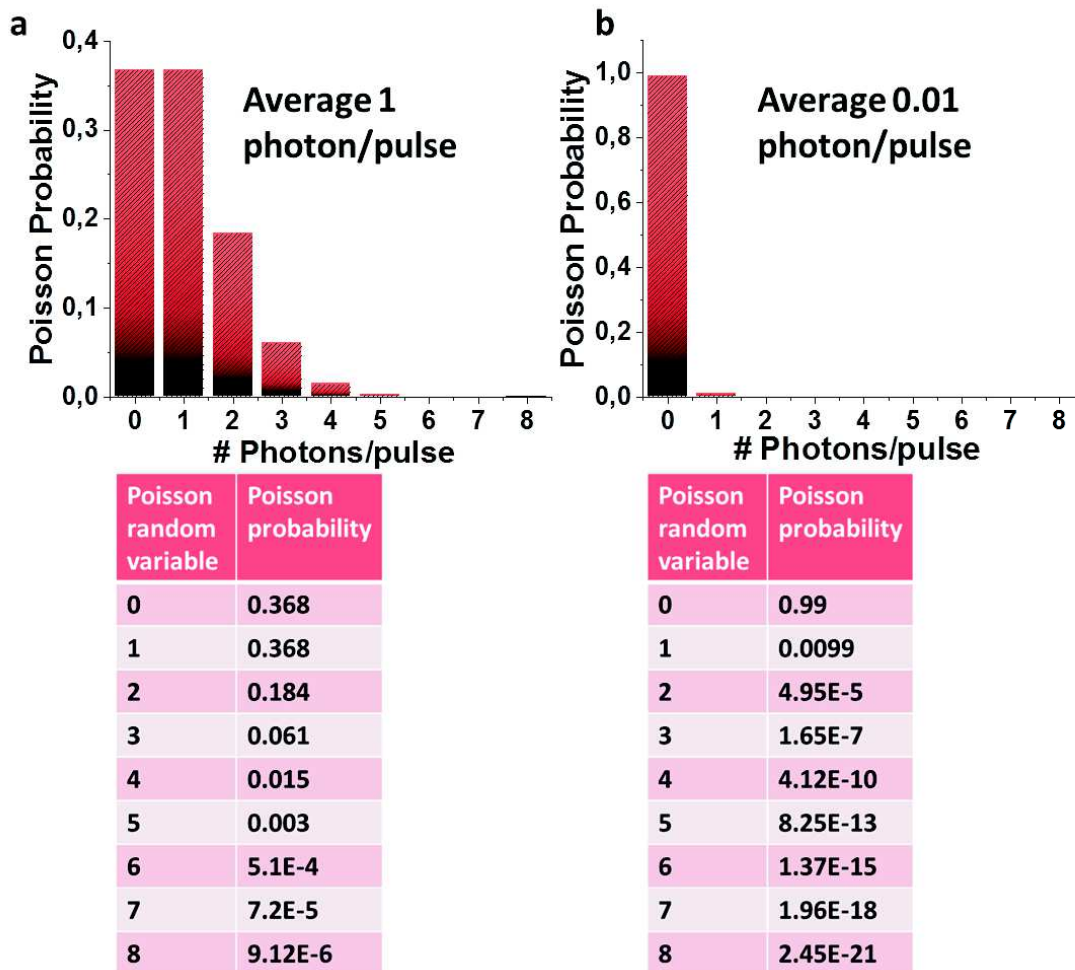


Figure 48-Calculation of Poisson probability for having a.1 or b. 0.01 photon/pulse detected.

Specifically if  $N^*$  chromophores are promoted in the singlet excited state by a single laser pulse, they will emit photons with an instantaneous emission rate as follows:  $k_r N^* f(t)$ , with  $k_r$  the chromophore radiative decay rate and  $f(t)$  the population in the excited state (see chapter II).

Here the photon collection rate will be as following:

$$k_c = \eta k_r N^*$$

Where  $\eta$  is a constant dependent on the quantum efficiency of the detector and the set up conditions (objective numerical aperture and optical filters).

In the undesirable case, where the probability of a second undetected photon reaching the detector becomes significant, we face the so called pile-up effect<sup>137,138</sup>, resulting in a distortion of the measured decay kinetics  $s(t)$  as compared to the real fluorescence decay  $f(t)$  as follows<sup>380</sup>:

$$s(t) = k_c f(t) \exp(-k_c \int_0^t f(u) du)$$

Consequently, pile up effect is taking place if the exponential term deviates from unity, for high  $k_c$ . In this case  $s(t)$  will decay faster than the real fluorescence decay curve  $f(t)$ .

In the mono-exponential case with  $f(t) = e^{-t/\tau}$  pile up appears<sup>137</sup> when  $\alpha = k_c \tau = \eta k_r N^* \tau$  reaches or exceeds unity. For small  $\alpha$  value, the detected function  $s(t)$  can be approximated by the expected monoexponential decay, and the resulting (detected) FLT  $\tau_d$  will deviate from the real FLT  $\tau$  as following (at first order in  $\alpha$ ):

$$\tau_d = \tau \left(1 - \frac{\alpha}{2}\right)$$

Practically in order to achieve accuracy better than 1% we need to maintain  $\alpha < 0.2$ <sup>380</sup>. Last when the period of the laser repetition  $1/k_L$  is bigger than the detector's dead time  $T_D$ , the average rate  $k_d$  of detected photons saturates with an increasing  $\alpha$  as follows:

$$k_d = k_L \int_0^\infty s(t) dt = k_L (1 - e^{-\alpha})$$

These considerations discuss the maximum photon counting rate  $k_c$  that one may use to measure a FLT with a given accuracy. The maximum achievable  $k_c$  is actually a fundamental limit for the application of TCSPC in high-throughput conditions, where the total sample exposure time is weak and therefore  $k_c$  should be increased to detect a significant amount of photons per sample. We will now explore whether this fundamental limitation precludes high-throughput applications.

### V.2.3 Which is the adequate amount of photons?

In a TCSPC histogram composed of  $N$  detected events, the derived lifetime  $\tau$  will statistically deviate from the real value by a standard deviation  $\sigma$ , depending on the total number of detected events  $N$ . Specifically for a monoexponential decay kinetics<sup>383</sup> the expression for  $\sigma$  has been derived as a function of  $N$  and  $b$ ,  $b$  is the bin width of the histogram. Here we use the result to introduce the coefficient of variation  $CV$  or relative standard deviation on the determination of  $\tau$ <sup>380</sup>.

$$CV = \frac{\sigma}{\tau}$$

More specifically for the appropriate bin size and time window, the minimum relative deviation on  $\tau$  is given by:

$$CV_{min} = \frac{1}{\sqrt{N}}$$

This means that in principle, for a monoexponential decay measured with the detection of  $N$  single photon events, the uncertainty of the FLT (limited by the Poissonian noise in the histogram) is fundamentally equal to the shot-noise limited uncertainty of the number  $N$  of photon, which is what is measured by FLINT. This is in contrast with the common belief (also spread in the literature, see e.g. Muretta et al.<sup>378</sup>) that FLT determination requires detecting more photons than FLINT for a given accuracy.

Here it needs to be underlined that for high-throughput applications,  $N$  should balance between the maximum desired photon detection rate and the undesirable pile up effect. In this regard, we stress that the lower  $N$  (i.e. the larger the shot-noise) uncertainty, the more tolerant we may be with the pile-up effect, which simply has to remain a weaker source of inaccuracy, than the shot-noise. Certainly for accurate FLT determinations (i.e. spectroscopy) a very large  $N$  is required (especially for multiexponential analysis) with very limited shot-noise and avoiding pile-up requires very low photon counting rates ( $\alpha < 0.1$  or  $0.01$ , depending on the ultimate targeted accuracy).

In the case of biosensing, in most cases one is interested in simply discriminating between two distinct values of the detected signal (here FLT) corresponding to positive and negative control samples.

To quantify the efficiency of a given bioassay protocol at making this discrimination, Zhang et al<sup>384</sup> have introduced a coefficient, named  $Z'$ -factor, in 1999. The  $Z'$ -factor is reflective both for assay signal dynamic range estimation and for data variation association with its signal measurements. Their criterion of  $Z' > 0.5$  expresses that the measured signal dispersion should remain significantly smaller than the difference between the signal average values for positive and negative control samples. For example if the assay targets to measure a defined fluorescence lifetime change between two values these could be named positive ( $\tau^+$ ) and negative ( $\tau^-$ ) controls, where  $\tau^+ > \tau^-$ . Assuming that the minimum CV value is obtained then the  $Z'$  would be:

$$Z' = 1 - \frac{3\sigma^+ + 3\sigma^-}{\tau^+ - \tau^-} \sim 1 - \frac{3}{\sqrt{N^+}(1 - \sqrt{r})}$$

Where  $r = \frac{\tau^-}{\tau^+}$  and  $N^+$  is the number of detected photons for the positive or negative control sample. We conclude, that even very limited number of photons per sample (i.e. no more than  $10^4$ ) should in principle be needed to achieve good  $Z'$  values (i.e.  $Z' > 0.5$ ), even in cases where the two FLT's vary by no more than 10% ( $r=0.9$ ). In a paper published in 2014 in Lab on chip<sup>380</sup>, we have demonstrated that TCSPC may be implemented in Droplet Microfluidics in such a way that shot-noise limited determination of FLT are possible in individual droplets at a rate of hundreds of droplets per second and several thousands of photons per droplets, verifying experimentally the limits on CV and the achievable values of  $Z'$ .

Below, we will review our latest experimental developments towards the implementation of TCSPC detection in Droplet Microfluidics and the proof-of-principle application to enzymatic activity assays.

## V.2.4 Experimental section

The development of a specific TCSPC acquisition system (from the pulsed laser source to the time-correlating electronics ) that is well-suited for integration in Droplet Microfluidic chips for high-throughput applications is the target of the collaboration with the group of Prof. Wilfried Urhing (ICUbe, Strasbourg), within several projects (Region Alsace, ANR PICO2 2015-19, Projet Prematuration CNRS 2016-17).

### V.2.4.1. Excitation sources for TCSPC

There is a long list of possible sources appropriate for TCSPC such as laser diodes, Ti:Sa laser, dye laser, Nd-YAG laser, chip laser, fiber laser etc.

However laser diodes are certainly the most common solution mainly because of their low cost. Other advantages are that they are easy to use, robust and durable (repairs and maintenance are rarely required)<sup>385</sup>. Moreover they are very flexible since an extensive product range with varying wavelengths, powers and designs is available, with output in the 375 - 2000 nm range and powers up to 3 W. The diodes can be operated at almost any pulse repetition rate from single shot up to values in the MHz range. They emit picosecond pulses with a full width at half maximum (FWHM) around 100 ps or below. For some laser heads even pulse widths below 40 ps are introduced (i.e. picoquant, omicron).

One special feature of laser diodes that the user should always take into account is their very small cavity, few  $\mu\text{m}$  long, resulting in light emission over a wide angle. Thus the diode emits light in a cone of elliptical cross section. Collimating the light cone with a simple lens will result in an elliptical beam with the light cone emitted slightly astigmatic, which results in differing divergences of the collimated beam in the horizontal and vertical planes. Nevertheless in most applications this does not cause any problem.

### V.2.4.2. Single Photon Avalanche Diode (SPAD)

SPADs are p-n junction reversed biased semiconductor devices. A p-n junction is an interface between two types of semiconductor material, p-type and n-type, inside a single crystal of semiconductor, where the "p" (positive) side contains an excess of holes and the "n" (negative) side contains an excess of electrons <sup>386</sup> (Figure 49). Reverse bias corresponds to connection of the p-type region to the negative terminal of the circuit and the n-type region to the positive terminal. These devices are working at a voltage higher than the breakdown voltage <sup>377</sup>. The breakdown voltage of an insulator is the minimum voltage that causes a portion of an insulator to become electrically conductive. At this bias, the electric field is so high that a single charge carrier injected in the depletion layer can trigger a self-sustaining avalanche. Thus when the primary carrier is photo-generated, the leading edge of the avalanche pulse registers the arrival time of the detected photon. The current continues to flow until the avalanche is quenched by lowering the bias voltage. In order to be able to detect the next photon, the bias voltage should be raised again above breakdown. Therefore, each time in order for a photon to be detected an avalanche process must be generated. This is the origin of the dead time introduced above.

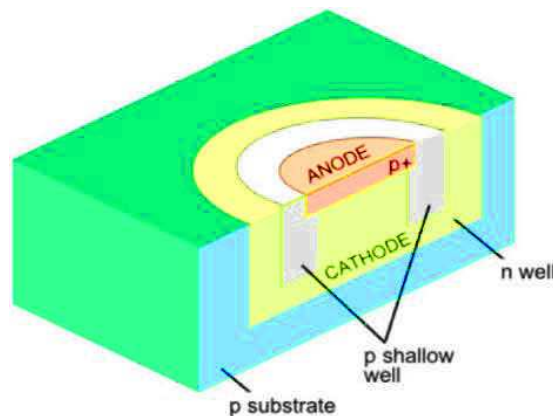


Figure 49-From<sup>387</sup>, SPAD cross section.

The parameters that we must take into consideration in order to perform a trustworthy experiment are dark counting rate (DCR) and after pulsing effect <sup>388</sup>. Even when the photodetector is kept in dark conditions, thermally generated carriers can trigger the avalanche and produce output current pulses. The average rates at which these output pulses are reproduced is named dark

counting rate (DCR) and it corresponds to the primary detector internal noise. In many applications of TCSPC, an as low DCR as possible is desired in order to extend maximally the accessible dynamic range between the “real” photon detection rate (limited by pile-up effect) and the DCR. In spectroscopic applications, a typical  $10^5$  dynamical range is accessible with a 100 kHz counting rate and a DCR=1Hz at best. For high-throughput applications, where the measurement time per sample is much less than 1 second, the need for a very low DCR is considerably reduced. We work with a (cheaper) SPAD characterized with a DCR  $\sim$  800 Hz at ambient temperature.

An additional contribution to the detector internal noise is the after pulsing effect, where carriers are trapped during the avalanche process and released randomly, with considerable delay. The after-pulse probability is a percentage of the total number of avalanche per time unit (detection rate). During the time between the quenching of the avalanche and the restoring of the bias to the operative level (commonly named dead time), the detector is insensitive to the trapped carriers. However, if the release takes place when the SPAD voltage is again above the breakdown level, the carrier can re-trigger the avalanche process leading to a false detected event. A logical conclusion would be then that the longer the dead time the smaller the probability of after-pulsing. However, a long dead time would result to a dramatic limitation of the maximum accepted counting rate. Moreover, the situation is even worse when the detector is cooled down in order to reduce the dark count rate, since the release from trapping states becomes even slower. In our high throughput application, where we achieve photon counting rates of a few MHz, a 0.1% to 1% after-pulsing probability which is typical when minimizing the dead time at maximum, would mean 1 to 10 kHz “detection” events resulting from secondary avalanches. This becomes the main limitation in the achievable dynamic range, and justifies why there is no need of a very low DCR for such applications.

The time resolution can be defined as the interval time (jitter) between the photon arrival time and the recording of the output current. The time resolution for thin, cooled SPADs can be as low as 20 ps<sup>389</sup> but the typical one is usually 50-100 ps<sup>390</sup>. A simple measurement of the overall jitter time is to record directly ps laser pulses. The acquired curve corresponds to the Instrument Response Function. The time resolution is usually considered the full-width at half maximum (FWHM) of this curve. It is typically 100 ps in our case.

### V.2.4.3. Time to Digital Converter (TDC)

#### Principle

Time-to-digital converters (TDC) are devices used to determine a time interval between two physical events and convert it into digital (binary) output. Originally the analog TDCs were based on a two-step approach translating the time interval into a voltage and this voltage into a digital value; however they were accompanied with resolution limitations<sup>391</sup>. Counter based time interval measurement and delay-line based digital TDCs were later introduced covering the need for higher time resolution.

#### Analog Time-to-Digital Converters

The traditional approach to TDC conversion is to convert the time interval into voltage. This voltage is then digitized by a conventional analog-to-digital converter (ADC). The start and stop event are used to form a pulse with width corresponding to the time interval to be measured. An analog integrator transforms this pulse into a voltage which is then fed to the ADC. Although this conversion principle is quite simple there are unfortunately several analog issues degrading the TDC performance. All building blocks, such as the pulse generator, the integrator, and the ADC have to meet the full linearity demands of the TDC principle. Moreover absolute time measurement requires the knowledge of the current and the capacitance value. For integrated TDC implementations this is not possible without calibration. This extra step that has to be done, from time domain into the analog and then to the digital domain information, complicates the procedure and introduces many delays.

#### Digital Time-to-Digital Converters

Obviously the advantages of the time domain can be better exploited if there is no analog conversion step in the time-to-digital conversion. The simplest technique used to quantize a time interval is the cycles counting of a reference clock fitting into the respective measurement

interval. The measurement interval would be defined by the start and stop signal that are completely asynchronous with respect to the reference clock signal.

The simplest version of this method was introduced by Roland Nutt <sup>392</sup> who is more known for his contribution in the development of Positron Emission Tomography. The Nutt method consists of three blocks; two fine measurement blocks and a coarse one. The role of the coarse block is to count the number  $N$  of reference clock periods between the start and stop signal. The fine blocks define the time uncertainties close to the start and stop signal as shown in Figure 50. The  $T_{FINE1}$  corresponds to the interval time between the start signal and the reference clock rising edge and respectively the  $T_{FINE2}$  between the stop signal and the next reference rising edge.

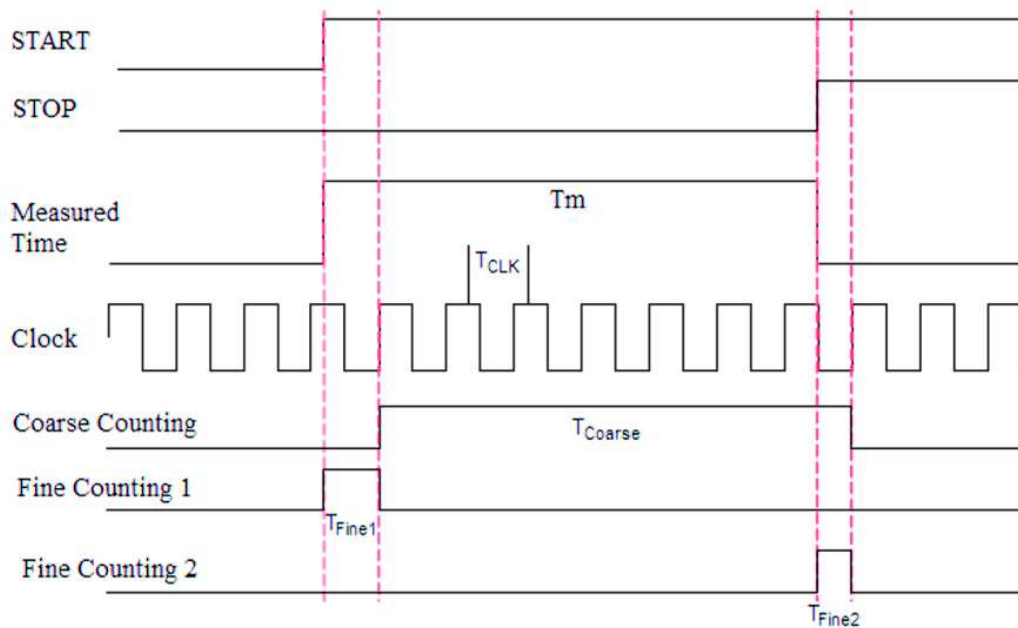


Figure 50-Operation principle of a TDC <sup>393</sup>.

Thus the measured time  $T_m$  would correspond to:

$$T_m = T_{Coarse} + T_{FINE1} - T_{FINE2}$$

$$T_{Coarse} = N * T_{clock}$$

$$T_m = N * T_{clock} + T_{FINE1} - T_{FINE2}$$

where  $T_{clock}$  is the reference clock period.

It has to be noted that the measurement accuracy can be increased by a higher clock frequency. However, the higher the clock frequency the higher will be the power consumption for the generation and the processing of the clock signal.

In our case, the start signal is synchronized with the reference clock which has 10 ns period, so the role of the  $T_{FINE1}$  is not needed. Instead of the  $T_{FINE2}$  we used the Tapped Delay Lines (TDL) architecture. A tapped delay line contains a number of cells with well-defined delay times. When the start signal arrives it starts propagating through the delay line. The state of the line is sampled at the time of the arrival of the stop signal; this is usually done by a line of flip-flop cells with a delay time. A flip-flop is a circuit that has two stable states and can store state information. The start signal propagates through this line of transparent flip-flops (transparent means that input signal changes cause immediate changes in output) and is delayed by a certain number of them. The output of each flip-flop is sampled on the fly. The stop signal latches all flip-flops while propagating through its channel un-delayed and the propagation of the start signal is terminated. Thus the time interval between start and stop signal is proportional to the number of flip-flops sampled as transparent.

In our experimental set-up the TDC function is performed by programming a commercial programmable electronic board, called FPGA.

### **V.2.1 Field Programmable Gate Array (FPGA)**

Arising applications demand ways of achieving better accuracy and higher resolution, while at the same time decreasing the size and power consumption. Developing application-specific integrated circuits (ASICs) is a time-consuming, expensive, and rigid process. Field-programmable gate arrays (FPGAs) are a cost-efficient alternative that have similar

characteristics to ASICs, meaning high performance with low power consumption, but can be custom reprogrammed unlimited times after manufacturing <sup>394</sup>. Another one of its desired properties is that it can treat high data throughput in real time and several functions can be executed in parallel <sup>395</sup>. Two main disadvantages of the FPGAs are the difficulty of hardware programming needed and the limited amount of data that can be kept in FPGA unit before reaching a processor.

The three fundamental ingredients included in the integrated circuit of an FPGA are 1. Combinational logic elements, 2. Memory elements and 3. Wiring to interconnect logic and memory elements. Any circuit consists of basic logic gates, which are combined by wiring their input and output ports together to form more complex combinational logic elements. Sequential logic consists of memory elements (such as flip-flops). It has the same characteristics as combinational logic but with memory added. This means that while the output of the combinational logic depends only on its present input, the output of sequential logic is a function of both present and past input.

The FPGAs used in the present project were programmed and provided by our collaborators in Icube. Thus the circuits and the details of the hardware programming will not be included here. However it has to be emphasized that the used FPGA triggered the laser diode in our set-up in MHz range. Moreover a time-to-digital converter was implemented in the FPGA card making possible the realization of TCSPC experiments.

## **TDC Implementation**

Electronic noise is added during the acquisition caused by fabrication defects. An ideal TDC would display the same photon counting probability per bin however in reality this is not the case since the bin width can vary slightly. In order to improve the transfer function linearity of the stop signal arriving on the TDC we introduced a post-processing correction that we name Temporal Size Bin Correction (TSBC) <sup>393</sup>, which is applicable for any kind of TDC independently of its structure and its material implementation. The TSBC requires, as

emphasized by its name, temporal size characterization of the TDC bins. This is performed by an acquisition of a uniformly distributed random uncorrelated photon events that can be generated for example from a continuous wave (cw) light source. With TSBC 1s acquisition time is enough to get a Fixed Pattern Noise (FPN) that can be used to define a scaling correction factor for each bin. Moreover due to Poisson statistics a random noise will be added on each bin. So a bin with a photon number  $N$  is affected by a random value equal with  $\sqrt{N}$  leading to a signal to noise ratio of the bin value also equal to that. So it must be taken into account that the detected FPN is well above this value. This way a better time resolution is achieved without the need of any time consuming calibration or any costly delay generator devices. The Figure below depicts an example of FPN acquired over a 40 ns range for 10 s. For an ideal TDC this acquired signal from non-correlated Poisson events should be flat.

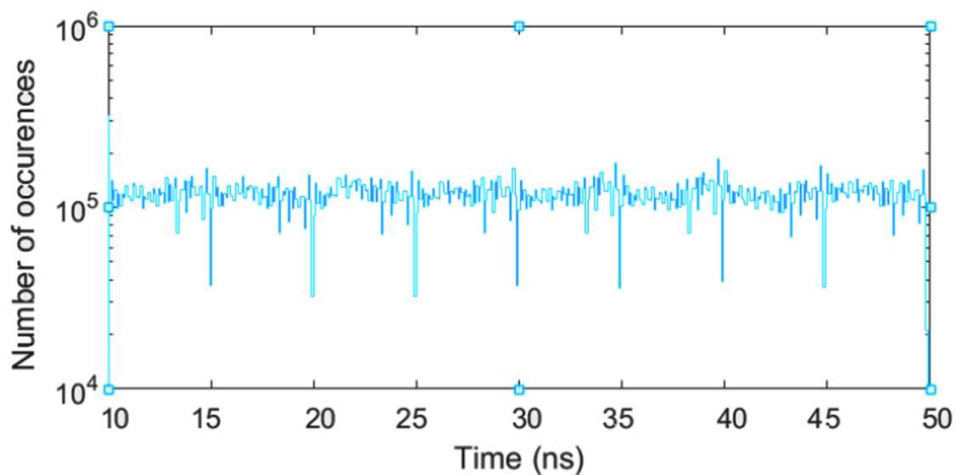


Figure 51-FPN measured over a range of 40 ns by the detection of a large number of non-correlated Poisson events generated by a SPAD illuminated with cw light.

The 5 ns periodicity observed above is caused by the fine TDC counted which is reinitiated every 5 ns when the coarse counter is incremented. It has to be underlined that these defects result from the FPGA implementation.

Figure 52 depicts an example of an acquisition conducted with fluorescein in PBS buffer with and without the TSBC correction post professional imposed on the data.

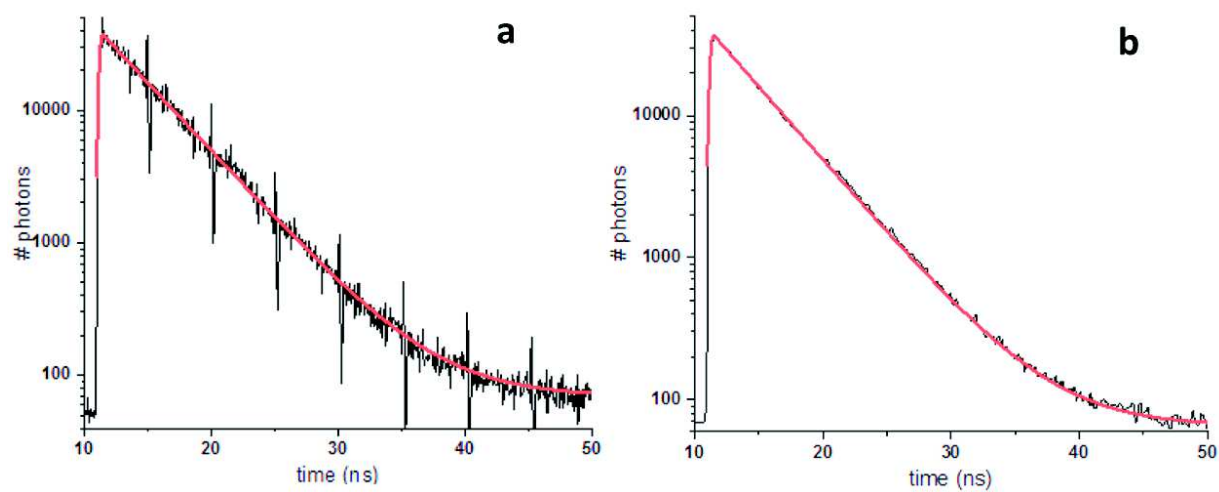


Figure 52-Fluorescence decay acquired with fluorescein in PBS (pH 7.4) solution a. before b. after TSBC correction.

## V.3. Application on a high throughput Enzymatic activity assay

This work was done in collaboration with Dr Ulrich Hassiepen from Novartis Pharma, Basel.

### Importance of enzymes in High-throughput screening

The biological processes occurring within all living organisms are mainly regulated by enzymes. Without them most of these reactions would not occur in a perceptible rate to sustain life. In 1833 the French chemist Anselme Payen did the first enzyme discovery that was named diastase<sup>396</sup>. The also French Louis Pasteur later studied the fermentation of sugar to alcohol by yeast<sup>397</sup>. In 1877 the German physiologist Wilhelm Kühne introduced the term enzyme<sup>398</sup>, which comes from the Greek word ἐνζυμο, which means “in the dough” or “leavened”.

Each enzyme interacts with only one or a group of substances, which are named substrates, to catalyze a specific reaction. In the majority of chemical reaction in the cell an energy barrier exists that needs to be overcome in order for the reaction to take place. This barrier is from the one side helpful since complex molecules such as proteins do not spontaneously degrade. On the other hand when metabolic changes are vital this existing energy barrier needs to be lowered and these complex molecules have to be broken down. This is where enzymes come into play. As shown in Figure 53, they bind to the specific substrate at a specific region of the enzyme called the active site. The active site is a groove or pocket formed by the folding pattern of the protein. Subsequently they form an intermediate complex that requires less energy for the reaction to proceed. Last this intermediate compound breaks down forming reaction products and the intact enzyme continues its travel. A typical enzyme molecule can convert 1000 substrate molecules per second.

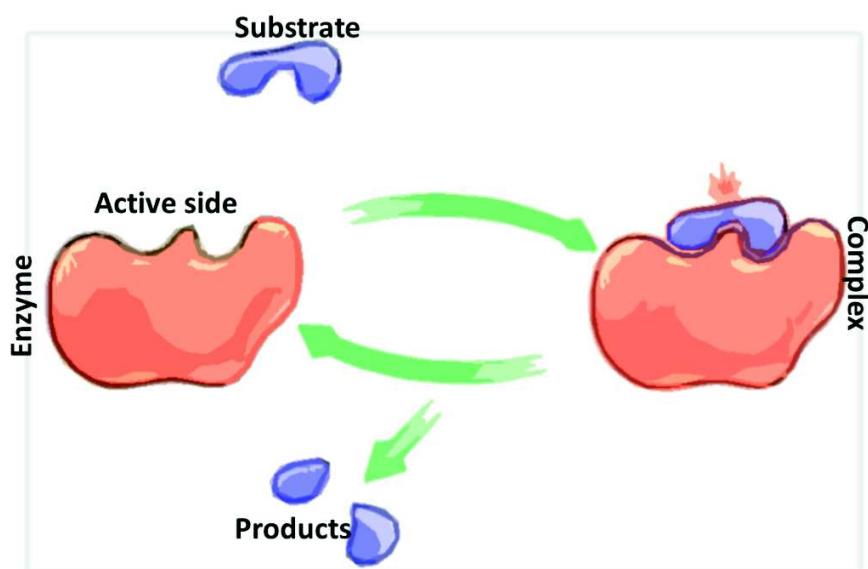


Figure 53-Schematic illustration of enzymatic function.

Competitive inhibition occurs when molecules very similar to the substrate molecules bind to the active site and prevent binding of the actual substrate. Noncompetitive inhibition occurs when an inhibitor binds to the enzyme at a location different than the active site. In some cases of noncompetitive inhibition, the inhibitor binds to the enzyme in such way to physically block the active site. Due to their high specificity enzymes are usually named after the addition of “-ase” to their substrate; for example urease for the enzyme catalyzing urea. Although there are exceptions in their naming, there are six principles categories in which they are divided.

Enzymes represent a growing market with many fields of application including drug discovery, food industry, cosmetics, fuel production, polymers and chemical industry<sup>399</sup>. They catalyze the diverse variety of bio-transformations that propel life's processes. The fermenting of wine, curdling of cheese, leavening of bread and brewing of beer have been practiced from earliest times, but it was only in the 19th century that these reactions understood to be the result of the catalytic activity of enzymes. Since then, enzymes have assumed an increasing significance in industrial processes that associate organic chemical reactions. The employment of enzymes in medicine incorporates deactivating harmful microorganisms, promoting healing, and diagnosing-healing of certain diseases. The enzyme engineering activities enrich vast enzyme libraries and therefore HTS applied for enzymes is needed for rapid, reliable and cost-efficient enzyme

collection with the desired properties. Enzymes such as kinases, proteases, phosphatases, oxidoreductases, phosphodiesterases, and transferases comprise the majority of biochemical targets in today's lead discovery efforts <sup>400</sup> as favorable targets for treating a large number of diverse diseases including cancer, HIV, and inflammatory and cardiovascular disorders <sup>401</sup>. Those assays rely on the biocatalytic conversion of a non-fluorogenic substrate to a fluorescent product and present broad potential to impact various stages of the drug discovery process, including lead identification and optimization. This way compounds that most effectively inhibit or activate the enzyme target are easily identified.

### **Trypsin**

The enzyme studied in the present project was trypsin. Trypsin is pancreatic serine protease with substrate specificity based upon positively charged lysine and arginine side chains. It is a medium-sized globular protein excreted by the pancreas, that takes part in the digestion of food proteins and other biological processes <sup>402</sup>. A few historical information about this enzyme is that it was discovered by W. Kuhne in 1877 <sup>398</sup>; he named it after the Greek word *tripsis* (rubbing). He described its proteolytic activity and discovered that the differentiating factor between trypsin and pepsin is the optimal pH. In 1931 the Nobel Prize winner JH Northrop and M. Kunitz purified trypsin by crystallization shortly after first purifying pepsin <sup>403</sup>. In 1974 the three dimensional structure was determined by RM Stroud <sup>404</sup>. Soon it was proven that a single mutation was responsible for causing pancreatitis<sup>405,406</sup> and since then it is part of the favorable targets for treating numerous diseases.

Initially some verification experiments were performed in the labs of Novartis Basel. Target was to find the desired ratio for the added enzyme in our assay. The assay was designed to evidence the activity of the protease human pancreatic trypsin on a peptidic substrate tagged with the PT14 dye (GE Healthcare), which is an acridone-based fluorophore. The laser emission wavelength was 405 nm with repetition rate of 10 MHz and the data was collected with the Tecan Ultra Evolution, I20044 microplate reader. As shown in the Figure 54 different ratios of enzyme were tried in several wells of the microplate reader for 10 circles of 3' each.

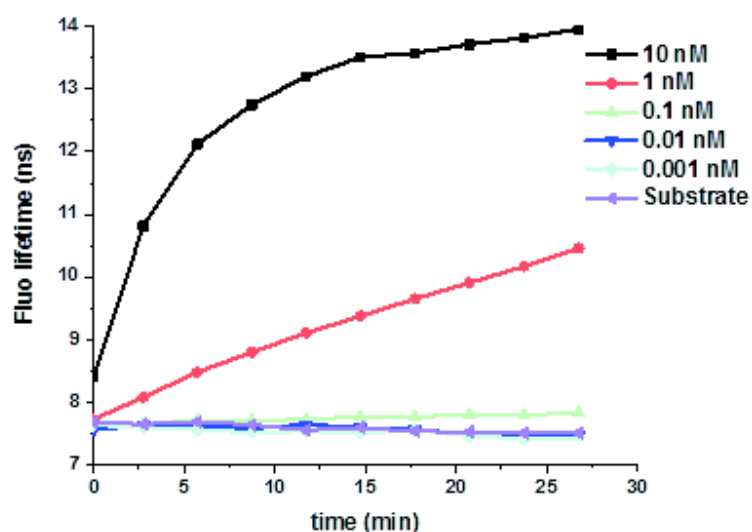


Figure 54-Kinetics of the PT14 FLT recovery upon substrate cleavage in the presence of 1-0.001 nM protease human pancreatic trypsin in 1 $\mu$ M substrate. Data recorded with a Tecan Ultra Evolution, I20044 microplate reader.

The preferred analogy here was 1 $\mu$ M substrate with 1 nM trypsin. In order to verify this we performed the following TRF experiment shown in Figure 55 with Tecan Ultra Evolution, I20044 microplate reader and with the analogy 10 $\mu$ M substrate with 1 nM trypsin, in order to get more photons.

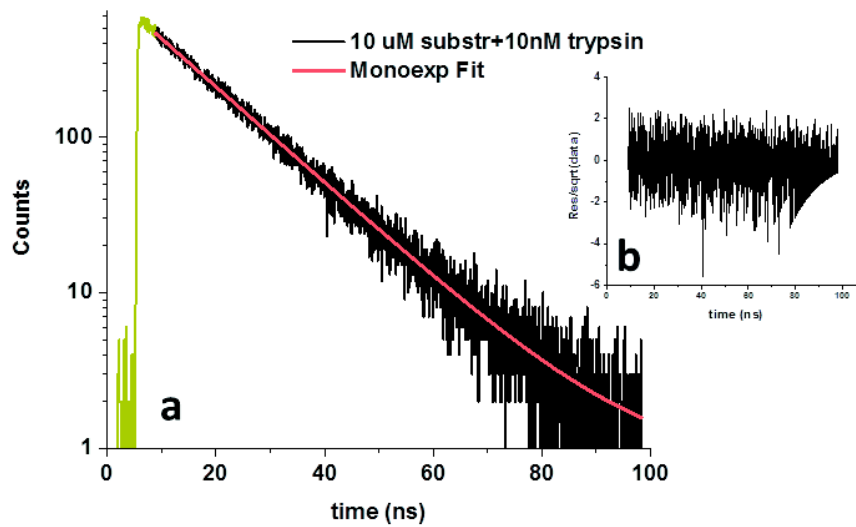


Figure 55-a. Fluorescence decay of 10 $\mu$ M substrate with 10nM trypsin added, mono-exponential fit on top. b. Plotted residuals.

After those preliminary steps in Novartis Basel we were provided the samples and continued in the IPCMS facilities. We demonstrated the feasibility of the above enzymatic activity assay in high throughput conditions by using the above technology implementing TCSPC in droplet microfluidics. All the details can be found in the attached paper published in *Methods and Applications in Fluorescence*.

## Methods and Applications in Fluorescence



PAPER

### Towards sensitive, high-throughput, biomolecular assays based on fluorescence lifetime

RECEIVED  
3 May 2017REVISED  
26 June 2017ACCEPTED FOR PUBLICATION  
12 July 2017PUBLISHED  
25 September 2017Anastasia Ioanna Skiliti<sup>1</sup>, Timothé Turko<sup>2</sup>, Damien Cianfarani<sup>1</sup>, Sophie Barre<sup>1</sup>, Wilfried Uhring<sup>2</sup>, Ulrich Hassiepen<sup>3</sup> and Jérémie Léonard<sup>1</sup><sup>1</sup> Université de Strasbourg, CNRS, Institut de Physique et Chimie des Matériaux de Strasbourg, UMR 7504, F-67000 Strasbourg, France<sup>2</sup> ICube, UMR 7357, CNRS—Université de Strasbourg, France<sup>3</sup> Novartis Institutes for Biomedical Research, Novartis Pharma AG, 4002 Basel, SwitzerlandE-mail: [Jeremie.Leonard@ipcms.unistra.fr](mailto:Jeremie.Leonard@ipcms.unistra.fr)**Keywords:** time-correlated single photon counting, biomolecular interaction assays, high-throughput screening, droplet microfluidics, time-resolved fluorescence

#### Abstract

Time-resolved fluorescence detection for robust sensing of biomolecular interactions is developed by implementing time-correlated single photon counting in high-throughput conditions. Droplet microfluidics is used as a promising platform for the very fast handling of low-volume samples. We illustrate the potential of this very sensitive and cost-effective technology in the context of an enzymatic activity assay based on fluorescently-labeled biomolecules. Fluorescence lifetime detection by time-correlated single photon counting is shown to enable reliable discrimination between positive and negative control samples at a throughput as high as several hundred samples per second.

#### 1. Introduction

Fluorescence detection is a widespread technique used in life sciences and pharmaceutical industry for e.g. wide field microscopy [1–3], flow cytometry [4, 5] cell sorting [6, 7] or high-throughput screening (HTS) [8–10]. Multiple variants of fluorescence-based detection techniques are used for sensing local physico-chemical environment properties or interactions between fluorescently-labeled biomolecules. They include fluorescence intensity (FLINT), fluorescence polarization/anisotropy (FP), single-molecule detection methods or fluorescence lifetime (FLT). Of particular interest, FLT is an intrinsic reporter of the fluorescence quantum yield of a fluorophore, and therefore of the fluorophore interactions with its microenvironment. This means in particular that parameters such as fluorophore concentration, excitation light intensity, excitation light screening or fluorescence reabsorption, which do not modify the fluorophore quantum yield, will not alter the fluorophore FLT. Instead they do alter all the other time-integrated fluorescence techniques (e.g. FLINT or FP), which makes them less reliable for the accurate sensing of fluorophore interactions. This well-known advantage of FLT detection is for instance at the origin of the

very successful development of fluorescence lifetime imaging microscopy (FLIM) [11–14].

In the context of HTS, the same argument has motivated the development of innovative biochemical constructs taking advantage of FLT detection for the efficient sensing of molecular interactions [15–24]. However, although the use of FLT for HTS was first explored more than 15 years ago [25–27], it has still not been commonly applied because implementing FLT in high-throughput conditions remains technologically more demanding than intensity-based fluorescence techniques. FLT sensing has long been applied to flow cytometry [28–30] using rapid, frequency-domain, FLT detection techniques which are applicable to high-throughput conditions. Conversely, FLT detection in the time domain by time-correlated single photon counting (TCSPC) is well-known to be the most sensitive and accurate technique also offering the best FLT time resolution [31]. TCSPC may therefore appear to be the preferred approach for FLT-based biosensing, however it requires counting and time-stamping photons one by one, with at maximum one photon detection event per excitation pulse [32]. A fluorescence decay kinetic trace is thus obtained by reconstructing the histogram of the distribution of detection times, after a large number of excitation

laser pulses. The method may thus appear relatively slow and was claimed to be inapplicable to high-throughput FLT detection [33]. Alternative time-domain FLT detection techniques have been specifically developed for HTS [33] or flow cytometry [34], but offering reduced sensitivity and time resolution compared to TCSPC. For instance, the so-called Direct Waveform Recording (DWR) technique [33] relies on the analog recording of the fluorescence decay kinetics triggered by single, nanosecond, intense laser shots at a multi-kHz repetition rate. This approach is much less sensitive in essence and its implementation more expensive than TCSPC because it requires much higher average laser power for excitation (i.e. 10 mW typically). Still, it was already very efficient at enabling FLT detection for HTS [20–23] and demonstrating the significant advantage of FLT [23, 35] (i.e. intrinsic reporter of local fluorophore interactions) over FLINT in this context.

In contrast to the initial motivations for developing e.g. DWR, however, several applications of TCSPC were recently demonstrated for accurate FLT detection under high throughput conditions [36–38]. In particular, using a microfluidic flow cytometer designed for efficient FLT detection by TCSPC at a throughput up to 3000 particles per minute, Nedbal *et al* [37] reported a comprehensive series of experiments demonstrating the superiority of FLT over FLINT for biomolecular interaction sensing in individual cells, based on the detection of Förster resonant energy transfer between ns-lived chromophores including fluorescent proteins. We instead have implemented TCSPC in microfluidic droplets and investigated the fundamental limitations imposed by the single photon detection technique on the photon acquisition rate and on the achievable signal-to-noise ratio in high throughput conditions [36]. We demonstrated that accurate discrimination between distinct FLTs (i.e. positive and negative control samples in a HTS protocol) is achievable with TCSPC at a droplet throughput exceeding 1 kHz. Droplet microfluidics (DmF) is a promising tool for biotechnologies because it lowers the volume of individual samples from  $\mu\text{l}$  range per well in microplates down to the 100 pL range or less in micro-droplets and it considerably increases the samples (droplets) manipulation rate [6, 39–42]. Consequently, DmF provides particularly challenging conditions in terms of throughput and required sensitivity, to assess the performances of TCSPC for high-throughput FLT detection.

In the present paper we review our latest developments towards demonstrating a high throughput, cost-efficient TCSPC detection technique. After describing the technical implementation, we in particular illustrate the potential of the approach by demonstrating the feasibility of an enzymatic activity assay relying on the detection of the FLT by TCSPC, in very high-throughput conditions, in microfluidic droplets. The choice of an enzymatic activity assay as a

validation for biomolecular interaction sensing was driven by the high biotechnological interest on enzymes [43–46]. Beyond, this paradigmatic assay paves the way for the application of TCSPC to high-throughput biomolecular interactions and biotechnologies in general.

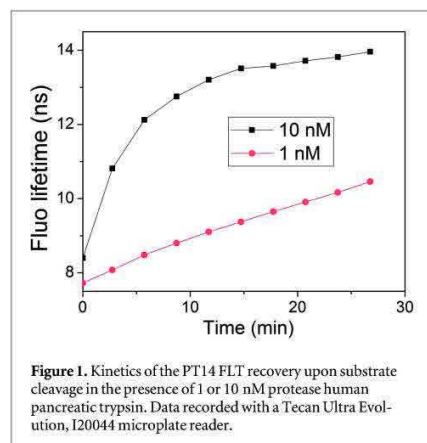
## 2. Materials and methods

### 2.1. Microfluidics

In this work water-in-oil microdroplets are used as small-volume reservoirs that contain the samples of interest and can be manipulated at very high throughput in microfluidic channels. As previously reported [36], we use the conventional ‘rapid prototyping’ technique [47] to manufacture polydimethylsiloxane microfluidic chips. A so-called T-junction is used for droplet generation: three aqueous inlets merge into one channel which intersects orthogonally a fourth channel flowed with immiscible oil (10:1 mixture of perfluorodecalin with 1H,1H,2H,2H-perfluorodecyl-trichlorosilane). The mixing of the three aqueous solutions is initiated by the droplet formation and is further accelerated by chaotic advection induced within the droplets by the wiggling shape of the channel after the T-junction [48]. The velocity, size and concentration of the droplets are precisely controlled by regulating the flow rates in the aqueous and oil channels using a commercial flow control system (Elveflow, Elveflow, France). Droplets of less than 200 pL volume and 1  $\mu\text{M}$  fluorophore or substrate concentration were used in the present work. This represents no more than 200 attomol ( $10^{-18}$  mol) of solute per droplet, i.e. per sample.

### 2.2. Enzyme activity assay

To illustrate the efficiency of the proposed FLT detection technology for HTS, we demonstrate the feasibility of an enzymatic activity assay relying on FLT detection. The assay [15, 18, 19] is designed to evidence the activity of the protease human pancreatic trypsin (from autolyzed human pancreas, Elastin Product Company, Inc., Owensville, MO, USA, catalog number TR127) on a peptide substrate tagged with the fluorescent probe PT14. Due to the structural flexibility of the peptide the probe undergoes dynamic quenching resulting in a FLT of 7 ns. When the enzyme cleaves the substrate, the probe is released, and its FLT of 14 ns is restored. Figure 1 displays the kinetics of FLT recovery after mixing 1  $\mu\text{M}$  substrate with 1 or 10 nM enzyme in PBS. In this work, the fluorescently-labeled substrate was Biosyntan 9385.1 C(PT14)-GFKY-NH<sub>2</sub>, purchased from Biosyntan (Berlin, Germany). It was, delivered as dry powder, dissolved in DMSO and kept at  $-20^\circ\text{C}$ . For all experiments it was dissolved in PBS (phosphate buffered saline, pH = 7.4) and 0.02% v/v TWEEN (polyethylene glycol sorbitan monolaurate) was



added. In the microfluidic droplets, the concentrations of substrate and enzyme were adjusted to  $1 \mu\text{M}$  and  $1 \text{ nM}$ , respectively.

### 3. Results

#### 3.1. FLT detection set-up

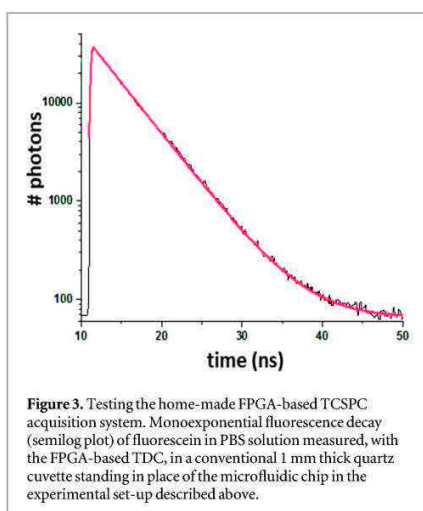
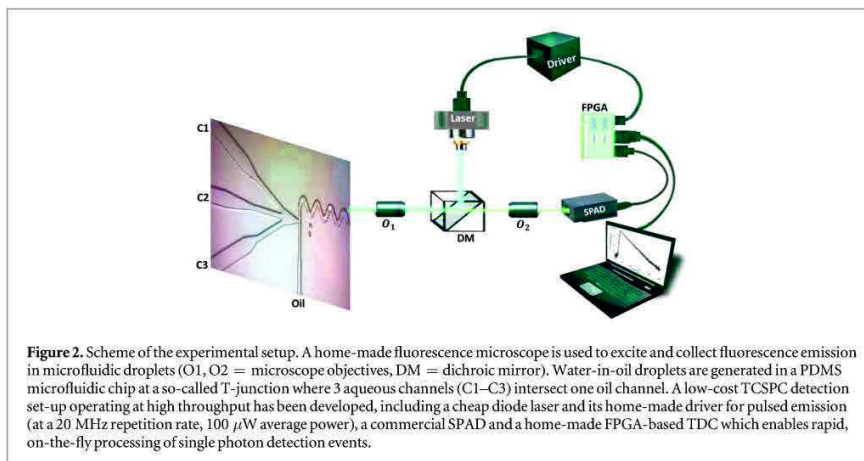
Figure 2 displays a sketch of the experimental set-up. A home-made fluorescence microscope is assembled to detect the fluorescence of water-in-oil droplets circulating in the microfluidic chip. A dichroic mirror (Semrock, BLP01-442R) is used to reflect the excitation light and transmit the fluorescence emission. A microscope objective (Nikon, x50, NA = 0.6) is used to focus the excitation beam to a  $\sim 5 \mu\text{m}$  spot inside the droplets circulating in the main microfluidic channel, and to collect and collimate the fluorescence emitted by the droplets. A second objective (Nikon, x20, NA = 0.4) is used to focus the fluorescence light on a single photon avalanche diode (SPAD, ID100, Idquantique, Switzerland). The excitation source is a diode laser (DL-4146-101S, Roithner Lasertechnik, Austria) emitting at 405 nm and operated in a pulsed mode, by a home-made, cost-effective driver consisting of a current pulse generator described previously [49]. The laser pulse repetition rate is fixed at 20 MHz with 80 ps duration FWHM. The laser average power is  $100 \mu\text{W}$ , attenuated to  $50 \mu\text{W}$  in the microfluidic experiments performed with the PT14 probe, which is however characterized by a relatively low extinction coefficient ( $\epsilon_{\text{max}} \sim 7600 \text{ M}^{-1} \text{ cm}^{-1}$  at 394 nm) [15].

According to conventional TCSPC experiments, a TDC is used to measure the time laps between each single photon detection event delivered by the SPAD and the previous laser pulse. As a TDC, we use here a Field-Programmable Gate Array (FPGA, Altera® Cyclone EP4CE55) board configured to realize the function of a TDC. The FPGA board actually generates the 20 MHz clock signal that triggers the laser diode

driver, acquires the signal delivered by the SPAD, and measures the time delay between trigger and SPAD signals as a conventional TDC. The design of this home-made, cost-effective, accurate FPGA-based TDC was described in detail elsewhere [50, 51]. It is characterized by a 42 ps time resolution, 1280 ns full scale, and 20 ns dead time. As an illustration, figure 3 displays the fluorescence decay of fluorescein dissolved to  $10 \mu\text{M}$  in PBS, acquired in a conventional spectroscopy cuvette with this FPGA-based TDC, and showing the expected monoexponential decay kinetics with a FLT of 4.2 ns.

The above FPGA-based TDC is used for TCSPC FLT detection in microfluidic droplets as illustrated in figure 2. A typical experimental run consists of circulating droplets of given size at a controlled flow rate and concentration, while detecting and time-stamping single photons continuously over seconds to minutes. Typical data are displayed in figure 4. Data processing is performed subsequently as follows. First the analysis of the instantaneous photon counting rate (computed as the number of photons detected over a  $40 \mu\text{s}$  long sliding acquisition window) allows us to detect the passage of successive droplets across the excitation laser, with a higher counting rate (i.e. above a fixed threshold) inside droplets, and lower (below threshold) in between two droplets. Second, all the time-correlated, single photon detection events corresponding to a given droplet are assembled in one histogram representing the fluorescence decay kinetics of this very droplet. At a typical MHz photon counting rate inside the droplets, fluorescence decay curves consisting of a few thousand photons in total may be collected per droplet, at a droplet circulation rate exceeding 300 per second. An automatic fitting procedure is programmed to extract the FLT of all single-droplet histograms, by performing a single parameter monoexponential fit (nonlinear least-square minimizing routine implemented with Matlab). More precisely, the fitting function is an exponential decay ( $N/\tau \times \exp(-t/\tau)$ , with  $N$  the total number of photons in the histogram, and  $\tau$  the FLT), convolved with the instrument response function, determined separately and modeled analytically by a gaussian function of 80 ps full width at half maximum. An example of such a fit is displayed in figure 4(c).

Previous investigation of the physical limitations of the photon counting technique in these very high throughput conditions allowed us to make several conclusions [36]. First, as a very general property of single photon counting, the measured FLT is accurate as long as the probability that more than one photon hitting simultaneously the SPAD remains low. If this condition is not fulfilled, the measured fluorescence decay histogram is distorted, and the FLT underestimated. This is known as the pile-up effect [52, 53]. In the present conditions, it can be shown to remain negligible [36] at photon detection rates lower than one tenth of the laser repetition rate typically, i.e.



2 MHz here. Second, due to this fundamental limitation in photon counting rate, the total number of photons detected during a typical 3 ms exposure time remains relatively small (few thousands), and consequently the photon detection noise (so-called 'shot noise') is the origin of the weak signal-to-noise ratio observed in the histograms of individual droplets (figure 4(b)). This is therefore also the dominant source of imprecision on the FLT, determined by the monoexponential fit of the noisy histograms. Third and most importantly, this shot noise limits the relative precision on the FLT value to  $1/\sqrt{N}$  at best, with  $N$  the total number of photons in the histogram [54, 55]. This is a well-known consequence of the Poissonian statistics which characterizes the shot noise inherent to single photon detection. This implies in particular that for a monoexponential decay,

measuring a FLT is in principle not less precise and does not require more photons than measuring a FLINT, since the latter is also characterized by the same  $1/\sqrt{N}$  imprecision at best. With the present experimental set-up, we have shown that the actual relative precision on the measured FLT approaches very closely the ultimate value of  $1/\sqrt{N}$ , to within a factor of 1.2–1.5 [36]. Therefore accurate discrimination between two distinct FLT's corresponding to positive and negative control samples is achievable in a screening experiment, even at a very high throughput implying the detection of a relatively limited number of photons per sample. This is what we will demonstrate below in a proof of principle experiment based on a biologically relevant, enzyme activity assay.

### 3.2. Application to the feasibility of an enzymatic activity assay

The enzyme activity assay was developed and validated previously [15, 18, 19]. It is based on the increase in the FLT of the PT14 probe which is initially quenched by collisions with the flexible tryrosine residue in the substrate. After trypsin has cleaved the substrate, the tyrosine is separated from PT14 and the probe's FLT is restored. Hence the increase of the FLT is the signature of the enzyme activity. As a test to demonstrate the feasibility of this assay by implementing TCSPC in the conditions illustrated in figures 3 and 4, we performed two successive experiments, where we measured the FLT of microdroplets circulating at a flow rate of about 300 per second. In the first one, the droplets were produced to contain the substrate solution at 1  $\mu$ M concentration (see Material and Methods), by injecting the same solution in the three aqueous inlets. In the second experiment, a solution of 1  $\mu$ M substrate and 1 nM enzyme was prepared about half an hour in advance such that the enzymatic reaction was initiated (see figure 1) before injection in the three aqueous inlets of the microfluidic chip. Hence, in these two

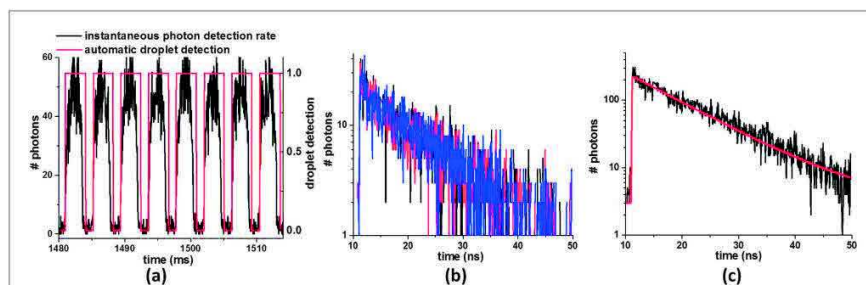


**Figure 4.** Implementation of TCSPC detection in microfluidic droplets containing  $1 \mu\text{M}$  substrate and  $1 \text{ nM}$  enzyme and illustration of the data processing. (a) Instantaneous photon detection rate as a function of time (black line). The passage of the successive droplets in the focused laser spot is automatically detected (red line). In this example, the fluorescence acquisition time is  $\sim 3 \text{ ms}$  per droplet, which is the droplet circulation time across the laser pulse. (b) Fluorescence decay histograms of three individual droplets, composed of  $\sim 2300$  photons each. (c) Sum of the histograms of ten identical, successive droplets with a mono-exponential fit (red line). This corresponds to a cumulated  $30 \text{ ms}$  fluorescence acquisition time, meaning a  $\sqrt{10}$  increase in the FLT precision in the case of a monoexponential decay (see text).

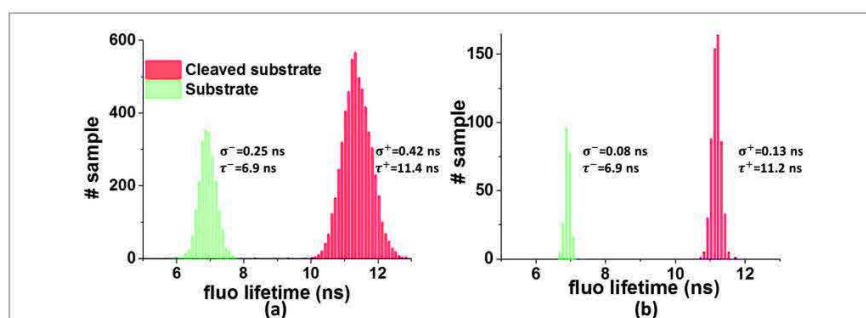


**Figure 5.** (a) Distribution of the FLT measured on individual droplets circulating at a flow rate of  $300 \text{ s}^{-1}$  across the excitation laser beam. The droplets contain  $1 \mu\text{M}$  substrate with (red) or without (green) addition of  $1 \text{ nM}$  enzyme. The CVs are 3.6% resulting in  $Z' = 0.55$  (see text). (b) Summing individual droplets histograms 10 by 10 is equivalent to a 10-fold increase of the effective droplets exposure time. Repeating the same statistical analysis on this second set of histograms containing ten times more photons on average reduces the CVs to 1.2% and yields  $Z' = 0.85$ .

experiments, each individual droplet is a new control sample to evaluate the FLT of the negative (first experiment) or positive (second experiment) control samples. Each acquisition run lasts for a few seconds only. By analyzing statistically the result of the FLT measurement in each individual droplet (sample), we quantify the precision with which the FLT of the negative and positive control samples may be determined in these very high throughput conditions, and very low sample volumes.

The fluorescence decay histograms obtained for individual droplets were composed of approximately 2300 photons and were fitted automatically as described above, with the FLT  $\tau$  as a unique fitting parameter. Figure 5(a) displays the distribution of the FLT's measured on thousands of droplets in both experiments. More precisely, the FLT of the negative control sample (first experiment) is determined to be  $\tau^- = 6.9 \text{ ns}$  with a RMS standard deviation of  $\sigma^- = 0.25 \text{ ns}$  (green distribution), while that of the positive control (second experiment) is  $\tau^+ = 11.4 \text{ ns}$

with  $\sigma^+ = 0.42 \text{ ns}$  (red distribution). The corresponding coefficients of variations (CVs) are thus no more than  $\sim 3.6\%$  in both cases. The feasibility of the enzymatic assay in these very high throughput conditions may be quantified by the so-called  $Z'$  factor [56]. In the present case of an assay based on a FLT measurement it writes:  $Z' = 1 - \frac{3\sigma^- + 3\sigma^+}{\tau^+ - \tau^-}$ , with the notations introduced above. With as little as  $3 \text{ ms}$  exposure time per sample we already achieve  $Z' = 0.55$ , which exceeds 0.5 and therefore demonstrates the feasibility of the assay in these conditions.

Finally, we note that since the precision on the FLT determination is limited by Poissonian photon shot noise [36], a 10 fold increase in the sample exposure time should improve by  $\sqrt{10}$  the CVs. This is easily confirmed by summing the histograms of ten successive droplets (all droplets are identical in a given experiment), before performing the automatic fit of the resulting histograms. The results are displayed in figure 5(b) and confirm that the CVs decrease to 1.2%

as expected. By this analysis, we show that extending the exposure time to 30 ms, i.e. reducing the throughput to 1800 samples per minute which is still very high, the assay can be performed with a  $Z'$  factor as large as  $Z' = 0.85$ .

#### 4. Discussion and conclusion

In assessing the performances of TCSPC for high-throughput FLT detection, it is important to remember that in a TCSPC experiment the precision achieved on the measured FLT theoretically scales as  $1/\sqrt{N}$ , where  $N$  is the total number of photons in the entire histogram (rather than the number of photons in the dominant bin). More precisely [54], it is in principle enough to detect  $10^4$  photons to achieve a relative precision (i.e. coefficient of variation, CV) of 1% on the FLT of a monoexponential decaying fluorescent probe. As in our previous work [36], the above results confirm that in a realistic, simple experimental implementation (home-made microscope), a CV value of 1.2% (see figure 5(b)) can easily be achieved by collecting about  $2 \times 10^4$  photons per histogram (as in figure 4(c)) in a cumulated 30 ms exposure time. This corresponds to an 800 kHz photon counting rate, which is low enough, in the present experiment performed with a 20 MHz laser repetition rate, to prevent any significant pile-up effect that would affect the accuracy of the determined FLT [36].

When comparing the performances of the DWR and TCSPC techniques for high throughput FLT detection, we note that DWR does not perform better in terms of acquisition speed, since 50 ms are required to achieve  $CV = 1.64\%$  when measuring the 4 ns FLT of Rhodamine 6G with the DWR technique [22]. Importantly, while the limitation on the FLT precision and its physical origin are well characterized in the case of TCSPC (due to Poissonian photon shot noise, therefore implying the  $1/\sqrt{N}$  scaling law), it is not the case for DWR, where the analog nature of the acquisition scheme introduces additional, electronic sources of noise. Their influence on the FLT precision is not straightforwardly characterized.

In terms of detection sensitivity, the single photon detection technique is certainly unparalleled. It enables detection of much lower sample volumes and molecule quantities, ultimately down to the single molecule level. In the present conditions, we emphasize that, the excitation laser average power is as low as 50  $\mu$ W despite the use of a not very bright PT14 chromophore. This certainly contributes making the TCSPC approach very cost-effective. What is more, considering that the sample volumes are as low as 200 pL, the results above demonstrate that the enzymatic activity assay is feasible with substrate (respectively enzyme) quantities as low as  $\sim 200$  attomol (respectively 0.2 attomol) per sample, and at a throughput as high as 300 samples per second. This

underlines the extreme sensitivity of TCSPC for FLT determination, even at very high throughput conditions.

Importantly, we stress that a major interest of using droplet microfluidics for the present demonstration is to realize very challenging conditions to assess the performances of TCSPC for very sensitive and accurate FLT sensing at very high throughput. Certainly the FLT detection technology proposed here and the conclusions of this work would be directly transposable to microplate readers which realize much less challenging conditions in terms of throughput and required sensitivity. Conversely, the present demonstration calls for the implementation of droplet sorting based on FLT detection in DmF chips. This would require on-the-fly processing of single photon detection events in order to (i) detect automatically the passage of successive droplets and (ii) determine the FLT in real-time. To the best of our knowledge, no available commercial TDC allows such real-time data processing which requires hardware programming to achieve the desired processing rates [38, 57].

In conclusion, the technical implications of the present work are twofold. First it demonstrates that FLT detection is achievable with good precision in very small volume samples and chromophore quantities at high detection throughput. This paves the way to replacing FLINT by FLT detection for microfluidic applications, including e.g. fluorescence-assisted droplet or cell sorting [6, 58]. Second it offers a FLT detection which is orders of magnitude more sensitive than DWR and equally (if not more efficiently) applicable to high-throughput acquisition and HTS in particular, also in conventional microplate readers.

Future development of the TCSPC technique towards improved sensitivity, better FLT precision or shorter exposure times will rely on the ability to increase the maximum photon counting rate. The later is presently limited to the few-MHz range, due to limitations in the SPAD's electrical operation which imposes a typical 40–50 ns dead time. However, present CMOS technology enables integrating in a single microelectronic chip multiple, independent channels for time-correlated, single-photon detection in order to parallelize the acquisition of the fluorescence emission of a given sample, so as to enhance significantly the effective photon counting rate [59, 60]. We are exploring the implementation of this technology for the present application.

#### Acknowledgments

This work is supported by the Région Alsace via the Contrat doctoral No. 493-14-C22, the Institut Carnot MICA via the "TR-Fluofluidics" project, and the French Agence Nationale de la Recherche via the ANR-15-CE11-0006 'PICO<sup>2</sup>' project. The above funders had no role in study design, data collection and

analysis, decision to publish, or preparation of the manuscript. The authors have declared that no conflicting interests exist.

## References

- [1] Wollman R and Stuurman N 2007 High throughput microscopy: from raw images to discoveries *J. Cell Sci.* **120** 3715–22
- [2] Pepperkok R and Ellenberg J 2006 High-throughput fluorescence microscopy for systems biology *Nat. Rev. Mol. Cell Biol.* **7** 690–96
- [3] Huang B, Bates M and Zhuang X 2009 Super-resolution fluorescence microscopy *Annu. Rev. Biochem.* **78** 993–1016
- [4] Nebe-von-Caron G, Stephens P, Hewitt C, Powell J and Badley R 2000 Analysis of bacterial function by multi-colour fluorescence flow cytometry and single cell sorting *Microb. Anal. Single Cell Level* **42** 97–114
- [5] Krutzyk P O and Nolan G P 2006 Fluorescent cell barcoding in flow cytometry allows high-throughput drug screening and signaling profiling *Nat. Methods* **3** 361–68
- [6] Mazutis L, Gilbert J, Ung W L, Weitz D A, Griffiths A D and Heyman J A 2013 Single-cell analysis and sorting using droplet-based microfluidics *Nat. Protocols* **8** 870–91
- [7] Ren L et al 2015 A high-throughput acoustic cell sorter *Lab Chip* **15** 3870–79
- [8] Pope A J, Haupts U M and Moore K J 1999 Homogeneous fluorescence readouts for miniaturized high-throughput screening: theory and practice *Drug Discovery Today* **4** 350–62
- [9] Popp D, Haeupl C and Doering K 2002 Nanosecond fluorescence lifetime analysis—a new dimension for detection in microplates *SBS 8th Ann. Conf. and Exhibition (The Hague, Netherlands)*
- [10] Gribbon P and Sewing A 2003 Fluorescence readouts in HTS: no gain without pain? *Drug Discovery Today* **8** 1035–43
- [11] Borst J W and Visser A J W G 2010 Fluorescence lifetime imaging microscopy in life sciences *Meas. Sci. Technol.* **21** 102002
- [12] Wallrabe H and Periasamy A 2005 Imaging protein molecules using FRET and FLIM microscopy *Anal. Biotechnol.* **16** 19–27
- [13] Levitt J A, Matthews D R, Ameer-Beg S M and Suhling K 2009 Fluorescence lifetime and polarization-resolved imaging in cell biology *Anal. Biotechnol.* **20** 28–36
- [14] Gerritsen H, Asselbergs M, Agronskaia A and Van Sark W 2002 Fluorescence lifetime imaging in scanning microscopes: acquisition speed, photon economy and lifetime resolution *J. Microsc.* **206** 218–24
- [15] Pritz S et al 2011 A fluorescence lifetime-based assay for abelson kinase *J. Biomol. Screen.* **16** 65–72
- [16] Pritz S, Doering K, Woelcke J and Hassiepen U 2011 Fluorescence lifetime assays: current advances and applications in drug discovery *Expert Opin. Drug Discovery* **6** 663–70
- [17] Lebakken C S, Hee C K and Vogel K W 2007 A fluorescence lifetime based binding assay to characterize kinase inhibitors *J. Biomol. Screen.* **12** 828–41
- [18] Doering K, Meder G, Hinnenberger M, Woelcke J, Mayr L M and Hassiepen U 2008 A fluorescence lifetime-based assay for protease inhibitor profiling on human kallikrein 7 *J. Biomol. Screen.* **14** 1–9
- [19] Boettcher A et al 2014 Fluorescence lifetime-based competitive binding assays for measuring the binding potency of protease inhibitors *in vitro J. Biomol. Screen.* **19** 870–77
- [20] Schaaf T M et al 2016 High-throughput spectral and lifetime-based FRET screening in living cells to identify small-molecule effectors of SERCA *J. Biomol. Screen.* **22** 262–73
- [21] Rebbeck R T et al 2016 High-throughput screens to discover small-molecule modulators of ryanodine receptor calcium release channels *J. Biomol. Screen.* **22** 176–86
- [22] Petersen K J, Peterson K C, Muretta J M, Higgins S E, Gillispie G D and Thomas D D 2014 Fluorescence lifetime plate reader: resolution and precision meet high-throughput *Rev. Sci. Instrum.* **85** 113101
- [23] Gruber S J et al 2014 Discovery of enzyme modulators via high-throughput time-resolved FRET in living cells *J. Biomol. Screen.* **19** 215–22
- [24] Margineanu A et al 2016 Screening for protein–protein interactions using Förster resonance energy transfer (FRET) and fluorescence lifetime imaging microscopy (FLIM) *Sci. Rep.* **6** 28186
- [25] Swift K M and Matayoshi E D 1995 High throughput screening using dynamic fluorescence *Proc. SPIE* **2388**, *Advances in Fluorescence Sensing Technology II* p 182
- [26] French P 2008 Fluorescence lifetime imaging for drug discovery and disease research. SPIE Newsroom (Accessed: 20 Dec 2016) <http://spie.org/x25793.xml>
- [27] French T E, Bailey B, Stumbo D P and Modlin D N 1999 Time-resolved fluorometer for high-throughput screening *Proc. SPIE* **3603**, *Systems and Technologies for Clinical Diagnostics and Drug Discovery II* p 272
- [28] Pinsky B G, Ladasky J J, Lakowicz J R, Berndt K and Hoffman R A 1993 Phase-resolved fluorescence lifetime measurements for flow cytometry *Cytometry A* **14** 123–35
- [29] Steinkamp J A and Crissman H A 1993 Resolution of fluorescence signals from cells labeled with fluorochromes having different lifetimes by phase-sensitive flow cytometry *Cytometry A* **14** 210–6
- [30] Houston J P, Naivar M A and Freyer J P 2010 Digital analysis and sorting of fluorescence lifetime by flow cytometry *Cytometry A* **77** 861–72
- [31] Boens N et al 2007 Fluorescence lifetime standards for time and frequency domain fluorescence spectroscopy *Anal. Chem.* **79** 2137–49
- [32] Becker W 2005 *Advanced Time-Correlated Single Photon Counting Techniques (Springer Series in Chemical Physics vol 81)* (Heidelberg: Springer)
- [33] Muretta J M, Kyrychenko A, Ladokhin A S, Kast D J, Gillispie G D and Thomas D D 2010 High-performance time-resolved fluorescence by direct waveform recording *Rev. Sci. Instrum.* **81** 103101
- [34] Li W, Vacca G, Castillo M, Houston K D and Houston J P 2014 Fluorescence lifetime excitation cytometry by kinetic dithering *Electrophoresis* **35** 1846–54
- [35] Cornea R L et al 2013 High-throughput FRET assay yields allosteric SERCA activators *J. Biomol. Screen.* **18** 97–107
- [36] Léonard J et al 2014 High-throughput time-correlated single photon counting *Lab Chip* **14** 4338–43
- [37] Nedbal J et al 2015 Time-domain microfluidic fluorescence lifetime flow cytometry for high-throughput Förster resonance energy transfer screening *Cytometry A* **87** 104–18
- [38] Della Rocca F M et al 2016 Real-time fluorescence lifetime actuation for cell sorting using a CMOS SPAD silicon photomultiplier *Opt. Lett.* **41** 673–76
- [39] deMello A J 2006 Control and detection of chemical reactions in microfluidic systems *Nature* **442** 394–402
- [40] Guo M T, Rotem A, Heyman J A and Weitz D A 2012 Droplet microfluidics for high-throughput biological assays *Lab Chip* **12** 2146
- [41] Miller O J et al 2012 High-resolution dose–response screening using droplet-based microfluidics *Proc. Natl Acad. Sci.* **109** 378–83
- [42] Choi J-W, Kang D-K, Park H, deMello A J and Chang S-I 2012 High-throughput analysis of protein–protein interactions in picoliter-volume droplets using fluorescence polarization *Anal. Chem.* **84** 3849–54
- [43] Cohen P 2002 Protein kinases—the major drug targets of the twenty-first century? *Nat. Rev. Drug Discovery* **1** 309–15
- [44] Turk B 2006 Targeting proteases: successes, failures and future prospects *Nat. Rev. Drug Discovery* **5** 785–99
- [45] Drag M and Salvesen G S 2010 Emerging principles in protease-based drug discovery *Nat. Rev. Drug Discovery* **9** 690–701
- [46] Jacques P et al 2017 High-throughput strategies for the discovery and engineering of enzymes for biocatalysis *Bioprocess Biosyst. Eng.* **40** 161–80

- [47] Duffy D C, McDonald J C, Schueller O J A and Whitesides G M 1998 Rapid prototyping of microfluidic systems in poly (dimethylsiloxane) *Anal. Chem.* **70** 4974–84
- [48] Song H, Tice J D and Ismagilov R F 2003 A microfluidic system for controlling reaction networks in time *Angew. Chem.* **115** 792–6
- [49] Uhring W, Zint C-V and Bartringer J 2004 A low-cost high-repetition-rate picosecond laser diode pulse generator *Proc. SPIE 5452, Semiconductor Lasers and Laser Dynamics* p 583
- [50] Dadouche F, Turko T, Uhring W, Malass I, Dumas N and Le Normand J-P 2015 New design-methodology of high-performance TDC on a low cost FPGA targets *Sensors Transducers* **193** 123–34
- [51] Dadouche F, Turko T, Malass I, Skiltisi A I, Léonard J and Uhring W 2016 Design, implementation and characterization of time to digital converter on low cost FPGA *Sensors and Applications in Measuring and Automation Control Systems (Advances in Sensors: Reviews vol 4)* ed S Yurish (Barcelona: International Frequency Sensor Association (IFSA)) pp 205–29
- [52] Coates P B 1968 The correction for photon pile-up in the measurement of radiative lifetimes *J. Phys. E: Sci. Instrum.* **1** 878
- [53] Holzapfel C 1974 On statistics of time-to-amplitude converter systems in photon counting devices *Rev. Sci. Instrum.* **45** 894–96
- [54] Hall P and Selinger B 1981 Better estimates of exponential decay parameters *J. Phys. Chem.* **85** 2941–46
- [55] Köllner M and Wolfrum J 1992 How many photons are necessary for fluorescence-lifetime measurements? *Chem. Phys. Lett.* **200** 199–204
- [56] Zhang J-H, Chung T D Y and Oldenburg K R 1999 A simple statistical parameter for use in evaluation and validation of high throughput screening assays *J. Biomol. Screen.* **4** 67
- [57] Lieske T, Uhring W, Dumas N, Léonard J and Fey D 2017 Embedded fluorescence lifetime determination for high throughput real-time droplet sorting with microfluidics *Conf. on Design and Architectures for Signal and Image Processing (DASIP) (Dresden, Germany)*
- [58] Baret J-C et al 2009 Fluorescence-activated droplet sorting (FADS): efficient microfluidic cell sorting based on enzymatic activity *Lab Chip* **9** 1850
- [59] Charbon E 2014 Single-photon imaging in complementary metal oxide semiconductor processes *Phil. Trans. R. Soc. Math. Phys. Eng. Sci.* **372** 20130100
- [60] Krstajić N et al 2015 05 billion events per second time correlated single photon counting using CMOS SPAD arrays *Opt. Lett.* **40** 4305

## V.4. Discussion and Conclusions

In this project it is demonstrated that FLT detection is indeed feasible in small volume samples with good precision and accuracy in high throughput conditions. This very sensitive and cost-effective technology is illustrated in the context of a biomolecular interaction assay based on fluorescently-labeled biomolecules. Fluorescence lifetime detection by TCSPC is shown to enable reliable discrimination between positive and negative control samples at a throughput as high as several hundred samples per second. Therefore FLT detection is capable of replacing FLINT and all other detection techniques that are being used up-to-date in HTS experiments. Since it overcomes the technical obstacles that lead it to be thought as a complicated technique, it rises above all the rest providing precision, cost efficiency and high speed.

## VI. Publications

### 1. Chapter in a book<sup>381</sup>

Title of chapter: Design, Implementation and Characterization of Time-to-Digital Converter on Low-Cost FPGA

Title of book: Sensors and Applications in Measuring and Automation Control Systems

Collection: Advances in sensors, Volume: 4, pages 205-229, Editor: Ed. Sergey Y. Yurish

Dadouche F., Turko Timothe, Malass Imane, Skilitsi Anastasia Ioanna, Léonard Jeremie, Uhring Wilfried

### 2. Conference publication<sup>393</sup>

Conference: SIGNAL, International Conference on Advances in Signal, Image and Video Processing

Year: 2016, Pages: 50-53

“Time to Digital Converter Transfer Function Improvement using Poisson Process Events”

Timothé Turko, Anastasia Skilitsi, Wilfried Uhring, Jean-Pierre Le Normand, Norbert Dumas, Foudil Dadouche, Jérémie Léonard

### 3. Conference publication<sup>407</sup>

Conference: International Conference on Ultrafast Phenomena

Editor: Optical Society of America, Year: 2016, Pages: UW4A–31

Ultrafast, Solvation-Controlled Excited-State Intramolecular Proton Transfer in 4'-Methoxy-3-Hydroxyflavone

Anastasia Ioanna Skilitsi, Damianos Agathangelou, Andrey Klymchenko, Yves Mély, Stefan Haacke, Jérémie Léonard

4. Journal publication<sup>408</sup>

Journal: Methods and Applications of Fluorescence, **2017**, 5 (3), 34002.

“Towards Sensitive, High-Throughput, Biomolecular Assays Based on Fluorescence Lifetime”

Anastasia Ioanna Skilitsi, Timothé Turko, Damien Cianfarani, Sophie Barre, Wilfried Uhring, Ulrich Hassiepen, Jérémie Léonard

5. In preparation

4'-methoxy-3-hydroxyflavone-Unique Fluorescent dye for protein structure sensing

Anastasia Ioanna Skilitsi, Damianos Agathangelou, Andrey Klymchenko, Yves Mély, Jérémie Léonard

6. In preparation

Cyan Fluorescent protein and its H148G variant-Correlation of proteins structure with their fluorescent properties

Anastasia Ioanna Skilitsi, Hélène Pasquier, Vincent Kemlin, Jérémie Léonard

**Conference Contributions:**

**Posters**

1. Congrès General de la Société Française de Physique (SFP), 24-28 August 2015, Strasbourg France

“Ultrafast Intramolecular proton transfer as probe for biomolecular structures”

Anastasia Ioanna Skilitsi, Damianos Agathangelou, Andrey Klymchenko, Yves Mély, Stefan Haacke, Jérémie Léonard

2. Conference on Methods and Applications in Fluorescence (MAF-14), 13-16 September 2015, Würzburg Germany

“Ultrafast Excited-State Intramolecular Proton Transfer in Hydroxycromone-based Structural Probes”

Anastasia Ioanna Skilitsi, Damianos Agathangelou, Jamie Conyard, Andrey Klymchenko, Yves Mély, Stefan Haacke, Jérémie Léonard

3. NovAliX Conference Biophysics in Drug Discovery, 7-10 June 2016, Strasbourg France

“High-throughput time-correlated single photon counting in microfluidic droplets for enzymatic activity assays”

Anastasia Ioanna Skilitsi, Timothe Turko, Wilfried Uhring, Jeremie Leonard

4. BioChem Forum, 2-3 June 2016, Strasbourg France

“Novel application of High-throughput time-correlated single photon counting in microfluidic droplets for enzymatic activity assays”, Anastasia Ioanna Skilitsi, Timothe Turko, Wilfried Uhring, Jeremie Leonard. **Best Poster award**

5. International Conference on Ultrafast Phenomena OSA The Optical Society, 17 - 22 July 2016, Santa Fe, New Mexico, USA,

“Ultrafast, Solvation-Controlled Excited-State Intramolecular Proton Transfer in 3-Hydroxy-Flavone”

Anastasia Ioanna Skilitsi, Damianos Agathangelou, Andrey Klymchenko, Yves Mély, Stefan Haacke, Jérémie Léonard

6. Fluorofest Conference, 24-26 April 2017, Glasgow, Scotland

“Tracking fluorescence lifetime changes in pH-jump experiments with the Cyan Fluorescent Protein CFP”

Anastasia Ioanna Skilitsi, Hélène Pasquier, Jérémie Léonard

7. 28th International Conference on Photochemistry, 16-21 July 2017, Strasbourg France

“Tracking fluorescence lifetime changes in pH-jump experiments with the Cyan Fluorescent Protein CFP and its H148G Variant”

Anastasia Ioanna Skilitsi, Hélène Pasquier, Jérémie Léonard

8. Conference on Methods and Applications in Fluorescence (MAF-15), 10-13 September 2017, Bruges Belgium

“Cyan Fluorescent protein and its H148G variant-Correlation of proteins structure with their fluorescent properties”

Anastasia Ioanna Skilitsi, Hélène Pasquier, Vincent Kemlin, Jérémie Léonard

### **Oral Seminar**

9. Workshop of the Department of Non-linear Optics and Nanophotonics of IPCMS (June 28 2017), La Petite Fosse, France

“Cyan Fluorescent protein and its H148G variant-Correlation of proteins structure with their fluorescent properties”

## VII. Final Conclusions and Perspectives

A plethora of methods, static or time resolved, were utilized in order to gain detailed information of micro-environmentally sensitive fluorescent probes assigned for biomolecular interaction studies. Each approach was selected carefully in order to address the response of fluorescent probes to different physicochemical properties of their microenvironment, such as difference in hydrogen bonding for the 3-Hydroxyflavone derivative, difference in pH for the CFP and its mutant and last difference in presence or absence of quenchers for the enzymatic assay. All the above research can be used as an inaugural point for numerous further applications.

In the first axis of experiments, concerning the 4M3HF probe, the aim was a fundamental investigation of its photoreactivity in different solvents varying polarity and H-bonding capabilities. Different approaches were used in order to address different characteristics of this probe. Specifically pump-probe measurements were utilized for the ultrafast kinetics and TRF for the slower kinetics. Also quantum yield and steady state absorption measurements were carried out. Our goal was then to rationalize the effect of the micro-environment on the photophysics of this promising probe. We successfully obtained a detailed understanding of the influence of the environment on the fluorophore photophysics which can be used as a prerequisite to the structural interpretation of the fluorescence properties of 4M3HF-labeled biomolecules. The future target here is to use the studied 3-Hydroxychromone derivative in order to label DNA or proteins and study their interactions or structural changes by observing the changes in the fluorophore photophysics of the label.

In the second axis, the target was to reach the first successful application of the original experimental approach combining TRF and Droplet Microfluidics for biomolecular interactions studies. This target was accomplished with ECFP and its mutant. Here it was identified the time scale needed from the dominating longest-lived fluorescence component to evolve upon sudden acidification. This piece of information highlights a slow configuration change taking place at the ground state and being triggered by pH change. This accomplishment lays the foundations for further research of interactions within out-of-equilibrium biomolecular complexes. The objective of a series of future experiments will be to use this innovative experimental approach to investigate the molecular mechanism of the chaperone activity (i.e. promoting DNA structural

rearrangements) of the NCp7 protein of the human immunodeficiency virus (HIV). Focus will be set on NCp7-promoting annealing of complementary DNA strands, in reactions involved in two essential steps of the virus life cycle. Various fluorescence labeling strategies of the different DNA strands on the one hand and of the NCp7 on the other hand will be explored (including possibly the use of synthetic amino acid recently developed based on the 4M3HF compound investigated in Chapter III) in order to reveal a mechanistic description of the protein – DNA interactions. This research target is among those of the PICO2 ANR Project, in collaboration with Prof .Yves Mély, (Pharmacy faculty, Université de Strasbourg). Generally the present set up including droplet microfluidics, can be used for the study of out of equilibrium systems that are slower than the mixing time (few ms) and faster than a few seconds to minutes. Furthermore the samples must be water soluble, since we create water droplets in oil and we want to prevent contamination or inhomogeneous droplet formation. Under these conditions the spectrum of possible biomolecular interaction experiments that can be studied is very broad.

In the third axis, with the more applied research achievement of the last project, we have been exploring the implementation of TRF by TCSPC in very high throughput conditions as a mean to perform efficient biomolecular interactions/activity assays. The numerous advantages of this approach, which are the high precision, the remarkable low material consumption and most remarkably the high speed of the measurements, reaching kHz sample (droplet) rate, make it appealing both for academic and industrial arenas. Next step is to enable real-time processing and analysis in order to allow on-the-fly TCSPC for high throughput bioassays. Furthermore parallelizing the single photon detection with a line of detectors able to detect and time-stamp photons simultaneously will allow a higher photon counting rate and thus even faster and more precise acquisitions. This technology can also be easily integrated to microplate readers used commonly in drug discovery, bioassay validation, quality control and manufacturing processes in the pharmaceutical and biotechnological industries and academic organizations. This technological application is patented and is being supported both by the PICO2 ANR project in collaboration with Dr. Wilfried Uhring (Icube) and by the pre-maturation CNRS project.

In conclusion, the perspectives offered by the present PhD work are about merging the different experimental approaches developed in the three, apparently distinct, topics investigated here (Chapter III to V). Indeed it is planned to use the studied 3-Hydroxychromone derivative (Chapter III) as a label for proteins structure and measured in out-of-equilibrium reaction

experiments combining TRF and Droplet Microfluidics in the same line as explained in Chapter IV. Furthermore, the team of Prof. Yves Mély is involved in a large research project aiming NCp7 inhibitors screening based on biochemical constructs that would rely on detecting the fluorescent changes in fluorescently labeled DNA strands using innovative fluorophores based on 4M3HF and others. The experimental development described in Chapter IV is to be explored for this application which can benefit largely from the use of TRF detection in such interaction assays. This target is also to be explored within the PICO2 project. Finally, regarding the enzymatic activity assays (Chapter V), there is strong interest in assaying the kinetics of enzymatic activities, which requires preparing out-of-equilibrium conditions by fast mixing. It is not obvious yet whether droplet microfluidics would surpass conventional microplate readers for this kind of high-throughput application. However, certainly the ability to perform very high-throughput TRF detection for high-throughput screening is a very appealing technological target (developed in collaboration with Dr Wilfried Urhing) for such an application.

## VIII. Bibliography

1. Trojanowski, J. Q. & LEE, V. M.-Y. 'Fatal attractions' of proteins: a comprehensive hypothetical mechanism underlying Alzheimer's disease and other neurodegenerative disorders. *Ann. N. Y. Acad. Sci.* **924**, 62–67 (2000).
2. Sanguansri, P. & Augustin, M. A. Nanoscale materials development – a food industry perspective. *Trends Food Sci. Technol.* **17**, 547–556 (2006).
3. Palmer, A. G. NMR Characterization of the Dynamics of Biomacromolecules. *Chem. Rev.* **104**, 3623–3640 (2004).
4. Zuiderweg, E. R. P. Mapping Protein–Protein Interactions in Solution by NMR Spectroscopy †. *Biochemistry (Mosc.)* **41**, 1–7 (2002).
5. Markwick, P. R. L., Malliavin, T. & Nilges, M. Structural Biology by NMR: Structure, Dynamics, and Interactions. *PLoS Comput. Biol.* **4**, e1000168 (2008).
6. Stocks, B. B. & Konermann, L. Time-Dependent Changes in Side-Chain Solvent Accessibility during Cytochrome c Folding Probed by Pulsed Oxidative Labeling and Mass Spectrometry. *J. Mol. Biol.* **398**, 362–373 (2010).
7. Stolz, M., Stoffler, D., Aebi, U. & Goldsbury, C. Monitoring Biomolecular Interactions by Time-Lapse Atomic Force Microscopy. *J. Struct. Biol.* **131**, 171–180 (2000).
8. Willemsen, O. H. *et al.* Biomolecular interactions measured by atomic force microscopy. *Biophys. J.* **79**, 3267–3281 (2000).
9. Guo, H., Peng, H. & Emili, A. Mass spectrometry methods to study protein-metabolite interactions. *Expert Opin. Drug Discov.* 1–10 (2017). doi:10.1080/17460441.2017.1378178

10. Haustein, E. & Schwille, P. Single-molecule spectroscopic methods. *Curr. Opin. Struct. Biol.* **14**, 531–540 (2004).
11. Xie, Z., Srividya, N., Sosnick, T. R., Pan, T. & Scherer, N. F. Single-molecule studies highlight conformational heterogeneity in the early folding steps of a large ribozyme. *Proc. Natl. Acad. Sci. U. S. A.* **101**, 534–539 (2004).
12. Hovius, R., Vallotton, P., Wohland, T. & Vogel, H. Fluorescence techniques: shedding light on ligand-receptor interactions. *Trends Pharmacol. Sci.* **21**, 266–273 (2000).
13. Weiss, S. Fluorescence Spectroscopy of Single Biomolecules. *Science* **283**, 1676–1683 (1999).
14. Al-Hashimi, H. M. & Walter, N. G. RNA dynamics: it is about time. *Curr. Opin. Struct. Biol.* **18**, 321–329 (2008).
15. Henzler-Wildman, K. & Kern, D. Dynamic personalities of proteins. *Nature* **450**, 964–972 (2007).
16. Sengupta, P. K. & Kasha, M. Excited state proton-transfer spectroscopy of 3-hydroxyflavone and quercetin. *Chem. Phys. Lett.* **68**, 382–385 (1979).
17. Formosinho, S. J. & Arnaut, L. G. Excited-state proton transfer reactions II. Intramolecular reactions. *J. Photochem. Photobiol. Chem.* **75**, 21–48 (1993).
18. Zhao, J., Ji, S., Chen, Y., Guo, H. & Yang, P. Excited state intramolecular proton transfer (ESIPT): from principal photophysics to the development of new chromophores and applications in fluorescent molecular probes and luminescent materials. *Phys Chem Chem Phys* **14**, 8803–8817 (2012).
19. Sholokh, M. *et al.* Fluorescent Amino Acid Undergoing Excited State Intramolecular Proton Transfer for Site-Specific Probing and Imaging of Peptide Interactions. *J. Phys. Chem. B* **119**, 2585–2595 (2015).
20. Lakowicz, J. R. *Principles of fluorescence spectroscopy*. (Springer, 2006).
21. Albani, J. R. *Principles and Applications of Fluorescence Spectroscopy*. (Wiley-Blackwell, 2008).
22. Hamilton, J. *Internal Conversion Processes*. (Academic Press, 1966).

23. Guilbault, G. *Practical Fluorescence*. (CRC Press, 1990).
24. Pringsheim, P. *Fluorescence and Phosphorescence*. (Interscience Publishers, 1963).
25. Galley, W. C. & Purkey, R. M. Role of heterogeneity of the solvation site in electronic spectra in solution. *Proc. Natl. Acad. Sci.* **67**, 1116–1121 (1970).
26. Rubinov, A. & Tomin, V. Bathochromic luminescence in solutions of organic dyes at low temperatures. *Opt Spectros USSR* **29**, 578–580 (1970).
27. Nigam, S. & Rutan, S. Principles and applications of solvatochromism. *Focal Point* **55**, 362–370 (2001).
28. Wu, Y. G., Tabata, M. & Takamuku, T. Preferential Solvation in Aqueous–Organic Mixed Solvents Using Solvatochromic Indicators. *J. Solut. Chem.* **31**, 381–395 (2002).
29. Dawber, J. G., Ward, J. & Williams, R. A. A study in preferential solvation using a solvatochromic pyridinium betaine and its relationship with reaction rates in mixed solvents. *J. Chem. Soc. Faraday Trans. 1 Phys. Chem. Condens. Phases* **84**, 713–727 (1988).
30. Paley, M. S., McGill, R. A., Howard, S. C., Wallace, S. E. & Harris, J. M. Solvatochromism: A new method for polymer characterization. *Macromolecules* **23**, 4557–4564 (1990).
31. Pietsch, C., Schubert, U. S. & Hoogenboom, R. Aqueous polymeric sensors based on temperature-induced polymer phase transitions and solvatochromic dyes. *Chem. Commun.* **47**, 8750 (2011).
32. Adams, D. J., Dyson, P. J. & Tavener, S. J. *Chemistry in alternative reaction media*. (John Wiley & Sons, 2005).
33. Reichardt, C. Polarity of ionic liquids determined empirically by means of solvatochromic pyridinium N-phenolate betaine dyes. *Green Chem.* **7**, 339 (2005).
34. Anastas, P. T. & Zimmerman, J. B. *Peer reviewed: design through the 12 principles of green engineering*. (ACS Publications, 2003).

35. Selvin, P. R. The renaissance of fluorescence resonance energy transfer. *Nat. Struct. Mol. Biol.* **7**, 730 (2000).
36. Stryer, L. & Haugland, R. Energy Transfer: A spectroscopic ruler. *Proc. Natl. Acad. Sci.* **58**, 719–726 (1967).
37. Forster, T. 10th Spiers Memorial Lecture. Transfer mechanisms of electronic excitation. *Discuss. Faraday Soc.* **27**, 7–17 (1959).
38. Valeur, B. *Molecular Fluorescence: Principles and Applications*. (Wiley-VCH, 2001).
39. Clegg, R. M. The history of FRET. in *Reviews in Fluorescence 2006* 1–45 (Springer, 2006).
40. Rajan, R. S., Illing, M. E., Bence, N. F. & Kopito, R. R. Specificity in intracellular protein aggregation and inclusion body formation. *Proc. Natl. Acad. Sci.* **98**, 13060–13065 (2001).
41. Desai, U. A. *et al.* Biologically active molecules that reduce polyglutamine aggregation and toxicity. *Hum. Mol. Genet.* **15**, 2114–2124 (2006).
42. Truong, K. & Ikura, M. The use of FRET imaging microscopy to detect protein–protein interactions and protein conformational changes in vivo. *Curr. Opin. Struct. Biol.* **11**, 573–578 (2001).
43. Shih, W. M., Gryczynski, Z., Lakowicz, J. R. & Spudich, J. A. A FRET-based sensor reveals large ATP hydrolysis–induced conformational changes and three distinct states of the molecular motor myosin. *Cell* **102**, 683–694 (2000).
44. Wouters, F. S., Bastiaens, P. I., Wirtz, K. W. & Jovin, T. M. FRET microscopy demonstrates molecular association of non-specific lipid transfer protein (nsL-TP) with fatty acid oxidation enzymes in peroxisomes. *EMBO J.* **17**, 7179–7189 (1998).
45. König, P. *et al.* FRET-CLSM and double-labeling indirect immunofluorescence to detect close association of proteins in tissue sections. *Lab. Invest.* **86**, 853 (2006).
46. Yuan, L., Lin, W., Zheng, K. & Zhu, S. FRET-Based Small-Molecule Fluorescent Probes: Rational Design and Bioimaging Applications. *Acc. Chem. Res.* **46**, 1462–1473 (2013).

47. Chou, P. T., Martinez, M. L. & Clements, J. H. Reversal of excitation behavior of proton-transfer vs. charge-transfer by dielectric perturbation of electronic manifolds. *J. Phys. Chem.* **97**, 2618–2622 (1993).
48. Sytnik, A., Gormin, D. & Kasha, M. Interplay between excited-state intramolecular proton transfer and charge transfer in flavonols and their use as protein-binding-site fluorescence probes. *Proc. Natl. Acad. Sci.* **91**, 11968–11972 (1994).
49. Swinney, T. C. & Kelley, D. F. Proton transfer dynamics in substituted 3-hydroxyflavones: Solvent polarization effects. *J. Chem. Phys.* **99**, 211–221 (1993).
50. Mordzinski, A. & Kuehnle, W. Kinetics of excited-state proton transfer in double benzoxazoles: 2, 5-bis (2-benzoxazolyl)-4-methoxyphenol. *J. Phys. Chem.* **90**, 1455–1458 (1986).
51. Douhal, A., Amat-Guerri, F., Lillo, M. P. & Acuna, A. U. Proton transfer spectroscopy of 2-(2'-hydroxyphenyl) imidazole and 2-(2'-hydroxyphenyl) benzimidazole dyes. *J. Photochem. Photobiol. Chem.* **78**, 127–138 (1994).
52. Sytnik, A. & Kasha, M. Excited-state intramolecular proton transfer as a fluorescence probe for protein binding-site static polarity. *Proc. Natl. Acad. Sci.* **91**, 8627–8630 (1994).
53. Sytnik, A., Gormin, D. & Kasha, M. Interplay between excited-state intramolecular proton transfer and charge transfer in flavonols and their use as protein-binding-site fluorescence probes. *Proc. Natl. Acad. Sci.* **91**, 11968–11972 (1994).
54. Cheng, Y.-M., Pu, S.-C., Hsu, C.-J., Lai, C.-H. & Chou, P.-T. Femtosecond Dynamics on 2-(2'-Hydroxy-4'-diethylaminophenyl)benzothiazole: Solvent Polarity in the Excited-State Proton Transfer. *ChemPhysChem* **7**, 1372–1381 (2006).
55. Klymchenko, A. S. *et al.* Novel two-band ratiometric fluorescence probes with different location and orientation in phospholipid membranes. *Chem. Biol.* **9**, 1199–1208 (2002).

56. Nemkovich, N. A., Baumann, W. & Pivovarenko, V. G. Dipole moments of 4'-aminoflavonols determined using electro-optical absorption measurements or molecular Stark-effect spectroscopy. *J. Photochem. Photobiol. Chem.* **153**, 19–24 (2002).
57. Klymchenko, A. S. & Mely, Y. Fluorescent Environment-Sensitive Dyes as Reporters of Biomolecular Interactions. in *Progress in Molecular Biology and Translational Science* **113**, 35–58 (Elsevier, 2013).
58. Klymchenko, A. S. Solvatochromic and Fluorogenic Dyes as Environment-Sensitive Probes: Design and Biological Applications. *Acc. Chem. Res.* **50**, 366–375 (2017).
59. Bissell, R. *et al.* Fluorescent PET (Photoinduced Electron Transfer) Sensors. *Top. Curr. Chem.* **168**, 1–42 (1993).
60. Bender, C. J. Theoretical models of charge-transfer complexes. *Chem. Soc. Rev.* **15**, 475–502 (1986).
61. Kavarnos, G. J. & Turro, N. J. Photosensitization by reversible electron transfer: theories, experimental evidence, and examples. *Chem. Rev.* **86**, 401–449 (1986).
62. Wasielewski, M. R. Photoinduced electron transfer in supramolecular systems for artificial photosynthesis. *Chem. Rev.* **92**, 435–461 (1992).
63. Kelley, S. & Barton, J. Electron Transfer Between Bases in Double Helical DNA. *Science* **283**, 375–381 (1999).
64. Kenmoku, S. *et al.* Rational design of novel photoinduced electron transfer type fluorescent probes for sodium cation. *Tetrahedron* **60**, 11067–11073 (2004).
65. Núñez, M. E., Hall, D. B. & Barton, J. K. Long-range oxidative damage to DNA: effects of distance and sequence. *Chem. Biol.* **6**, 85–97 (1999).
66. Schuster, G. B. Long-Range Charge Transfer in DNA: Transient Structural Distortions Control the Distance Dependence. *Acc. Chem. Res.* **33**, 253–260 (2000).
67. Giese, B. Long-Distance Charge Transport in DNA: The Hopping Mechanism. *Acc. Chem. Res.* **33**, 631–636 (2000).

68. Giese, B. Electron transfer in DNA. *Curr. Opin. Chem. Biol.* **6**, 612–618 (2002).
69. Jose, D., Datta, K., Johnson, N. P. & von Hippel, P. H. Spectroscopic studies of position-specific DNA ‘breathing’ fluctuations at replication forks and primer-template junctions. *Proc. Natl. Acad. Sci.* **106**, 4231–4236 (2009).
70. Jiao, Y., Stringfellow, S. & Yu, H. Distinguishing ‘Looped-Out’ and ‘Stacked-In’ DNA Bulge Conformation Using Fluorescent 2-Aminopurine Replacing a Purine Base. *J. Biomol. Struct. Dyn.* **19**, 929–934 (2002).
71. Rachofsky, E. L., Osman, R. & Ross, J. B. A. Probing Structure and Dynamics of DNA with 2-Aminopurine: Effects of Local Environment on Fluorescence<sup>†</sup>. *Biochemistry (Mosc.)* **40**, 946–956 (2001).
72. Guest, C. R., Hochstrasser, R. A., Sowers, L. C. & Millar, D. P. Dynamics of mismatched base pairs in DNA. *Biochemistry (Mosc.)* **30**, 3271–3279 (1991).
73. Avilov, S. V., Piemont, E., Shvadchak, V., de Rocquigny, H. & Mely, Y. Probing dynamics of HIV-1 nucleocapsid protein/target hexanucleotide complexes by 2-aminopurine. *Nucleic Acids Res.* **36**, 885–896 (2007).
74. Gelot, T., Tourón-Touceda, P., Crégut, O., Léonard, J. & Haacke, S. Ultrafast Site-Specific Fluorescence Quenching of 2-Aminopurine in a DNA Hairpin Studied by Femtosecond Down-Conversion. *J. Phys. Chem. A* **116**, 2819–2825 (2012).
75. Godet, J. *et al.* Specific implications of the HIV-1 nucleocapsid zinc fingers in the annealing of the primer binding site complementary sequences during the obligatory plus strand transfer. *Nucleic Acids Res.* **39**, 6633–6645 (2011).
76. Manoj, P., Min, C.-K., Aravindakumar, C. T. & Joo, T. Ultrafast charge transfer dynamics in 2-aminopurine modified double helical DNA. *Chem. Phys.* **352**, 333–338 (2008).

77. Nordlund, T. M. *et al.* Structure and dynamics of a fluorescent DNA oligomer containing the EcoRI recognition sequence: fluorescence, molecular dynamics, and NMR studies. *Biochemistry (Mosc.)* **28**, 9095–9103 (1989).
78. Jean, J. M. & Hall, K. B. 2-Aminopurine fluorescence quenching and lifetimes: role of base stacking. *Proc. Natl. Acad. Sci.* **98**, 37–41 (2001).
79. Liang, J. & Matsika, S. Pathways for Fluorescence Quenching in 2-Aminopurine  $\pi$ -Stacked with Pyrimidine Nucleobases. *J. Am. Chem. Soc.* **133**, 6799–6808 (2011).
80. Voltz, K. *et al.* Quantitative sampling of conformational heterogeneity of a DNA hairpin using molecular dynamics simulations and ultrafast fluorescence spectroscopy. *Nucleic Acids Res.* **44**, 3408–3419 (2016).
81. Zhang, X.-X. *et al.* pH-Sensitive Fluorescent Dyes: Are They Really pH-Sensitive in Cells? *Mol. Pharm.* **10**, 1910–1917 (2013).
82. Yu, K.-K. *et al.* A single design strategy for dual sensitive pH probe with a suitable range to map pH in living cells. *Sci. Rep.* **5**, (2015).
83. Lee, M. H. *et al.* Two-Color Probe to Monitor a Wide Range of pH Values in Cells. *Angew. Chem. Int. Ed.* **52**, 6206–6209 (2013).
84. Shi, W., Li, X. & Ma, H. A Tunable Ratiometric pH Sensor Based on Carbon Nanodots for the Quantitative Measurement of the Intracellular pH of Whole Cells. *Angew. Chem.* **124**, 6538–6541 (2012).
85. Wu, S., Li, Z., Han, J. & Han, S. Dual colored mesoporous silica nanoparticles with pH activable rhodamine-lactam for ratiometric sensing of lysosomal acidity. *Chem. Commun.* **47**, 11276 (2011).
86. Yang, H. *et al.* Hg<sup>2+</sup>-selective fluorescent chemosensor based on cation- $\pi$  interaction. *Chem. Res. Chin. Univ.* **30**, 910–914 (2014).

87. Rink, T. J., Tsien, R. Y. & Pozzan, T. Cytoplasmic pH and free Mg<sup>2+</sup> in lymphocytes. *J. Cell Biol.* **95**, 189–196 (1982).
88. Izumi, H. *et al.* Cellular pH regulators: potentially promising molecular targets for cancer chemotherapy. *Cancer Treat. Rev.* **29**, 541–549 (2003).
89. Davies, T. *et al.* Non-age related differences in thrombin responses by platelets from male patients with advanced Alzheimer's disease. *Biochem. Biophys. Res. Commun.* **194**, 537–543 (1993).
90. Cooper, M. E., Gregory, S., Adie, E. & Kalinka, S. pH-sensitive cyanine dyes for biological applications. *J. Fluoresc.* **12**, 425–429 (2002).
91. Andersson, R. M., Carlsson, K., Liljeborg, A. & Brismar, H. Characterization of Probe Binding and Comparison of Its Influence on Fluorescence Lifetime of Two pH-Sensitive Benzo[c]xanthene Dyes Using Intensity-Modulated Multiple-Wavelength Scanning Technique. *Anal. Biochem.* **283**, 104–110 (2000).
92. Han, J. & Burgess, K. Fluorescent Indicators for Intracellular pH. *Chem. Rev.* **110**, 2709–2728 (2010).
93. Rotkiewicz, K., Grellmann, K. . & Grabowski, Z. . Reinterpretation of the anomalous fluorescence of p-n,n-dimethylamino-benzonitrile. *Chem. Phys. Lett.* **19**, 315–318 (1973).
94. Grabowski, Z. ., Rotkiewicz, K., Siemiarczuk, A., Cowley, D. . & Baumann, W. Twisted intramolecular charge transfer states (TICT). A new class of excited states with a full charge separation. *Nouv.J.Chim* **3**, 443–454 (1979).
95. Grabowski, Z. . & Dobkowski, J. Twisted intramolecular charge transfer (TICT) excited states: energy and molecular structure. *Pure Appli Chem* 245–252 (1983).
96. Park, M., Kim, C. H. & Joo, T. Multifaceted Ultrafast Intramolecular Charge Transfer Dynamics of 4-(Dimethylamino)benzonitrile (DMABN). *J. Phys. Chem. A* **117**, 370–377 (2013).
97. Lippert, E. von. Spektroskopische Bestimmung des Dipolmomentes aromatischer Verbindungen im ersten angeregten Singulettzustand. *Berichte Bunsenges. Für Phys. Chem.* **61**, 962–975 (1957).

98. Rettig, W. Photoinduced Electron Transfer in twisted pi-systems. in *Dynamics and Mechanisms of Photoinduced Electron Transfer and Related Phenomena* 57–70 (Elsevier, 1992).
99. Haidekker, M. A. & Theodorakis, E. A. Molecular rotors—fluorescent biosensors for viscosity and flow. *Org Biomol Chem* **5**, 1669–1678 (2007).
100. Michl, J. & Sykes, E. C. H. Molecular Rotors and Motors: Recent Advances and Future Challenges. *ACS Nano* **3**, 1042–1048 (2009).
101. Kottas, G. S., Clarke, L. I., Horinek, D. & Michl, J. Artificial Molecular Rotors. *Chem. Rev.* **105**, 1281–1376 (2005).
102. Seintis, K. *et al.* Femtosecond to nanosecond studies of octupolar molecules and their quadrupolar and dipolar analogues. *Phys Chem Chem Phys* **19**, 16485–16497 (2017).
103. Rettig, W. Intramolecular Rotational Relaxation of Compounds Which Form ‘Twisted Intramolecular Charge Transfer’ (TICT) Excited States. *J. Phys. Chem.* **86**, 1970–1976 (1982).
104. Sasaki, S., Drummen, G. P. C. & Konishi, G. Recent advances in twisted intramolecular charge transfer (TICT) fluorescence and related phenomena in materials chemistry. *J Mater Chem C* **4**, 2731–2743 (2016).
105. Haberhauer, G. Planarized and Twisted Intramolecular Charge Transfer: A Concept for Fluorophores Showing Two Independent Rotations in Excited State. *Chem. - Eur. J.* **23**, 9288–9296 (2017).
106. Goh, W. L. *et al.* Molecular Rotors As Conditionally Fluorescent Labels for Rapid Detection of Biomolecular Interactions. *J. Am. Chem. Soc.* **136**, 6159–6162 (2014).
107. Ghosh, R., Kushwaha, A. & Das, D. Conformational Control of Ultrafast Molecular Rotor Property: Tuning Viscosity Sensing Efficiency by Twist Angle Variation. *J. Phys. Chem. B* (2017).  
doi:10.1021/acs.jpcc.7b05947

108. Sherin, P. S. *et al.* Visualising the membrane viscosity of porcine eye lens cells using molecular rotors. *Chem Sci* **8**, 3523–3528 (2017).
109. Haidekker, M. A. *et al.* Phospholipid-bound molecular rotors: synthesis and characterization. *Bioorg. Med. Chem.* **10**, 3627–3636 (2002).
110. Kuimova, M. K., Yahioglu, G., Levitt, J. A. & Suhling, K. Molecular Rotor Measures Viscosity of Live Cells via Fluorescence Lifetime Imaging. *J. Am. Chem. Soc.* **130**, 6672–6673 (2008).
111. Kim, H. M. *et al.* Two-Photon Fluorescent Turn-On Probe for Lipid Rafts in Live Cell and Tissue. *J. Am. Chem. Soc.* **130**, 4246–4247 (2008).
112. Mori, T. *et al.* Molecular rotors confined at an ordered 2D interface. *Phys Chem Chem Phys* (2017). doi:10.1039/C7CP04256F
113. Kelly, T. R. *et al.* A molecular brake. *J. Am. Chem. Soc.* **116**, 3657–3658 (1994).
114. Kelly, T. R., Tellitu, I. & Sestelo, J. P. In search of molecular ratchets. *Angew. Chem. Int. Ed.* **36**, 1866–1868 (1997).
115. Kelly, T. R., De Silva, H. & Silva, R. A. Unidirectional rotary motion in a molecular system. *Nature* **401**, 150 (1999).
116. Kelly, T. R., Silva, R. A., Silva, H. D., Jasmin, S. & Zhao, Y. A Rationally Designed Prototype of a Molecular Motor. *J. Am. Chem. Soc.* **122**, 6935–6949 (2000).
117. Stokes, G. G. On the Change of Refrangibility of Light. *Phil Trans R Soc Lond* **142**, 463–562 (1852).
118. Weljie, A. . & Vogel, H. . Steady State Fluorescence Spectroscopy. in *Calcium-Binding Protein Protocols: Methods and Techniques* **2**, 75–87 (Vogel H.J., 2002).
119. Bose, S. *Use of Steady-state and Time-resolved Fluorescence Spectroscopy as a Tool to Investigate Photophysics of Biologically and Environmentally Relevant Systems.* (Iowa State University, 2010).

120. Courtney-Pratt, J. A new method for the photographic study of fast transient phenomena. *Res. J. Sci. Its Appl.* **2**, 287–94 (1949).
121. Courtney-Pratt, J. A new photographic method for studying fast transient phenomena. *Proc. R. Soc.* **204**, 27 (1950).
122. Zavoiskii, E. . & Fanchenko, S. . Studies of very fast light processes. *Dokl Akad Nauk SSSR* **100**, 661 (1955).
123. Zavoiskii, E. . & Fanchenko, S. . Physical fundamentals of electron-optical chronography. *Sov Phys Dokl* **1**, 285 (1956).
124. Malyutin, A. & Shchelev, M. Investigation of the Temporal Structure of Neodymium-laser Emission in the Mode Self-locking Regime. *J. Exp. Theor. Phys. Lett.* **9**, 266 (1969).
125. Bradley, D. J., Liddy, B. & Sleat, W. E. Direct linear measurement of ultrashort light pulses with a picosecond streak camera. *Opt. Commun.* **2**, 391–395 (1971).
126. Schelev, M. Y., Richardson, M. C. & Alcock, A. J. Image-converter streak camera with picosecond resolution. *Appl. Phys. Lett.* **18**, 354–357 (1971).
127. Butslov, M. ., Demidov, B. ., Fanchenko, S. ., Frolov, V. . & Chikin, R. . Observation of processes of picosecond duration by electron-optical chronography. *Dokl Akad Nauk SSSR* **209**, 1060 (1973).
128. Arthurs, E. G., Bradley, D. J. & Roddie, A. G. Picosecond measurements of 3, 3'-diethyloxadicyanone iodide and photoisomer fluorescence. *Chem. Phys. Lett.* **22**, 230–234 (1973).
129. Shapiro, S. L., Hyer, R. C. & Campillo, A. J. Polyatomic molecular relaxation in the absence of collisions. *Phys. Rev. Lett.* **33**, 513 (1974).
130. Campillo, A. J., Hyer, R. C. & Shapiro, S. L. Fluorescence risetime of NE 102 scintillator. *Nucl. Instrum. Methods* **120**, 533–534 (1974).

131. Campillo, A. J., Kollman, V. H. & Shapiro, S. L. Ultrafast Streak Camera. *Science* **189**, 410–410 (1975).
132. Campillo, A. J., Hyer, R. C., Kollman, V. H., Shapiro, S. L. & Sutphin, H. D. Fluorescence lifetimes of  $\alpha$ - and  $\beta$ -carotenes. *Biochim. Biophys. Acta BBA-Bioenerg.* **387**, 533–535 (1975).
133. Takahashi, A. New Femtosecond Streak Camera with Temporal Resolution of 180 fs Akira Takahashi, Mitsunori Nishizawa, Yoshinori Inagaki, Musubu Koishi and Katsuyuki Kinoshita Hamamatsu Photonics KK 812, Joko-cho, Hamamatsu City, 431-31, Japan. *Proc SPIE* **275**, (1994).
134. Bollinger, L. M. & Thomas, G. E. Measurement of the Time Dependence of Scintillation Intensity by a Delayed-Coincidence Method. *Rev. Sci. Instrum.* **32**, 1044–1050 (1961).
135. O'Connor, D. V. O. & Phillips, D. *Time-correlated Single Photon Counting*. (1984).
136. Becker, W. *Advanced time-correlated single photon counting techniques*. (Springer, 2005).
137. Holzapfel, C. On statistics of time-to-amplitude converter systems in photon counting devices. *Rev. Sci. Instrum.* **45**, 894–896 (1974).
138. Coates, P. B. The correction for photonpile-up' in the measurement of radiative lifetimes. *J. Phys. [E]* **1**, 878 (1968).
139. Xu, J. & Knutson, J. R. Ultrafast Fluorescence Spectroscopy via Upconversion: Applications to biophysics. in *Methods in Enzymology* **450**, 159–184 (Elsevier INC, 2008).
140. Valeur, B. & Berberan-Santos, M. N. *Molecular Fluorescence: Principles and Applications*. (Wiley, 2012).
141. Briand, J. *et al.* Coherent ultrafast torsional motion and isomerization of a biomimetic dipolar photoswitch. *Phys. Chem. Chem. Phys.* **12**, 3178 (2010).
142. Abgrall, P. & Gué, A.-M. Lab-on-chip technologies: making a microfluidic network and coupling it into a complete microsystem—a review. *J. Micromechanics Microengineering* **17**, R15–R49 (2007).

143. Yang, R.-J., Hou, H.-H., Wang, Y.-N. & Fu, L.-M. Micro-magnetofluidics in microfluidic systems: A review. *Sens. Actuators B Chem.* **224**, 1–15 (2016).
144. Faustino, V., Catarino, S. O., Lima, R. & Minas, G. Biomedical microfluidic devices by using low-cost fabrication techniques: A review. *J. Biomech.* **49**, 2280–2292 (2016).
145. Karle, M., Vashist, S. K., Zengerle, R. & von Stetten, F. Microfluidic solutions enabling continuous processing and monitoring of biological samples: A review. *Anal. Chim. Acta* **929**, 1–22 (2016).
146. Nilsson, J., Evander, M., Hammarström, B. & Laurell, T. Review of cell and particle trapping in microfluidic systems. *Anal. Chim. Acta* **649**, 141–157 (2009).
147. Kuswandi, B., Nuriman, Huskens, J. & Verboom, W. Optical sensing systems for microfluidic devices: A review. *Anal. Chim. Acta* **601**, 141–155 (2007).
148. Maillot, S. *et al.* Out-of-equilibrium biomolecular interactions monitored by picosecond fluorescence in microfluidic droplets. *Lab. Chip* **14**, 1767 (2014).
149. Yuen, P. K. & Goral, V. N. Low-cost rapid prototyping of flexible microfluidic devices using a desktop digital craft cutter. *Lab Chip* **10**, 384–387 (2010).
150. Lu, Y., Shi, W., Jiang, L., Qin, J. & Lin, B. Rapid prototyping of paper-based microfluidics with wax for low-cost, portable bioassay. *ELECTROPHORESIS* **30**, 1497–1500 (2009).
151. Ballerini, D. R., Li, X. & Shen, W. Patterned paper and alternative materials as substrates for low-cost microfluidic diagnostics. *Microfluid. Nanofluidics* **13**, 769–787 (2012).
152. Tomazelli Coltro, W. K., Cheng, C.-M., Carrilho, E. & de Jesus, D. P. Recent advances in low-cost microfluidic platforms for diagnostic applications: Microfluidics and Miniaturization. *ELECTROPHORESIS* **35**, 2309–2324 (2014).
153. Brouzes, E. *et al.* Droplet microfluidic technology for single-cell high-throughput screening. *Proc. Natl. Acad. Sci.* **106**, 14195–14200 (2009).

154. Guo, M. T., Rotem, A., Heyman, J. A. & Weitz, D. A. Droplet microfluidics for high-throughput biological assays. *Lab. Chip* **12**, 2146 (2012).
155. Chabert, M. & Viovy, J.-L. Microfluidic high-throughput encapsulation and hydrodynamic self-sorting of single cells. *Proc. Natl. Acad. Sci.* **105**, 3191–3196 (2008).
156. Rohde, C. B., Zeng, F., Gonzalez-Rubio, R., Angel, M. & Yanik, M. F. Microfluidic system for on-chip high-throughput whole-animal sorting and screening at subcellular resolution. *Proc. Natl. Acad. Sci.* **104**, 13891–13895 (2007).
157. Chance, B. The accelerated-flow method for rapid reactions. *J. Frankl. Inst.* **229**, 737–766 (1940).
158. Knight, J. B., Vishwanath, A., Brody, J. P. & Austin, R. H. Hydrodynamic focusing on a silicon chip: mixing nanoliters in microseconds. *Phys. Rev. Lett.* **80**, 3863 (1998).
159. Mao, X., Waldeisen, J. R. & Huang, T. J. ‘Microfluidic drifting’—implementing three-dimensional hydrodynamic focusing with a single-layer planar microfluidic device. *Lab. Chip* **7**, 1260 (2007).
160. Mao, X., Lin, S.-C. S., Dong, C. & Huang, T. J. Single-layer planar on-chip flow cytometer using microfluidic drifting based three-dimensional (3D) hydrodynamic focusing. *Lab. Chip* **9**, 1583 (2009).
161. Lee, G.-B., Chang, C.-C., Huang, S.-B. & Yang, R.-J. The hydrodynamic focusing effect inside rectangular microchannels. *J. Micromechanics Microengineering* **16**, 1024–1032 (2006).
162. Sundararajan, N., Pio, M. S., Lee, L. P. & Berlin, A. A. Three-Dimensional Hydrodynamic Focusing in Polydimethylsiloxane (PDMS) Microchannels. *J. Microelectromechanical Syst.* **13**, 559–567 (2004).
163. Ismagilov, R. F., Stroock, A. D., Kenis, P. J. A., Whitesides, G. & Stone, H. A. Experimental and theoretical scaling laws for transverse diffusive broadening in two-phase laminar flows in microchannels. *Appl. Phys. Lett.* **76**, 2376–2378 (2000).
164. Song, H., Tice, J. D. & Ismagilov, R. F. A microfluidic system for controlling reaction networks in time. *Angew. Chem.* **115**, 792–796 (2003).

165. Kamholz, A. & Yager, P. Molecular diffusive scaling laws in pressure-driven microfluidic channels: deviation from one-dimensional Einstein approximations. *Sens Actuators B* **82**, 117–121 (2002).
166. deMello, A. J. Control and detection of chemical reactions in microfluidic systems. *Nature* **442**, 394–402 (2006).
167. Song, H. & Ismagilov, R. F. Millisecond Kinetics on a Microfluidic Chip Using Nanoliters of Reagents. *J. Am. Chem. Soc.* **125**, 14613–14619 (2003).
168. Wang, G. *et al.* Surface-enhanced Raman scattering in nanoliter droplets: towards high-sensitivity detection of mercury (II) ions. *Anal. Bioanal. Chem.* **394**, 1827–1832 (2009).
169. Casadevall i Solvas, X., Srisa-Art, M., deMello, A. J. & Edel, J. B. Mapping of Fluidic Mixing in Microdroplets with 1  $\mu$ s Time Resolution Using Fluorescence Lifetime Imaging. *Anal. Chem.* **82**, 3950–3956 (2010).
170. Kintses, B., van Vliet, L. D., Devenish, S. R. & Hollfelder, F. Microfluidic droplets: new integrated workflows for biological experiments. *Curr. Opin. Chem. Biol.* **14**, 548–555 (2010).
171. Chabert, M., Dorfman, K. D. & Viovy, J.-L. Droplet fusion by alternating current (AC) field electrocoalescence in microchannels. *ELECTROPHORESIS* **26**, 3706–3715 (2005).
172. Liu, S. *et al.* The electrochemical detection of droplets in microfluidic devices. *Lab. Chip* **8**, 1937 (2008).
173. Link, D. R. *et al.* Electric Control of Droplets in Microfluidic Devices. *Angew. Chem. Int. Ed.* **45**, 2556–2560 (2006).
174. Brouzes, E., Kruse, T., Kimmerling, R. & Strey, H. H. Rapid and continuous magnetic separation in droplet microfluidic devices. *Lab Chip* **15**, 908–919 (2015).
175. Sugiura, S., Nakajima, M., Iwamoto, S. & Seki, M. Interfacial Tension Driven Monodispersed Droplet Formation from Microfabricated Channel Array. *Langmuir* **17**, 5562–5566 (2001).

176. Sugiura, S., Nakajima, M., Ushijima, H., Yamamoto, K. & Seki, M. Preparation Characteristics of Monodispersed Water-in-Oil Emulsions Using Microchannel Emulsification. *J. Chem. Engineering Jpn.* **34**, 757–765 (2001).
177. Thorsen, T., Roberts, R. W., Arnold, F. H. & Quake, S. R. Dynamic Pattern Formation in a Vesicle-Generating Microfluidic Device. *Phys. Rev. Lett.* **86**, 4163–4166 (2001).
178. Steegmans, M. L. J., Schroën, K. G. P. H. & Boom, R. M. Characterization of Emulsification at Flat Microchannel Y Junctions. *Langmuir* **25**, 3396–3401 (2009).
179. Abate, A. R., Thiele, J. & Weitz, D. A. One-step formation of multiple emulsions in microfluidics. *Lab Chip* **11**, 253–258 (2011).
180. Sivasamy, J., Wong, T.-N., Nguyen, N.-T. & Kao, L. T.-H. An investigation on the mechanism of droplet formation in a microfluidic T-junction. *Microfluid. Nanofluidics* **11**, 1–10 (2011).
181. Nisisako, T., Torii, T. & Higuchi, T. Droplet formation in a microchannel network. *Lab Chip* **2**, 24–26 (2002).
182. Garstecki, P., Fuerstman, M. J., Stone, H. A. & Whitesides, G. M. Formation of droplets and bubbles in a microfluidic T-junction—scaling and mechanism of break-up. *Lab. Chip* **6**, 437 (2006).
183. Abate, A. R. *et al.* Impact of inlet channel geometry on microfluidic drop formation. *Phys. Rev. E* **80**, (2009).
184. Gupta, A. & Kumar, R. Effect of geometry on droplet formation in the squeezing regime in a microfluidic T-junction. *Microfluid. Nanofluidics* **8**, 799–812 (2010).
185. Wang, C., Nguyen, N.-T. & Wong, T. N. Optical measurement of flow field and concentration field inside a moving nanoliter droplet. *Sens. Actuators Phys.* **133**, 317–322 (2007).
186. Sarrazin, F. *et al.* Mixing characterization inside microdroplets engineered on a microcoalescer. *Chem. Eng. Sci.* **62**, 1042–1048 (2007).
187. Teh, S.-Y., Lin, R., Hung, L.-H. & Lee, A. P. Droplet microfluidics. *Lab. Chip* **8**, 198 (2008).

188. Hsieh, A. T.-H., Pan, P. J.-H. & Lee, A. P. Rapid label-free DNA analysis in picoliter microfluidic droplets using FRET probes. *Microfluid. Nanofluidics* **6**, 391–401 (2009).
189. Liao, A., Karnik, R., Majumdar, A. & Cate, J. H. D. Mixing Crowded Biological Solutions in Milliseconds. *Anal. Chem.* **77**, 7618–7625 (2005).
190. Cordero, M. L. *et al.* Mixing via thermocapillary generation of flow patterns inside a microfluidic drop. *New J. Phys.* **11**, 75033 (2009).
191. Bassous, E., Taub, H. H. & Kuhn, L. Ink jet printing nozzle arrays etched in silicon. *Appl. Phys. Lett.* **31**, 135–137 (1977).
192. Anderson, J. R., Chiu, D. T., Wu, H., Schueller, O. J. & Whitesides, G. M. Fabrication of microfluidic systems in poly (dimethylsiloxane). *Electrophoresis* **21**, 27–40 (2000).
193. McDonald, J. C. & Whitesides, G. M. Poly(dimethylsiloxane) as a Material for Fabricating Microfluidic Devices. *Acc. Chem. Res.* **35**, 491–499 (2002).
194. Lyubovitsky, J. G., Gray, H. B. & Winkler, J. R. Mapping the Cytochrome *c* Folding Landscape. *J. Am. Chem. Soc.* **124**, 5481–5485 (2002).
195. Ratner, V., Sinev, M. & Haas, E. Determination of intramolecular distance distribution during protein folding on the millisecond timescale. *J. Mol. Biol.* **299**, 1363–1371 (2000).
196. Beechem, J. M. & Haas, E. Simultaneous determination of intramolecular distance distributions and conformational dynamics by global analysis of energy transfer measurements. *Biophys. J.* **55**, 1225–1236 (1989).
197. Bilsel, O., Kayatekin, C., Wallace, L. A. & Matthews, C. R. A microchannel solution mixer for studying microsecond protein folding reactions. *Rev. Sci. Instrum.* **76**, 14302 (2005).
198. Batabyal, S., Rakshit, S., Kar, S. & Pal, S. K. An improved microfluidics approach for monitoring real-time interaction profiles of ultrafast molecular recognition. *Rev. Sci. Instrum.* **83**, 43113 (2012).

199. Kimura, T., Lee, J. C., Gray, H. B. & Winkler, J. R. Site-specific collapse dynamics guide the formation of the cytochrome *c'* four-helix bundle. *Proc. Natl. Acad. Sci.* **104**, 117–122 (2007).
200. Benningen, R. *et al.* Time-resolved fluorescence imaging of solvent interactions in microfluidic devices. *Opt. Express* **13**, 6275–6285 (2005).
201. Srisa-Art, M., Dyson, E. C., deMello, A. J. & Edel, J. B. Monitoring of Real-Time Streptavidin–Biotin Binding Kinetics Using Droplet Microfluidics. *Anal. Chem.* **80**, 7063–7067 (2008).
202. Benz, C., Retzbach, H., Nagl, S. & Belder, D. Protein–protein interaction analysis in single microfluidic droplets using FRET and fluorescence lifetime detection. *Lab. Chip* **13**, 2808 (2013).
203. Tsopeles, C. & Sutton, R. Why certain dyes are useful for localizing the sentinel lymph node. *J. Nucl. Med.* **43**, 1377–1382 (2002).
204. Klymchenko, A. S., Pivovarenko, V. G. & Demchenko, A. P. Elimination of the Hydrogen Bonding Effect on the Solvatochromism of 3-Hydroxyflavones. *J. Phys. Chem. A* **107**, 4211–4216 (2003).
205. Warshel, A. Calculations of Enzymatic Reactions: Calculations of pKa, Proton Transfer Reactions, and General Acid Catalysis Reactions in Enzymes. *Biochemistry (Mosc.)* **20**, 3167–3177 (1981).
206. Barbara, P. F., Walsh, P. K. & Brus, L. E. Picosecond kinetic and vibrationally resolved spectroscopic studies of intramolecular excited-state hydrogen atom transfer. *J. Phys. Chem.* **93**, 29–34 (1989).
207. Klymchenko, A. S. & Demchenko, A. P. Multiparametric probing of intermolecular interactions with fluorescent dye exhibiting excited state intramolecular proton transfer. *Phys. Chem. Chem. Phys.* **5**, 461–468 (2003).
208. Klymchenko, A. S., Kenfack, C., Duportail, G. & Mély, Y. Effects of polar protic solvents on dual emissions of 3-hydroxychromones. *J. Chem. Sci.* **119**, 83–89 (2007).

209. Klymchenko, A. S. & Demchenko, A. P. Electrochromic Modulation of Excited-State Intramolecular Proton Transfer: The New Principle in Design of Fluorescence Sensors. *J. Am. Chem. Soc.* **124**, 12372–12379 (2002).
210. Shvadchak, V. V., Klymchenko, A. S., de Rocquigny, H. & Mely, Y. Sensing peptide-oligonucleotide interactions by a two-color fluorescence label: application to the HIV-1 nucleocapsid protein. *Nucleic Acids Res.* **37**, e25–e25 (2009).
211. Postupalenko, V. Y. *et al.* Monitoring membrane binding and insertion of peptides by two-color fluorescent label. *Biochim. Biophys. Acta BBA - Biomembr.* **1808**, 424–432 (2011).
212. Sarkar, M. & Sengupta, P. K. Influence of different micellar environments on the excited-state proton-transfer luminescence of 3-hydroxyflavone. *Chem. Phys. Lett.* **179**, 68–72 (1991).
213. Sarkar, M., Guha Ray, J. & Sengupta, P. K. Effect of reverse micelles on the intramolecular excited state proton transfer (ESPT) and dual luminescence behaviour of 3-hydroxyflavone. *Spectrochim. Acta. A. Mol. Biomol. Spectrosc.* **52**, 275–278 (1996).
214. Basu, S., Mondal, S. & Mandal, D. Proton transfer reactions in nanoscopic polar domains: 3-hydroxyflavone in AOT reverse micelles. *J. Chem. Phys.* **132**, 34701 (2010).
215. Klymchenko, A. S., Duportail, G., Mély, Y. & Demchenko, A. P. Ultrasensitive two-color fluorescence probes for dipole potential in phospholipid membranes. *Proc. Natl. Acad. Sci.* **100**, 11219–11224 (2003).
216. Duportail, G., Klymchenko, A., Mely, Y. & Demchenko, A. P. Neutral fluorescence probe with strong ratiometric response to surface charge of phospholipid membranes. *Febs Lett.* **508**, 196–200 (2001).
217. Mohapatra, M., Subuddhi, U. & Mishra, A. K. Photophysical behaviour of ground state anion and phototautomer of 3-hydroxyflavone in liposome membrane. *Photochem. Photobiol. Sci.* (2009).  
doi:10.1039/b905906g

218. McMorrow, D. & Kasha, M. Proton-transfer spectroscopy of 3-hydroxychromones. Extreme sensitivity to hydrogen-bonding perturbations. *J. Am. Chem. Soc.* **105**, 5133–5134 (1983).
219. Kenfack, C. A., Klymchenko, A. S., Duportail, G., Burger, A. & Mély, Y. Ab initio study of the solvent H-bonding effect on ESIPT reaction and electronic transitions of 3-hydroxychromone derivatives. *Phys. Chem. Chem. Phys.* **14**, 8910 (2012).
220. Shynkar, V. V. *et al.* Picosecond Time-Resolved Fluorescence Studies Are Consistent with Reversible Excited-State Intramolecular Proton Transfer in 4'-(Dialkylamino)-3-hydroxyflavones. *J. Phys. Chem. A* **107**, 9522–9529 (2003).
221. Roshal, A. ., Organero, J. . & Douhal, A. Tuning the mechanism of proton-transfer in a hydroxyflavone derivative. *Chem. Phys. Lett.* **379**, 53–59 (2003).
222. Muehlpfordt, A., Bultmann, T., Ernsting, N. P. & Dick, B. Excited-state intramolecular proton transfer in 3-hydroxyflavone: Comparison of time- and frequency-domain spectroscopy. *Verh.-K. Ned. Akad. Van Wet. Afd. Natuurkunde Eerste Reeks* **42**, 83–89 (1994).
223. Chou, P.-T. *et al.* Femtosecond Dynamics on Excited-State Proton/ Charge-Transfer Reaction in 4'-N , N-Diethylamino-3-hydroxyflavone. The Role of Dipolar Vectors in Constructing a Rational Mechanism. *J. Phys. Chem. A* **109**, 3777–3787 (2005).
224. Ameer-Beg, S. *et al.* Ultrafast Measurements of Excited State Intramolecular Proton Transfer (ESIPT) in Room Temperature Solutions of 3-Hydroxyflavone and Derivatives. *J. Phys. Chem. A* **105**, 3709–3718 (2001).
225. Schwartz, B. J., Peteanu, L. A. & Harris, C. B. Direct observation of fast proton transfer: femtosecond photophysics of 3-hydroxyflavone. *J. Phys. Chem.* **96**, 3591–3598 (1992).
226. Ormson, S. M., Brown, R. G., Vollmer, F. & Rettig, W. Switching between charge- and proton-transfer emission in the excited state of a substituted 3-hydroxyflavone. *J. Photochem. Photobiol. Chem.* **81**, 65–72 (1994).

227. Parsapour, F. & Kelley, D. F. Torsional and proton transfer dynamics in substituted 3-hydroxyflavones. *J. Phys. Chem.* **100**, 2791–2798 (1996).
228. Strandjord, A. J. G. & Barbara, P. F. The proton-transfer kinetics of 3-hydroxyflavone: solvent effects. *J. Phys. Chem.* **89 (11)**, 2355–2361 (1985).
229. Klymchenko, A. S., Pivovarenko, V. G. & Demchenko, A. P. Perturbation of planarity as the possible mechanism of solvent-dependent variations of fluorescence quantum yield in 2-aryl-3-hydroxychromones. *Spectrochim. Acta. A. Mol. Biomol. Spectrosc.* **59**, 787–792 (2003).
230. Woolfe, G. J. & Thistlethwaite, P. J. Direct observation of excited state intramolecular proton transfer kinetics in 3-hydroxyflavone. *J. Am. Chem. Soc.* **103 (23)**, 6916–6923 (1981).
231. Itoh, M. *et al.* Time-resolved and steady-state fluorescence studies of the excited-state proton transfer in 3-hydroxyflavone and 3-hydroxychromone. *J. Am. Chem. Soc.* **104**, 4146–4150 (1982).
232. Itoh, M., Tanimoto, Y. & Tokumura, K. Transient absorption study of the intramolecular excited-state and ground-state proton transfer in 3-hydroxyflavone and 3-hydroxychromone. *J Am Chem Soc* **105**, 3339–3340 (1983).
233. Strandjord, A. J. G., Courtney, S. H., Friedrich, D. M. & Barbara, P. F. Excited-state dynamics of 3-hydroxyflavone. *J. Phys. Chem.* **87**, 1125–1133 (1983).
234. Chou, P., McMorrow, D., Aartsma, T. J. & Kasha, M. The proton-transfer laser. Gain spectrum and amplification of spontaneous emission of 3-hydroxyflavone. *J. Phys. Chem.* **88**, 4596–4599 (1984).
235. Itoh, M., Fujiwara, Y., Sumitani, M. & Yoshihara, K. Mechanism of intramolecular excited-state proton transfer and relaxation processes in the ground and excited states of 3-hydroxyflavone and related compounds. *J. Phys. Chem.* **90**, 5672–5678 (1986).
236. Dzugan, T. P., Schmidt, J. & Aartsma, T. J. On the ground-state tautomerization of 3-hydroxyflavone. *Chem. Phys. Lett.* **127**, 336–342 (1986).

237. Brucker, G. A. & Kelley, D. F. Proton transfer in matrix-isolated 3-hydroxyflavone and 3-hydroxyflavone complexes. *J. Phys. Chem.* **91**, 2856–2861 (1987).
238. Rulliere, C. & Declémy, A. A picosecond transient absorption study of the intramolecular excited state proton transfer in 3-hydroxyflavone: assignment of the observed bands. *Chem. Phys. Lett.* **134**, 64–69 (1987).
239. Brewer, W. E., Studer, S. L., Standiford, M. & Chou, P. T. Dynamics of the triplet state and the reverse proton transfer of 3-hydroxyflavone. *J. Phys. Chem.* **93**, 6088–6094 (1989).
240. Parthenopoulos, D. & Kasha, M. Ground state anion formation and picosecond excitation dynamics of 3-hydroxyflavone in formamide. *Chem. Phys. Lett.* **173**, 303–309 (1990).
241. Martinez, M. L., Studer, S. L. & Chou, P. T. Direct evidence of the triplet-state origin of the slow reverse proton transfer reaction of 3-hydroxyflavone. *J. Am. Chem. Soc.* **112**, 2427–2429 (1990).
242. Brucker, G. A., Kelley, D. F. & Swinney, T. C. Proton-transfer and solvent polarization dynamics in 3-hydroxyflavone. *J. Phys. Chem.* **95**, 3190–3195 (1991).
243. Cornard, J. P., Vrielynck, L., Merlin, J. C. & Wallet, J. C. Structural and vibrational study of 3-hydroxyflavone and 3-methoxyflavone. *Spectrochim. Acta. A. Mol. Biomol. Spectrosc.* **51**, 913–923 (1995).
244. Mandal, P. K. & Samanta, A. Evidence of Ground-State Proton-Transfer Reaction of 3-Hydroxyflavone in Neutral Alcoholic Solvents. *J. Phys. Chem. A* **107**, 6334–6339 (2003).
245. Zhu, A., Wang, B., White, J. O. & Drickamer, H. G. Effect of Pressure on the Excited-State Proton Transfer of 3-Hydroxyflavone. *J. Phys. Chem. B* **107**, 9973–9976 (2003).
246. Tomin, V. I. & Javorski, R. Intramolecular proton transfer from the highest singlet states in 3-hydroxyflavone. *Opt. Spectrosc.* **103**, 745–749 (2007).
247. Chevalier, K. *et al.* Transient IR spectroscopy and ab initio calculations on ESIPT in 3-hydroxyflavone solvated in acetonitrile. *Phys. Chem. Chem. Phys.* **14**, 15007 (2012).

248. Chou, P.-T., Martinez, M. L. & Clements, J. H. The observation of solvent-dependent proton-transfer/charge-transfer lasers from 4'-diethylamino-3-hydroxyflavone. *Chem. Phys. Lett.* **204**, 395–399 (1993).
249. Kimura, Y., Fukuda, M., Suda, K. & Terazima, M. Excited State Intramolecular Proton Transfer Reaction of 4'-N,N-Diethylamino-3-hydroxyflavone and Solvation Dynamics in Room Temperature Ionic Liquids Studied by Optical Kerr Gate Fluorescence Measurement. *J. Phys. Chem. B* **114**, 11847–11858 (2010).
250. Fukuda, M., Terazima, M. & Kimura, Y. Study on the excited state intramolecular proton transfer of 4'-N,N-diethylamino-3-hydroxyflavone in imidazolium-based room temperature ionic liquids. *Chem. Phys. Lett.* **463**, 364–368 (2008).
251. Suda, K., Terazima, M., Sato, H. & Kimura, Y. Excitation Wavelength Dependence of Excited State Intramolecular Proton Transfer Reaction of 4'-N,N-Diethylamino-3-hydroxyflavone in Room Temperature Ionic Liquids Studied by Optical Kerr Gate Fluorescence Measurement. *J. Phys. Chem. B* **117**, 12567–12582 (2013).
252. Szakács, Z. *et al.* The kinetics and mechanism of photooxygenation of 4'-diethylamino-3-hydroxyflavone. *Photochem Photobiol Sci* **15**, 219–227 (2016).
253. Ameer-Beg, S. *et al.* Ultrafast Measurements of Charge and Excited-State Intramolecular Proton Transfer in Solutions of 4'-(N,N-Dimethylamino) Derivatives of 3-Hydroxyflavone. *J. Phys. Chem. A* **108**, 6938–6943 (2004).
254. Zhu, A., Wang, B., White, J. O. & Drickamer, H. G. The Effects of Pressure on the Intramolecular Proton Transfer and Charge Transfer of 4'-N-Dimethylamino-3-hydroxyflavone<sup>†</sup>. *J. Phys. Chem. B* **108**, 891–894 (2004).

255. Barroso, M. *et al.* Dramatic Pressure-Dependent Quenching Effects in Supercritical CO<sub>2</sub> Assessed by the Fluorescence of 4'-Dimethylamino-3-hydroxyflavone. Thermodynamic versus Kinetics Control of Excited-State Intramolecular Proton Transfer. *J. Phys. Chem. A* **110**, 13419–13424 (2006).
256. Hino, K., Nakajima, K., Kawahara, M., Kiyota, I. & Sekiya, H. Polymorphism of 4'-Dimethylamino-3-hydroxyflavone. *Bull. Chem. Soc. Jpn.* **84**, 1234–1236 (2011).
257. Zhang, W., Shi, B. & Shi, J. Time-dependent density functional investigation on electronic spectra of 4'-N-dimethylamino-3-hydroxyflavone. *J. Mol. Struct. THEOCHEM* **731**, 219–224 (2005).
258. Ghosh, D., Batuta, S., Begum, N. A. & Mandal, D. Unusually slow intramolecular proton transfer dynamics of 4'-N,N-dimethylamino-3-hydroxyflavone in high n-alcohols: involvement of solvent relaxation. *Photochem Photobiol Sci* **15**, 266–277 (2016).
259. Hayaki, S., Kimura, Y. & Sato, H. Ab Initio Study on an Excited-State Intramolecular Proton-Transfer Reaction in Ionic Liquid. *J. Phys. Chem. B* **117**, 6759–6767 (2013).
260. Ozturk, T. *et al.* New 3-hydroxyflavone derivatives for probing hydrophobic sites in microheterogeneous systems. *Tetrahedron* **63**, 10290–10299 (2007).
261. Klymchenko, A. S., Pivovarenko, V. G., Ozturk, T. & Demchenko, A. P. Modulation of the solvent-dependent dual emission in 3-hydroxychromones by substituents. *New J. Chem.* **27**, 1336 (2003).
262. Nemkovich, N. A., Baumann, W., Pivovarenko, V. G. & Rubinov, A. N. Determination of the dipole moments of the molecules of 4'-substituted 3-hydroxyflavones using the electrooptic absorption method. *J. Appl. Spectrosc.* **70**, 230–237 (2003).
263. Bader, A. N., Pivovarenko, V. G., Demchenko, A. P., Ariese, F. & Gooijer, C. Excited State and Ground State Proton Transfer Rates of 3-Hydroxyflavone and Its Derivatives Studied by Shpol'skii Spectroscopy: The Influence of Redistribution of Electron Density <sup>†</sup>. *J. Phys. Chem. B* **108**, 10589–10595 (2004).

264. Zamotaiev, O. M. *et al.* Improved Hydration-Sensitive Dual-Fluorescence Labels For Monitoring Peptide–Nucleic Acid Interactions. *Bioconjug. Chem.* **22**, 101–107 (2011).
265. Das, R., Klymchenko, A. S., Duportail, G. & Mély, Y. Unusually slow proton transfer dynamics of a 3-hydroxychromone dye in protic solvents. *Photochem. Photobiol. Sci.* **8**, 1583 (2009).
266. Enander, K. *et al.* A peptide-based, ratiometric biosensor construct for direct fluorescence detection of a protein analyte. *Bioconjug. Chem.* **19**, 1864–1870 (2008).
267. Demchenko, A. P., Mély, Y., Duportail, G. & Klymchenko, A. S. Monitoring biophysical properties of lipid membranes by environment-sensitive fluorescent probes. *Biophys. J.* **96**, 3461–3470 (2009).
268. Loving, G. S., Sainlos, M. & Imperiali, B. Monitoring protein interactions and dynamics with solvatochromic fluorophores. *Trends Biotechnol.* **28**, 73–83 (2010).
269. Pace, C. N. Energetics of protein hydrogen bonds: in this issue, an article gives insight into the microenvironment’s influence on the contribution of hydrogen bonds to protein stability. *Nat. Struct. Mol. Biol.* **16**, 681–683 (2009).
270. Melhuish, W. H. Quantum efficiencies of fluorescence of organic substances: effect of solvent and concentration of the fluorescent solute<sup>1</sup>. *J. Phys. Chem.* **65**, 229–235 (1961).
271. Stewart, G. W. On the Early History of the Singular Value Decomposition. *Soc. Ind. Appl. Math.* **35**, 551–566 (1993).
272. Verveer, P. J., Squire, A. & Bastiaens, P. I. Global analysis of fluorescence lifetime imaging microscopy data. *Biophys. J.* **78**, 2127–2137 (2000).
273. Pelet, S., Previte, M. J. R., Laiho, L. H. & So, P. T. C. A Fast Global Fitting Algorithm for Fluorescence Lifetime Imaging Microscopy Based on Image Segmentation. *Biophys. J.* **87**, 2807–2817 (2004).

274. Barber, P. . *et al.* Multiphoton time-domain fluorescence lifetime imaging microscopy: practical application to protein-protein interactions using global analysis. *J. R. Soc. Interface* **6**, S93–S105 (2009).
275. Warren, S. C. *et al.* Rapid Global Fitting of Large Fluorescence Lifetime Imaging Microscopy Datasets. *PLoS ONE* **8**, e70687 (2013).
276. Shaner, N. C., Steinbach, P. A. & Tsien, R. Y. A guide to choosing fluorescent proteins. *Nat. Methods* **2**, 905–909 (2005).
277. Zhang, J., Jensen, M. K. & Keasling, J. D. Development of biosensors and their application in metabolic engineering. *Curr. Opin. Chem. Biol.* **28**, 1–8 (2015).
278. Chudakov, D. M., Matz, M. V., Lukyanov, S. & Lukyanov, K. A. Fluorescent Proteins and Their Applications in Imaging Living Cells and Tissues. *Physiol. Rev.* **90**, 1103–1163 (2010).
279. Shimomura, O. The discovery of aequorin and green fluorescent protein. *J. Microsc.* **217**, 3–15 (2005).
280. Shimomura, O., Johnson, K. & Saiga, Y. Extraction, purification and properties of aequorin, a bioluminescent protein from the luminous hydromedusan, *Aequorea*. *J. Cell. Comp. Physiol.* **59**, 223–239 (1962).
281. Morin, J. G. & Hastings, J. W. Energy transfer in a bioluminescent system. *J. Cell. Physiol.* **77**, 313–318 (1971).
282. Morise, H., Shimomura, O., Johnson, F. H. & Winant, J. Intermolecular energy transfer in the bioluminescent system of *Aequorea*. *Biochemistry (Mosc.)* **13**, 2656–2662 (1974).
283. Hastings, J. & Morin, J. Comparative biochemistry of calcium activated photoproteins from the ctenophore. *Mnemiopsis* and the coelenterates *Aequorea*, *Obelia*, *Pelagia* and *Renilla*. *Biol Bull* **137**, 402 (1969).

284. Shimomura, O. Structure of the chromophore of Aequorea Green Fluorescent Protein. *Febs Lett.* **104**, 220–222 (1979).
285. Prasher, D. C., Eckenrode, V., Ward, W. W., Prendergast, F. & Cormier, M. Primary structure of the Aequorea Victoria Green Fluorescent Protein. *Gene* **111**, 229–233 (1992).
286. Chalfie, M., Tu, Y., Euskirchen, G., Ward, W. W. & Prasher, D. C. Green fluorescent protein as a marker for gene expression. *Science* 802–805 (1994).
287. Heim, R., Prasher, D. C. & Tsien, R. Y. Wavelength mutations and posttranslational autoxidation of green fluorescent protein. *Proc. Natl. Acad. Sci.* **91**, 12501–12504 (1994).
288. Heim, R., Cubitt, A. & Tsien, R. Improved green fluorescence. *Nature* **373**, 663–664 (1995).
289. Cubitt, A. B. *et al.* Understanding, improving and using green fluorescent proteins. *Trends Biochem. Sci.* **20**, 448–455 (1995).
290. Forster, T. Energiewanderung und fluoreszenz. *Naturwissenschaften* **33**, 166–175 (1946).
291. Tsien, R. & Miyawak, A. Seeing the Machinery of Live Cells. *Science* **280**, 1954–1955 (1998).
292. Bunt, G. & Wouters, F. S. FRET from single to multiplexed signaling events. *Biophys. Rev.* **9**, 119–129 (2017).
293. Becirovic, E. *et al.* AAV Vectors for FRET-Based Analysis of Protein-Protein Interactions in Photoreceptor Outer Segments. *Front. Neurosci.* **10**, (2016).
294. King, C., Raicu, V. & Hristova, K. Understanding the FRET Signatures of Interacting Membrane Proteins. *J. Biol. Chem.* **292**, 5291–5310 (2017).
295. Patel, M. J., Bhatia, L., Yilmaz, G., Biswas-Fiss, E. E. & Biswas, S. B. Multiple conformational states of DnaA protein regulate its interaction with DnaA boxes in the initiation of DNA replication. *Biochim. Biophys. Acta BBA - Gen. Subj.* **1861**, 2165–2174 (2017).
296. van der Feltz, C. & Hoskins, A. A. Methodologies for studying the spliceosome's RNA dynamics with single-molecule FRET. *Methods* (2017). doi:10.1016/j.ymeth.2017.05.011

297. Johnson, D. E. *et al.* Red Fluorescent Protein pH Biosensor to Detect Concentrative Nucleoside Transport. *J. Biol. Chem.* **284**, 20499–20511 (2009).
298. Li, B., Yu, Q. & Duan, Y. Fluorescent labels in biosensors for pathogen detection. *Crit. Rev. Biotechnol.* **35**, 82–93 (2015).
299. Zamani, P., Sajedi, R. H., Hosseinkhani, S., Zeinoddini, M. & Bakhshi, B. A luminescent hybridoma-based biosensor for rapid detection of *V. cholerae* upon induction of calcium signaling pathway. *Biosens. Bioelectron.* **79**, 213–219 (2016).
300. Bononi, A. *et al.* BAP1 regulates IP3R3-mediated Ca<sup>2+</sup> flux to mitochondria suppressing cell transformation. *Nature* (2017). doi:10.1038/nature22798
301. Lemke, E. A. & Schultz, C. Principles for designing fluorescent sensors and reporters. *Nat. Chem. Biol.* **7**, 480 (2011).
302. Gonzalez-Vera, J. & Morris, M. Fluorescent Reporters and Biosensors for Probing the Dynamic Behavior of Protein Kinases. *Proteomes* **3**, 369–410 (2015).
303. Zhao, M. *et al.* A sensitive fluorescence biosensor for alkaline phosphatase activity based on the Cu(II)-dependent DNAzyme. *Anal. Chim. Acta* **948**, 98–103 (2016).
304. Boehm, C. R., Ueda, M., Nishimura, Y., Shikanai, T. & Haseloff, J. A Cyan Fluorescent Reporter Expressed from the Chloroplast Genome of *Marchantia polymorpha*. *Plant Cell Physiol.* **57**, 291–299 (2016).
305. Goedhart, J. *et al.* Structure-guided evolution of cyan fluorescent proteins towards a quantum yield of 93%. *Nat. Commun.* **3**, 751 (2012).
306. Markwardt, M. L. *et al.* An Improved Cerulean Fluorescent Protein with Enhanced Brightness and Reduced Reversible Photoswitching. *PLoS ONE* **6**, e17896 (2011).
307. Erard, M. *et al.* Minimum set of mutations needed to optimize cyan fluorescent proteins for live cell imaging. *Mol BioSyst* **9**, 258–267 (2013).

308. Otto-Duessel, M., Tew, B. Y., Vonderfecht, S., Moore, R. & Jones, J. O. Identification of neuron selective androgen receptor inhibitors. *World J. Biol. Chem.* **8**, 138 (2017).
309. Corby, M. J. *et al.* Quantitative microspectroscopic imaging reveals viral and cellular RNA helicase interactions in live cells. *J. Biol. Chem.* **292**, 11165–11177 (2017).
310. Knorr, J. M., Jackson, J., Batie, M. R., Narmoneva, D. A. & Jones, D. C. Application of strain and calibration of Förster Resonance Energy Transfer (FRET) emission for in vitro live cell response to cytoskeletal deformation. *J. Biomech.* **49**, 3334–3339 (2016).
311. Scott, B. L. & Hoppe, A. D. Three-Dimensional Reconstruction of Three-Way FRET Microscopy Improves Imaging of Multiple Protein-Protein Interactions. *PLOS ONE* **11**, e0152401 (2016).
312. Bozza, W. P. *et al.* The Use of a Stably Expressed FRET Biosensor for Determining the Potency of Cancer Drugs. *PLoS ONE* **9**, e107010 (2014).
313. He, L. *et al.* Flow cytometric measurement of fluorescence (Förster) resonance energy transfer from cyan fluorescent protein to yellow fluorescent protein using single-laser excitation at 458 nm. *Cytometry* **53A**, 39–54 (2003).
314. Chirgadze, D. Y. *et al.* Crystal structure of the NK1 fragment of HGF/SF suggests a novel mode for growth factor dimerization and receptor binding. *Nat. Struct. Mol. Biol.* **6**, 72–79 (1999).
315. Mérola, F., Erard, M., Fredj, A. & Pasquier, H. Engineering fluorescent proteins towards ultimate performances: lessons from the newly developed cyan variants. *Methods Appl. Fluoresc.* **4**, 12001 (2016).
316. Hyun Bae, J. *et al.* Expansion of the Genetic Code Enables Design of a Novel ‘Gold’ Class of Green Fluorescent Proteins. *J. Mol. Biol.* **328**, 1071–1081 (2003).
317. Tramier, M. *et al.* Picosecond-hetero-FRET microscopy to probe protein-protein interactions in live cells. *Biophys. J.* **83**, 3570–3577 (2002).

318. Habuchi, S. *et al.* Resonance energy transfer in a calcium concentration-dependent cameleon protein. *Biophys. J.* **83**, 3499–3506 (2002).
319. Borst, J. W. *et al.* ATP Changes the Fluorescence Lifetime of Cyan Fluorescent Protein via an Interaction with His148. *PLoS ONE* **5**, e13862 (2010).
320. Seifert, M. H. J. *et al.* Slow Exchange in the Chromophore of a Green Fluorescent Protein Variant. *J. Am. Chem. Soc.* **124**, 7932–7942 (2002).
321. Villoing, A. *et al.* Complex Fluorescence of the Cyan Fluorescent Protein: Comparisons with the H148D Variant and Consequences for Quantitative Cell Imaging<sup>†</sup>. *Biochemistry (Mosc.)* **47**, 12483–12492 (2008).
322. Miyawaki, A. & Tsien, R. Y. Monitoring protein conformations and interactions by fluorescence resonance energy transfer between mutants of green fluorescent protein. *Methods Enzymol.* **327**, 475–500 (2000).
323. Ai, H., Henderson, J., Remington, S. J. & Campbell, R. Directed evolution of a monomeric, bright and photostable version of *Clavularia* cyan fluorescent protein: structural characterization and applications in fluorescence imaging. *Biochem. J.* **400**, 531–540 (2006).
324. Rizzo, M. A., Springer, G. H., Granada, B. & Piston, D. W. An improved cyan fluorescent protein variant useful for FRET. *Nat. Biotechnol.* **22**, 445–449 (2004).
325. Shu, X. *et al.* Ultrafast Excited-State Dynamics in the Green Fluorescent Protein Variant S65T/H148D. 1. Mutagenesis and Structural Studies<sup>†, ‡</sup>. *Biochemistry (Mosc.)* **46**, 12005–12013 (2007).
326. Esposito, A., Gralle, M., Dani, M. A. C., Lange, D. & Wouters, F. S. pHlameleons: A Family of FRET-Based Protein Sensors for Quantitative pH Imaging<sup>†</sup>. *Biochemistry (Mosc.)* **47**, 13115–13126 (2008).
327. Heim, R. & Tsien, R. Y. Engineering green fluorescent protein for improved brightness, longer wavelengths and fluorescence resonance energy transfer. *Curr. Biol.* **6**, 178–182 (1996).

328. Tsien, R. Y. The Green Fluorescent Protein. *Ann Rev Biochem* **67**, 509–544 (1998).
329. Lelimosin, M. *et al.* Intrinsic Dynamics in ECFP and Cerulean Control Fluorescence Quantum Yield. *Biochemistry (Mosc.)* **48**, 10038–10046 (2009).
330. Meech, S. R. Excited state reactions in fluorescent proteins. *Chem. Soc. Rev.* **38**, 2922 (2009).
331. Fredj, A. *et al.* The Single T65S Mutation Generates Brighter Cyan Fluorescent Proteins with Increased Photostability and pH Insensitivity. *PLoS ONE* **7**, e49149 (2012).
332. Malo, G. D. *et al.* X-ray Structure of Cerulean GFP: A Tryptophan-Based Chromophore Useful for Fluorescence Lifetime Imaging<sup>†, ‡</sup>. *Biochemistry (Mosc.)* **46**, 9865–9873 (2007).
333. Vallverdu, G. *et al.* Relation between pH, structure, and absorption spectrum of Cerulean: A study by molecular dynamics and TD DFT calculations. *Proteins Struct. Funct. Bioinforma.* **78**, 1040–1054 (2010).
334. Pereira, D. A. & Williams, J. A. Origin and evolution of high throughput screening. *Br. J. Pharmacol.* **152**, 53–61 (2007).
335. Ibrahim, S. F. & van den Engh, G. Flow Cytometry and Cell Sorting. in *Cell Separation* (eds. Kumar, A., Galaev, I. Y. & Mattiasson, B.) **106**, 19–39 (Springer Berlin Heidelberg, 2007).
336. Ibrahim, S. F. & van den Engh, G. High-speed cell sorting: fundamentals and recent advances. *Curr. Opin. Biotechnol.* **14**, 5–12 (2003).
337. Wolff, A. *et al.* Integrating advanced functionality in a microfabricated high-throughput fluorescent-activated cell sorter. *Lab. Chip* **3**, 22 (2003).
338. Krutzik, P. O. & Nolan, G. P. Fluorescent cell barcoding in flow cytometry allows high-throughput drug screening and signaling profiling. *Nat. Methods* **3**, 361–368 (2006).
339. Nicoletti, I., Migliorati, G., Pagliacci, M. C., Grignani, F. & Riccardi, C. A rapid and simple method for measuring thymocyte apoptosis by propidium iodide staining and flow cytometry. *J. Immunol. Methods* **139**, 271–279 (1991).

340. Godin, J. *et al.* Microfluidics and photonics for Bio-System-on-a-Chip: A review of advancements in technology towards a microfluidic flow cytometry chip. *J. Biophotonics* **1**, 355–376 (2008).
341. Baret, J.-C. *et al.* Fluorescence-activated droplet sorting (FADS): efficient microfluidic cell sorting based on enzymatic activity. *Lab. Chip* **9**, 1850 (2009).
342. Matthews, D. R. *et al.* A high-content screening platform utilizing polarization anisotropy and FLIM microscopy. in *Imaging, Manipulation, and Analysis of Biomolecules, Cells, and Tissues VI* **6859**, (2008).
343. Nedbal, J. *et al.* Time-domain microfluidic fluorescence lifetime flow cytometry for high-throughput Förster resonance energy transfer screening: Microfluidic Fluorescence Lifetime Flow Cytometry. *Cytometry A* **87**, 104–118 (2015).
344. Rocca, F. M. D. *et al.* Real-time fluorescence lifetime actuation for cell sorting using a CMOS SPAD silicon photomultiplier. *Opt. Lett.* **41**, 673 (2016).
345. Miller, O. J. *et al.* High-resolution dose–response screening using droplet-based microfluidics. *Proc. Natl. Acad. Sci.* **109**, 378–383 (2012).
346. Beneyton, T. *et al.* Droplet-based microfluidic high-throughput screening of heterologous enzymes secreted by the yeast *Yarrowia lipolytica*. *Microb. Cell Factories* **16**, (2017).
347. Barber, P. R. *et al.* Towards high-throughput FLIM for protein-protein interaction screening of live cells and tissue microarrays. in *Biomedical Imaging: From Nano to Macro, 2008. ISBI 2008. 5th IEEE International Symposium on* 356–359 (IEEE, 2008).
348. Jones, E., Michael, S. & Sittampalam, G. S. Basics of assay equipment and instrumentation for high throughput screening. (2016).
349. He, N., Liu, T. & Liu, B. Technologies and Applications in Micro-Volume Liquid Handling. *J. Nanosci. Nanotechnol.* **16**, 58–66 (2016).

350. Mayr, L. M. & Fuerst, P. The Future of High-Throughput Screening. *J. Biomol. Screen.* **13**, 443–448 (2008).
351. Guo, M. T., Rotem, A., Heyman, J. A. & Weitz, D. A. Droplet microfluidics for high-throughput biological assays. *Lab. Chip* **12**, 2146 (2012).
352. Brouzes, E. *et al.* Droplet microfluidic technology for single-cell high-throughput screening. *Proc. Natl. Acad. Sci.* **106**, 14195–14200 (2009).
353. Lagus, T. P. & Edd, J. F. A review of the theory, methods and recent applications of high-throughput single-cell droplet microfluidics. *J. Phys. Appl. Phys.* **46**, 114005 (2013).
354. Fallah-Araghi, A., Baret, J.-C., Ryckelynck, M. & Griffiths, A. D. A completely in vitro ultrahigh-throughput droplet-based microfluidic screening system for protein engineering and directed evolution. *Lab. Chip* **12**, 882 (2012).
355. Mazutis, L. *et al.* Droplet-Based Microfluidic Systems for High-Throughput Single DNA Molecule Isothermal Amplification and Analysis. *Anal. Chem.* **81**, 4813–4821 (2009).
356. Sjostrom, S. L. *et al.* High-throughput screening for industrial enzyme production hosts by droplet microfluidics. *Lab Chip* **14**, 806–813 (2014).
357. Abate, A. R., Hung, T., Mary, P., Agresti, J. J. & Weitz, D. A. High-throughput injection with microfluidics using picoinjectors. *Proc. Natl. Acad. Sci.* **107**, 19163–19166 (2010).
358. Chen, D. *et al.* The chemistode: a droplet-based microfluidic device for stimulation and recording with high temporal, spatial, and chemical resolution. *Proc. Natl. Acad. Sci.* **105**, 16843–16848 (2008).
359. Emptage, N. J. Fluorescent imaging in living systems. *Curr. Opin. Pharmacol.* **1**, 521–525 (2001).
360. Pope, A. J., Haupts, U. M. & Moore, K. J. Homogeneous fluorescence readouts for miniaturized high-throughput screening: theory and practice. *Drug Discov. Today* **4**, 350–362 (1999).

361. Ross, J. & Jameson, D. Time-resolved methods in biophysics. Frequency domain fluorometry: applications to intrinsic protein fluorescence. *Photochem Photobiol Sci* **7**, 1301–1312 (2008).
362. Cundall, R. *Time-Resolved Fluorescence Spectroscopy in Biochemistry and Biology*. **69**, (Springer US, 1983).
363. *High Throughput Screening*. **565**, (Humana Press, 2009).
364. Zhang, T. *et al.* High-throughput fluorescence polarization method for identifying ligands of LOX-11. *Acta Pharmacol. Sin.* **27**, 447–452 (2006).
365. Perrin, F. Polarisation de la lumière de fluorescence. Vie moyenne des molécules dans l'état excité. *J Phys Radium* **7**, 390–401 (1926).
366. Magde, D., Elson, E. & Webb, W. W. Thermodynamic fluctuations in a reacting system—measurement by fluorescence correlation spectroscopy. *Phys. Rev. Lett.* **29**, 705 (1972).
367. Kask, P., Palo, K., Ullmann, D. & Gall, K. Fluorescence-intensity distribution analysis and its application in biomolecular detection technology. *Proc. Natl. Acad. Sci.* **96**, 13756–13761 (1999).
368. Swift, K. M. & Matayoshi, E. D. High throughput screening using dynamic fluorescence. in *Photonics West'95* 182–189 (International Society for Optics and Photonics, 1995).
369. French, T. E. *et al.* Fluorescence-lifetime technologies for high-throughput screening. in *BiOS'98 International Biomedical Optics Symposium* 209–218 (International Society for Optics and Photonics, 1998).
370. French, T. E., Bailey, B., Stumbo, D. P. & Modlin, D. N. Time-resolved fluorometer for high-throughput screening. in *BiOS'99 International Biomedical Optics Symposium* 272–280 (International Society for Optics and Photonics, 1999).
371. Lebakken, C. S., Hee Chol Kang & Vogel, K. W. A Fluorescence Lifetime Based Binding Assay to Characterize Kinase Inhibitors. *J. Biomol. Screen.* **12**, 828–841 (2007).

372. Gross, S., Rahal, R., Stransky, N., Lengauer, C. & Hoeflich, K. P. Targeting cancer with kinase inhibitors. *J. Clin. Invest.* **125**, 1780–1789 (2015).
373. Doering, K. *et al.* A Fluorescence Lifetime-Based Assay for Protease Inhibitor Profiling on Human Kallikrein 7. *J. Biomol. Screen.* **14**, 1–9 (2008).
374. Pritz, S. *et al.* A Fluorescence Lifetime-Based Assay for Abelson Kinase. *J. Biomol. Screen.* **16**, 65–72 (2011).
375. Paterson, M. J. *et al.* A fluorescence lifetime-based assay for serine and threonine kinases that is suitable for high-throughput screening. *Anal. Biochem.* **402**, 54–64 (2010).
376. Maltman, B. A. *et al.* 9-Aminoacridine peptide derivatives as versatile reporter systems for use in fluorescence lifetime assays. *Chem. Commun.* **46**, 6929 (2010).
377. D.V. O'Connor & D. Phillips. *Time Correlated Single Photon Counting*. (Academic Press, London, 1984).
378. Muretta, J. M. *et al.* High-performance time-resolved fluorescence by direct waveform recording. *Rev. Sci. Instrum.* **81**, 103101 (2010).
379. Petersen, K. J. *et al.* Fluorescence lifetime plate reader: Resolution and precision meet high-throughput. *Rev. Sci. Instrum.* **85**, 113101 (2014).
380. Léonard, J. *et al.* High-throughput time-correlated single photon counting. *Lab Chip* **14**, 4338–4343 (2014).
381. F. Dadouche *et al.* Design, Implementation and Characterization of Time-to-Digital Converter on Low-Cost FPGA. in *Sensors and Applications in Measuring and Automation Control Systems* **4**, 205–229 (Ed. Sergey Y. Yurish, 2016).
382. Schottky, W. Über spontane Stromschwankungen in verschiedenen Elektrizitätsleitern. *Ann. Phys.* **362**, 541–567 (1918).

383. Hall, P. & Selinger, B. Better estimates of exponential decay parameters. *J. Phys. Chem.* **85**, 2941–2946 (1981).
384. J.-H. Zhang, T. D. Y. Chung & K. R. Oldenburg. A simple statistical parameter for use in evaluation and validation of High Throughput Screening Assays. *J Biomol Screen.* 67 (1999).
385. Becker, W. *Advanced time-correlated single photon counting techniques.* (Springer, 2005).
386. Shockley, W. The Theory of p-n Junctions in Semiconductors and p-n Junction Transistors. *Bell Labs Tech. J.* **28**, 435–489 (1949).
387. Charbon, E. CMOS integration enables massively parallel single-photon detection. *SPIE Newsroom* (2011). doi:10.1117/2.1201102.003182
388. Zappa, F., Tisa, S., Tosi, A. & Cova, S. Principles and features of single-photon avalanche diode arrays. *Sens. Actuators Phys.* **140**, 103–112 (2007).
389. Cova, S., Lacaïta, A., Ghioni, M., Ripamonti, G. & Louis, T. A. 20-ps timing resolution with single-photon avalanche diodes. *Rev. Sci. Instrum.* **60**, 1104–1110 (1989).
390. Cova, S., Longoni, A. & Andreoni, A. Towards picosecond resolution with single-photon avalanche diodes. *Rev. Sci. Instrum.* **52**, 408–412 (1981).
391. Henzler, S. *Time-to-Digital Converters.* **29**, (Springer Netherlands, 2010).
392. Nutt, R. Digital Time Intervalometer. *Rev. Sci. Instrum.* **39**, 1342–1345 (1968).
393. T. Turko *et al.* Time to Digital Converter Transfer Function Improvement using Poisson Process Events. *Signal 2016 ISBN: 978-1-61208-48*, 50–53 (2016).
394. Yuan, Q., Zhang, B., Wu, J. & Zaghloul, M. E. A high resolution time-to-digital converter on FPGA for Time-Correlated Single Photon Counting. in *Circuits and Systems (MWSCAS), 2012 IEEE 55th International Midwest Symposium on* 900–903 (IEEE, 2012).

395. García, G. *et al.* A Survey on FPGA-Based Sensor Systems: Towards Intelligent and Reconfigurable Low-Power Sensors for Computer Vision, Control and Signal Processing. *Sensors* **14**, 6247–6278 (2014).
396. Payen F W & Persoz J F. Memoire sur la diastase, les principaux produits de ses reaction, et leurs applications aux arts industriels. *Ann Chim Phys* **53**, 73–92 (1833).
397. Manchester, K. L. Louis Pasteur (1822–1895)—chance and the prepared mind. *Trends Biotechnol.* **13**, 511–515 (1995).
398. Kuhne, W. Über das Verhalten verschiedener organisirter und sog. ungeformter Fermente. *Verhandlungen Naturhistorisch-Med. Ver. Zu Heidelber* **1**, 190–193 (1877).
399. Jacques, P. *et al.* High-throughput strategies for the discovery and engineering of enzymes for biocatalysis. *Bioprocess Biosyst. Eng.* (2016). doi:10.1007/s00449-016-1690-x
400. Overington, J. P., Al-Lazikani, B. & Hopkins, A. L. How many drug targets are there? *Nat. Rev. Drug Discov.* **5**, 993–996 (2006).
401. Mario Geysen, H., Schoenen, F., Wagner, D. & Wagner, R. A guide to drug discovery: Combinatorial compound libraries for drug discovery: an ongoing challenge. *Nat. Rev. Drug Discov.* **2**, 222–230 (2003).
402. Chen, N. *et al.* Designing Protease Sensors for Real-Time Imaging of Trypsin Activation in Pancreatic Cancer Cells <sup>†</sup>. *Biochemistry (Mosc.)* **48**, 3519–3526 (2009).
403. Northrop, J. & Kunitz, M. Isolation of protein crystals possessing tryptic activity. *Science* **73**, 262–263 (1931).
404. Stroud, R. A Family of Protein-Cutting Proteins. *Sci. Am.* **231**, 74–88 (1974).
405. Whitcomb, D., Gorry, M., Preston, R. & Furey, W. Hereditary pancreatitis is caused by a mutation in the cationic trypsinogen gene. *Nature* **14**, 141–145 (1996).

406. Hirota, M., Ohmuraya, M. & Baba, H. The role of trypsin, trypsin inhibitor, and trypsin receptor in the onset and aggravation of pancreatitis. *J. Gastroenterol.* **41**, 832–836 (2006).
407. Skilitsi, A. I. *et al.* Ultrafast, Solvation-Controlled Excited-State Intramolecular Proton Transfer in 4'-Methoxy-3-Hydroxyflavone. in *International Conference on Ultrafast Phenomena* UW4A–31 (Optical Society of America, 2016).
408. Skilitsi, A. I. *et al.* Towards sensitive, high-throughput, biomolecular assays based on fluorescence lifetime. *Methods Appl. Fluoresc.* **5**, 34002 (2017).



**Thèse** présentée par :

**Anastasia Ioanna Skilitsi**

soutenue le: **30 Novembre 2017**

pour obtenir le grade de : **Docteur de l'Université de Strasbourg**

Discipline/ Spécialité: **Physique**

## **Applications de la spectroscopie ultrarapide à l'étude de sondes locales d'environnement et d'interactions biomoléculaires**



**Directeur de thèse: Dr. Léonard Jérémie** Chargé de recherche CNRS, IPCMS

**Rapporteurs: Dr. Ameer-Beg Simon** (Professeur, King's College London), **Dr. Mérola Fabienne** (Directeur de Recherche, Université Paris Sud)

**Examineurs: Dr. Didier Pascal** (Professeur, Université de Strasbourg), **Dr. Hassiepen Ulrich** (Research Investigator, Novartis Basel)

La compréhension approfondie des interactions dynamiques biomoléculaires est essentielle pour le diagnostic et le traitement des maladies<sup>1</sup> ainsi que pour la conception de produits hautement fonctionnels, tels que les nanoparticules appliquées dans l'industrie alimentaire<sup>2</sup> et les cosmétiques utilisés dans la vie quotidienne.

La caractéristique fondamentale des interactions biomoléculaires pour l'adaptabilité fonctionnelle et la polyvalence est leur hétérogénéité structurale, c'est-à-dire la coexistence de multiples conformations moléculaires. Les structures, les abondances relatives et la dynamique des différentes conformations doivent être identifiées car elles contiennent des informations cruciales sur le mécanisme biologique au niveau moléculaire. Plusieurs techniques de haute ou très haute résolution spatiale telles que la spectroscopie par résonance magnétique nucléaire (RMN), la spectrométrie de masse, la microscopie à

force atomique (AFM) etc. ont été appliquées dans cette direction<sup>3-9</sup>. Cependant, dans la plupart des cas, elles révèlent des structures moyennes et ne sont donc pas adaptées pour résoudre l'hétérogénéité structurale. D'autre part, les méthodes de spectroscopie de fluorescence se sont avérées être des outils puissants pour l'étude quantitative et qualitative des interactions biomoléculaires homologues et hétérologues. En dépit d'une résolution spatiale relativement faible, les spectroscopies de fluorescence résolues en temps ou sur molécule unique restent uniques pour révéler l'hétérogénéité structurale, les intermédiaires structuraux, les conformations hautement fluctuantes ou intrinsèquement désordonnées<sup>10-13</sup>.

La spectroscopie de fluorescence résolue dans le temps (TRF) a longtemps été une flèche importante dans le carquois de la spectroscopie de fluorescence, appliquée pour étudier les interactions et la structure biomoléculaires. A cette fin, des fluorophores sensibles à l'environnement peuvent être utilisés pour marquer de manière synthétique des macromolécules biologiques et rendre compte de leurs changements structuraux locaux. De telles sondes structurales sont choisies ou spécifiquement fonctionnalisées pour tirer profit des changements de leurs propriétés de fluorescence en réponse à une modification physicochimique de leur microenvironnement, telle qu'une différence de polarité, de liaison hydrogène, de pH, etc.

La TRF étudie les événements se produisant pendant la durée de vie de l'état singulet excité chromophore. Cette échelle de temps va de subpicosecondes à des dizaines de nanosecondes. Les événements photophysiques se produisant dans ce domaine temporel comprennent une interaction avec des molécules de solvant ou des changements conformationnels structuraux locaux provoquant l'interaction avec des résidus d'acides aminés voisins ou des nucléotides. En général, la cinétique de décroissance de fluorescence est résolue en termes de composantes multi-exponentielles, où les valeurs des constantes de temps et leurs amplitudes correspondantes sont associées à des conformations particulières et à leurs populations relatives. L'interprétation structurale quantitative reste en revanche difficile et nécessite une compréhension profonde du mécanisme photophysique fondamental contrôlant les propriétés émissives des fluorophores. En outre, des changements conformationnels à grande échelle dans les biomolécules, tels que le repliement des protéines ou la liaison des ligands, qui se connectent aux fonctions biologiques efficaces, se produisent à des échelles de temps<sup>14,15</sup> (ms à sec) plus longues que celles accessibles avec TRF. D'autres approches expérimentales peuvent être utilisées, telles que des expériences de type « stopped-flow », pour déclencher sur une échelle de temps suffisamment courte les conditions hors d'équilibre qui entraînent une dynamique structurale plus lente ou un échange de population entre des sous-populations. Dans ce contexte, dans la présente thèse, la spectroscopie résolue en temps a été appliquée pour étudier la photophysique de différents systèmes moléculaires sensibles à l'environnement, mais aussi comme outil innovant pour révéler des interactions moléculaires ou dynamiques structurales sur une échelle de temps beaucoup plus lente en combinaison avec la microfluidique de gouttes pour déclencher la relaxation structurale par des conditions initiales hors d'équilibre. Trois projets ont été développés avec succès dans la présente thèse de doctorat en collaboration avec des domaines interdisciplinaires de la science.

Le premier projet visait l'étude fondamentale de la photoréactivité d'un dérivé de 3-Hydroxyflavone (3HF) 16,17, nommé 4-Methoxy-3-Hydroxyflavone (4M3HF). Comme représenté sur la Figure 1, 4M3HF porte un groupe méthoxy en position para sur le fragment 2-phényle.

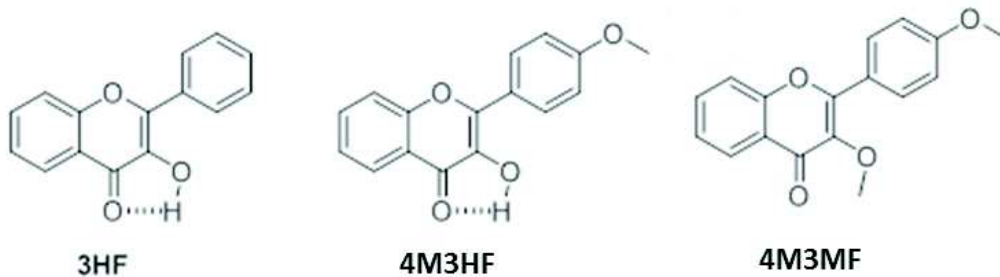


Figure 1-Structure de 3HF, 4M3HF et du dérivé 4M3HF méthylé (4M3MF).

Les dérivés de 3HF subissent un transfert de proton intramoléculaire à l'état excité (ESIPT)<sup>16</sup>, selon le mécanisme suivant (Figure 2). L'absorption d'un photon produit l'état N\* (normal) suivi de la relaxation de la couche de solvation. Par la suite, l'état N\* peut émettre un photon ou subir l'ESIPT produisant l'état T\* (tautomérique). L'émission d'un photon à partir de T\* produit l'état fondamental T avec une relaxation subséquente et un transfert du proton inverse vers l'état N, fermant le photocycle. Ceci résulte en deux bandes d'émission bien séparées résultant de la formation de deux espèces excitées (N\* normal et T\* tautomère). L'intensité relative de ces deux bandes est contrôlée par la vitesse ou le déplacement d'équilibre de la réaction ESIPT, eux-mêmes influencés par la nature physico-chimique de l'environnement local. Le rapport des intensités de fluorescence des deux bandes apparaît donc comme un sonde intrinsèque du microenvironnement du fluorophore<sup>17</sup>. Pour cette raison, les dérivés de 3HF sont utilisés comme sondes locales des interactions biomoléculaires et des changements conformationnels correspondants<sup>18,19</sup>.

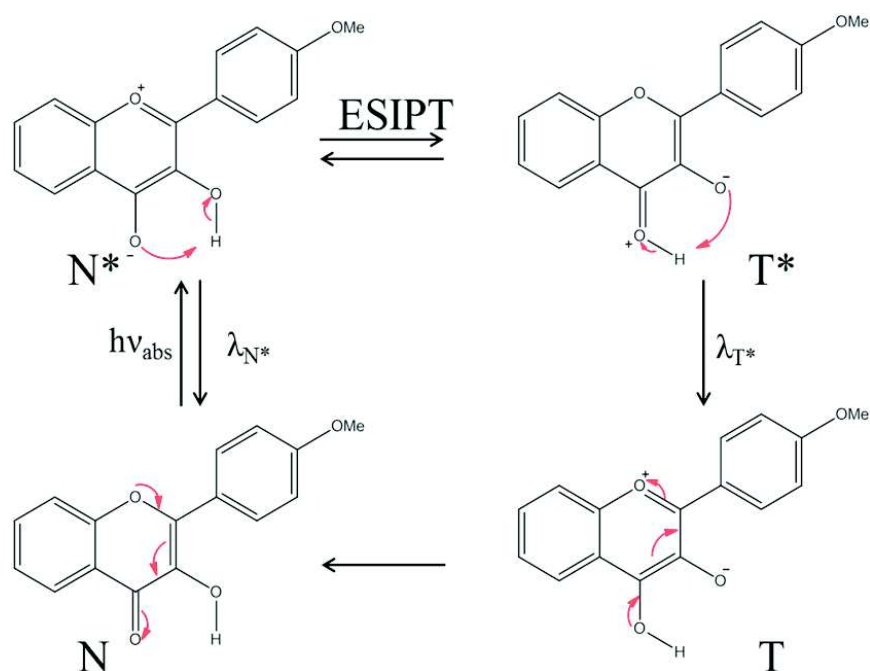


Figure 2-Illustration schématique de la réaction d'ESIPT dans 4M3HF.

Dans la présente étude, les spectroscopies d'absorption transitoire (c'est-à-dire pompe-sonde) et de fluorescence résolue dans le temps, ainsi que des mesures de rendement quantique et d'absorption à l'état stationnaire ont été effectuées pour 4M3HF. La photophysique de ce composé a été systématiquement étudiée dans quatre solvants différents caractérisés par des polarités et des capacités de liaison H différentes: méthanol (MeOH, polaire, protique), diméthylformamide (DMF, polaire, aprotique mais accepteur de liaison H), acétonitrile (ACN, polaire, aprotique) et toluène (non polaire, aprotique). Afin de distinguer les signatures spécifiques de solvation ou de dynamique intramoléculaire de celles de la réaction ESIPT, nous étudions également un second composé (voir Figure 1), où le groupe 3-hydroxyle est remplacé par un groupe 3-méthoxyle, empêchant ainsi la réaction ESIPT.

La Figure 3 montre les spectres d'absorption et d'émission à l'état d'équilibre des deux composés dans les quatre solvants correspondants. Pour les deux composés, les spectres d'absorption sont faiblement affectés par le solvant, avec une longueur d'onde d'absorption maximale  $\lambda_{max}$  à 350-355 nm pour 4M3HF et à 325-330 nm pour le composé méthylé. Dans ce dernier composé, l'ESIPT est interdite en raison de la méthylation du groupe 3-OH, seule une bande d'émission N\* à un  $\lambda_{max}$  de 430-440 nm apparaît, spectralement peu dépendante du solvant.

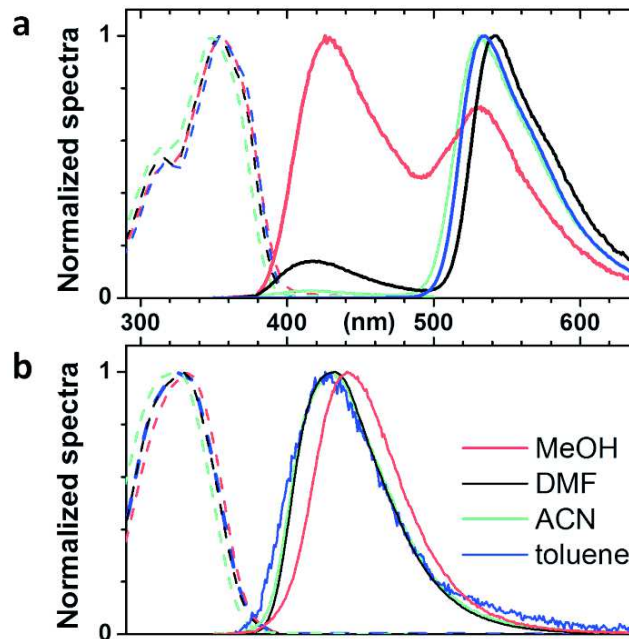


Figure 3-Les spectres d'absorption à l'état stationnaire (lignes pointillées) et d'émission (lignes pleines) de a. 4M3HF et b. 4M3MF pour lequel aucune réaction d'ESIPT n'est possible, en MeOH (rouge), DMF (noir), ACN (vert) et toluène (bleu).

L'étude détaillée de la cinétique de la réaction ESIPT de 4M3HF dans divers solvants par spectroscopie ultrarapide révèle la gamme remarquablement large de taux de réactions d'ESIPT qui sont observés en fonction des capacités de liaison H de son microenvironnement. Ceci est attribué à la force intermédiaire, bien adaptée, du donneur d'électrons du groupe 4'-MeO, qui affaiblit la liaison H intramoléculaire de ce composé (par rapport à 3HF), et réduire le caractère de transfert de charge du N\* état par rapport à 4'-dialkylamino-3HF. Cette gamme élargie d'échelles de temps de la réaction d'ESIPT (couvrant plus de 3 ordres de grandeur de 100 fs à 100 ps) améliore la sensibilité du composé utilisé comme sonde de liaisons H avec son microenvironnement, et donc comme sonde fluorescente pour la structure ou les interactions des protéines<sup>20-22</sup>. En outre, cette distribution des taux d'ESIPT permet de mettre en évidence une distribution de sous-populations de chromophores subissant divers degrés de liaisons H avec leur microenvironnement. Le 4M3HF apparaît donc comme une sonde structurale prometteuse de l'hétérogénéité structurale locale, c'est-à-dire de la coexistence de multiples conformères biomoléculaires, à condition que la distribution des taux d'ESIPT correspondants soit résolue dans le temps.

2. Dans le deuxième projet, l'accent a été mis sur les propriétés de fluorescence de deux dérivés de la protéine fluorescente verte (GFP), à savoir la Protéine Fluorescente Enhanced-Cyan (ECFP) et l'un de ses mutants, portant une mutation ponctuelle sur la position H148. L'ECFP est à ce jour la molécule la protéine fluorescente (FP) la plus largement utilisée pour les expériences de transfert résonant d'énergie de Förster (FRET)<sup>23-28</sup>. ECFP subit des conformations structurales sensibles au pH résultant en une altération de la cinétique de décroissance multiexponentielle de fluorescence<sup>29-32</sup>. Afin de contribuer à corréler la structure des protéines avec leurs propriétés de fluorescence, nous avons caractérisé la

cinétique de relaxation de structure et donc de changement de propriétés d'émission de fluorescence sous un saut de pH.

À cette fin, une nouvelle approche expérimentale basée sur la combinaison de la microfluidique de gouttes avec la TRF offre la possibilité d'étudier la dynamique de relaxation de systèmes biomoléculaires structurellement hétérogènes. La microfluidique de gouttes a été utilisée pour produire un système moléculaire hors d'équilibre par mélange rapide, et la détection TRF a été utilisée comme rapporteur de l'hétérogénéité structurelle le long de la relaxation du système pendant sa propagation le long du canal microfluidique.

Des études de relaxation structurelle dans des biomolécules hors d'équilibre utilisant la détection de TRF ont déjà été mises en œuvre avec des appareils à écoulement arrêté<sup>33-35</sup> et à flux continu<sup>36-39</sup>. Ces approches ont permis de rendre compte de l'hétérogénéité structurelle et des intermédiaires structuraux tout au long de la réaction. Dans la présente étude, TRF est combiné avec La microfluidique de gouttes, conduisant à une approche plus avantageuse. La microfluidique de gouttes offre un mélange rapide (ms), de longs temps de propagation sans dispersion de réactif et une relation précise entre la distance de propagation et le temps. Par conséquent, la relaxation structurelle des complexes moléculaires hors d'équilibre peut être suivie de quelques ms à plusieurs secondes. Pour les expériences de saut de pH, comme illustré sur la Figure 4, le mélange est réalisé dans une « jonction en T » avec deux entrées de solution tampon hautement concentré de pH 5, une entrée contenant 1  $\mu$ M de protéine ECFP dans une solution tampon faiblement concentrée à pH 7,4 et la dernière contenant de l'huile non miscible. Les gouttelettes sont d'environ 250 pl et se propagent avec une vitesse de 12 mm / s dans le canal microfluidique, avec un temps de mélange (temps moyen nécessaire pour obtenir un mélange homogène) de 25 ms.

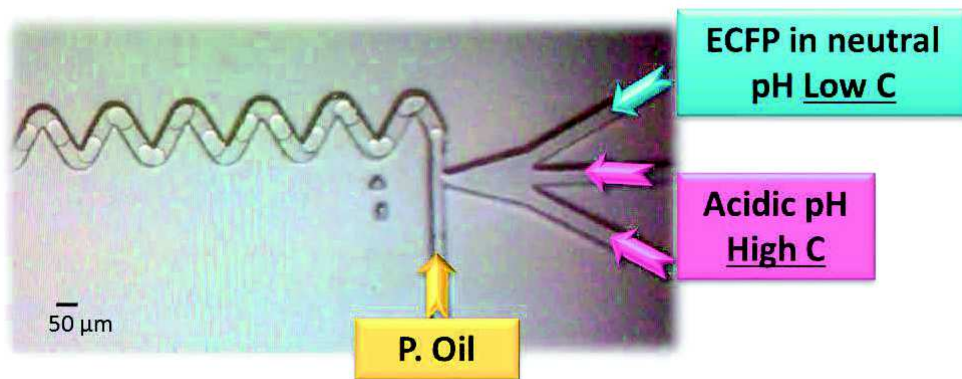


Figure 4-Puce microfluidique-photographie de la jonction « T » d'une puce microfluidique.

Par la suite, une imagerie à champ large de la puce microfluidique est réalisée le long de la photocathode linéaire d'une caméra à balayage de fente tel que représenté sur la Figure 5. En détail: La puce microfluidique est éclairée par une nappe de lumière produite par une lentille cylindrique et imagée sur la photocathode d'une caméra à balayage de fente (SC). La photocathode est un fil de 4,5 mm de long

offrant un champ de vision de 2 mm de large avec la configuration optique actuelle. Dans ces conditions, plusieurs déclins de fluorescence peuvent être enregistrés simultanément à différents endroits correspondant à des temps de propagation différents dans le canal microfluidique. Les données acquises avec le SC le long du canal microfluidique principal ont été organisées dans une matrice incorporant des courbes de décroissance de fluorescence en fonction du temps de propagation. De nombreuses traces de déclin de fluorescence sont enregistrées successivement à des endroits consécutifs le long du canal microfluidique principal. Chaque déclin de fluorescence résulte de la moyenne sur un grand nombre de gouttelettes identiques successives acquises à différents temps de réaction. La cinétique de la décroissance de la fluorescence peut être enregistrée sur des fenêtres temporelles distinctes de quelques ns à microsec, la fenêtre temporelle la plus courte offrant la meilleure résolution temporelle de  $\sim 8$  ps.

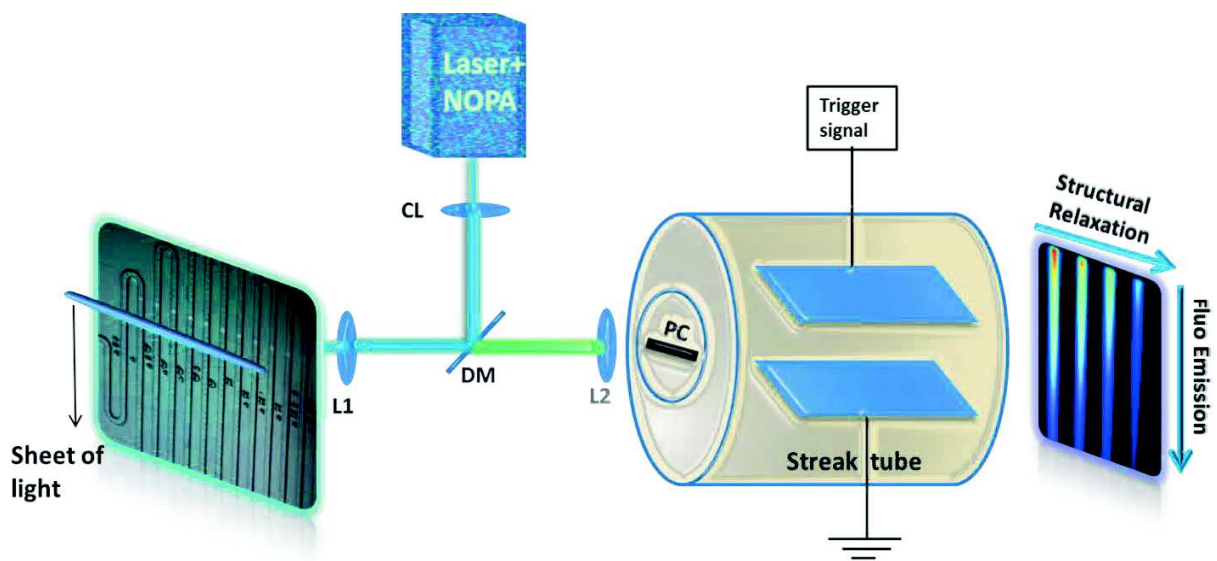


Figure 5- Illustration schématique du montage combinant la microfluidique de gouttes avec TRF. La fluorescence émise par des gouttelettes individuelles circulant dans le canal microfluidique principal est imagée le long du fil photocathode (PC) d'une caméra à balayage. Les jeux de données 2D sont acquis avec la dimension le long du fil PC étant l'axe du temps de relaxation structurale (propagation dans la puce microfluidique sur quelques secondes) et la seconde dimension étant la cinétique de décroissance de fluorescence, qui révèle la distribution des durées de vie.

Les applications de cette approche originale ont été étendues avec l'expérience de saut de pH qui a permis le suivi de la relaxation structurale dans les protéines fluorescentes. Celle-ci vise la caractérisation simultanée de la dynamique de relaxation structurale induite par le pH (durant l'échelle temporelle de propagation des gouttelettes dans le canal microfluidique) tout en révélant l'hétérogénéité structurale transitoire (codée dans la cinétique de décroissance multiexponentielle de la fluorescence).

Les données enregistrées supportent l'hypothèse que les temps de déclin de fluorescence correspondent à des structures protéiques distinctes préexistantes dans l'état fondamental (c'est-à-dire une hétérogénéité structurale). Il semble que la photoréactivité (durée de vie de l'état excité) du

chromophore affichant la constante de temps la plus courte soit peu affectée par les changements structuraux induits par le pH. Cette constante de temps correspondrait à une structure protéique où la poche de liaison du chromophore est peu affectée par le pH. Les sous-populations de la protéine ECFP, correspondant aux chromophores à vie longue, sont affectées par le pH. Pour cette population, la durée de vie des chromophores excités passe de 3,5 ns à pH 7,4 à 2,65 ns à pH 5 en raison d'un changement structurel intervenant sur l'échelle de temps de 320 ms, qui modifie l'interaction locale du chromophore avec sa poche de liaison. Les présents résultats mettent en évidence un changement de configuration lent, induit par le pH, se produisant dans l'état fondamental. Ce phénomène lent suggère que le mécanisme structurel peut impliquer un franchissement de barrière de potentiel élevé, éventuellement causé par un changement structurel important ou un ensemble de changements structurels nécessairement concomitants conduisant à un événement différent.

D'autre part, la comparaison détaillée de ECFP avec son ECFP-H148G mutant fournit des informations précieuses sur la relation entre la structure de la protéine et ses propriétés de fluorescence. Cela permet la prédiction de mutations supplémentaires conduisant à des protéines de fluorescence optique appropriées pour l'imagerie quantitative et l'interprétation des données solides. D'autre part, le deuxième objectif de ce projet était de démontrer l'application de l'approche expérimentale originale combinant TRF et Droplet Microfluidics pour les études d'interactions biomoléculaires. Le travail expérimental présenté a montré que cette nouvelle configuration expérimentale peut efficacement révéler la dynamique structurelle sur des ms à sec (ou même min avec l'aide d'un canal principal plus long). Cette approche jette ainsi les bases d'une recherche plus approfondie des interactions au sein de complexes biomoléculaires hors d'équilibre.

3. Dans le troisième projet, avec un objectif de recherche plus appliqué, la mise en œuvre du TRF par comptage de photons uniques corrélés au temps (TCSPC) dans des conditions de très haut débit a été explorée comme un moyen d'effectuer des analyses biomoléculaires efficaces pour les arènes académiques et industrielles. Le criblage à haut débit (HTS) est généralement la première étape vers la découverte de médicaments. Une fois qu'une cible potentiellement intéressante est identifiée, un point de départ moléculaire peut être trouvé en "criblant" systématiquement l'interaction avec un grand nombre de composés (c'est-à-dire de petites molécules). Par exemple, la société Novartis Pharma possède environ 2,5 millions de composés dans sa bibliothèque. Un test doit être rapide, fiable et rentable. L'intensité de fluorescence (FLINT) est, de loin, la méthode la plus utilisée au fil des ans. Cependant, bien que ce soit une méthode facilement appliquée (instrumentation simple) et sensible, elle est sans défense contre les perturbations du signal causées par les différences de concentration, de fluctuation de la source laser, d'auto-fluorescence etc. Les mesures ratiométriques limitent dans une certaine mesure ces problèmes, bien qu'elles ne fournissent en aucun cas une solution complète. À ce stade, l'originalité de ce projet a consisté à remplacer l'intensité de la fluorescence par la détection de la durée de vie de la fluorescence, ce qui est technologiquement plus difficile. L'avantage pour la bio-détection, cependant, est que la durée de vie de fluorescence d'un fluorophore est une mesure intrinsèque du fluorophore interagissant avec son environnement, restant non affecté par les conditions de préparation de l'échantillon. La combinaison des outils susmentionnés avec une approche d'ingénierie innovante (microélectronique, collaboration avec ICUBE) a conduit à démontrer que TCSPC peut être mis

en œuvre dans des conditions de très haut débit dans la microfluidique de gouttes, comme illustré sur la Figure 6. Les avantages de cette configuration sont: la très faible consommation de molécules et la très grande vitesse de manipulations des échantillons atteignant le kHz ( 1000 gouttelettes/s).

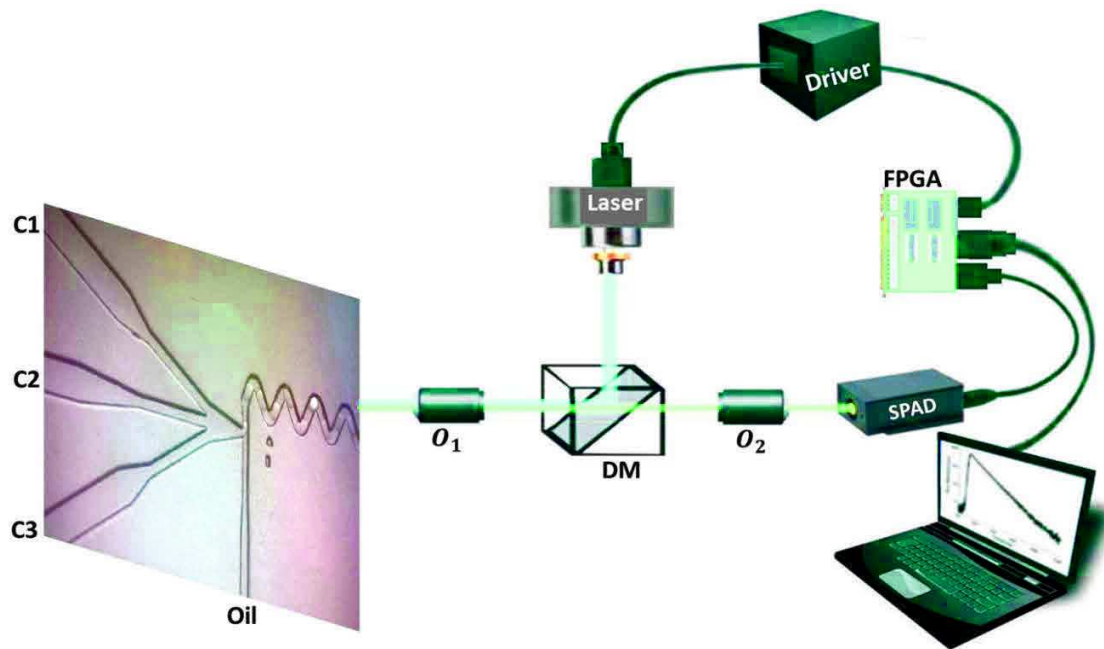


Figure 6- Illustration schématique de l'expérience. Un microscope à fluorescence est utilisé pour exciter et collecter l'émission de fluorescence dans des gouttelettes microfluidiques (objectifs O1, O2 microscope, miroir dichroïque DM). Des gouttes d'eau dans l'huile sont générées dans une puce microfluidique PDMS au niveau d'une jonction dite T où trois entrées d'eau (C1-C3) croisent un canal d'huile. Une installation de détection TCSPC à faible coût fonctionnant à haut débit a été développée, y compris un laser à diode rentable et son pilote maison pour l'émission pulsée, un SPAD commercial et un TDC maison basé FPGA qui permet un traitement rapide, à la volée de événements de détection de photons uniques.

Le passage des gouttelettes successives, devant le point laser de focalisation, est automatiquement détecté. Le temps d'acquisition de fluorescence était de 3 ms par gouttelette de 100 pl de volume. Des histogrammes de déclin de fluorescence composés d'une moyenne de 2300 photons ont été acquis pour des gouttes individuelles. Pour une meilleure précision, la somme de plusieurs gouttelettes a été faite, résultant en un plus grand nombre de photons acquis. Dans le cas présenté sur la figure 7, la somme des histogrammes de dix gouttelettes successives identiques a été réalisée avec un ajustement monoexponentiel. Cela s'est traduit par un temps d'acquisition de 30 ms et 10 fois plus de photons (23000 photons).

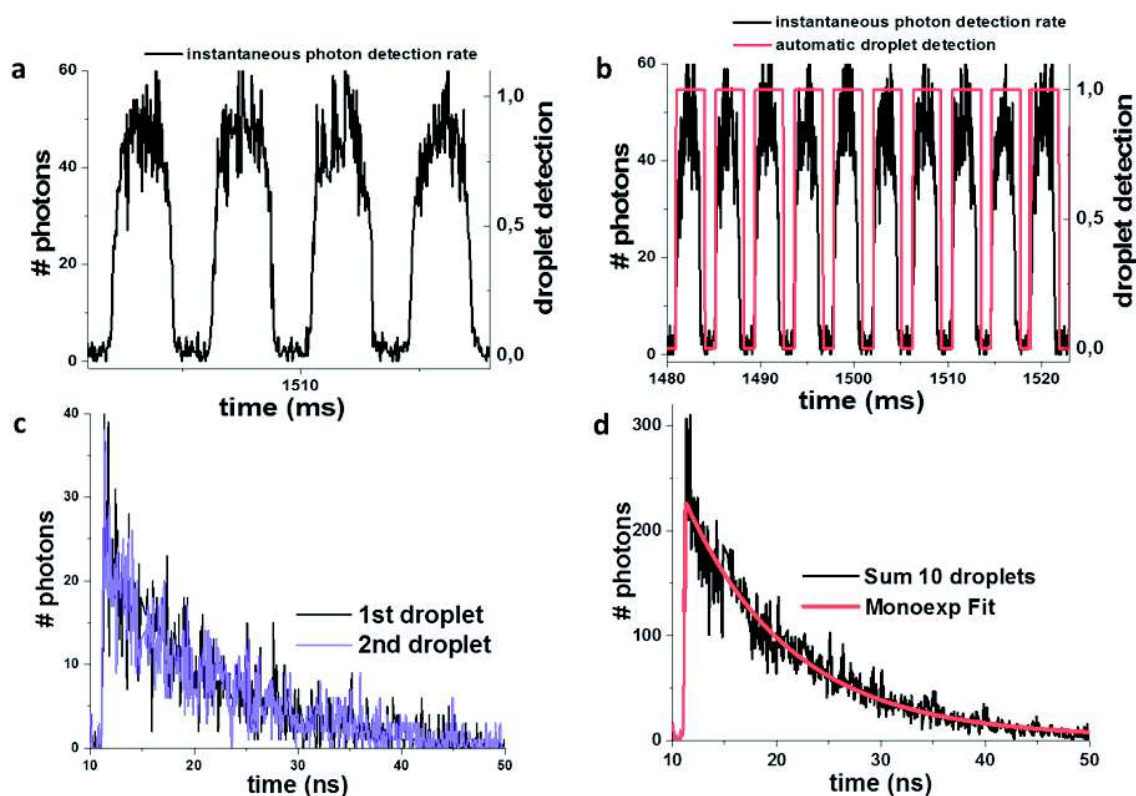


Figure 7- Implémentation de la détection TCSPC dans les gouttelettes microfluidiques. a. Taux de détection instantané des photons en fonction du temps (ligne noire). b. Le passage des gouttelettes successives dans le spot laser focalisé est automatiquement détecté (ligne rouge). Dans cet exemple, le temps d'acquisition de fluorescence est de  $\sim 3$  ms par gouttelette, qui est le temps de circulation des gouttelettes à travers le faisceau laser. c. Histogrammes de décroissance de fluorescence de deux gouttelettes successives, composées de  $\sim 2300$  photons chacune. d. Somme des histogrammes de dix gouttelettes identiques et successives avec un ajustement mono-exponentiel (ligne rouge).

Après avoir décrit la mise en œuvre technique, le potentiel de l'approche a été illustré en démontrant la faisabilité d'un test d'activité enzymatique reposant sur la détection du FLT par TCSPC, dans des conditions de très haut débit, dans des gouttelettes microfluidiques. Le choix d'un test d'activité enzymatique comme validation de la détection d'interaction biomoléculaire a été motivé par l'intérêt biotechnologique élevé pour les enzymes<sup>43-46</sup>.

Ainsi, les implications techniques du présent projet étaient de deux ordres. Tout d'abord, il a démontré que la détection FLT est réalisable avec une bonne précision dans des échantillons de très petits volumes et des quantités de chromophores à un débit de détection élevé. Ceci ouvre la voie au remplacement de la détection FLINT par FLT pour des applications biotechnologiques à haut débit, y compris par ex. tri de cellules assisté par fluorescence (FACS)<sup>47,48</sup>. Deuxièmement, il offrait une détection de FLT qui est plus sensible à d'autres techniques proposées et également (sinon plus efficacement) applicable à l'acquisition à haut débit et au HTS en particulier, également dans les lecteurs de microplaques conventionnels.

En conclusion, dans ce travail de doctorat, de nombreuses méthodes, statiques ou résolues en temps, ont été utilisées afin d'obtenir des informations détaillées sur les sondes fluorescentes sensibles à l'environnement et dédiées aux études d'interactions biomoléculaires. Chaque approche a été sélectionnée avec soin afin d'adresser la réponse des sondes fluorescentes aux différentes propriétés physicochimiques de leur microenvironnement, telles que la différence de liaison hydrogène pour le dérivé 3-Hydroxyflavone, différence de pH pour l'ECFP et son mutant ou finalement présence ou absence d'enzyme active. Toutes les recherches ci-dessus peuvent être utilisées comme point de départ pour de nombreuses autres applications.

## References

1. Trojanowski, J. Q. & LEE, V. M.-Y. 'Fatal attractions' of proteins: a comprehensive hypothetical mechanism underlying Alzheimer's disease and other neurodegenerative disorders. *Ann. N. Y. Acad. Sci.* **924**, 62–67 (2000).
2. Sanguansri, P. & Augustin, M. A. Nanoscale materials development – a food industry perspective. *Trends Food Sci. Technol.* **17**, 547–556 (2006).
3. Palmer, A. G. NMR Characterization of the Dynamics of Biomacromolecules. *Chem. Rev.* **104**, 3623–3640 (2004).
4. Zuiderweg, E. R. P. Mapping Protein–Protein Interactions in Solution by NMR Spectroscopy<sup>†</sup>. *Biochemistry (Mosc.)* **41**, 1–7 (2002).
5. Markwick, P. R. L., Malliavin, T. & Nilges, M. Structural Biology by NMR: Structure, Dynamics, and Interactions. *PLoS Comput. Biol.* **4**, e1000168 (2008).
6. Stocks, B. B. & Konermann, L. Time-Dependent Changes in Side-Chain Solvent Accessibility during Cytochrome c Folding Probed by Pulsed Oxidative Labeling and Mass Spectrometry. *J. Mol. Biol.* **398**, 362–373 (2010).
7. Stolz, M., Stoffler, D., Aebi, U. & Goldsbury, C. Monitoring Biomolecular Interactions by Time-Lapse Atomic Force Microscopy. *J. Struct. Biol.* **131**, 171–180 (2000).
8. Willemsen, O. H. *et al.* Biomolecular interactions measured by atomic force microscopy. *Biophys. J.* **79**, 3267–3281 (2000).
9. Guo, H., Peng, H. & Emili, A. Mass spectrometry methods to study protein-metabolite interactions. *Expert Opin. Drug Discov.* 1–10 (2017). doi:10.1080/17460441.2017.1378178
10. Haustein, E. & Schwille, P. Single-molecule spectroscopic methods. *Curr. Opin. Struct. Biol.* **14**, 531–540 (2004).

11. Xie, Z., Srividya, N., Sosnick, T. R., Pan, T. & Scherer, N. F. Single-molecule studies highlight conformational heterogeneity in the early folding steps of a large ribozyme. *Proc. Natl. Acad. Sci. U. S. A.* **101**, 534–539 (2004).
12. Hovius, R., Vallotton, P., Wohland, T. & Vogel, H. Fluorescence techniques: shedding light on ligand-receptor interactions. *Trends Pharmacol. Sci.* **21**, 266–273 (2000).
13. Weiss, S. Fluorescence Spectroscopy of Single Biomolecules. *Science* **283**, 1676–1683 (1999).
14. Al-Hashimi, H. M. & Walter, N. G. RNA dynamics: it is about time. *Curr. Opin. Struct. Biol.* **18**, 321–329 (2008).
15. Henzler-Wildman, K. & Kern, D. Dynamic personalities of proteins. *Nature* **450**, 964–972 (2007).
16. Zhao, J., Ji, S., Chen, Y., Guo, H. & Yang, P. Excited state intramolecular proton transfer (ESIPT): from principal photophysics to the development of new chromophores and applications in fluorescent molecular probes and luminescent materials. *Phys Chem Chem Phys* **14**, 8803–8817 (2012).
17. Klymchenko, A. S. & Demchenko, A. P. Multiparametric probing of intermolecular interactions with fluorescent dye exhibiting excited state intramolecular proton transfer. *Phys. Chem. Chem. Phys.* **5**, 461–468 (2003).
18. Demchenko, A. P., Mély, Y., Duportail, G. & Klymchenko, A. S. Monitoring biophysical properties of lipid membranes by environment-sensitive fluorescent probes. *Biophys. J.* **96**, 3461–3470 (2009).
19. Loving, G. S., Sainlos, M. & Imperiali, B. Monitoring protein interactions and dynamics with solvatochromic fluorophores. *Trends Biotechnol.* **28**, 73–83 (2010).
20. Zamotaiev, O. M. *et al.* Improved Hydration-Sensitive Dual-Fluorescence Labels For Monitoring Peptide–Nucleic Acid Interactions. *Bioconjug. Chem.* **22**, 101–107 (2011).
21. Dziuba, D. *et al.* Rational Design of a Solvatochromic Fluorescent Uracil Analogue with a Dual-Band Ratiometric Response Based on 3-Hydroxychromone. *Chem. - Eur. J.* **20**, 1998–2009 (2014).

22. Sholokh, M. *et al.* Fluorescent Amino Acid Undergoing Excited State Intramolecular Proton Transfer for Site-Specific Probing and Imaging of Peptide Interactions. *J. Phys. Chem. B* **119**, 2585–2595 (2015).
23. Otto-Duessel, M., Tew, B. Y., Vonderfecht, S., Moore, R. & Jones, J. O. Identification of neuron selective androgen receptor inhibitors. *World J. Biol. Chem.* **8**, 138 (2017).
24. Corby, M. J. *et al.* Quantitative microspectroscopic imaging reveals viral and cellular RNA helicase interactions in live cells. *J. Biol. Chem.* **292**, 11165–11177 (2017).
25. Knorr, J. M., Jackson, J., Batie, M. R., Narmoneva, D. A. & Jones, D. C. Application of strain and calibration of Förster Resonance Energy Transfer (FRET) emission for in vitro live cell response to cytoskeletal deformation. *J. Biomech.* **49**, 3334–3339 (2016).
26. Scott, B. L. & Hoppe, A. D. Three-Dimensional Reconstruction of Three-Way FRET Microscopy Improves Imaging of Multiple Protein-Protein Interactions. *PLOS ONE* **11**, e0152401 (2016).
27. Bozza, W. P. *et al.* The Use of a Stably Expressed FRET Biosensor for Determining the Potency of Cancer Drugs. *PLoS ONE* **9**, e107010 (2014).
28. He, L. *et al.* Flow cytometric measurement of fluorescence (Förster) resonance energy transfer from cyan fluorescent protein to yellow fluorescent protein using single-laser excitation at 458 nm. *Cytometry* **53A**, 39–54 (2003).
29. Seifert, M. H. J. *et al.* Slow Exchange in the Chromophore of a Green Fluorescent Protein Variant. *J. Am. Chem. Soc.* **124**, 7932–7942 (2002).
30. Hyun Bae, J. *et al.* Expansion of the Genetic Code Enables Design of a Novel ‘Gold’ Class of Green Fluorescent Proteins. *J. Mol. Biol.* **328**, 1071–1081 (2003).
31. Villoing, A. *et al.* Complex Fluorescence of the Cyan Fluorescent Protein: Comparisons with the H148D Variant and Consequences for Quantitative Cell Imaging<sup>†</sup>. *Biochemistry (Mosc.)* **47**, 12483–12492 (2008).

32. Mérola, F., Erard, M., Fredj, A. & Pasquier, H. Engineering fluorescent proteins towards ultimate performances: lessons from the newly developed cyan variants. *Methods Appl. Fluoresc.* **4**, 12001 (2016).
33. Lyubovitsky, J. G., Gray, H. B. & Winkler, J. R. Mapping the Cytochrome c Folding Landscape. *J. Am. Chem. Soc.* **124**, 5481–5485 (2002).
34. Ratner, V., Sinev, M. & Haas, E. Determination of intramolecular distance distribution during protein folding on the millisecond timescale. *J. Mol. Biol.* **299**, 1363–1371 (2000).
35. Beechem, J. M. & Haas, E. Simultaneous determination of intramolecular distance distributions and conformational dynamics by global analysis of energy transfer measurements. *Biophys. J.* **55**, 1225–1236 (1989).
36. Bilsel, O., Kayatekin, C., Wallace, L. A. & Matthews, C. R. A microchannel solution mixer for studying microsecond protein folding reactions. *Rev. Sci. Instrum.* **76**, 14302 (2005).
37. Batabyal, S., Rakshit, S., Kar, S. & Pal, S. K. An improved microfluidics approach for monitoring real-time interaction profiles of ultrafast molecular recognition. *Rev. Sci. Instrum.* **83**, 43113 (2012).
38. Kimura, T., Lee, J. C., Gray, H. B. & Winkler, J. R. Site-specific collapse dynamics guide the formation of the cytochrome c' four-helix bundle. *Proc. Natl. Acad. Sci.* **104**, 117–122 (2007).
39. Benningen, R. *et al.* Time-resolved fluorescence imaging of solvent interactions in microfluidic devices. *Opt. Express* **13**, 6275–6285 (2005).
40. Song, H. & Ismagilov, R. F. Millisecond Kinetics on a Microfluidic Chip Using Nanoliters of Reagents. *J. Am. Chem. Soc.* **125**, 14613–14619 (2003).
41. Srisa-Art, M., Dyson, E. C., deMello, A. J. & Edel, J. B. Monitoring of Real-Time Streptavidin–Biotin Binding Kinetics Using Droplet Microfluidics. *Anal. Chem.* **80**, 7063–7067 (2008).
42. Benz, C., Retzbach, H., Nagl, S. & Belder, D. Protein–protein interaction analysis in single microfluidic droplets using FRET and fluorescence lifetime detection. *Lab. Chip* **13**, 2808 (2013).

43. Cohen, P. Protein kinases—the major drug targets of the twenty-first century? *Nat. Rev. Drug Discov.* **1**, 309–315 (2002).
44. Turk, B. Targeting proteases: successes, failures and future prospects. *Nat. Rev. Drug Discov.* **5**, 785–799 (2006).
45. Drag, M. & Salvesen, G. S. Emerging principles in protease-based drug discovery. *Nat. Rev. Drug Discov.* **9**, 690–701 (2010).
46. Jacques, P. *et al.* High-throughput strategies for the discovery and engineering of enzymes for biocatalysis. *Bioprocess Biosyst. Eng.* (2016). doi:10.1007/s00449-016-1690-x
47. Mazutis, L. *et al.* Single-cell analysis and sorting using droplet-based microfluidics. *Nat. Protoc.* **8**, 870–891 (2013).
48. Baret, J.-C. *et al.* Fluorescence-activated droplet sorting (FADS): efficient microfluidic cell sorting based on enzymatic activity. *Lab. Chip* **9**, 1850 (2009).

**Summary in English**

In the context of the present thesis, UV-Vis time-resolved spectroscopy was applied targeting the photophysics investigation of different environmentally sensitive molecular systems, but also as a biosensing approach to reveal molecular interactions or structural dynamics on much slower time scales (sec to min), using droplet microfluidics triggering structural relaxation through out-of-equilibrium initial conditions. I thus investigated on a three-axis-target spanning from 1) the in-depth investigation of the emissive properties of biosensors in order to allow their quantitative use in biomolecular interaction studies, to 2) the development of an original experimental approach to enable resolving the structural relaxation kinetics of an out-of-equilibrium distribution of biomolecular structures, and finally 3) the technological application of time resolved fluorescence for precise, rapid, cost effective, biomolecular interaction assays, appealing both for academic and industrial arenas.

**Résumé en français**

La spectroscopie UV-Vis résolue en temps a été appliquée à l'étude de différents systèmes moléculaires dont la photophysique est contrôlée par leur interaction avec l'environnement, mais aussi comme outil pour révéler des interactions moléculaires ou des dynamiques structurales à des échelles de temps comparativement lentes (sec à min.), en utilisant la microfluidique de gouttes pour déclencher une relaxation structurale par des conditions initiales hors équilibre. J'ai appliqué cette approche selon trois axes allant de 1) l'étude approfondie des propriétés émissives des biosensors afin de permettre leur utilisation quantitative dans les études d'interactions biomoléculaires, à 2) le développement d'une approche expérimentale originale pour permettre la résolution la cinétique de relaxation structurale d'une répartition hors équilibre des structures biomoléculaires, et enfin 3) l'application aux biotechnologies à haut débit de la fluorescence résolue en temps pour des analyses d'interactions biomoléculaires précises et rapides, pertinente à la fois pour les domaines académiques et industriels.